Imperial College London

# Electrochemical-mechanical corrosion phenomena

Aigerim Omirkhan

April 2021

Department of Materials

Imperial College London

Submitted in part fulfilment of the requirements for the degree of

Doctor of Philosophy of Imperial College London

and the Diploma of Imperial College London

# Abstract

The substantial number of parameters and their interdependence makes the modelling and prediction of erosion-corrosion rates a challenging task, yet owing to increasing computational capacity one that is potentially solvable. To accurately estimate the rate of material loss, universally accepted explanations of the mechanisms of combined erosion and corrosion must be developed. The absence of reliable data can undermine the safety and predictability of industrial processes, such as oil and gas transportation. The aim of this work is to demonstrate the application of an electrode scratching technique coupled with microstructural characterisation for improved understanding of synergy in erosion-corrosion.

In this PhD thesis, a rotating disc electrode scratching setup, with well-defined and controlled flow conditions, was developed to study the factors affecting erosion-corrosion. Linear potentiodynamic and potentiostatic polarization techniques were used to reproducibly monitor the kinetics of dissolution and repassivation of API X65 carbon steel and AISI 316L stainless steel electrodes upon scratching. Samples characterised using high-resolution scanning electron microscopy (SEM) and white-light interferometry (WLI), confirm the synergy; the losses due to erosion-corrosion are larger than that of the summation of the separate contributions of erosion and corrosion. Focused Ion Beam (FIB) milling was implemented for *in-situ* lift-out of lamellae from scratched samples for Transmission Electron Microscopy (TEM) characterisation. Distinct microstructural changes in the vicinity of scratches were confirmed with nanoscale grain refinement and orientation changes observed. These results, coupled with electrochemical data and micro-hardness measurements, suggest time-dependent surface-hardening processes affect material loss rates during mechanical-electrochemical coupled corrosion. Samples subject to jet impingement erosion-corrosion confirm similar microstructural changes take place, thus making an electrode scratching setup a versatile tool for studying erosion-corrosion, as well as a quick assay tool for development and testing of corrosion inhibitor formulations for industrial applications as demonstrated in this thesis.

# Declaration of originality

I hereby declare the thesis is the result of my own work, and information derived from other's work have been acknowledged and referenced accordingly.

# Copyright declaration

# Acknowledgements

Children start school at the age of 6 in Kazakhstan. My mom was a college chemistry teacher at the time and used to collect me from school. She took me with her to work and I used to sit at the back of the chemistry class trying to be as quiet as possible. There was a huge wall-sized periodic table, known as 'Mendeleyev's table of elements' back home, and molecular model kits I used to play with. Sometimes mom would take me to her small lab at the back of the class, where every item looked mysterious and fascinating (talk about beautiful vintage balances, but as one can expect, children were not really allowed to play with them). I guess this is my frail attempt of trying to how grateful I am to my mom **Raisa** for showing me into the scientific world. To **Amanbek**, my little brother, for his support and being next to mom when I was over 2700 miles away from home. To all my big family for their love and encouragement.

When I embarked on a PhD journey I did not know what the future held for me. I was very lucky to meet my colleague, turned boyfriend, fiancé and husband at Imperial. The submission of this thesis would not have been possible without you, **Kris**. Your support, care and love were shining through every day - be it long hours in the lab or the electron microscopy suite, through the time difference in Dallas and Tokyo, or writing up/tackling writers' block in the confinement of the London apartment during lockdown. Thank you for your kind heart and for always being there for me.

I would like to express my immense gratitude to my supervisors Professor **Mary Ryan** and Professor **Jason Riley** for their academic guidance, intellectually stimulating conversations and their sincere belief in my abilities. Their office doors were always open for me and they were truly my guiding stars. Mary, you are a brilliant role model to me and many other women in science and I am so happy I have a chance to work with you.

The funding for this work was provided by Shell International *via* Shell-Imperial Advanced Interfacial Materials Science (AIMS) centre. I would like to thank my mentor Dr **Tom Bos** for his valuable insights regarding this thesis and his technical advice. Dr Damodaran Raghu, Dr Hans Sonke, Dr Steve Paterson, Lauriane Larquey, Dr Guoqiang Yang, Dr Brian Chambers,

Dr Richard Pollard and other Shell team I forgot to mention for their advice and scientific discussions. Thanks to Irina Ward, Roger Pun and Zhumassulu Bissekenova for hosting me during a month-long internship at North Caspian Operating Company as a corrosion engineer. I also would like to express my gratitude to Dr Izumi Taniguchi and Ayaulym for hosting me in their lab during Imperial-Tokyo Tech exchange.

I really appreciate the advice and discussions held with Dr Finn Giuliani, Dr Ben Britton, Giorgio, Tommaso and Eden regarding nanoindentation. Many thanks to Professor Julian Wharton for providing me with access to nCATS facilities and Dr Terry Harvey for his help with jet impingement experiments. I am deeply grateful to Harvey Flowers Electron Microscopy facility staff Dr Mahmoud Ardakani, Dr Ecaterina Ware and Dr Catriona McGilvery for their continuous support with microscopy; Dr Sarah Fearn for her support with SIMS, as well as Dr Richard Chater, Professor Daniele Dini and Pawel Orzlowski for WLI access. Thanks go to the departmental technician Ben for his help with metal preparation and materials workshop supervisor Russel for his help with building the scratching setup and disc cutting. Special thanks to Catherine, Darakshan and Alba for their help with PhD admin.

To my colleagues and peers, who made doing PhD fun and endurable. Thank you Milly for answering all AIMS related questions and fun days at SLAC in Stanford; Dr Jiahui Qi for being the first person I approached with lab related questions; Mak, Liya, Emma, Noora, Fatima, Mariyam and Ahmed for insightful discussions regarding corrosion and science; thank you Eleonora and Joe for helping out with sample characterisation when the labs closed due to Covid-19; Sarah and Caoimhe for friendly lunches (and belly dancing), later joined by Jon and Elena for 'remote' coffee calls over Teams; Minos, Faisal, Dafni, Lukas, Ornapsorn and Ahmad for being brave enough to go from MSc to PhD with me. #KzPhdGirlsUnion project for inspiring me to keep going with my STEM career; Elya, Dana, Iggy for making me feel at home in London and all the hiking trips; my best friends in Kazakhstan Guska, Araika and Zhanka for their love and emotional support. For all my friends who encouraged me to keep going (Nazym, Marzhan, Sanya, Galiya, Dalida, Nouf and many others), I am deeply thankful that you believed in me. Last but not least, I am indebted to my *alma mater* Nazarbayev University for the fantastic opportunities and Imperial College London for the brilliant scientific community.

...Ğalym bolmai nemene,
Balalyqty qisaŋyz?
Bolmasaŋ da uqsap baq,
Bir ğalymdy korseŋiz.
Ondai bolmaq qaida dep,
Aitpa ğylym suiseŋiz.
Sizge ğylym kim berer,
Janbai jatyp sonseŋiz?

Abai Qunanbaiūly (1845–1904)

# Contents

# List of Figures

# List of Tables

# List of Acronyms

**AIMS** Advanced Interfacial Materials Science centre

**AISI** American Iron and Steel Institute

**API** The American Petroleum Institute

**ASA** Alemnis Standard Assembly

**ASTM** American Society for Testing and Materials

**bcc** body-centered cubic

**bct** body-centered tetragonal

**BF** bright field

**BSE** backscattered electron

**CBED** convergent beam electron diffraction

**CCD** charge-coupled device

**CE** counter electrode

**CI** corrosion inhibitor

**CMC** critical micelle concentration

**CRA** corrosion resistant alloy

**DF** dark field

**DI** deionised

**DO** dissolved oxygen

**DTAB** (1-dodecyl)trimethylammonium bromide

**EDM** electrical discharge machining

**EDS** energy-dispersive spectroscopy

**fcc** face-centered cubic

**FEG** field emission electron gun

**FIB** focused ion beam

**GND** geometrically necessary dislocation

**HAADF** high angle annular dark field

**HER** hydrogen evolution reaction

**HV** Vickers hardness

**ICP** inductively coupled plasma

**ISE** indentation size effect

**KHP** potassium hydrogen phthalate

**LMIG** liquid metal ion gun

**LMIS** liquid metal ion source

**LSV** linear scanning voltammetry

**MCP** micro channel plate

**MSE** mercury-mercury sulphate electrode

**nCATS** national Centre for Advanced Tribology

**NHE** normal hydrogen electrode

**OCP** open-circuit potential

**OD** outer diameter

**OES** optical emission spectrometry

**PEEK** polyether ether kethone

**PMT** photo-multiplier tube

**ppb** parts per billion

**ppm** parts per million

**PTFE** polytetrafluoroethylene

**RDE** rotating disc electrode

**RE** reference electrode

**RPM** rotations per minute

**SAED/SAD** selected area electron diffraction

**SE** secondary electron

**SEM** scanning electron microscopy/microscope

**SIMS** secondary ion mass spectrometry

**SSD** statistically stored dislocations

**STC** Shell Technology Centre

**STEM** scanning transmission electron microscopy

**TEM** transmission electron microscopy/microscope

**ToF** time-of-flight

**TTAB** (1-tetradecyl)trimethylammonium bromide

**WE** working electrode

**WLI** white light interferometry

# Chapter 1

# Introduction

The mechanism of metal degradation taking place during the combined action of erosion and corrosion is not fully understood owing to the complexity of the problem. **Erosion-corrosion**, also known as mechanical-electrochemical coupled corrosion, may occur under both single and multiphase flow conditions. Severe material degradation of oil and gas production and transportation systems is known to take place in multiphase flow systems, including flows that have suspended solid particles (*e.g.* sand), vapour bubbles in liquid flow (*e.g.* carbon dioxide or hydrogen sulfide in transportation of hydrocarbons), or liquid droplets in gas flow (*e.g.* condensation of water in steam turbines).

Special attention is paid to accelerated material loss in locations at which the geometry changes suddenly, such as pipe bends, tube inlets or orifice plates - places where disturbed flow conditions arise [1]. Surface defects on smooth pipelines; such as deposits, corrosion pits or weld beads, also create localised disturbed flow. The hydrodynamic and diffusion boundary layers are disrupted under such flow, leading to the establishment of a transient condition, rather than the equilibrium condition. Hence, corrosion rates predicted using equilibrium conditions fail to foresee higher localised corrosion rates under disturbed flow [2].

Impacts from particles initiate solid particle erosion of the material that contacts the carrier fluid. The erosion rate depends on hardness, ductility, toughness and surface roughness of the target wall (pipeline), as well as on particle properties such as hardness, shape, size and sharpness. The concentration, velocity and impact angle of the particles also affect the erosion rate [3].

It is known that the presence of corrosive media usually exacerbates material degradation rate. Despite the individual components being extensively studied, when it comes to combined action of erosion and corrosion, the mechanisms of material loss are still unclear. The **synergy**

between these processes results in material loss rates that are different from the sum of individual erosion and corrosion rates. Introduction of the electrochemical corrosion component increases the number of variables that affect material loss rate. These include environmental parameters such as temperature, pH and dissolved oxygen, as well as the development of surface roughness during corrosion [4].

The substantial number of parameters and their interdependence makes the modelling and prediction of erosion-corrosion rates a challenging task, yet owing to increasing computational capacity potentially solvable. However, more fundamentally, the lack of universally accepted explanations of the mechanisms of combined erosion and corrosion leads to the absence of an accurate material loss rate estimation model. This can lead to serious health and safety related issues, particularly in the oil and gas production and transportation, where significant amounts of solid particles can be found in fluids. The motivation for this project, therefore, comes from the aspiration to gain an understanding of interdependent mechanisms and thus to improve the corrosion prediction and protection of materials.

The aim of this PhD project is to elucidate the mechanisms of the electrochemical-mechanical corrosion of metals, which have applications in the oil and gas industry, such as API 5L X65 steel and 316 stainless steel. The robust electrode scratching apparatus was built to estimate the individual degradation rates of erosion-corrosion components under well-defined flow conditions. The electrochemical methods were applied to study the influence of flow rates, solution chemistry and corrosion inhibitors on both repassivation and degradation of the metals. Samples subject to erosion-corrosion were also studied using advanced materials characterisation techniques to gain an insight into the mechanisms at the micro- and nanoscale.

The outline of the thesis is the following. **Chapter 2** provides the review of the relevant erosion-corrosion literature. The parameters influencing erosion-corrosion are presented, including the properties of the pipeline material, erodent and the environment. Along with the erosion-corrosion mechanisms, metal repassivation studies are summarised as they lay an important foundation of the electrode scratching technique implemented in the current work.

**Chapter 3** presents the theoretical background to the experimental techniques used in this study. The general experimental approach is also summarised, yet more specific methodology is provided in the subsequent Chapters 4, 5, 6 and 7, where the results of this study are presented.

**Chapter 4** studies the fundamental erosion-corrosion behaviour of X65 carbon steel and 316 stainless steel using the electrode scratching setup. Initially, the corrosion mechanisms of samples were studied using the linear scanning voltammetry. The samples were then scratched repeatedly under potentiostatic control, for conditions where the metals would be under ca-

thodic protection, active corrosion and anodic passivation.

**Chapter 5** demonstrates the application of the electrode scratching setup for decoupling the components of erosion-corrosion. Using the combination of the electrochemical measurements with white light interferometry the rates of pure erosion, pure corrosion and synergy were estimated for both X65 carbon steel and 316 stainless steel.

The influence of erosion-corrosion on the microstructure of X65 carbon steel and 316 stainless steel is investigated in **Chapter 6**. Methods such as scratch cross-section microindentation and transmission electron microscopy were used. Furthermore, the results of the jet impingement erosion-corrosion and the subsequent microsctructural evolution are presented.

Another application of the electrode scratching setup as a corrosion inhibitor testing technique is demonstrated in **Chapter 7**. The influence of (1-tetradecyl)trimethylammonium bromide and sodium nitrite on corrosion inhibition and passivation was evaluated.

Finally, the conclusions of this thesis, along with the recommendations for future work are given in **Chapter 8**.

# Bibliography

[1] J. Postlethwaite and S. Nešić. Erosion-Corrosion: Recognition and Control. *Uhlig's Corrosion Handbook: Third Edition*, pages 907–913, 2011.

[2] Flow effects on corrosion. In R. W. Revie, editor, *Uhlig's Corrosion Handbook*, chapter 17, pages 203–213. John Wiley & Sons, Inc., third edition, 2011.

[3] A. Levy. *Solid particle erosion and erosion-corrosion of materials*. ASM International, Materials Park, 1995.

[4] M. Parsi, K. Najmi, F. Najafifard, S. Hassani, B. S. McLaury, and S. A. Shirazi. A comprehensive review of solid particle erosion modeling for oil and gas wells and pipelines applications. *Journal of Natural Gas Science and Engineering*, 21:850–873, 2014.

# Chapter 2

# Literature review

## 2.1 Introduction

Erosion-corrosion can be defined as a combination of erosion and corrosion processes taking place in a flowing corrosive media, in which material degradation takes place [1]. In the majority of cases erosion-corrosion leads to accelerated material loss, however, on rare occasions repassivation of the protective oxide layer can slow down the degradation rate [2]. To avoid confusion owing to inconsistencies in the terminology used in the field, definitions are presented based on ASTM G40-15 standard and some reported studies [3, 4, 5]. The total material loss rate, $\dot{w}$ , is defined as the sum of individual erosion, $\dot{e}$, and corrosion rates, $\dot{c}$ (Equation 2.1).

$$\dot{w} = \dot{e} + \dot{c} \tag{2.1}$$

Material wastage rate due to erosion is the sum of pure erosion, $\dot{e}_0$, and corrosion-enhanced erosion rates, $\dot{e}_c$ (Equation 2.2), whereas corrosion is comprised of pure corrosion, $\dot{c}_0$, and erosion-enhanced corrosion, $\dot{c}_e$ (Equation 2.3).

$$\dot{e} = \dot{e_0} + \dot{e_c} \tag{2.2}$$

$$\dot{c} = \dot{c_0} + \dot{c_e} \tag{2.3}$$

Hence, the rate of synergy, which is an indicator of accelerated material wastage due to erosion-corrosion, $\dot{s}$, can be defined as the sum of corrosion-enhanced erosion and erosion-enhanced corrosion rates as shown in Equation 2.4.

$$\dot{s} = \dot{e_c} + \dot{c_e} \tag{2.4}$$

Poulson [6] described a spectrum of erosion-corrosion processes where degradation mecha-

nisms vary from film dissolution to mechanical process dominated. Figure 2.1 describes this in detail: on the left the processes are dissolution dominant, while the mechanical damage dominated processes are shown on the right. From a mechanistic point of view, understanding and determining the erosion-corrosion rates under conditions where the passivating film is removed and mechanical damage takes places (indicated by the red rectangle in Figure 2.1) is quite challenging. An ability to deconvolute each of the erosion-corrosion components would be indispensable in gaining mechanistic understanding of complex erosion-corrosion processes.

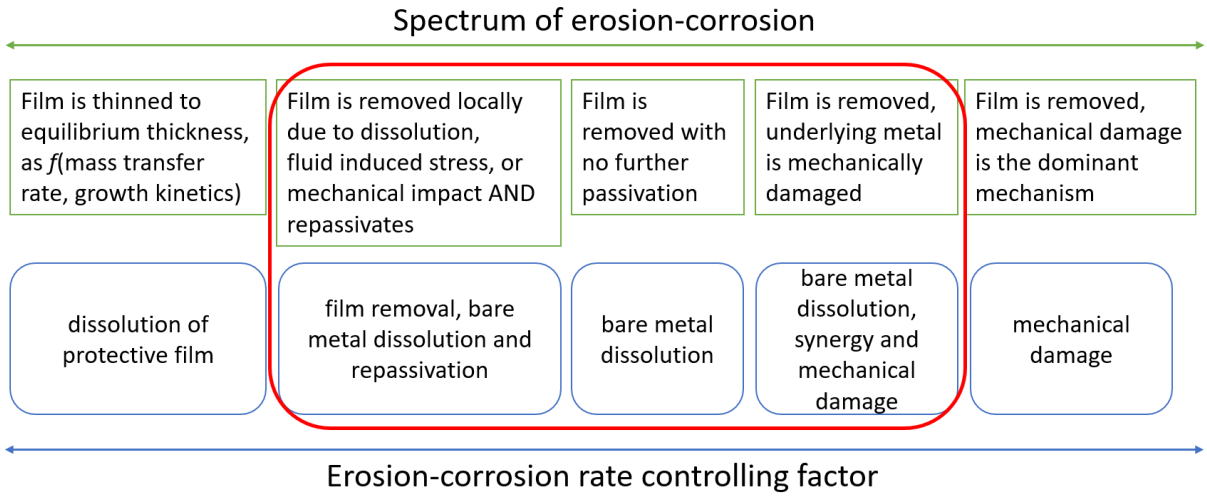


Figure 2.1: Erosion-corrosion spectrum. Adapted from Poulson [6].

The complexity of erosion-corrosion processes can be demonstrated using an example of oil and gas transportation pipelines. Various fluid-wall interactions occur in these pipelines, initiating erosion-corrosion events. As such, an underlying metal may corrode due to flow-induced dissolution of the protective film. Particles in the flow can also mechanically rupture the oxide layer and erode the bare metal, leading to greater localised corrosion. Figure 2.2 summarizes some of the fluid-wall interactions taking place in the system.

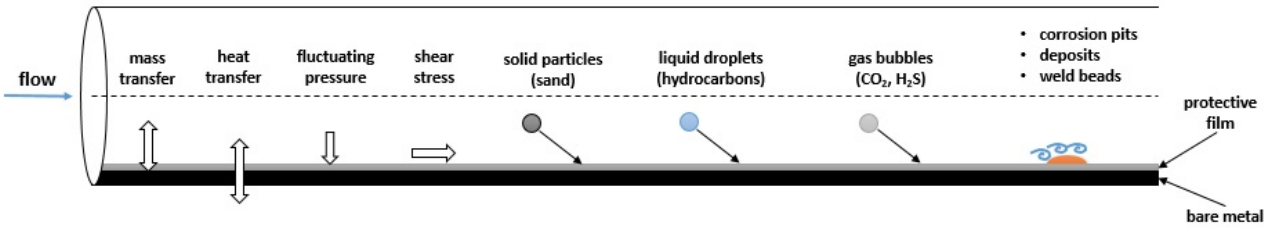


Figure 2.2: Fluid-wall interactions that lead to erosion-corrosion of the pipelines. Adapted from Postlethwaite and Nešić [7].

Postlethwaite and Nešić [7] classified the next five types of mechanical impacts initiating erosion-corrosion: turbulent flow, solid particle impingement, liquid droplet impingement, gas bubble collision and collapse of vapour bubbles. The large diameter oil and gas transportation pipelines create turbulent flow conditions, under which it is difficult to differentiate between the individual inputs of mechanical forces and enhanced mass transport. Erosion-corrosion studies require controlled alteration of the parameters under well defined flow conditions. The research done in the field use a wide range of techniques to study erosion-corrosion, normally altering several different parameters. Many of these focus on identifying overall material wastage rates and are often empirical. Comparison of the results is challenging due to usage of varying steel grades, impinging particles and environment.

This chapter will provide an overview of the erosion-corrosion literature with a focus on low carbon steel and stainless steel. The former is a widely used material for transportation pipelines, while the latter is used in locations susceptible to erosion, such as bends and tees. The first part of the literature review concentrates on the analysis and evaluation of the parameters influencing erosion-corrosion, including properties of the pipeline material, fluid flow and erodent particles. It is followed by a critical investigation of the mechanisms of synergy in erosion-corrosion and the methods used to study them. Furthermore, knowledge gaps in the field, upon which the motivation for this work was drawn, are discussed.

## 2.2 Parameters influencing erosion-corrosion

The degree of degradation of pipelines under corrosive fluids containing gas bubbles or solid particles depends on various parameters. For oil and gas transportation pipelines, these can be divided into the properties of the pipeline material, fluid flow and the particulates. Parametric effect of the variables are presented accordingly.

### 2.2.1 Properties of the pipeline material

#### Corrosion resistance

Carbon steel is widely implemented in oil and gas transportation pipelines due to its relatively low price. However, low alloy carbon steel is susceptible to corrosion as the oxide layer formed on its surface is not protective under most operating conditions. Its corrosion can be described by the anodic reactions shown in Equation 2.5. Under de-aerated conditions the cathodic reaction is that in Equation 2.6, while in presence of oxygen and in neutral or alkaline conditions the

reaction in Equation 2.7 takes place [8].

The overall reaction then results in formation of ferrous ($Fe(OH)_2$) and ferric ($Fe(OH)_3$) hydroxides on the surface that is commonly referred to as scale or a diffusion barrier. Scale is formed by anodic dissolution of the bare metal followed by precipitation. It is relatively thick, porous and prone to damage compared to passive films, hence carbon steels experience more severe erosion-corrosion attack in slurry flow [7].

$$Fe \longrightarrow Fe^{2+} + 2\,e^- \quad \text{(anodic dissolution of iron to ferrous ions)} \tag{2.5}$$

$$2\,H^+ + 2\,e^- \longrightarrow H_2 \quad \text{(cathodic reduction of hydrogen)} \tag{2.6}$$

$$O_2 + 2\,H_2O + 4\,e^- \longrightarrow 4\,OH^- \quad \text{(cathodic reduction of oxygen)} \tag{2.7}$$

The structure of the scales is very complex and changes depending on the environmental conditions. The scales formed in air, aqueous solutions or at high temperatures under oxidising conditions will have different characteristics. The thickness of the scale and the thickness ratios of its constituents vary depending on formation temperature, heat treatment and alloying [9].

The layer closest to the metal substrate is called wüstite (FeO) and has the lowest oxygen content. The interlayer is formed of magnetite ($Fe_3O_4$), whereas the final thin oxygen rich layer is haematite ($Fe_2O_3$).

The scale on carbon steel may serve as a physical barrier to further oxidation of the bare metal, however under erosion-corrosion it can be easily damaged due to the hydrodynamic effects of the flow and impact of solids or gases. This behaviour is different to that seen in passive film forming steels such as stainless steel. To discuss the erosion-corrosion phenomena in thin oxide layer forming alloys, it is necessary to introduce passivity in metals and alloys. **Passivity** is the resistance of the metal or alloy to oxidation despite a high thermodynamic driving corrosion force. It is known that stainless steel owes its resistance to corrosion to the formation of a very thin (1-3 $nm$), yet strong oxide layer on its surface. The composition and nanostructure of the passive layer depends on the environment as well as processing and electrochemical history of the material. A detailed review of this can be found in the literature [10].

One key aspect of austenitic stainless steel is the tendency to form multi-layer passive films whenever the bare surface is exposed to an oxidising environment, thus preventing further dissolution of the metal. Surface studies of austenitic steels in acidic media have suggested a three-layer model of passive film formation, where a 'hydroxide layer' is formed as the outer layer and an 'oxide layer' is found in the inner layer - these layers have varying amounts of

Fe and Cr depending on the formation conditions. The oxy-hydroxide layers are followed by a nickel enriched layer that originates from the preferential oxidation of iron and chromium [11]. The composition of the passive film is strongly dependent on the environment: the one formed in alkaline solution is different from that formed in acidic conditions since the solubility of the iron is low, limiting the chromium enrichment of the passive layer [10].

The complexity of predicting erosion-corrosion rate of a material can be inferred from the dynamic nature of the passive film. The composition of the passive film changes from system to system and is dependent on environmental parameters such as potential, presence of aggressive ions such as chlorides; pH, temperature, as well as microstructure and phase [10]. Adding erodent particles and flow to the system complicates it further. Further discussion on passivation of metals based on electrode scratching approaches can be found in section 2.5.

### Hardness

Carbon steel pipeline grades such as API X65 and X70 are usually employed as materials for oil and gas transportation pipelines. Corrosion resistant alloy grades like 316L stainless steel are employed in chemical process applications and at those parts of the transportation lines which are particularly erosion-corrosion prone such as pipe bends. Physical properties of the pipeline material, including hardness and density, were incorporated into the early models of erosion by Wada, Watanabe [12] and Hutchings [13], where erosion was related *via* a power law to the ratio of target material hardness to erodent particle hardness. It was found that for pure metals, erosion rate decreased with target material hardness, while alloys hardened *via* conventional mechanisms did not show this behaviour [14]. Alloys may work-harden upon impact of particles and the localisation of plastic deformation at impact sites determines the susceptibility to erosion. As such, the erosion rate typically decreases with increasing ratio of hardness to Young's modulus [15].

Barik *et al.* [15] studied the surface hardness change of a copper alloy under erosion and erosion-corrosion conditions. Studies with jet impingement rigs showed a surface hardness increase from 1.8 $GPa$ up to 4.0 $GPa$ at the bottom of the scars after particle impacts, as measured by Vickers microhardness indenter. Nevertheless, under erosion conditions only this led to higher mass loss rates, while in corrosive 3.5% NaCl electrolyte, lower mass loss rates were recorded. The authors related this to selective phase corrosion of the alloy. Hence, to grasp a full picture of the phenomenon, it is necessary to understand the transformation of intrinsic properties of the pipeline material, including microstructure evolution, under specific flow conditions.

### Microstructure

Stainless steel can be divided into four main groups by microstructure: austenitic, ferritic, duplex (mixed austenitic and ferritic) and martensitic. Due to its corrosion resistance, austenitic stainless steel is commonly used in the oil and gas industry. Austenitic stainless steel is alloyed with $\gamma$-phase stabilisers such as nickel, and chromium and molybdenum are added to increase the resistance to both general and localised corrosion. The advantages of austenitic stainless steels are higher toughness, ductility and corrosion resistance. They can also be cold worked to achieve a yield strength of up to 2000 $MPa$ [16].

The microstructural changes taking place in austenitic 316 stainless steel after erosion and erosion-corrosion slurry pot tests were studied by Wood *et al.* [17, 18]. Examination of surface morphology by SEM revealed the presence of impact craters and the formation of lips. A sub-surface microstructure study using cross-sectional FIB and TEM showed the presence of extended cracks along with embedded particles from impacts. Selected area electron diffraction showed the transformation of the original fcc $\gamma$-phase to bct $\alpha$'-martensite both after pure erosion and combined erosion-corrosion experiments (see Figure 2.3). During pure erosion tests, phase transformation happens due to lattice slip and distortion upon the impact of the particles. Hence, work hardening of the surface takes place, and the characteristic length of the formed lips under erosion conditions is smaller than that for erosion-corrosion. Notably, introduction of the corrosive solution (NaCl) resulted in a reduction of martensitic phase as seen from Figure 2.3. The authors claim it is unlikely that the presence of corrosive media affected the impacts, therefore it was assumed that preferential dissolution of the martensitic phase took place. Less martensitic phase results in less work-hardening, leading to formation of longer lips as evidenced by micrographs. This result contradicts the findings of Li and Li [19] who claimed that lips formed upon impacts on copper would dissolve preferentially. However, the passivation mechanism of the stainless steel is different, which partially explains the discrepancy in predictions, although both metals require stabilisation by an oxide. Previous study by Yin and Li [20] also showed an increased corrosion rate of impact-fractured AISI 1045 steel specimens compared to undeformed specimens. Here, higher dislocation density created by the impacts established favourable conditions for electrochemical dissolution as identified by electron work function values and polarisation studies. Overall, it is agreed that erosion-corrosion leads to a higher mass-loss rate. Whether it is a dissolution of the particular phase or that of the lips formed upon particle impacts is not clear yet.

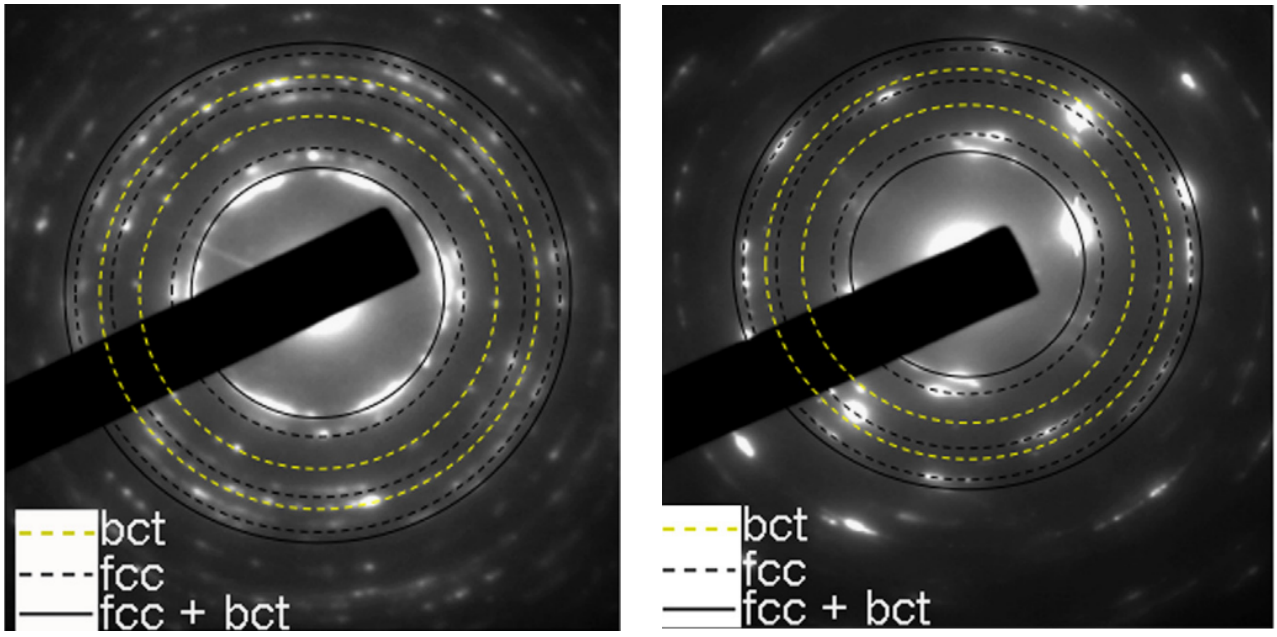


(a) (b)

Figure 2.3: SAED pattern observed in the sample exposed to: a) erosion and b) erosion-corrosion. Reprinted from Wood *et al.* [17] with permission. Copyright (2013) Elsevier B.V.

Wang *et al.* [21] studied the influence of the carbon steels microstructure on erosion-corrosion. The relationship between material wastage rates and the microstructure was deemed complex, with contributions from the ductility and the strength of the metal, as well as the properties of the scale formed on the surface. The authors concluded that increasing the amount of pearlite and having smaller grain size creates improved paths for chromium diffusion, hence creating a protective scale with higher chromium content [21]. A study conducted by Islam and Farhat [22] concluded that API X42 steel consisting of 86% proeutectoid ferrite and 14% pearlite (alternating lamellae of eutectoid ferrite and cementite $Fe_3C$) by microstructure, showed preferential dissolution of the eutectoid ferrite, leaving behind the network of cementite in pearlite. Subject to the morphology of cementite networks, they can provide better anchoring of the oxide film to the surface, thus protecting the metal from further oxidation.

### Surface roughness

Sasaki and Burstein [23] studied the correlation between surface roughness of 304L stainless steel and its pitting potential. The pitting potential, in electrochemistry, describes the tendency of the metal or alloy to undergo pitting, a form of localized corrosion; and defines the potential at which stable pitting occurs. They concluded that a higher surface roughness reduced the pitting potential, therefore making the pit more likely to survive and propagate. Metastable pits existing at deeper, less open sites, such as those generated by surface roughness, were less

likely to repassivate and die. The authors showed that pre-ground samples subject to solid particle erosion had lower pitting potential than those subject to grinding only. Hence, erosion also enhances pitting susceptibility of the stainless steel, owing to the probability of the stable pit being generated at occluded sites where the oxide was removed due to solid impingement.

Li and Li [19] also observed electrochemical effects of surface roughening for copper. The work function, which is the minimum energy required to remove an electron to a region adjacent to the solid, was measured using a scanning Kelvin probe on surfaces with varying roughness. It was concluded that rougher surfaces had higher corrosion rates and lower work function. Preferential dissolution of the peaks was observed as the surfaces became smoother after corrosion. Similar result was shown by Kim *et al.* [24], where carbon steel corrosion rates increased with the surface roughness. Rougher surfaces with higher Volta potential difference between the peak and the valley had a thermodynamic inclination towards corrosion.

### 2.2.2 Properties of the flow

#### Velocity

A review of the velocity effects on erosion-corrosion should be carried out with great care since two types of velocity are generally reported in the literature: one being the velocity of the *flow*, and the other being the velocity of the *particles*. The velocity of the particles has a prominent effect on erosion since it directly influences the impact energy, and in addition, at higher velocities the time between successive impacts shortens, leaving less time for repassivation of the surface. Material loss rate is related to velocity *via* a power law (Equation 2.8).

$$\dot{w} \propto KV^n \tag{2.8}$$

where $K$ is the system-dependent constant, $V$ is the velocity of the particle and $n$ is the velocity exponent which usually varies between 1.6 and 2.6 depending on the test equipment and environment used [25].

Experiments with 316 stainless steel identified the exponent to be 2.1 in pure erosion conditions with silica sand at 1 $wt.\%$ concentration [26], while in a solid-free environment it was equal to 1.07 for austenitic cast iron. However, when the media is corrosive, the mechanism becomes more complicated. As such, the velocity of the fluid increases corrosion rate *via* enhancing the mass transfer. At the same time, the rate of repassivation of the protective layer can be increased by improved dissolved oxygen transfer. Therefore, depassivation (activation) and repassivation rates play crucial roles in investigating erosion-corrosion of stainless steels.

Cheng and Yang [27] studied the parametric effects on erosion-corrosion of X65 carbon steel in oil sand slurries. Rates of individual constituents of erosion-corrosion were obtained at flow velocities of 1, 3 and 5 $m\,s^{-1}$ using a jet impingement loop system. It was shown that the material degradation rate increased with increasing velocity and the contribution of corrosion to this increase was negligible. Potentiodynamic polarisation curves of X65 steel after 12h of experiment at 5 $wt.\%$ sand-loading are presented in Figure 2.4. The authors argued that under static conditions the metal is in the passive state. Tafel extrapolation of the cathodic and anodic polarization curves shows that the corrosion current increased from *ca.* $7 \times 10^{-6}$ $A\,cm^{-2}$ to *ca.* $2 \times 10^{-4}$ $A\,cm^{-2}$, once the transition from static to flowing conditions was made.

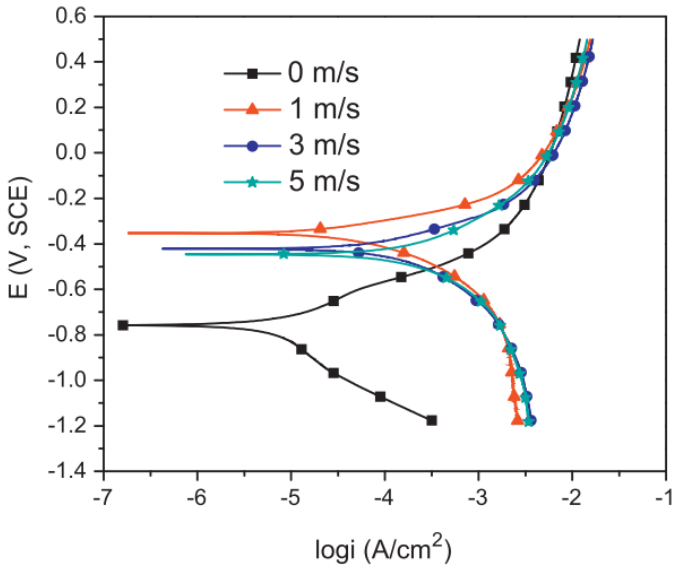


Figure 2.4: Polarisation curves of X65 steel in oil sands slurry at different flow velocities. Reprinted with permission from Yang and Cheng [27]. Copyright (2011) Elsevier B.V.

The behaviour of two different grades of stainless steel in a marine environment was studied with a similar jet impingement setup by Meng *et al.* [28]. A change in anodic current densities was observed with depassivation of stainless steel taking place when the velocity was increased from 7 to 20 $m\,s^{-1}$ at $20^{o}\,C$. Nevertheless, the sand loadings used for the tests were rather low - 50 and 500 $ppm$; compared to 1-2 $wt.\%$ sand particle loadings encountered in oil and gas transportation pipelines.

A study by Harvey *et al.* [5] revealed the dependence of corrosion and erosion-corrosion on fluid-free stream velocity between 3 and 12 $m\,s^{-1}$ at 1 $wt.\%$ sand loadings in 3.5% NaCl solution. They identified that the corrosion rate of carbon steel (En3B) was consistent with non-passivating metal degradation rates. The products of the metal oxidation are flushed away at higher velocities, hence increasing the overall corrosion rate. This is contrary to the previously mentioned study [27], where corrosion rate was deemed insignificant. However, it

should be noted that a slurry pot tester was used in Harvey's study. Also, the corrosion rate was determined from weight loss measurements using Faraday's equation, not *via* electrochemical polarisation studies. This can result in decreased accuracy of the corrosion rate predictions. Moreover, their experimental conditions cannot be directly related to oil and gas field conditions – erosion-corrosion mainly takes place inside the pipeline that is not exposed to sea water and it is highly improbable that the fluid would contain such a high concentration of salt.

At this point it is becoming clear why there is no agreement of mechanisms of erosion-corrosion of steels – researchers have performed experiments using different setups, different parameters, and different environments.

### Turbulence

Turbulence in the pipelines adds complexity in predicting hydrodynamic conditions. Nevertheless, the majority of transportation pipelines develop turbulent flow regimes due to their large diameter. Transition from well-defined laminar flow to turbulent flow depends on the value of the Reynolds number that changes with fluid viscosity, velocity and the characteristic dimensions of the pipeline. Hence, the effect of turbulence on erosion-corrosion can be closely related to that of velocity. However, calculation of the true Reynolds number under erosion-corrosion conditions is difficult as the friction factor of a pipeline also changes as surface degradation takes place during erosion [29]. Generally, the corrosion rates of steels increase with increasing degrees of turbulence due to increased mass transport – electroactive species are constantly supplied to the surface.

### Single and multiphase flow

Single flow is defined as a fluid flow of either gas or liquid. The mass transfer rate and wall shear stress relationships are applicable directly to flow regime modelling. However, most oil and gas transportation systems operate under multiphase flow regimes such as plug flow, annular flow, slug flow and others [30]. Flow regimes resulting from gas/water/oil/solid ratios and velocities affect the water turbulence and the type of pipeline wear. For example, one can expect highest wear rates at the '6 o'clock' location of the pipeline in slurry transportation systems. Slug flow, which takes place at very high turbulence, leads to flow-induced corrosion. On the other hand, stratified flow occurs in laminar conditions where corrosion takes place *via* underdeposit or pitting corrosion mechanisms. It is believed that slug flow, where large shear stress fluctuations take place, causes the most severe erosion-corrosion in oil and gas transportation systems [7].

### Dissolved oxygen

The effect of dissolved oxygen (DO) on the erosion-corrosion rate is dependent on oxygen transport that affects the corrosion rate. Equations 2.9 and 2.6 describe cathodic reactions that take place in acidic and basic aqueous media respectively. For these reactions to take place, the oxygen molecules need to be transported to the surface of the metal *via* diffusion or convection. If the oxygen reduction rate increases very quickly so that the amount of available oxygen molecules decreases, the rate of reduction will be limited by the transport of oxygen species through the media to the metal surface. This leads to a limiting cathodic current density that is independent of potential. The limiting current increases with an increased amount of the reducing oxygen species, otherwise termed DO. Therefore, increasing the amount of DO is expected to facilitate mass transport of the oxygen species to the surface of the metal [31]. This consequently is expected to increase the corrosion rate and is illustrated in Figure 2.5.

$$O_2 + 4\,H^+ + 4\,e^- \longrightarrow 2\,H_2O \tag{2.9}$$

Indeed, multiple studies of erosion-corrosion in solutions with varying dissolved oxygen content showed good correlation with this theory. For example, the study that concentrated on the effects of dissolved oxygen on erosion-corrosion in aqueous slurries, concluded that material degradation rate in slurry purged with nitrogen at 0.016 *ppm* [DO] was lower compared to the one in 1.56 *ppm* [DO] [32].

It should be noted that iron can passivate in certain solutions and requires a critical concentration of oxygen to passivate. This is well reported in the literature [8] but is not discussed in this work.

### pH

Several researchers have attempted to build erosion-corrosion wastage maps, which show the change of material degradation rate with different electrochemical parameters. Erosion-corrosion rates of the steels at different values of hydrogen ion concentrations often shows correlation with the behaviour predicted by Pourbaix diagrams. However, it should be noted that no reaction kinetics information can be obtained from them. Jana and Stack [34] composed erosion-corrosion wastage maps for pure metals including iron, copper, nickel and aluminium. They identified that at low pH values, the wastage of the metal was dominated by dissolution as predicted by thermodynamics. Comparable results were obtained when degradation of aluminium was studied in alkaline, neutral and acidic media. Erosion-corrosion maps were dominated by high

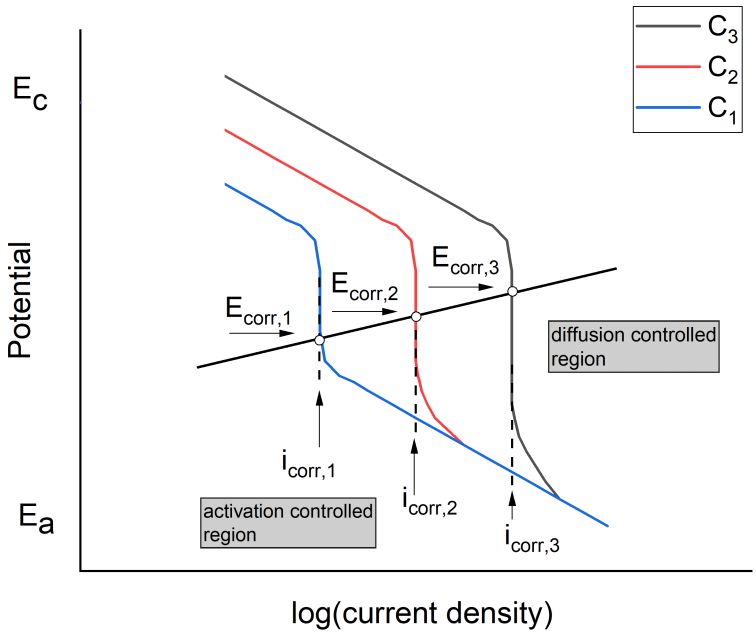


Figure 2.5: Dependence of corrosion behaviour on increasing amount of reducible species $C_1 < C_2 < C_3$ when mass transport is the rate controlling step. Redrawn from Thomas [33].

wastage regime at high pH in accordance with the corrosion of aluminium [35]. When alloying elements are added to pure metals (ex. Cr to Fe in stainless steel), erosion-corrosion maps echo the modified Pourbaix diagrams, *i.e.* there was a decrease of high wastage areas due to ability of stainless steel to form a passivating film therefore reducing corrosion rate of the material [36].

It was argued that not only the change of the pH affects the corrosion of the material but it also degrades the surface hardness of the material. Lu *et al.* performed *in-situ* nano-indentation tests to assess the change of the surface hardness of a carbon steel in acidic, neutral and basic media [3, 37, 38]. The researchers measured the change in hardness under cathodic protection and galvanostatic control. It was identified that severe corrosion-enhanced erosion took place due to reduced surface hardness of carbon steel according to Equation 2.10.

$$\frac{\Delta H_v}{H_v} = -B \log \left( \frac{i_A}{i_{th}} \right) \tag{2.10}$$

where $H_v$ is the surface hardness, $B$ is the material and test conditions constant, $i_A$ is the anodic current density, and $i_{th}$ is the threshold current density beyond which surface hardness changes. It should be noted that since the oxide layer is very thin, the hardness measured still has some contributions from the bare metal, therefore, such results should be interpreted with great care.

### Temperature

First and foremost, the rate of corrosion is known to change with temperature, with activation controlled reaction rates (*e.g.* proton reduction) seeing the highest impact. The rate of corrosion is affected by the change of exchange current density with temperature as per the Butler-Volmer equation (See Equation 3.9). Depending on whether the anodic oxidation happens film-free, *via* film formation or active-passive transition, the effect of temperature can vary and is described in detail in the literature [8].

The effect of the temperature on erosion-corrosion is well studied even though the mechanism is often quite complex. In the study completed by Hu and Neville [39], $CO_2$ corrosion of X65 carbon steel was studied in an oxygen free 100 $g\ L^{-1}$ $Cl^-$ solution using jet impingement apparatus at 20 $m\ s^{-1}$ velocity and 200 $mg\ L^{-1}$ sand concentration. An almost three-fold increase of material degradation rate was recorded when the temperature changed from $20^o\ C$ to $70^o\ C$, where the majority of material degradation happened due to erosion-enhanced corrosion (Figure 2.6). Despite the fact that the $FeCO_3$ is usually more protective at higher temperatures, constant flow over the metal surface does not allow the formation of the protective $FeCO_3$ scale, which normally prevents further bare metal oxidation in the presence of $CO_2$. This result needs to be interpreted with great care since the erosion component of the total weight loss was measured in a tap water solution using gravimetric analysis. It is arguable that such measurements can completely eliminate the corrosion component, as the steel is known to corrode in tap water under equilibrium conditions. Cathodic protection measurements are a more reliable way to calculate pure erosion as the anodic currents are much smaller in that case.

Under high operating temperatures in dry environments, the effect of temperature on erosion-corrosion of austenitic steel has been studied using a sand blast erosion tester at different impact angles. The target material is eroded using sand particles carried by dry air and the incidence angle of the particles can be varied by rotating the target material. Material degradation rate was shown to be almost constant at an impact angle of $30^o$ until reaching $400^o\ C$, with a rapid increase of mass loss rates at higher temperatures. At an impact angle of $90^o$ erosion rates slightly decrease with temperature until reaching a minimum at $400^o\ C$, after which mass loss rate of 310 stainless steel is known to rapidly increase. The tests were carried out in an undried nitrogen environment and the velocity of silicon carbide erodents was 30 $m\ s^{-1}$ [40]. For combined erosion-corrosion a similar trend was observed in 304 stainless steel in an air atmosphere using alumina particles of 1.2 $m\ s^{-1}$ velocity at an impact angle

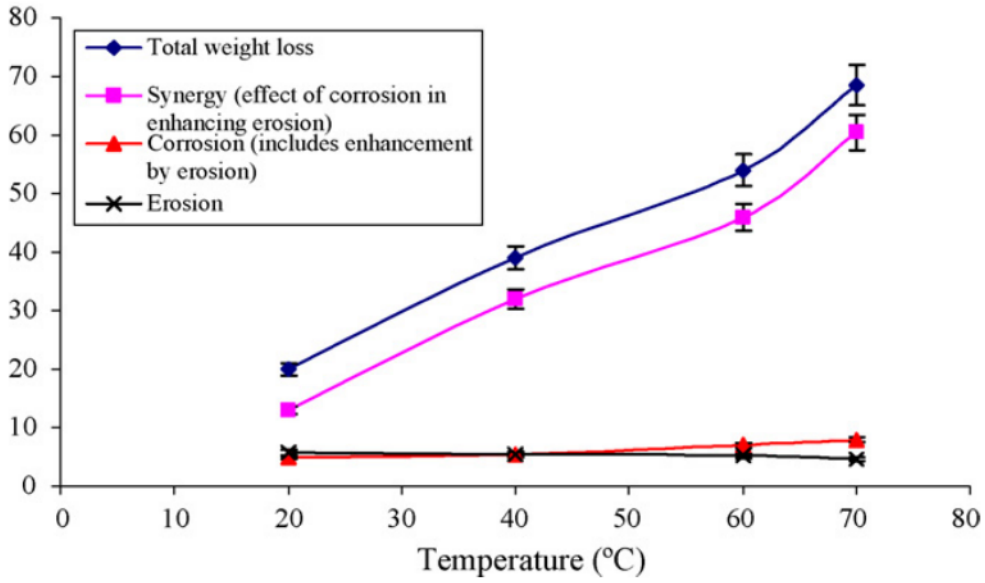


Figure 2.6: Erosion-corrosion (in mg) as a function of temperature at 20 $m\ s^{-1}$ jet impingement velocity and 200 $mg\ L^{-1}$ sand concentration. Reprinted with permission from Hu and Neville [39]. Copyright (2009) Elsevier B.V.

of $30^o$. Initially, material wastage rate slowly decreased until $350^o\ C$ possibly due to particle strengthening of the surface. This was followed by rapid material loss observed until $700^o\ C$ due to oxidation [41] It should be noted that at these high temperatures there is a risk of oxide instability, as noticed by the researchers. Care should be taken to deconvolute the complex effects of the temperature on erosion-corrosion components.

High temperature erosion-corrosion of materials was reviewed by Stack *et al.* [14]. The mechanism of material loss is said to be erosion dominated at lower temperatures and reaches a maximum due to the escalation of oxidation rate. As temperature increases, the exponential increase in the oxide formation rate is seen to follow Equation 2.11 [14].

$$K_p = K_o exp(-\frac{K}{T}) \tag{2.11}$$

where $K_p$ is the parabolic rate constant (given the scale growth is parabolic), $K_o$ and $K$ are constants for the particular oxide and $T$ is the temperature. This is followed by a decrease in material loss due to the thickening of the oxide scale layer such that less bare metal surface is exposed during the next impact event. The degradation mechanism happens mainly due to brittle chipping of the previously formed scale. It is important to say that the critical temperature, at which the oxide layer is thick and cohesive enough to not be removed, shifts to higher temperatures with increasing particle impact energy and increased oxidation resistance. This is illustrated in Figure 2.7.

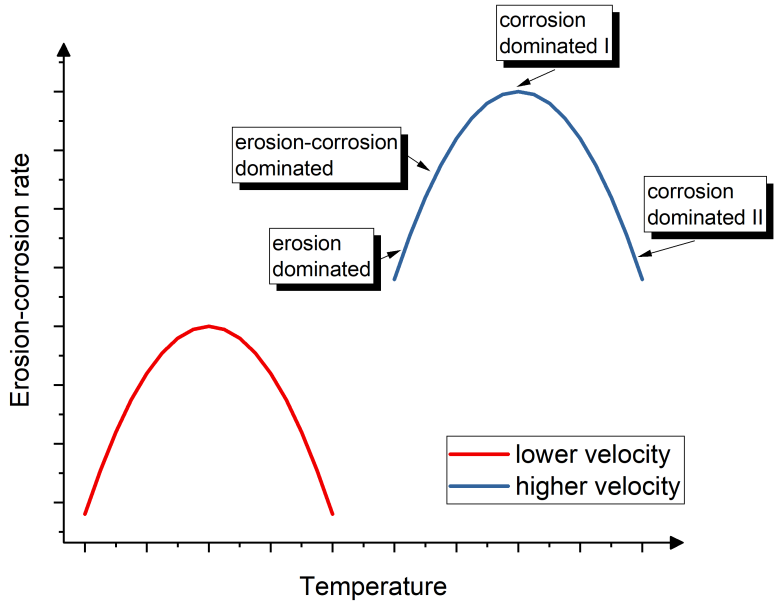


Figure 2.7: Schematic diagram showing erosion-corrosion regimes *versus* temperature at different velocities. Redrawn from Stack *et al.* [14].

It should be noted that the temperature also has an indirect impact on erosion-corrosion as well. Some examples include solubility of the carbon dioxide that changes pH of the media, or evolution of hydrogen and its transport within a microstructure [42]. Similarly, the oxygen diffusion coefficient increases 3% per degree K but its solubility decreases with temperature [8]. Therefore, it is important to account for the overall effect of temperature on the system, rather than considering its direct impact on erosion-corrosion.

### Particle impact angle

Erosion rate *versus* the angle at which incoming particles hit the target wall was quantified by Levy [40]. The severity of erosion of the target changes from brittle to ductile materials, which have different mechanisms of erosion. It is established that ductile erosion takes place *via* a platelet formation mechanisms, which is sometimes referred to as the ploughing mechanism [40]. In contrast, brittle materials mainly erode *via* initiation of micro-cracks, followed by their propagation. Material removal takes place during subsequent impacts [43]. Therefore, the maximum material loss for ductile materials, such as metals, takes place at impact angles between $30^o$ and $80^o$, for brittle materials this is known to occur at angles normal to the surface [2].

Under corrosive conditions, similar behaviour is seen for X65 carbon steel in oil sands slurry with sand concentrations up to 20 *wt.*%. The erosion component changed with angle, with

maximum material loss rate at $30^o$. Corrosion, however, remained unchanged on impact angle variation [27]. 304L stainless steel showed maximum erosion and erosion-corrosion rates at oblique angles between $40^o$ and $50^o$. Notably, positive synergy was recorded at all examined angles, *i.e.* the erosion-corrosion rate was higher than the erosion rate in 0.6 M NaCl solutions containing 13 $wt.\%$ silica particles under 3.8 $m\ s^{-1}$ flow velocity. [44]. No clear trend could be obtained on synergy *vs.* impact angle: the peak happened at $30^o$, followed by a decrease until $50^o$, after which it increased again until $70^o$.

The relationship between erosion and erosion-enhanced corrosion is subtle, but it was mainly explained by the pitting susceptibility of the stainless steel at oblique angles. At normal angles, the metal is indented, thus the passive film is still present at the surface preventing corrosion, albeit, depending on the properties of the film it may still be damaged. The disadvantage of the study is that the pure corrosion component was disregarded after 1 $h$ of potentiostatic tests [44]. However, under flowing conditions the thinning of the oxide film followed by either pitting or bare metal oxidation is expected to take place. While the particle size and its impact velocity had insignificant effect on impact angle dependence, care should be taken in interpreting the impact angle results in gases and liquids. Due to the larger drag experienced by the particles in liquid flow, the actual angle of incidence would be lower than the nominal incidence angle.

### Particle concentration

Two types of solid particles are most commonly employed in erosion-corrosion studies: alumina that show higher erosivity due to their higher hardness relative to steel, and silica that represent sand particulates commonly found in oil and gas transportation systems. At low sand loading conditions (up to 5 $wt.\%$), erosion-corrosion of steels is known to be directly related to the concentration of the particles [26]. This effect is observed for both AISI 1020 carbon steel and 316L stainless steel in 0.3 $M$ HCl and 0.1 $M$ NaOH environments. A similar result was reported when a carbon steel was used in another study, with mass loss to sand concentration slope being equal to 2.7 [5]. The increase of material degradation rate with increasing sand loading is associated with higher impact energy. Continuous attack from the solids rips away the protective film, therefore promoting the oxidation of the bare metal. Good correlation with material behaviour is seen with stainless steel having lower mass loss rates compared to carbon steel. Passive film forming 316L stainless steel yields lower erosion-corrosion rates owing to its rapid repassivation kinetics.

As the concentration of the sand increases, the 'screening' effect is expected to take place

[45]. During this effect, the particles near the material surface shield it from subsequent impacts, therefore leading to lower erosion rates at high particle concentrations. Yang and Cheng [27]] did not observe any 'screening' effect, possibly due the fact that it has mainly been observed when hard particulates such as alumina and glass were used. In contrast, material wastage rates increased with solid concentration.

#### Chemical species

The influence of different anions and cations in the solution on erosion-corrosion of materials has not been studied extensively. A study by El-Kader and El-Raghy proposed that an increase in the concentration of chloride ions can hinder the oxygen transport to the surface therefore inhibiting cathodic reactions [46]. This was evidenced from the linear polarisation experiments on a fresh stainless steel surface, where lower corrosion current densities were recorded at higher concentration of chlorides.

There are some theories relating to the effect of anions on degradation of surface properties to the Rehbinder effect. Rehbinder described deterioration of mechanical properties of metals when in contact with surface active media. In the original experiment mercury-coated single crystal zinc showed several-fold decrease of Young modulus [47]. A study carried out by Lu and Luo suggested that increased amounts of adsorbed anions lead to stronger chemo-mechanical interaction as identified by erosion-corrosion weight-loss measurements and *in-situ* surface hardness degradation [37]. Due to lack of research and evidence, especially on the effect of cations on erosion-corrosion, the effect of chemical species remains unclear.

### 2.2.3 Properties of the erodent

Solid particles encountered in oil and gas transportation systems include various materials such as silica, barite, calcium carbonate. Properties of these erodents, including hardness, size, shape, sharpness, and impact angle influence erosion-corrosion of the target material, *i.e.* the pipeline.

#### Particle material, shape and sharpness

One of the pioneering pieces of research on the influence of erodent composition and shape was performed by Levy and Chik [48]. In a series of experiments performed in a nozzle tester using particles such as calcite, apatite, sand, alumina, and silicon carbide researchers identified that when the soft particles meet the ductile carbon steel surface of the target, they break into

smaller pieces and cannot concentrate the localized force necessary for erosion. The erosion rate of the target material increases as the hardness of the erodent increases, until reaching a cut-off erodent hardness of approximately 700 $kgf\ mm^{-2}$. It is believed that beyond this value particles are hard enough to maintain their integrity and not break into smaller pieces. This leads to work-hardening of the target wall surface keeping the erosion rates *versus* hardness of the erodent almost linear once the threshold hardness is reached. The erodents in the same density range as silica, silicon carbide and alumina possess the same erosivity.

Not only the properties of erodent material but also those of target wall affect erosion-corrosion. Hence, it is reasonable to expect that damage mechanisms incurred by brittle and ductile materials will be different. This was discussed in the target wall properties section 2.2.1 above.

Shape and sharpness of the particles play a crucial role in erosion-corrosion of materials. As such, it was postulated that angular, *i.e.* sharper particles can result in erosion rates up to four times higher than those of round particles [40]. As mentioned previously, the kinetic energy of the particles was related directly to the damage done to the target surface. It is believed that the geometry of the particle is related to how effectively this force can be concentrated. Hence angular particles impose more damage than round ones.

Another subtle property of the erodents is that they may *change* size and shape upon impact. This can be quantified, *via* measuring the change in specific surface and volumetric area after impact and correlating to the particle and target wall hardness. Figure 2.8 indicates that if the hardness of the particle is comparable to that of the target wall, considerable surface area change takes place. In contrast, if the erodent is much harder that the target material, surface area change is relatively low [43]. Therefore, when the target wall is harder than the erodent, up to five times particle breakup takes place. However, the analysis of volumetric size distribution of the particles showed that fracture of the material did not occur throughout the whole body of the particle. Rather, sharp corners of the particle were chipped off. This essentially shows that the shape and sharpness of the particles is a changing property. Round particles may become angular during the transport process and models predicting erosion-corrosion of materials need to account for this. Levy also argued that shattered erodents may blanket a target surface thus decreasing erosion rates [48] . However, this effect is deemed insignificant compared to other factors.

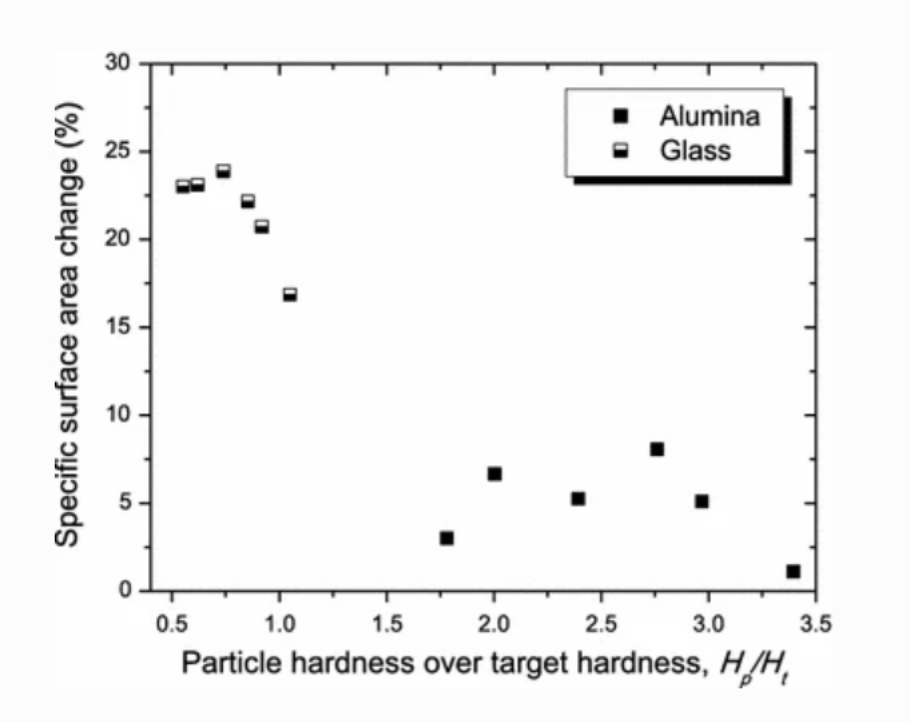


Figure 2.8: Specific surface area change as a function of particle to target hardness ratio. Reprinted with permission from Bousser *et al.* [43]. Copyright (2013) Springer.

### Particle size

According to Rajahram *et al.* there exists a threshold sand size above which material wastage rates decrease [26, 49]. In a series of experiments performed in a slurry pot erosion tester, the effect of three different sized particles on erosion-corrosion of carbon steel and stainless steel was studied. Particularly, single particle impact experiments showed the highest corrosion currents when medium sized (150–300 $\mu m$ ) particles were used. The effect of sand size is complex, largely due to the change in the number of collisions with particle size. This influences the kinetic energy of the particles, therefore impacting overall material wastage mechanisms. The previously mentioned 'screening' effect might take place as particle size increases, where large particles rebounding from the surface collide with incoming particles decreasing their kinetic energy.

It is known that under pure erosion conditions there is a positive correlation between the particle size and erosion rate until a critical size, above which erosion is independent of the size [40]. A similar trend was observed when chromium containing steel was studied in 1M NaOH solution. Erosion-corrosion rates decreased beyond particle size of 100 $\mu$m [50]. What remains unclear is how varying the size of the erodent affects individual components of erosion-corrosion, including synergy. A study carried out using 1 $gL^{-1}$ $Al_2O_3$ nano- and microparticles suggests that diffusion of oxygen species is hindered by nanoparticles leading to lower corrosion

rates, while a substantial corrosion component was seen when microparticles were used [51, 52]. Uncertainty regarding particle size change during erosion-corrosion events remains. Coupled with sharpness and shape evolution, particle size variation negatively affects the accuracy of erosion-corrosion rate prediction.

## 2.3 Mechanisms of erosion-corrosion synergy

So far, synergy in erosion-corrosion has been described in relation to the multiple parameters that affect erosion-corrosion. In this section, potential mechanisms of erosion-corrosion are summarised based on the current literature.

As was briefly mentioned before, there are two generally accepted mechanisms of erosion, ductile and brittle erosion. According to the micro-geometry model of ductile erosion proposed by Finnie, erosion took place *via* micro-cutting of the surface [53]. Particles incoming at low angles create a crater upon impact, which increases in size during further impacts. The material piles up around the crater and is removed after continued collisions of particles with the surface. Further work by Bellman and Levy showed that three types of craters; indentation, ploughing and smear craters; form on initial scratch-free surface of the metal [54] . At small impact angles smear craters are dominant, while at higher impact angles a ploughing mechanism takes place, followed by formation of indentation craters as illustrated in Figure 2.9.

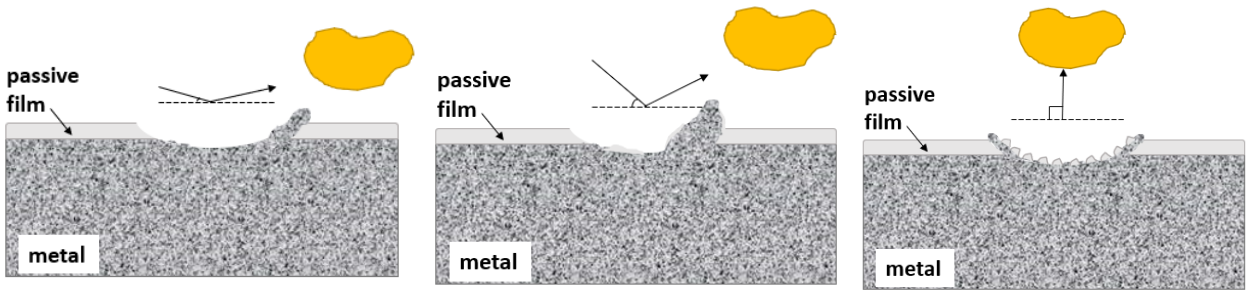


(a) (b) (c)

Figure 2.9: The illustration showing: a) smear, b) ploughing and c) indentation types of wear on ductile metals. Redrawn from Burstein and Sasaki [44].

Continuous impact from particles cause surface roughening due to plastic deformation and is denoted by forge-extruded craters. Partial conversion of the kinetic energy of incoming particles to thermal energy develops a heat affected zone and accelerates platelet formation. Below the surface, gradual work hardening takes place due to the temperature difference. Once there is no more fresh metal surface to be damaged, the prevailing mechanism of erosion happens due to ploughing [54]. Brittle materials, in turn, erode due to crack formation. Subsequent particle impacts lead to enlargement of lateral and radial cracks. Brittle chipping of the material then forms eroded craters [25].

The erosion mechanism of brittle scales on metals was also investigated by Levy [40]. Plastic deformation of the oxide layer due to particle impact develops stress fields that lead to horizontal and vertical crack growth. During this initial period, material loss rate is negligible due to continuous formation of the lips. However, once the threshold period is reached, the oxide scale is chipped off. Further impacts create the network of cracks that are also prone to spalling.

Rajahram *et al.* proposed the mechanism that was applicable to erosion-corrosion of passive film forming alloys such as stainless steel [18]. Although being largely similar to the erosion mechanism for brittle scale forming metals, it incorporates some modifications regarding corrosion of the material. Initially, the lips and craters are formed on the impact of the particle, which also might fragment into smaller pieces. The impact leads to oxide scale rupture, therefore increasing anodic dissolution of the metal. The oxide layer may grow back; however, it depends on material depassivation-repassivation kinetics in the specific environment. Fragments of the particles and oxide scale can be embedded into the material. The work-hardened subsurface transitions into the brittle erosion mode after continuous particle impacts. This leads to straining of the material that initiates martensitic transformation, which together with particle fragments and chromium oxide form the composite structure. Repeated stress and strain lead to fatigue crack formation on the material surface. Corrosive media leads to propagation of the cracks, where anodic oxidation or localised corrosion takes place [18]. It is evident that the proposed mechanism concentrates on the erosive component of the material degradation. However, no plausible explanation of the corrosion component and the synergy is provided. In fact, it is not clear how corrosion kinetics and transport changes during these events. Depassivation and repassivation of the material differs from system to system and deeper understanding of this process in various erosion-corrosion conditions is necessary.

## 2.4 Methods used in erosion-corrosion testing

Combined erosion-corrosion tests can be performed using different rigs, including slurry pot erosion tester, jet impingement rigs, pipe flow loops, and rotating disc electrodes. Among these, the pipe flow loop represents field conditions well, and whilst they provide accurate estimates of material loss they do not typically provide mechanistic information. Some of the erosion-corrosion techniques are briefly introduced below.

### 2.4.1 Slurry pot erosion tester

This rig shown in Figure 2.10 consists of a corrosion resistant pot, which contains baffles that prevent vortex creation and provides mixing, therefore ensuring that slurry does not settle. The specimens are attached to the motor driven rotator that is in electrical contact with the silver loaded graphite brush. The assembly also contains reference and counter electrodes to collect *in-situ* electrochemical measurements. High energy input of the system requires a cooler that is fed by tap water. The pot is enclosed in a Faraday cage that reduces the electrical noise and acts as a safety barrier. Weight loss measurements can then be performed on the specimens to determine total material degradation rates [5]. While the ability of collecting *in-situ* electrochemical data is useful, it should be noted that the measurements made in such erosion tester have several drawbacks. The set up of the electrodes does not minimize the solution resistance, along with the electrochemical data recorded being a cumulative of all simultaneous events taking place between the sample and the particle movement, which can be quite random.

### 2.4.2 Liquid jet impingement tester

In this system, flat specimens submerged into the liquid are bombarded by the solid particles carried by a liquid electrolyte delivered *via* nozzles. The slurry flow and the recirculation is delivered by pumps. The specimens can be connected to a potentiostat to gather electrochemical data during the tests [55]. The angle of solid particle incidence can be varied through tilting the specimen holder. In a sand blast erosion tester a similar principle is used, however, the specimens are not submerged in liquid and air is used as a sand carrier [56]. Corrosion measurements cannot be carried out *in-situ* in this variation of jet impingement.

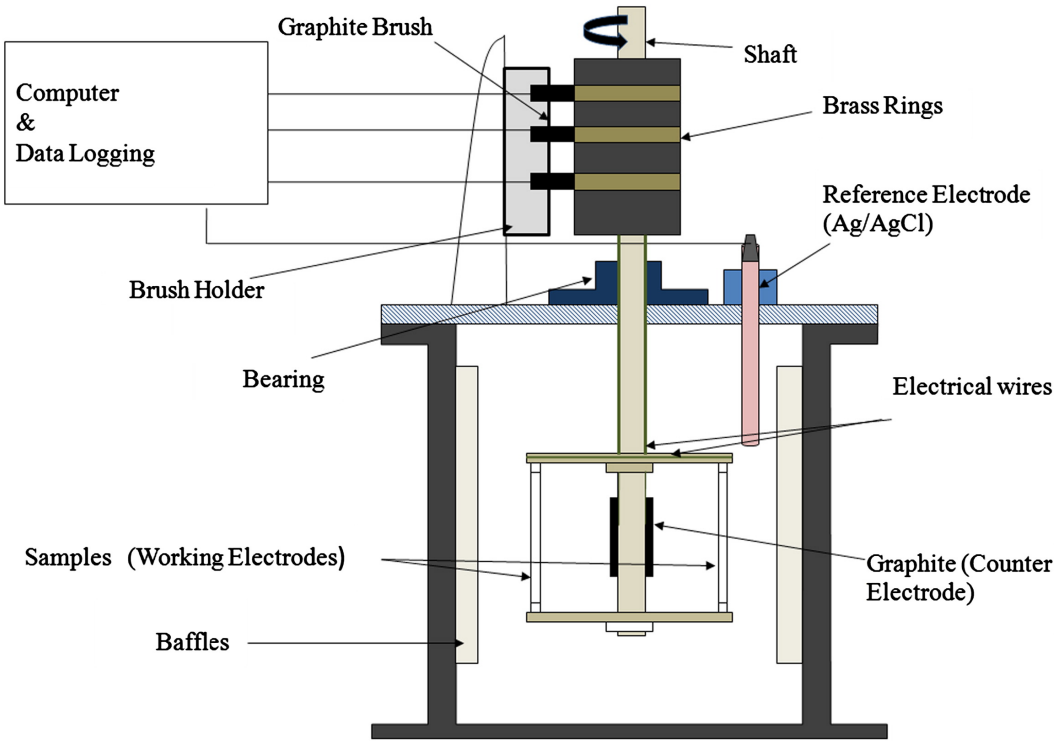


Figure 2.10: Schematic representation of a slurry pot erosion tester. Reprinted with permission from Rajahram *et al.* [49]. Copyright (2010) Elsevier Ltd.

### 2.4.3 Scratch experiments

The importance of repassivation studies under the flowing conditions was reiterated multiple times in the above review. Due to the rapid kinetics of steel oxide repassivation, it is necessary to combine flowing conditions with depassivation. One way of doing this in a controlled manner is *via* scratching tests. A rotating disc electrode that controls the flow velocity is scratched with a diamond stylus during the rotation. The depth of scratch is controlled *via* external loads that are released by the solenoid and is set to remove the oxide layer completely [57, 58, 59].

Such exposure of the bare metal to solution leads to anodic oxidation of the metal, which is accompanied by an initial current increase. As the metal oxidizes and repassivates, the current levels off and the rate of dissolution is decreased due to repassivation. The kinetics of repassivation are described by current and charge density transients originating from scratch initiation, represented by $i(t)$ and $q(t)$ respectively and defined in Equations 2.12 and 2.13.

$$i(t) = \frac{1}{2\pi\omega y t_c}[I(t) - I_b] \tag{2.12}$$

$$q(t) = \frac{1}{2\pi\omega y t_c}\int_0^t [I(t) - I_b]dt \tag{2.13}$$

Here, $y$ is the width of the scratch, $r$ is the distance of scratch to the centre of rotation, $I_b$

is the base current of the electrode before the scratch and $t$ is the current measurement time [60]. Kinetic parameters of oxide repassivation can then be obtained for various solutions. Characterisation of such oxides can give useful insight into the surface degradation that is seen during erosion-corrosion of steels under slurry flow. Figure 2.11 shows the rotating disc electrode equipped with a scratching stylus. Additional to electrochemical data, one can study erosion-corrosion using this setup and decouple its the individual components [59].

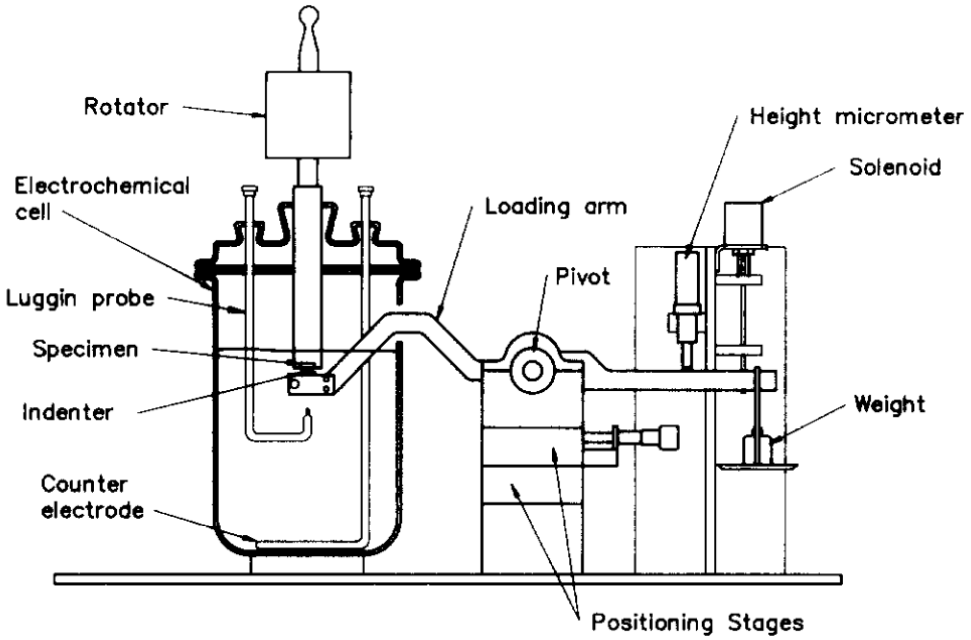


Figure 2.11: Schematic representation of the scratching apparatus. Reprinted with permission from from Adler and Walters [59]. Copyright (1993) Elsevier B.V.

## 2.5 On passivation of metals

G. Tim Burstein and co-workers pioneered application of the electrode scratching technique for iron repassivation studies in the 1980s. While being a relatively simple technique, electrode scratching offered insight into how iron and its alloys dissolved and repassivated in various aqueous environments.

The electrochemical behaviour of the scratched iron was studied in aqueous electrolytes [61]. Polarisation curves were obtained for 'bare' surfaces in pH ranges of 0 –14. The current density originating from the scratched metal under potentiostatic conditions, $i_s$, was defined by Equation 2.14, where $\frac{\mathrm{d}I}{\mathrm{d}t}$ represented the slope of the linear rising part of the current transient.

$$i_s = \frac{1}{2\pi r \omega y} \frac{\mathrm{d}I}{\mathrm{d}t} \tag{2.14}$$

The bare scratch current densities at cathodic and anodic potentials were then plotted as linear polarisation graphs. Scratching-accelerated electrochemical reactions and current densities of up to *ca.* 10 $A\,cm^{-2}$ were recorded. The intermediate reactions were elucidated and the kinetics followed Tafel's law. As the metal is scratched, the first step is the adsorption of water, which takes place immediately behind the scratching tip (Equation 2.15). The adsorption is followed by Equation 2.16 in acidic media, and Equations 2.17 and 2.18 in basic solutions. Burstein's work determined that FeOH was formed below the equilibrium potential for film formation [58, 61]. Hence, the FeOH layer is the intermediate in dissolution and passivation of the iron, as well as the cathodic reduction of $Fe^{2+}$ and $H^{+}$.

$$\mathrm{Fe} + \mathrm{H_2O} \rightleftharpoons \mathrm{Fe \cdot H_2O_{ads}} \tag{2.15}$$

$$\mathrm{Fe \cdot H_2O_{ads}} \rightarrow \mathrm{FeOH_{ads}} + \mathrm{H^+} + \mathrm{e^-} \tag{2.16}$$

$$\mathrm{Fe \cdot H_2O_{ads}} \rightleftharpoons \mathrm{FeOH^-_{ads}} + \mathrm{H^+} \tag{2.17}$$

$$\mathrm{FeOH^-_{ads}} \rightarrow \mathrm{FeOH_{ads}} + \mathrm{e^-} \tag{2.18}$$

The electrode scratching method was used to elucidate the kinetics of film repassivation on 304L stainless steel [60, 62, 63]. The scratch current density was calculated using Equation 2.12. The decay of current transient originating from the bare surface repassivation followed a $\log(i) \propto \log(t)$ relationship represented by Equation 2.19.

$$\frac{i}{\hat{i}} = \left(\frac{\hat{t}}{t}\right)^{\alpha} \tag{2.19}$$

where $\hat{i}$, $\hat{t}$, $\alpha$ are the empirical constants. The value of $\alpha$ for 304L stainless steel in 1 $M$ KOH solution was between 1.04±0.11[60].

Using the electrode scratching method Burstein and Marshall described stainless steel film growth parameters [62, 60]. The high field ion conduction was said to take place during oxide film growth according to Equation 2.20. Two different high field mechanisms took place at higher and lower current densities.

$$i = A \exp\left(\frac{BV}{x}\right) \tag{2.20}$$

where $V$ is the potential drop across the film, $x$ is the film thickness, $A$ and $B$ are parameters related to the ion movement.

By assuming no iron dissolution takes place at pH 14, the charge density flowing from the scratched electrode of thickness $x$ can be calculated *via* Equation 2.21.

$$q = \frac{nF\rho x}{M} \tag{2.21}$$

where $\rho$ is the film density, $M$ is its molecular weight and $n$ is the number of electrons involved in metal oxidation.

The relationship between the current flowing from the scratch and the charge can be obtained by solving for $x$ in Equation 2.21, substituting it into Equation 2.20 and taking logarithms of both sides of the equation. This results in linear relationship of $log(i)$ *vs.* $q^{-1}$ as shown in Equation 2.22.

$$log(i) = log(A) + \frac{BVnF\rho}{2.3Mq} \tag{2.22}$$

The effects of pH on the repassivation of 304 stainless steel were also studied. The high field mechanism, along with the kinetic parameters $A$ and $B$, was confirmed to be independent of pH. It should be noted that both film dissolution and passivation took place in acidic solutions [62]. The dissolution of stainless steel in perchloric acid solution was further explored in the subsequent paper by Burstein and Marshall [63]. The authors were able to establish that dissolution takes place from the film, not from the bulk of the metal in the studied solutions with pH -0.4 to 0.6. During the passivating film growth, the electric field across the film relaxes and the iron in the film starts dissolving. The dissolution takes place at a specific electric field that varies with pH. This results in a chromium enriched film, which produces passivity, commonly encountered in stainless steels. The computed composition profiles of $Fe^{2+}$ suggest that the concentration profiles of the iron ions increase gradually from electrolyte-film to film-metal interface. The dissolution kinetics of the iron through the film are limited by the ion migration step in the oxide for which the diffusion coefficient is $5 \times 10^{-14}\ cm^2\ s^{-1}$.

## 2.6 Summary and aims

Based on the review of current literature on erosion-corrosion of pipeline materials and the effect of individual parameters, the following gaps of knowledge might be outlined. First, the mechanism of synergy of coupled mechanical-electrochemical material degradation is not fully understood. Some works concentrate on an explanation of erosion mechanisms, and tend to overlook the corrosion component, even if synergy was reported to be responsible for up to 60% of material loss [40, 15, 18]. There is a controversy regarding the dissolution rate of platelets formed during particle impacts: researchers report both more elongated lips formed during erosion-corrosion compared to erosion only [17], and preferential dissolution of the platelets [19, 23]. In general, more insight into the microstuctural changes taking place during erosion-corrosion are needed.

Regarding the properties of the flow, the correlation of surface hardness degradation due to anodic current generation in acidic media needs to be better understood. The effect of the temperature, especially with relation to individual components of erosion-corrosion needs more insight. Specifically, there is a lack of research that measures the change in corrosion (including pure corrosion and erosion enhanced corrosion) using polarisation experiments. Another interesting area is the interplay of anions and cations on depassivation and repassivation during erosion-corrosion and their effect on synergy. As for properties of the erodent, the effect of particle sharpness (the measure of sharpness of particle's corners and edges) and its change during the erosion-corrosion, as well as its input on further performance of the material needs to be clarified.

A test system is designed and set up with a well-defined probe (shape and impact force) as well as well-controlled flow conditions to enable the study of the individual contributions. This is based on a rotating electrode setup, with bespoke control of the scratch system. The overall aim is to enable clear deconvolution of the contributing parameters to erosion-corrosion, and to correlate this with microstructural characterisation of the materials.

# Bibliography


[1] R. Baboian. Corrosion Tests and Standards: Application and Interpretation, 2005.

[2] R. G. Wellman. *Tribocorrosion of passive metals and coatings.* Woodhead Publishing Limited, Cornwall.

[3] B. Lu, D. Xia, and J. Luo. Mechanism of corrosion-enhanced erosion of steels in oil and gas production. TMS (The Minerals, Metals  Materials Society), 2014.

[4] ASTM International. Standard Terminology realting to Wear and Erosion (G40-15), 2015.

[5] T. J. Harvey, J. A. Wharton, and R. J. K. Wood. Development of synergy model for erosion–corrosion of carbon steel in a slurry pot. *Tribology*, 1(1):33–47, 2007.

[6] B. Poulson. Complexities in predicting erosion corrosion. *Wear*, 233-235:497–504, 1999.

[7] J. Postlethwaite and S. Nešić. Erosion-Corrosion: Recognition and Control. *Uhlig's Corrosion Handbook: Third Edition*, pages 907–913, 2011.

[8] L. L. Shreir. *Corrosion: Metal/environment reactions.* Newnes-Butterworths, 1979.

[9] S. Garber. Structure of scale on plain carbon steels. *Nature*, pages 1387–1388, 1959.

[10] C. Olsson and D. Landolt. Passive films on stainless steels - Chemistry, structure and growth. *Electrochimica Acta*, 48(9 SPEC.):1093–1104, 2003.

[11] I. Olefjord and B. Elfstrom. The Composition of the Surface during Passivation of Stainless Steels. *Corrosion*, 38(1):46–52, 1982.

[12] S. Wada and N. Watanabe. Solid particle erosion of brittle materials (part 1). *International Journal of High Technology Ceramics*, 3(3):258, jan 1987.

[13] I. M. Hutchings. Ductile-brittle transitions and wear maps for the erosion and abrasion of brittle materials. *Journal of Physics D: Applied Physics*, pages A212–A221, 1992.

[14] M. M. Stack, F. H. Stott, and G. C. Wood. Review of mechanisms temperatures of erosion-corrosion of alloys at elevated. *Wear*, 162-164:706–712, 1993.

[15] R. C. Barik, J. A. Wharton, R. J. K. Wood, and K. R. Stokes. Electro-mechanical interactions during erosion-corrosion. *Wear*, 267(11):1900–1908, 2009.

[16] M. McGuire. Austenitic Stainless Steels. *Stainless Steels for Design Engineers*, pages 69–78, 2008.

[17] R. J. K. Wood, J. C. Walker, T. J. Harvey, S. Wang, and S. S. Rajahram. Influence of microstructure on the erosion and erosion-corrosion characteristics of 316 stainless steel. *Wear*, 306(1-2):254–262, 2013.

[18] S. S. Rajahram, T. J. Harvey, J. C. Walker, S. C. Wang, and R. J. K. Wood. Investigation of erosion-corrosion mechanisms of UNS S31603 using FIB and TEM. *Tribology International*, 46(1):161–173, 2012.

[19] W. Li and D. Y. Li. Influence of surface morphology on corrosion and electronic behavior. *Acta Materialia*, 54(2):445–452, 2006.

[20] S. B. Yin and D. Y. Li. Corrosion and corrosive wear of annealed, impact-fractured and slow bending-fractured surface layers of AISI 1045 steel in a 3.5% NaCl solution. *Wear*, 259(1-6):383–390, 2005.

[21] B. Q. Wang, G. Q. Geng, and A. V. Levy. Effect of microstructure on the erosion-corrosion of steels. *Wear*, 151:351–364, 1991.

[22] M. A. Islam and Z. N. Farhat. Mechanical and Electrochemical Synergism of API X42 Pipeline Steel During Erosion–Corrosion. *Journal of Bio- and Tribo-Corrosion*, 1(4):26, 2015.

[23] K. Sasaki and G. T. Burstein. The generation of surface roughness during slurry erosion-corrosion and its effects on the pitting potential. *Corrosion Science*, 38(12):2111–2120, 1996.

[24] S. K. Kim, I. J. Park, D. Y. Lee, and J. G. Kim. Influence of surface roughness on the electrochemical behavior of carbon steel. *Journal of Applied Electrochemistry*, 43(5):507–514, 2013.

[25] M. Parsi, K. Najmi, F. Najafifard, S. Hassani, B. S. McLaury, and S. A. Shirazi. A comprehensive review of solid particle erosion modeling for oil and gas wells and pipelines applications. *Journal of Natural Gas Science and Engineering*, 21:850–873, 2014.

[26] S. S. Rajahram, T. J. Harvey, and R. J. K. Wood. Erosion-corrosion resistance of engineering materials in various test conditions. *Wear*, 267(1-4):244–254, 2009.

[27] Y. Yang and Y. F. Cheng. Parametric effects on the erosion-corrosion rate and mechanism of carbon steel pipes in oil sands slurry. *Wear*, 276-277:141–148, 2012.

[28] H. Meng, X. Hu, and A. Neville. A systematic erosion-corrosion study of two stainless steels in marine conditions via experimental design. *Wear*, 263(1-6 SPEC. ISS.):355–362, 2007.

[29] Q. J. M. Slaimana and B. O. Hasan. Study on corrosion rate of carbon steel pipe under turbulent flow conditions. *Canadian Journal of Chemical Engineering*, 88(6):1114–1120, 2010.

[30] Flow effects on corrosion. In R. W. Revie, editor, *Uhlig's Corrosion Handbook*, chapter 17, pages 203–213. John Wiley & Sons, Inc., third edition, 2011.

[31] M. Stern. Fundamentals of Electrode Processes in Corrosion. *Corrosion*, 13:97–104, 1957.

[32] B. Yu, D. Y. Li, and A. Grondin. Effects of the dissolved oxygen and slurry velocity on erosion-corrosion of carbon steel in aqueous slurries with carbon dioxide and silica sand. *Wear*, 302(1-2):1609–1614, 2013.

[33] J. G. N. Thomas and G. Hinds. The Electrochemistry of Corrosion.

[34] B. D. Jana and M. M. Stack. Modelling impact angle effects on erosion-corrosion of pure metals: Construction of materials performance maps. *Wear*, 259(1-6):243–255, 2005.

[35] M. M. Stack and N. Pungwiwat. Particulate erosion – corrosion of Al in aqueous conditions: some perspectives on pH effects on the erosion – corrosion map. 35:651–660, 2002.

[36] M. M. Stack, N. Corlett, and S. Turgoose. Some recent advances in the development of theoretical approaches for the construction of erosion-corrosion maps in aqueous conditions. *Wear*, 233-235:535–541, 1999.

[37] B. T. Lu and J. L. Luo. Correlation between surface-hardness degradation and erosion resistance of carbon steel - Effects of slurry chemistry. *Tribology International*, 83:146–155, 2015.

[38] H. X. Guo, B. T. Lu, and J. L. Luo. Interaction of mechanical and electrochemical factors in erosion-corrosion of carbon steel. *Electrochimica Acta*, 51(2):315–323, 2005.

[39] X. Hu and A. Neville. $CO_2$ erosion-corrosion of pipeline steel (API X65) in oil and gas conditions-A systematic approach. *Wear*, 267(11):2027–2032, 2009.

[40] A. Levy. *Solid particle erosion and erosion-corrosion of materials*. ASM International, Materials Park, 1995.

[41] R. Norling and A. Nylund. The influence of temperature on oxide-scale formation during erosion-corrosion. *Oxidation of Metals*, 63(1-2):87–111, 2005.

[42] W. Y. Zheng. Stress corrosion cracking of oil and gas pipelines in near neutral pH environment: review of recent research. *Energy Materials: Materials Science and Engineering for Energy Systems*, 3(4):220–226, 2008.

[43] E. Bousser, L. Martinu, and J. E. Klemberg-Sapieha. Effect of erodent properties on the solid particle erosion mechanisms of brittle materials. *Journal of Materials Science*, 48(16):5543–5558, 2013.

[44] G. T. Burstein and K. Sasaki. Effect of impact angle on the slurry erosion-corrosion of 304L stainless steel. *Wear*, 240(1-2):80–94, 2000.

[45] S. Turenne, M. Fiset, and J. Masounave. The effect of sand concentration on the erosion of materials by a slurry jet. *Wear*, 133(1):95–106, 1989.

[46] H. Abd El-Kader and S. M. El-Raghy. Electrochemical kinetics of stainless steel in aerated chloride solutions during wear process. *Electrochimica Acta*, 30(7):841–849, 1985.

[47] P. A. Rebinder and E. D Shchukin. Surface phenomena in solids during the course of their deformation and failure. *Soviet Physics Uspekhi*, 15(5):533–669, 1973.

[48] A. V. Levy and P. Chik. The effects of erodent composition and shape on the erosion of steel. *Wear*, 89(2):151–162, 1983.

[49] S. S. Rajahram, T. J. Harvey, and R. J. K. Wood. Electrochemical investigation of erosion-corrosion using a slurry pot erosion tester. *Tribology International*, 44(3):232–240, 2011.

[50] M. M. Stack, J. S. James, and Q. Lu. Erosion-corrosion of chromium steel in a rotating cylinder electrode system: Some comments on particle size effects. *Wear*, 256(5):557–564, 2004.

[51] M. Rashidi, M. Paknezhad, M. R. Mohamadi-Ochmoushi, and M. Moshrefi-Torbati. Comparison of erosion, corrosion and erosion-corrosion of carbon steel in fluid containing micro- and nanosize particles. *Tribology - Materials, Surfaces & Interfaces*, 7(3):114–121, 2013.

[52] A. M. Rashidi, M. Packnezhad, M. Moshrefi-Torbati, and F. C. Walsh. Erosion-corrosion synergism in an alumina/sea water nanofluid. *Microfluidics and Nanofluidics*, 17(1):225–232, 2014.

[53] I. Finnie. Some reflection on the past and future of erosion. *Wear*, 186-187(1):1–10, 1995.

[54] R. Bellman and A. Levy. Erosion mechanism in ductile metals. *Wear*, 70(1):1–27, 1981.

[55] X. Hu, K. Alzawai, A. Gnanavelu, A. Neville, C. Wang, A. Crossland, and J. Martin. Assessing the effect of corrosion inhibitor on erosion-corrosion of API-5L-X65 in multiphase jet impingement conditions. *Wear*, 271(9-10):1432–1437, 2011.

[56] Md Aminul Islam, Z. N. Farhat, E. M. Ahmed, and A. M. Alfantazi. Erosion enhanced corrosion and corrosion enhanced erosion of API X-70 pipeline steel. *Wear*, 302(1-2):1592–1601, 2013.

[57] T. P. Hoar and W. R. Jacob. Breakdown of Passivity of Stainless Steel by Halide Ions. *Nature*, 216(12):1299–1301, 1967.

[58] G. T. Burstein and D. H. Davies. The effects of anions on the behaviour of scratched iron electrodes in aqueous solutions. *Corrosion Science*, 20(10):1143–1155, 1980.

[59] T. A. Adler and R. P. Walters. Wear and scratch hardness of 304 stainless steel investigated with a single scratch test. *Wear*, 162-164(PART B):713–720, 1993.

[60] G. T. Burstein and P. I. Marshall. Growth of passivating films on scratched 304L stainless steel in alkaline solution. *Corrosion Science*, 23(2):125–137, 1983.

[61] G. T. Burstein and D. H. Davies. The Electrochemical Behavior of Scratched Iron Surfaces in Aqueous Solutions. *Journal of The Electrochemical Society*, 128(1):33, 1981.

[62] P. I. Marshall and G. T. Burstein. The effects of pH on the repassivation of 304L stainless steel. *Corrosion Science*, 23(11):1219–1228, 1983.

[63] G. T. Burstein and P. I. Marshall. The coupled kinetics of film growth and dissolution of stainless steel repassivating in acid solutions. *Corrosion science*, 24(5):449–462, 1984.

# Chapter 3

# Experimental techniques

## 3.1 Overview

This chapter presents the theoretical background to the experimental techniques used in this study. General experimental approaches are described. However, more specialised methodologies are described in the subsequent chapters of this work.

## 3.2 Electrochemical methods

Due to the redox nature of corrosion, electrochemical methods have found widespread use in corrosion science. Both thermodynamic and kinetic aspects of metal corrosion should be considered. While the former concerns the feasibility of the reaction, the latter describes the rate at which it takes place.

### 3.2.1 Thermodynamic aspects of corrosion

Consider the reversible aqueous reaction shown in Equation 3.1, where aqueous species A and B react, producing aqueous species C and D [1].

$$A + B \underset{k_2}{\overset{k_1}{\rightleftharpoons}} C + D \tag{3.1}$$

For an ideal solution the rates of forward and reverse reactions are given by Equations 3.2 and 3.3. At equilibrium, the rates of these equations are equal and the equilibrium constant is expressed as per Equation 3.4.

$$r_1 = k_1[A][B] \tag{3.2}$$

$$r_2 = k_2[C][D] \tag{3.3}$$

$$K = \frac{k_1}{k_2} = \frac{[C][D]}{[A][B]} \tag{3.4}$$

From thermodynamics, the reaction is spontaneous when the change in Gibb's free energy is negative ($\Delta G < 0$). Gibb's free energy at non-standard conditions can be calculated using Equation 3.5.

$$\Delta G = \Delta G^0 + RTln\frac{[C][D]}{[A][B]} \tag{3.5}$$

Taking into account the relationship between Gibb's free energy and the cell potential $\Delta G^0 = nFE_0$ and $\Delta G = nFE$ and dividing Equation 3.5 by $nF$ results in the Nernst equation shown in Equation 3.6. The Nernst equation can be used to calculate the reduction potential of the electrochemical cell based on the standard electrode potential, temperature and concentration. In concentrated solutions activity coefficients deviate from unity, hence solution activities need to be used instead of the concentrations. The general form of the Nernst equation is shown in Equation 3.7.

$$E = E^0 + \frac{RT}{nF}ln\frac{[C][D]}{[A][B]} \tag{3.6}$$

$$E = E^0 + \frac{2.303RT}{nF}log\frac{\Pi a_{reactants}}{\Pi a_{products}} \tag{3.7}$$

where $E^0$ is the standard electrode potential, $R$ is the universal gas constant, $T$ is the temperature, $n$ is the number of electrons transferred in a reaction, $F$ is Faraday's constant, and $a_i$ is the activity of species i.

### 3.2.2 Corrosion rate determination

Application of an overpotential, $\eta$, can drive the electrode reaction such that there will be a current flow, $i$. The overpotential is defined as the deviation of the applied potential from the equilibrium potential (Equation 3.8). The net current flowing at the electrode for well-stirred solutions is expressed using the Butler-Volmer equation shown in 3.9.

$$\eta = E - E_e \tag{3.8}$$

$$i = i_0 \left( exp\left\{ \frac{(1-\alpha)nF\eta}{RT} \right\} - exp\left\{ \frac{-\alpha nF\eta}{RT} \right\} \right) \tag{3.9}$$

where $i_0$ is the exchange current density (under equilibrium), $\alpha$ is the transfer coefficient describing the fraction of overpotential taken by the reduction reaction and is usually equal to 0.5 for single step reactions.

At high overpotentials where the electrode processes are anodic or cathodic driven, Equation 3.9 can be simplified and rearranged into Equations 3.10 and 3.11 respectively. These are known as Tafel equations, which relate the overpotential to the reaction rate in electrochemistry.

$$\eta_a = \beta_a log\left(\frac{i_a}{i_0}\right) \tag{3.10}$$

$$\eta_c = \beta_c log\left(\frac{i_c}{i_0}\right) \tag{3.11}$$

where $\beta_a = \frac{2.303RT}{(1-\alpha)nF}$ and $\beta_c = \frac{2.303RT}{\alpha nF}$ are anodic and cathodic Tafel constants.

Tafel equations have practical application in determining corrosion rates of metals and alloys in certain environments. Potential is scanned negative and positive relative to the open circuit potential and the current is measured on the working electrode. The graph of electrode potential *vs.* the logarithm of current can be built. With increasing polarisation, the measured current is dominated by anodic reactions, while in the opposite direction the cathodic processes dominate the net current. **Tafel extrapolation** is based on extrapolating linear parts of anodic and cathodic curves that usually represent oxidation of metal and hydrogen reduction reactions under deaerated conditions. The intersection of two lines readily provides information about the corrosion potential, $E_{corr}$, and the corrosion current density, $i_{corr}$. This is demonstrated schematically in Figure 3.1. It should be noted that the $E$ *vs.* $log(i)$ convention is seen within corrosion science community; however, in this work linear polarisation plots are given as $log(i)$ *vs.* $E$ as the potential is varied and the current is measured.

It is recommended that at least one decade of linearity is observable on the graph to determine $i_{corr}$ accurately. Usually it is difficult to obtain representative linearity for anodic polarisation due to the irreversibility of the metal oxidation reaction. However, anodic current density can be estimated from Equation 3.12.

$$i_{app,a} = i_a - i_c \tag{3.12}$$

where $i_{app,a}$ is the applied anodic current density, $i_a$ and $i_c$ are anodic and cathodic current densities.

Corrosion rate in *mils per year* (1 mil = 0.001 inch = 0.0254 mm) is calculated using Equation 3.13:

$$\text{Corrosion rate (mpy)} = \frac{0.13 i_{corr}(Eq.wt)}{\rho} \tag{3.13}$$

With $Eq.wt$ representing the equivalent weight of the corroding material ($g$), $\rho$ density ($g\,cm^{-3}$), $i_{corr}$ is corrosion current density ( $\mu A\,cm^{-2}$). Equivalent weight is defined as the mass of species that react with one Coulomb of charge; it is found by dividing the atomic weight of the active metal by the number of electrons taking place in redox reactions. For alloys, $Eq.wt$ is the summation of the individual equivalent weights multiplied by the weight fraction of each active alloy constituent.

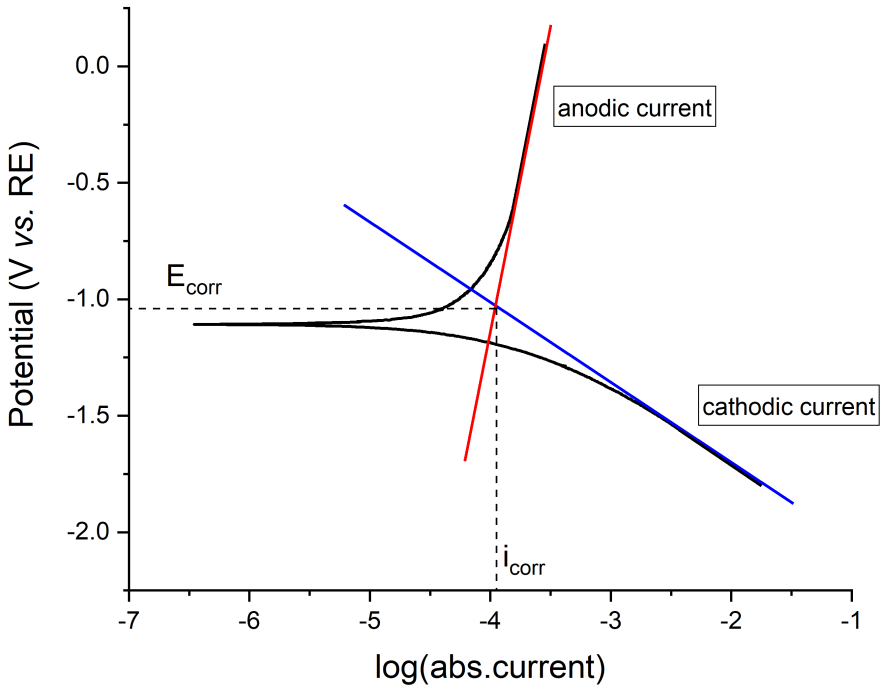


Figure 3.1: Schematic representation of Tafel plot obtained from current applied to corroding aqueous metal system.

Another widespread polarisation method is **linear polarisation resistance**. Here, the potential is swept at low overvoltages, typically 25-30 $mV$ below and above the corrosion potential. The technique is derived from the linear change of corrosion current at low overvoltages according to the following equation:

$$\frac{\Delta E}{\Delta i} = \frac{\beta_a \beta_c}{2.3(\beta_a + \beta_c) i_{corr}} \tag{3.14}$$

where $\frac{\Delta E}{\Delta i}$ is the slope of the line (i.e. polarisation resistance), $\beta_a$ and $\beta_c$ are the anodic and

cathodic Tafel constants defined earlier. The accuracy of the linear polarisation resistance method largely depends on an accurate estimation of the Tafel constants. This method is non-destructive and can be performed quickly once the equilibrium between anodic and cathodic reactions is established.

Polarisation experiments were performed on a three-electrode system controlled *via* either an Autolab 302N potentiostat with GPES interface or an Ivium CompacStat potentiostat at room temperature. The three-electrode system enables measurement of current flow between the working electrode and counter electrode, while the potential is recorded *versus* the reference electrode. The sample of interest was used as a working electrode, while a Pt spiral electrode served as a counter electrode. The reference electrode of choice was a mercury-mercury sulfate electrode (MSE) in saturated $K_2SO_4$ solution (0.64 $V$ *vs.* NHE) to avoid the interference from chloride ions that are released to solution from typical saturated calomel electrodes. All potential values are reported *vs.* MSE.

### 3.2.3 Rotating disc electrode scratching setup

A rotating disc electrode (RDE) is a setup that enables the introduction of controlled forced convection to the mass transport of electrochemical species. It also allows the effects of the flow velocity on the working electrode to be studied in corrosion science. In an RDE setup, a metal disc is inserted into a cylindrical rod made of electrochemically passive material such as Teflon. This assembly is mounted on the shaft and the cylinder is rotated about its vertical axis, which enables a constant supply of fresh solution to the surface of the electrode with well defined flow contours under laminar flow conditions (Figure 3.2b). The condition for such flow to remain laminar is that the Reynolds number must be smaller than $1 \times 10^5$ (Equation 3.15 ). The solution away from the electrode under rotation is well-stirred due to convection, while the velocity at the electrode surface needs is zero. The hydrodynamic boundary layer thickness of this relatively stagnant layer is defined using Equation 3.16. Adjacent to the electrode surface, within this hydrodynamic boundary layer, there is a very thin layer where the transport of the species is dominated by diffusion. The thickness of the diffusion layer is found *via* Equation 3.17, where $D$ is the diffusion coefficient of the species of interest. As mass transport is governed by both convection and diffusion, the limiting current density is obtained by solving Equation 3.18 at steady-state. The limiting current density Equation 3.19 is named after Levich, who first described the transport in a rotating disc electrode system [2, 3].

$$Re = \frac{\omega r_c^2}{\nu} \tag{3.15}$$

where $r_c$ is the radius of the cylindrical rod, $\omega$ is the angular rotation rate of the electrode and $\nu$ is the kinematic viscosity of the electrolyte solution.

$$\delta_H = 3.6(\nu/\omega)^{1/2} \tag{3.16}$$

$$\delta_D = 1.61 D^{1/3} \nu^{1/6} \omega^{-1/2} \tag{3.17}$$

$$\frac{\partial [C_i]}{\partial t} = D \frac{\partial^2 [C_i]}{\partial^2 z} - v_z \frac{\partial [C_i]}{\partial z} \tag{3.18}$$

where $[C_i]$ is the concentration of species $i$ and $v_z$ is the velocity component.

$$i_L = 0.620 n F A D^{2/3} \nu^{-1/6} C_{bulk} \omega^{1/2} \tag{3.19}$$

A **rotating disc electrode scratching setup** was built in-house developing upon a design provided in the literature [4, 5]. Figure 3.2c shows the assembly. The connection to the potentiostat allowed electrochemical measurements under hydrodynamic conditions. The setup was also connected to the solenoid that releases the scratching arm in a controlled manner, as programmed by an Arduino microcontroller. Upon the release of the solenoid the diamond tip scratches the rotating disc made of a sample of interest. Exposure of the bare metal to the acidic solution leads to anodic oxidation of the material, which is accompanied by an initial current increase. As the metal oxidizes and repassivates, the current levels off and dissolution decreases due to repassivation. The kinetics of repassivation is described by current and charge density originating from the scratch, represented by $i(t)$ and $q(t)$ respectively (Equation 3.20 and 3.21).

$$i(t) = \frac{1}{2\pi r w y t_c} [I(t) - I_b] \tag{3.20}$$

$$q(t) = \frac{1}{2\pi r w y t_c} \int_0^t [I(t) - I_b] dt \tag{3.21}$$

Here, $2\pi r \omega y$ represents the surface area of the scratch, $r$ is the distance of scratch to the centre of rotation, $\omega$ is the rotation rate, $y$ is the width of the scratch, $t_c$ is the contact time of the tip, $I(t)$ is the current at time t, $I_b$ is the base current of the electrode before the scratch, and $t$ is current measurement time [6]. Kinetic parameters of oxide repassivation can be obtained for various solutions.

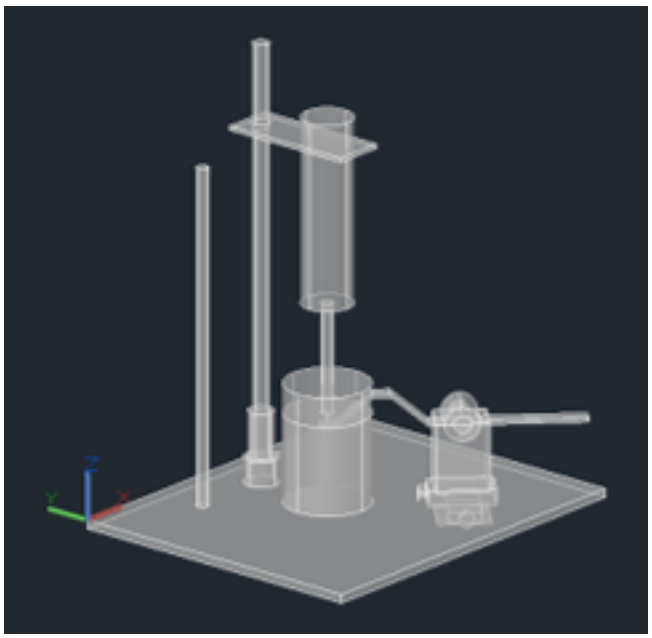

(a)

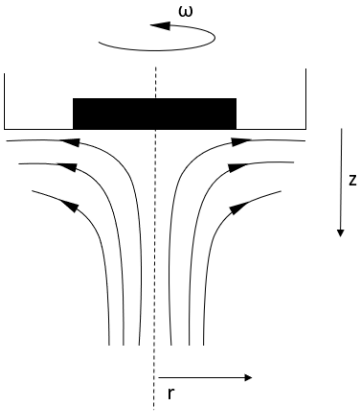


(b)

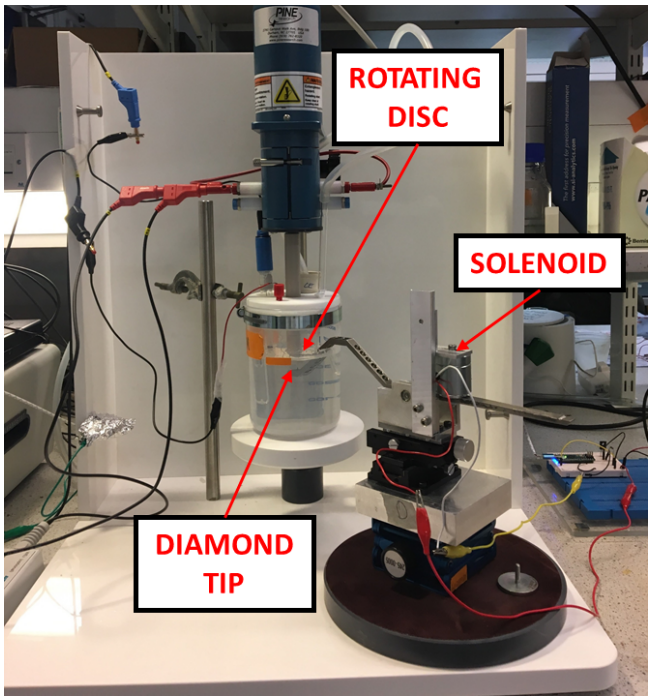


(c)

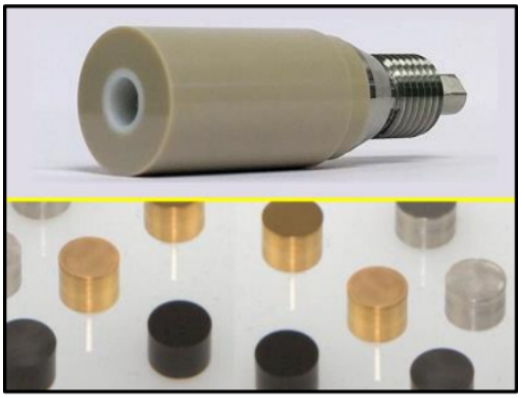

(d)

Figure 3.2: a) CAD drawing of the scratching setup, b) the illustration of the laminar flow lines during RDE operation, c) the photo of the assembled electrode scratching setup, d) RDE tip with removable discs (Copyright Pine Research Instrumentation, Inc. (2013-2017) [3]).

A modulated Speed Rotator (Pine Research Instrumentation, Inc.) with a precision rotating disc electrode (RDE) shaft was used with E5TQ Series ChangeDisk RDE tip made of polyether ether ketone (PEEK). X65 carbon steel and 316 stainless steel discs were used as working electrodes in the RDE assembly. The discs were inserted into the RDE tip with PTFE U-cup to prevent crevice corrosion (See Figure 3.2d). The electrical connection of the working

electrode was ensured *via* a gold connector. Disc inserts/samples were retracted after the experiment and stored in a desiccator prior to further characterisation.

The rotating disc electrode was scratched with a steel scribe with a diamond tip of 127 $\mu m$ radius with an included angle of 60°. The depth of scratch was controlled *via* an external load released by the solenoid and was set to remove the metal oxide layer completely. The force on the indenter was equal to 0.192 $N$ (19.92 $gf$). The exact scratching regimes are described in detail in the subsequent chapters of this work.

## 3.3 Characterisation methods

### 3.3.1 Transmission electron microscopy

Microstructural characterisation of the samples was performed using transmission electron microscopy (TEM) in this study. Modern TEM microscopes can resolve features down to *ca.* 0.1 $nm$ due to improved aberration correction. The main components of the TEM microscope are shown in Figure 3.3 and can be divided into three main parts: illumination, objective lens/stage and projection systems [7]. The electron beam generated by the electron gun using either thermionic source or field electron gun, is accelerated through a potential drop. The kinetic energy of the electron beam is calculated using Equation 3.22. Substituting the electron velocity found from Equation 3.22 into the momentum equation, and solving for the electron wavelength using De Broglie's equation gives the wavelength of the electrons (Equation 3.24). This equation shows an important inverse relationship between the non-relativistic electron wavelength and the accelerating voltage.

$$eV = \frac{m_0 v^2}{2} \tag{3.22}$$

$$p = m_0 v = \sqrt{2 m_0 e V} \tag{3.23}$$

$$\lambda = \frac{h}{p} = \frac{h}{\sqrt{2 m_0 e V}} \tag{3.24}$$

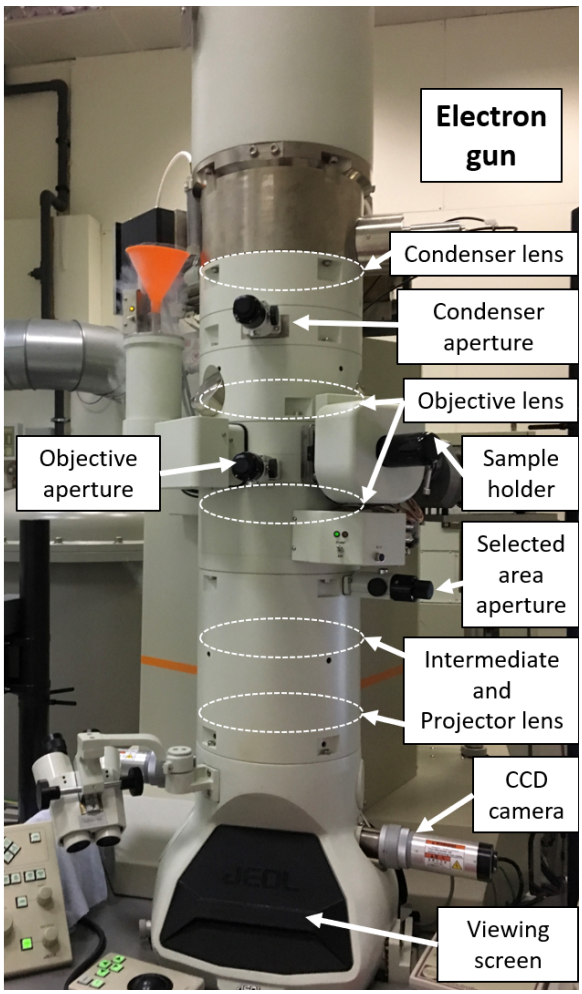


Figure 3.3: A JEOL2100F TEM column showing the main components of the microscope. Lens locations are not exact and given for illustration purposes only.

The illumination system transfers the electrons to the specimen either as a parallel beam for TEM imaging and selected area electron diffraction (SAED), or a convergent beam for scanning transmission electron microscopy (STEM), spectroscopy or convergent beam electron diffraction (CBED). The objective lens forms an intermediate image of the sample, which is located inside the objective lens. All interactions between the beam and the sample take place here, and are projected and magnified onto the viewing screen in the projection system. The objective aperture that selects certain diffracted beams to form an image, therefore enhancing the contrast, is inserted into the back focal plane of the microscope. During SAED, a selected area aperture is inserted into the image formation plane to select a specific area for analysis. Figure 3.4 illustrates this process using a ray diagram [7].

The types of **contrast in TEM** imaging are classified into mass-thickness, diffraction and phase contrast. Elastically scattered electrons can undergo either Rutherford scattering or diffraction. Rutherford scattering is a Coulombic interaction of the high-energy electrons with the nucleus. This incoherent scattering depends on the atomic number $Z$ and the thickness,

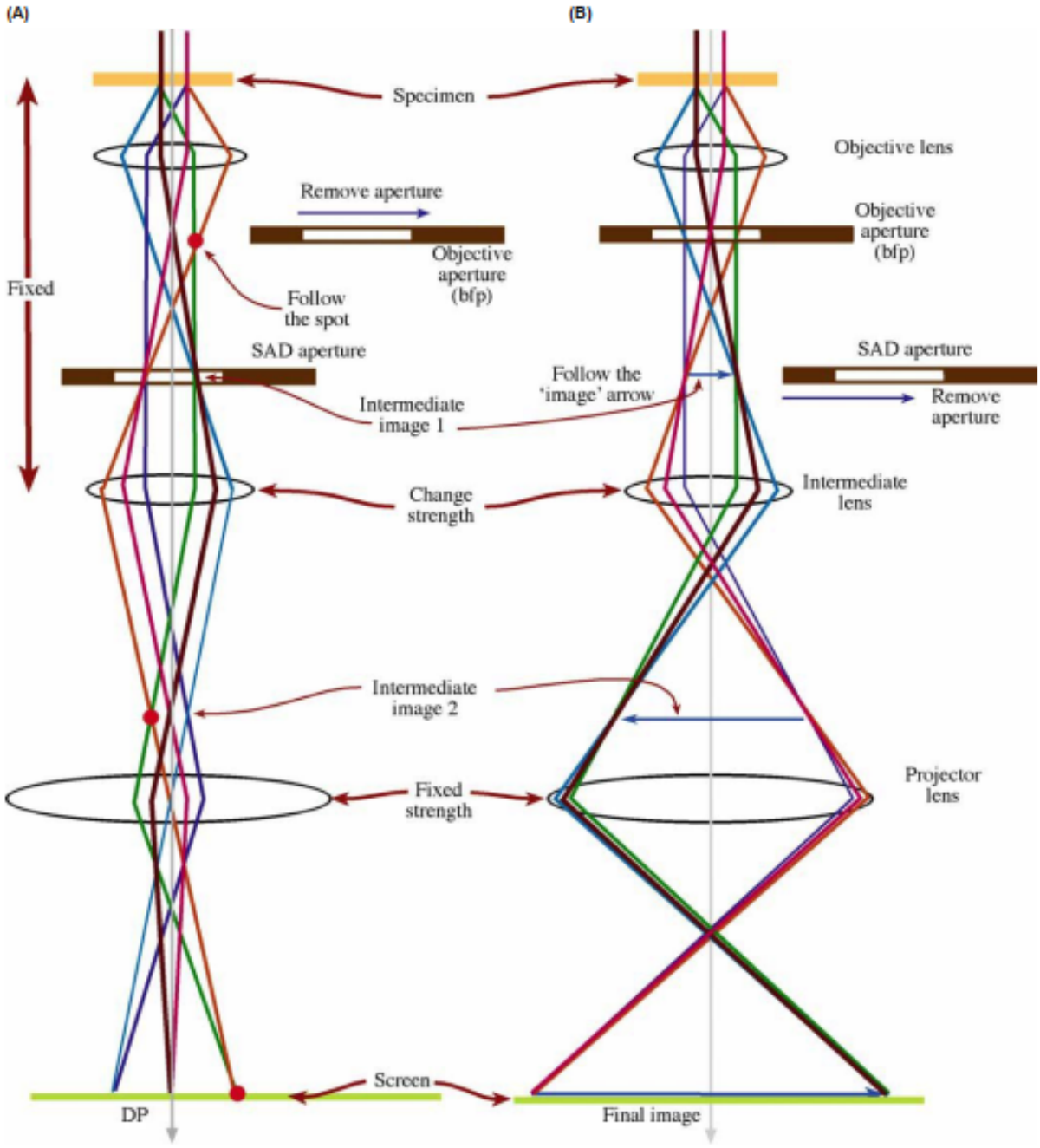


Figure 3.4: Ray diagrams showing a) diffraction mode and b) imaging mode. Reproduced from Williams and Carter [7] with permission. Copyright (2009) Springer.

and is characterised by high scattering angles. Other parameters being equal, high Z areas of the sample have more scattering compared to low Z areas, as do thicker regions *versus* thinner regions. For bright field (BF) imaging this means that high Z and/or thicker regions appear darker than low Z and/or thinner regions [7]. This is known as *mass-thickness* contrast and is an important TEM contrast for amorphous samples. Coherent elastic interaction of the electron beam with the electron cloud around the atom results in *diffraction*. This scattering follows Bragg's law and varies with the crystallographic orientation. Local defects in the crystal such as

dislocations can also be seen in diffraction contrast. *Phase* contrast in TEM images is seen from the phase difference of the electron waves used for imaging. It requires the selection of more than one beam for interference to occur. Periodicity noticed in TEM imaging occurs due to this phase contrast and includes lattice fringes from interference maxima of multiple diffracted beams, Moire fringes from two crystals overlaid upon each other, and Fresnel contrast that occurs near holes or edges.

Samples in this work were characterised using JEOL 2100Plus $LaB_6$ source and JEOL JEM-2100F field emission electron gun (FEG) source transmission electron microscopes. Bright field imaging was carried out in the former instrument, while chemical analysis using Oxford Instruments INCA/AZtec EDS detector system with STEM was mainly performed on the latter instrument. The accelerating voltage was equal to 200 $kV$.

Selected area electron diffraction (SAED) was performed using both TEM instruments. The crystal planes giving rise to the diffraction patterns were assigned by identifying allowed reflections for the crystal structure and applying Bragg's equation 6.1.

$$d = \frac{\lambda L}{R_b} \tag{3.25}$$

where $d$ is the interplanar spacing, $\lambda$ is the wavelength of the electrons at an accelerating voltage of 200 $kV$, $L$ is the camera length, and $R_b$ is the distance between the direct and diffracted beams.

### 3.3.2 Scanning electron microscopy

Morphological and topographical analysis of the metal samples in this study was performed using scanning electron microscopy (SEM). In SEM, signal is generated from the interaction of the focused electron beam and the sample as the beam rasters across the surface. This signal is converted into a digital micrograph point by point.

SEM components include the electron gun, condenser aperture and lens, scan coils, objective lens and aperture, stigmators and detectors. Similar to the TEM, in SEM the electrons are generated using either a thermionic source or a field emission gun. The probe size is controlled by a condenser lens that demagnifies the beam, while the objective lens focuses the beam on the sample. The apertures control the convergence semi-angle thus affecting the resolution, while stigmators correct for astigmatism. By changing the current in the scan coils, the beam is rastered across the sample surface generating different signals that are picked up by detectors [8].

When the high energy electron beam interacts with the sample, a variety of signals are generated (See Figure 3.5). Out of those, secondary electrons (SEs), backscattered electrons (BSEs) and characteristic X-Rays are most commonly used for characterisation.

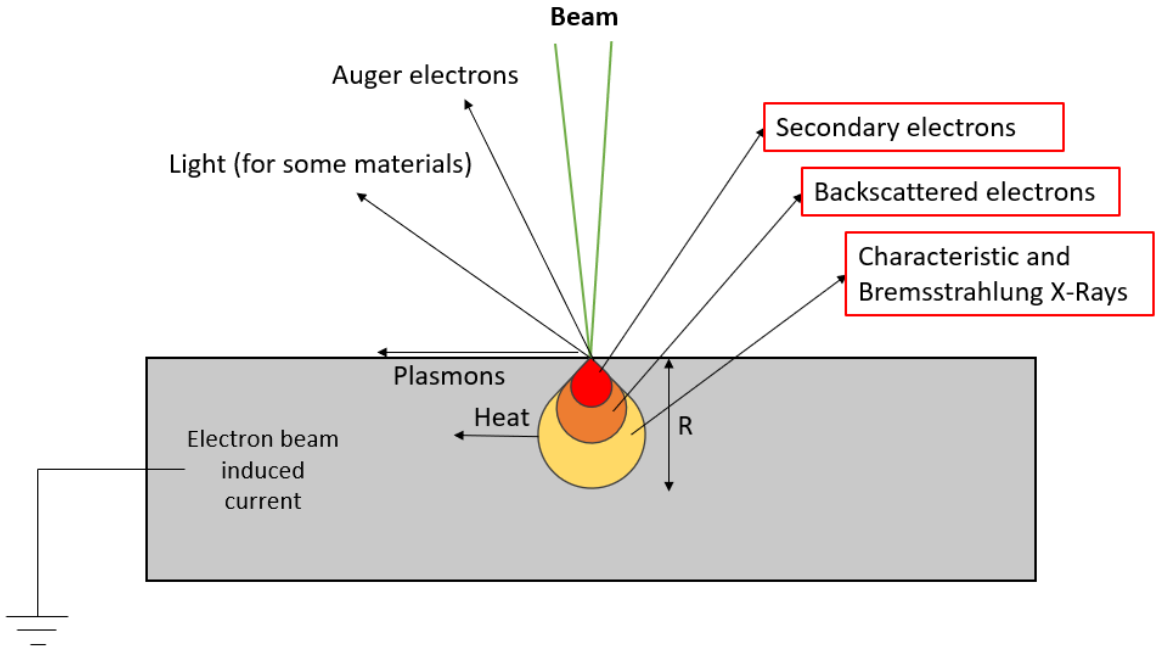


Figure 3.5: Schematic representation of the signals produced during electron beam – sample interaction. Range (R) is the distance travelled by each electron in the sample. Redrawn from Moram [8].

SEs are low energy electrons that were knocked off the sample by the beam's high energy electrons. The energy of SEs is within the 0.1 to 50 $eV$ range, which allows efficient collection of them from the surface of the sample by application of a small positive bias to the SE detector. SE imaging is used to obtain morphological and topographical information from the sample.

BSEs are high energy electrons from the beam, which escape the surface after elastically interacting with the sample. The BSE yield changes with atomic number (Z) and the specimen porosity, hence BSE imaging can be used for obtaining phase contrast.

Characteristic X-Rays are produced during the excitation of the inner shell electrons of an atom by an incident beam: electrons transition from the higher energy outer shell to the lower energy inner shell to fill the electron hole left by the ejected electron. X-Rays produced during this transition have unique photon energy for each element, hence they are used for elemental analysis of the sample. In energy-dispersive spectroscopy (EDS) the X-Rays are collected as a function of their energy using a cold reverse-biased Li-doped p-i-n junction [9]. A Be window is used to protect the detector from impurities, it absorbs X-Rays from lighter elements. Combined with the dominance of Auger electron generation for light atoms, elements

lighter than Na can not be detected using EDS [8]. Additionally, the sampling and interaction volumes are roughly the same for X-Rays meaning that information on chemical composition obtained using EDS is not surface specific. The spatial resolution of X-Ray maps is about 1 $\mu m$.

Zeiss LEO Gemini 1525 FEG SEM at an accelerating voltage of 5 $kV$ was used for topographical and morphological analysis using SEs. Surface characterisation was complemented with EDS at 20 $kV$ collected *via* Oxford Instruments X-ray detector. The INCA software was used for EDS analysis in Point & ID mode with quantitative optimisation carried out for iron. Prior to characterisation samples were taken out of the desiccator and mounted on an Al stub using a quick-drying silver paint (Agar Scientific) without prior gold sputtering.

### 3.3.3 Focused ion beam milling

SEM microscopes can be coupled with focused ion beam (FIB) in a cross beam configuration. In this work, FIB-SEM was used for cross section observation and TEM lamella fabrication.

The FIB column consists of the ion source, an extractor that controls the voltage, beam acceptance aperture that defines the maximum ion current. Below these are a beam shaping lens and beam defining apertures with different hole sizes to control the final ion current. A beam blanking mechanism is present to prevent sample damage during beam write back. At the end of the column are the deflection octupoles, which raster the ion beam and the lens that focus the beam onto the sample.

A $Ga^+$ liquid metal ion source (LMIS) is the most widely used ion source in FIB microscopes. The advantages of $Ga^+$ are low vapour pressure, low melting point and relatively high atomic mass, resulting in high sputter rates. Additionally, $Ga^+$ ion sources have a wide range of currents from 50 $nA$ down to 1 $pA$ [10].

In FIB milling, the momentum of $Ga^+$ ions is transferred to the sample during the ion bombardment process. Provided the transferred kinetic energy is larger than the surface binding energy of the sample, the atoms are sputtered away from it. Depending on the ion beam current and the sample material, arriving ions are either implanted or backscattered. The amount of ion implantation depends on the sample as well as the set ion beam voltage and current. Higher ion currents are associated with higher ion implantation range and should be used with care. During the TEM lamella preparation the ion current is reduced gradually removing the ions implanted from the previous milling step.

Cross beam FIB-SEM microscopes are equipped with both an electron and ion column.

The columns are at an angle of 52°, allowing simultaneous SEM and FIB imaging, which is especially useful for slice and view applications. The presence of the SEM column is necessary for high resolution cross section imaging due to the inferiority of the FIB SE imaging when a $Ga^+$ source is used. In SEM secondary electrons are generated from the primary beam as well as the backscattered electrons. However, in FIB almost no ion backscattering takes place, hence leading to decreased secondary electron generation. Additionally, for all other ion sources, except He, the large mass is associated with a shorter ion range that leads to secondary electron generation closer to the surface in the cascade. This results in poor resolution, as the emission area is larger than the ion beam spot size. Nevertheless, excellent contrast can be obtained from FIB SE imaging due to preferential ion channeling along favourable lattice planes. It should be mentioned that secondary ion imaging in FIB is not widespread due to insufficient ion yield [10].

The FEI Helios NanoLab™ 600 DualBeam™ FIB-SEM was used for the TEM lamella preparation in this work. The exact lamella preparation process is outlined in Chapter 6.

### 3.3.4 Secondary ion mass spectrometry

In secondary ion mass spectrometry (SIMS) a high energy primary ion beam (0.1 – 20 $keV$) bombards the surface of the sample resulting in sputtering of atoms, molecules and secondary ions [11]. Time-of-flight (ToF) SIMS employs the detector where the ions' mass-to-charge ($m/z$) ratio is determined from their time of flight from the sample to the detector. The primary ion beam is pulsed as it rasters across the sample, resulting in pulses of the secondary ions originating from the sample. The extraction plate at constant potential (2 – 8 $keV$) is used to accelerate the ions into the time-of-flight analyser [11]. The ions with the same kinetic energy will then have the velocities inversely proportional to the square root of their mass. Mass-to-charge ($m/z$) is identified from Equation 3.26.

$$\frac{m}{z} = \frac{2Vt^2}{L_t^2} \tag{3.26}$$

where $V$ is the accelerating voltage of the plate, $L_t$ is the length of the ToF detector's flight tube, $t$ is the time taken for ions to travel through the flight tube. A micro channel plate (MCP) is used to detect the secondary ions. A MCP has several million channels each of which act as electron multiplier. As Equation 3.26 suggests, heavier ions are detected later than lighter ions. The typical mass resolution ($M/\Delta M$) of ToF-SIMS is 10000. SIMS characterisation is done in ultra high vacuum to enable high sensitivity.

Dual-beam ToF-SIMS can be operated in static and dynamic modes. In *static* mode the primary ion beam is used to sputter the top layer of the specimen. To enable this surface sensitivity ion beam dose is limited and very short pulses are used when the beam scans the surface. In *dynamic* mode the second ion beam (sputter gun) is rastered across the defined analysis area at higher ion doses removing the material in a controlled manner. The primary beam is then rastered across a smaller area in short pulses and the ions are accelerated towards the detector. This process is repeated layer by layer allowing a depth profile of positive and negative secondary ions from the sample to be obtained.

In this study dual-beam ToF-SIMS was to obtain depth profiles of the samples. A bismuth LMIG source was used as a primary ion beam due to its improved yield of secondary ions, as it can be used in polyatomic ion configuration, *e.g.* $Bi_3^+$ [12]. The dynamic depth profiling mode employed a caesium $Cs^+$ sputter ion source in addition to the primary ion beam.

### 3.3.5 Inductively coupled plasma - optical emission spectrometry

During optical emission spectrometry (OES) the sample is heated to temperatures where not only dissociation into atoms, but also ionisation of the sample occurs *via* collisional excitation. These excited atoms and ions can transition into lower states by radiative and thermal decay. The wavelength of the emitted light can be correlated to a specific element, while its intensity is used to determine the concentration. The advantage of OES stems from the ability of high temperature sources to simultaneously populate numerous energy levels for several elements. The excited atoms and ions emit light at characteristic wavelengths almost at the same time, thus offering a wide choice of wavelengths for analysis. Several elements may be analysed at the same time and this increases the probability of the interference of their emission lines [13].

High energy ionized gases, *i.e.* plasmas, are used as a thermal source for optical emission spectrometers. Inert gases such as argon flow through a torch that consists of three concentric tubes. The torch end is surrounded by a copper foil that oscillates at a radio frequency creating an electromagnetic field at the top of the torch. The Ar gas is ignited with a spark, which removes some of the electrons from the Ar. The electrons are accelerated by the electromagnetic field in a process known as inductive coupling. The collision of electrons with other argon atoms causes a chain reaction producing more ions. This high temperature (*ca.* 6000–10000 $K$) plasma is called an inductively coupled plasma (ICP) discharge and consists of argon atoms, ions and electrons.

The sample in liquid form is formed into a fine mist using a nebulizer. This aerosol is car-

ried by an inner argon flow into the plasma. The aerosol undergoes desolvation, vaporisation, atomisation, ionisation and/or excitation. Finally, the light emitted from the excited species is resolved *via* a monochromator and captured by photosensitive detectors such as a photomultiplier tube (PMT) and charge-coupled device (CCD) [14]. While ICP-OES can be used to identify ppm levels of a wide range of elements, elements with high excitation energy (*e.g.* halogens) are not identified by this technique. Additionally, the concentration of trace contaminants present in the argon gas (C from $CO_2$), elements present in the solvent and radioactive elements with short half-live can not be determined using ICP-OES.

The procedure for ICP-OES analysis includes preparation of standard solutions with known concentrations. The calibration curve of signal intensity *vs.* element concentration is obtained. The solution concentration is found by comparing the recorded intensity to the intensity of the calibration curve. The concentration of Fe in samples subject to erosion-corrosion was identified using the Thermo Scientific iCAP 6000 series ICP Emission Spectrometer connected to an autosampler. The exact procedure is further outlined in Chapter 5.

### 3.3.6 White light interferometry

White light interferometry (WLI), also known as coherence scanning interferometry, is a method used in a non-contact 3D optical profiling for topographical analysis and surface height measurement. Light from the profiler is split in two within the interferometric objective, whereby one beam is reflected from a sample surface and the other beam is reflected from a reference mirror (usually aluminized glass or silicon carbide). Surface irregularities of the tested material result in different travel wavefronts. The reflected lights are out of phase, and form an interference pattern during recombination [15, 16]. The sample is scanned by vertically moving objective and the intensities are recorded by either a CCD or CMOS camera, which are then converted into the height maps. In-plane maps are created by spatially sampling the individual CCD pixels.

The schematic of the typical white light interferometer is given in Figure 3.6. The setup is similar to the optical microscope, with more complex objective lens, which host an interferometer and the piezoelectric z-stage. The objective and the tube lens decide the magnification of the image. Depending on the desired magnification either Mirau or Michelson objectives can be used. Objectives with Michelson interferometeres are employed for low numerical aperture and low magnification scans, while objectives with Mirau interferometers are used in higher magnification and higher numerical aperture scans [17]. In this work, the New View™ 7000

3D optical profilometer by Zygo Corporation with 2.5X Michelson objective (3.8 $\mu m$ optical resolution) was used to measure the wear profiles of the scratched samples. Detailed procedure is outlined in Chapter 5.

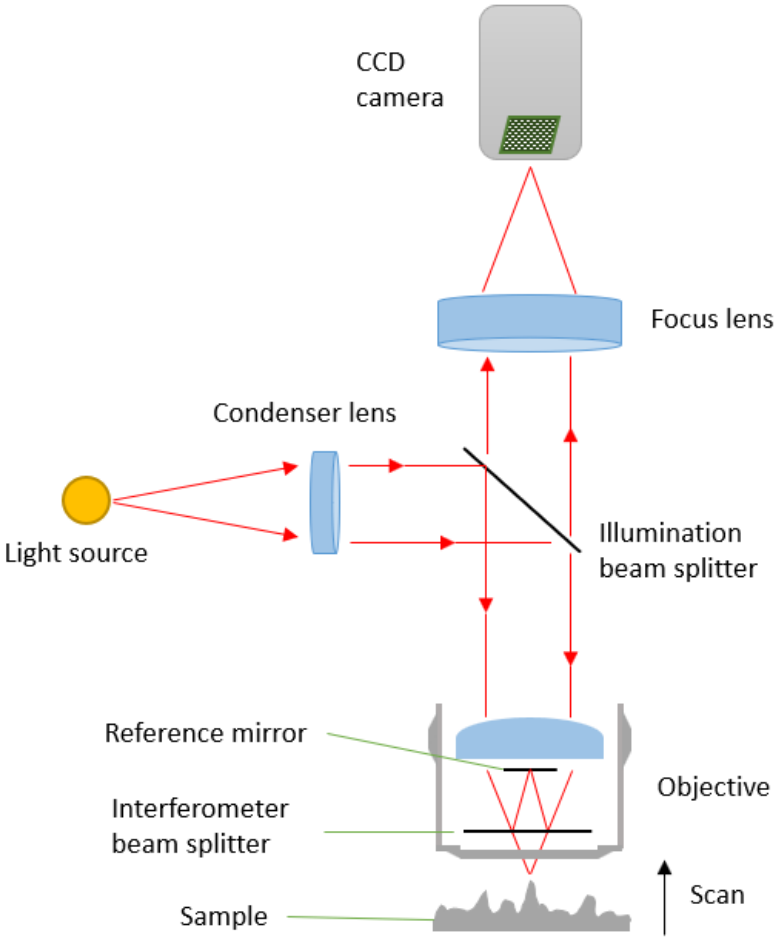


Figure 3.6: Schematic representation of WLI. Redrawn from de Groot [15].

# Bibliography


[1] V. S. Sastri, E. Ghali, and M. Elboujdaini. Introduction and Principles of Corrosion. In *Corrosion Prevention and Protection: Practical Solutions*, chapter 1. John Wiley & Sons, Inc., 2007.

[2] A. C. Fisher. *Electrode Dynamics*. Oxford University Press Inc., New York, 1996.

[3] Pine Research Instrumentation Inc. Modulated Speed Rotator (MSR) User Guide, 2016.

[4] T. A. Adler and R. P. Walters. Corrosion and wear of 304 stainless steel using a scratch test. *Corrosion Science*, 33(12):1855–1876, 1992.

[5] G. T. Burstein and D. H. Davies. The Electrochemical Behavior of Scratched Iron Surfaces in Aqueous Solutions. *Journal of The Electrochemical Society*, 128(1):33, 1981.

[6] P. I. Marshall and G. T. Burstein. The effects of pH on the repassivation of 304L stainless steel. *Corrosion Science*, 23(11):1219–1228, 1983.

[7] C. B. Carter and D. B. Williams. *Transmission electron microscopy: Diffraction, imaging, and spectrometry*. 2016.

[8] S. Moram. MSE 302 Electron Microscopy Course Notes. Lectures 1-10, 2015.

[9] D. Brandon and W. D. Kaplan. *Microstructural Characterization of Materials*. John Wiley & Sons, Incorporated, Hoboken, United Kingdom, 2013.

[10] D. C. Cox. *Introduction to focused ion beam nanometrology*. 2015.

[11] S. Fearn. *An Introduction to Time-of-Flight Secondary Ion Mass Spectrometry (ToF-SIMS) and its Application to Materials Science*. 2015.

[12] J. Brison, S. Muramoto, and D. G. Castner. ToF-SIMS Depth Profiling of Organic Films: A Comparison between Single-Beam and Dual-Beam Analysis. *The Journal of Physical Chemistry C*, 114(12):5565–5573, 2010.

[13] C. B. Boss and K. J. Fredeen. *Concepts, Instrumentation and techniques in ICP-OES*. 2004.

[14] X. Hou and B. Jones. Inductively Coupled Plasma/Optical Emission Spectroscopy. In R.A Meyers, editor, *Encyclopedia of Analytical Chemistry*, pages 9468–9485. John Wiley & Sons, Ltd, 2000.

[15] Peter de Groot. Principles of interference microscopy for the measurement of surface topography. *Advances in Optics and Photonics*, 7(1):1, mar 2015.

[16] Zygo Corporation. ZYGO Nexview NX2 Operating Manual, OMP-0618B, 2018.

[17] Rong Su. Coherence scanning interferometry. In *Advances in Optical Surface Texture Metrology*, 2053-2563, pages 2–1 to 2–27. IOP Publishing, 2020.

# Chapter 4

# Investigation of the fundamentals of erosion-corrosion in X65 carbon and 316 stainless steels

## 4.1 Overview

In this chapter a study of the fundamental erosion-corrosion behaviour of X65 carbon steel and 316 stainless steel is presented. The results of this chapter lay a foundation for decoupling erosion-corrosion components experiments in the following chapters.

The potentiodynamic polarisation of steel samples was conducted in various electrolytes, including 0.10 $M$ sulphuric acid, 0.05 $M$ potassium hydrogen phthalate buffer and 0.20 $M$ borate buffer with corresponding pH values of 1.0, 4.0 and 8.3 respectively to represent the conditions that might be seen in industry. Corrosion rates of X65 carbon steel and 316 stainless steel were calculated *via* Faraday's law using Tafel extrapolation. The surfaces of the polarised metal electrodes were characterised using SEM and SIMS. The combination of surface characterisation and the results of the electrochemical studies allowed the optimal conditions for studying mechanical-electrochemical behaviour of steels to be chosen.

A rotating disc electrode scratching setup was built to allow potentiostatic induction of the different modes of erosion-corrosion. A potentiostatic amperometry technique was used to study the current transients evolving on the X65 carbon steel and 316 stainless steel electrodes. The effect of single and multiple repeated scratches on the current density was studied. The conditions suitable for decoupling the individual components of erosion-corrosion, including pure erosion, pure corrosion and the synergy were successfully identified using this technique.

## 4.2 Experimental

### 4.2.1 Electrolytes

Three solutions with pH of 1.0, 4.0 and 8.3 were used in this study. The electrolytes were made from analytical grade chemicals dissolved in ultra-pure deionised (DI) water. 98 $wt.\%$ sulphuric acid stock solution (VWR Chemicals, AnalaR NORMAPUR®) was diluted to make 0.1 $M$ $H_2SO_4$ solution. The resultant solution had pH 1.00±0.05 measured by JENWAY 3510 pH meter, which was calibrated prior to the experiment. 10.211 $g$ of potassium hydrogen phthalate (VWR Chemicals, ≥99.5% AnalaR NORMAPUR® ) was dissolved in 500 ml of double-distilled DI water, to which 13 $mL$ of 0.1 $M$ NaOH and DI water was added to yield 1 $L$ solution. The pH of this buffer solution was 4.00±0.05. The final solution was prepared from 12.24 $g$ $H_3BO_3$, 19 $g$ $Na_2B_4O_7 \cdot 10\,H_2O$ and double-distilled DI water to yield a 1 $L$ solution. The pH of this buffer was measured to be pH 8.30±0.05 at 20$^o$C.

### 4.2.2 Materials

API X65 carbon steel samples were received from the Shell Technology Centre Houston (STCH). The chemical composition ($wt.\%$) of samples correspond to C 0.09, Cr 0.11, Cu 0.14, Mn 1.07, Mo 0.09, Ni 0.10, Si 0.28 and Fe balance. The microstructure of X65 carbon steel is lower bainitic, with austenitic and ferritic grains visible, see Figure 4.1.

5 $mm$ outer diameter (OD) discs were cut using Electrical Discharge Machining (EDM). The discs were embedded in bakelite resin, ground and polished to 1 $\mu m$ finish using Buehler PlanarMet™ 300 Planar Grinder. The samples were cleaned between each grinding and polishing step using water and isopropanol. Ultrasonic cleaning in ethanol was done after the final polishing step to ensure the removal of debris. Metal samples were left overnight in a desiccator to allow the sample to develop a reproducible oxide surface.

5 $mm$ OD AISI 316L stainless steel rods purchased from RS Components have the chemical composition ($wt.\%$) of Cr 16.50–18.50, Ni 10.00–13.00, Mo 2.00–2.50 and Fe balance. The microstructure of 316 stainless steel is austenitic as seen in Figure 4.2. Rods were cut to the discs of needed height using a precision saw, embedded in bakelite, ground and polished using the above mentioned method.

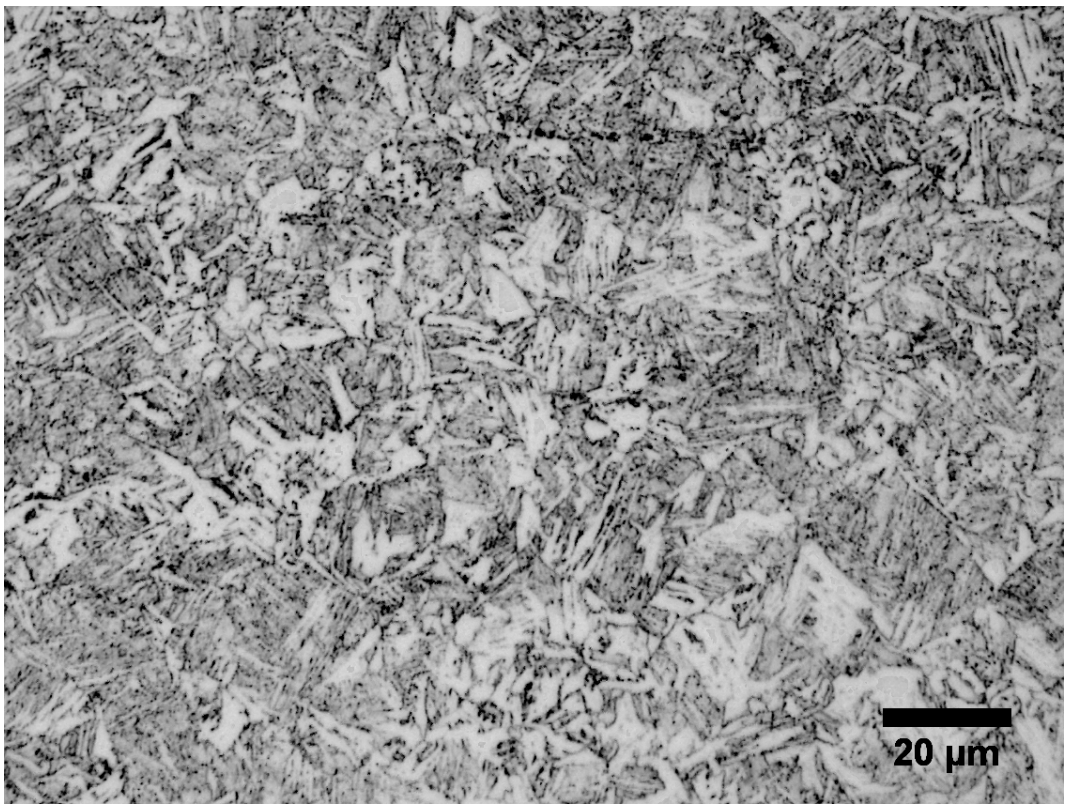


Figure 4.1: Optical micrograph of X65 carbon steel received from STC, Houston showing the microstructure of lower bainitic steel. Etchant: Nital (2% $HNO_3$ in ethanol), time: 5 *s*.

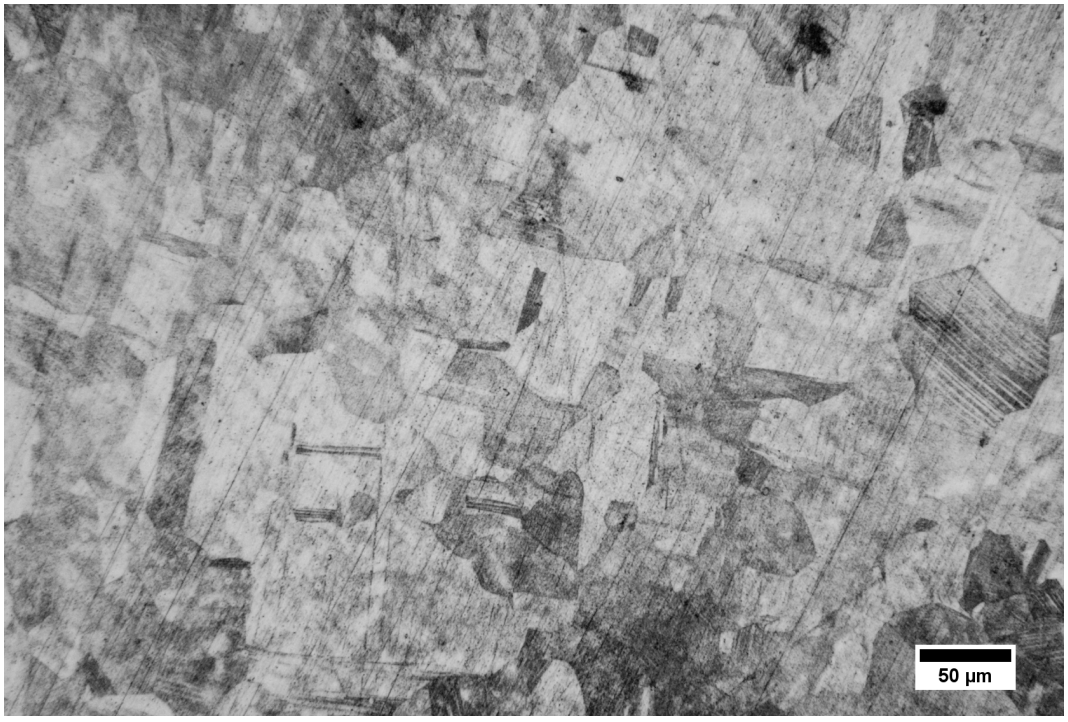


Figure 4.2: Optical micrograph showing the austenitic microstructure of 316 stainless steel rods used to produce working electrode discs. Etchant: Kalling's reagent, time: *ca.* 30 *s*.

### 4.2.3 Electrochemical measurements

Electrochemical measurements were performed on a three-electrode system controlled *via* Autolab 302N or Ivium CompacStat potentiostats. The three-electrode system enables measurement of the current flowing between the working and counter electrode, while the potential of the working electrode is controlled *versus* the reference electrode. The steel sample of interest was used as a working electrode, while a platinum spiral electrode served as a counter electrode. The reference electrode of choice was mercury-mercury sulfate electrode (MSE) in saturated $K_2SO_4$ solution (0.64 $V$ *vs.* NHE) to avoid the interference from chloride ions that are released to solution from saturated calomel electrodes. All potential values are reported *versus* MSE.

Measurements in static solutions were performed in a five neck glass cell filled with electrolyte at room temperature. The solutions were deaerated prior to experiments with high purity argon or nitrogen for 1 hour. Bubbling was maintained throughout the measurements to sustain an oxygen-free environment in the cell with a gas blanket above the solution. The equilibrium potential of the samples was recorded prior to performing polarisation with a threshold value of potential change rate of 0.01 $V min^{-1}$.

A rotating disc electrode setup was used for measurements under controlled mass-transfer conditions (See Chapter 3, section 3.2.3). A polypropylene flask with a custom made PTFE cap was used to host electrodes and the electrolyte during electrochemical measurements.

#### Linear scanning voltammetry

During linear scanning voltammetry (LSV), the potential was swept from negative to positive in the chosen voltage ranges at a sweep rate of 0.167 $mV\ s^{-1}$. Corrosion rates were estimated using the Tafel extrapolation method. Equivalent weights were calculated as 27.93 $g$ for X65 carbon steel and 25.35 $g$ for 316 stainless steel. Corresponding densities were equal to 7.85 $g\ cm^{-3}$ and 8.02 $g\ cm^{-3}$. Equivalent weight is defined as the mass of species that reacts with one mole of charge; it is found by dividing the atomic weight of the active metal by the number of electrons taking place in redox reactions. For alloys, $Eq.wt$ is the summation of the individual equivalent weights multiplied by the weight fraction of each active alloy constituent. Corrosion rate ($mm\ year^{-1}$) can then be calculated using Equation 4.1.

$$CR\ (mm\ year^{-1}) = \frac{3272 \times i_{corr}(Eq.wt)}{\rho} \tag{4.1}$$

with $Eq.wt$ representing the equivalent weight of the corroding material ($g$), $\rho$ density ($g\ cm^{-3}$), and $i_{corr}$ corrosion current density ($A\ cm^{-2}$).

#### Scratching procedure

The steel working electrode was held at the chosen potential for *ca.* 300 $s$, after which the scratching tip was released 1 and 100 times during single and multiple scratching experiments respectively. The tip contact time was *ca.* 2 $s$. For multiple scratching experiments, the time between successive scratches was equal to 10 $s$ during cathodic polarisation and 20 $s$ during anodic polarisation. The working electrode was set to rotate at $30 \pm 2$ $RPM$. The scratching tip radius was equal to 127 $\mu m$ with an angle of the tip of 60°. The load at the end of the scratching arm was equal to 19.92 $g$. Table 4.1 summarises these experimental parameters, with $t_c$, $\Delta t$, $\omega$, and Re denoting contact time of the scribe with the sample,time between successive scribe contact, the angular rotation rate (radians per second), and Reynolds number respectively.

Table 4.1: Experimental parameters used for scratching tests in Chapter 4. Both X65 carbon steel and 316 stainless steel were tested in pH 4.0 KHP solution.

| Experiment type | No. of scr. | RPM | $t_c$, $s$ | $\Delta t, s$ | $\omega$, $rad/s$ | Re | Flow regime |
|---|---|---|---|---|---|---|---|
| Single scratching | 1 | 30 | 2 | n/a | 3.14 | 176 | laminar |
| Multiple scratching | 100 | 30 | 2 | 10 (cathodic)<br>20 (anodic) | 3.14 | 176 | laminar |

### 4.2.4 Characterisation

#### Scanning Electron Microscopy

A LEO Gemini 1525 FEG SEM at an accelerating voltage of 5 $kV$ was used for topographical and morphological analysis. Surface characterisation was coupled with Energy-dispersive X-ray spectroscopy (EDS) at 20 $kV$ collected *via* Oxford Instruments X-ray detector.

#### Secondary Ion Mass Spectrometry

Time-of-flight SIMS was employed to obtain 2D chemical maps and depth profiling of selected specimens. A bismuth liquid metal ion-gun source (LMIG/S) was used as a primary ion beam due to its improved yield of secondary ions [1]. The dynamic depth profiling mode employed a caesium sputter ion source in addition to the primary ion beam. The crater size varied from 300 x 300 $\mu m^2$ to 500 x 500 $\mu m^2$, while secondary ions were collected from 100 x 100 $\mu m^2$ area. Beam energies of 0.5 $kV$ and 2 $kV$ were employed depending on the sample.

## 4.3 Results and discussion

### 4.3.1 Electrochemical behaviour of steels

This subsection presents the results and discussion of preliminary investigation of electrochemical behaviour of X65 carbon steel and 316 stainless steel in static solutions at varying pH.

Studying linear scanning voltammograms of both carbon and stainless steel allows comparison of the thermodynamic stability of these alloys, along with providing vital information on the kinetics of the oxidation and reduction processes. LSV tests can also be used to check the electrochemical technique and instrumentation itself, as suggested by some standardised methods such as ASTM G5-14 [2]. Optimal conditions, including pH and potential can then be chosen for further erosion-corrosion experiments.

#### Potentiodynamic polarisation of steel samples in pH 1 electrolyte

In highly acidic media, the linear polarisation graphs of passive film forming 316 stainless steel showed an active-passive transition, while X65 carbon steel actively corroded. Figures 4.3 and 4.4 illustrate the difference of polarisation of X65 carbon steel and 316 stainless steel respectively in pH 1 $H_2SO_4$ deaerated aqueous electrolyte. As the potential is swept from negative to positive values a decrease of current is observed until the corrosion potential is reached. The corrosion potential can be identified as the equilibrium potential at which cathodic reaction rates are equal to anodic reaction rates. In concentrated sulphuric acid under deaerated conditions, it can be interpreted as the point where cathodic reduction rate of hydrogen ions (*i.e.* hydrogen evolution) equals the oxidation rate of the metal to metal oxide or dissolved species (Equations 4.2 and 4.3). After passing this point, as seen from Figure 4.3, carbon steel continuously corrodes, corresponding to a measured increasing current density. Tafel extrapolation gives $i_{corr} = 2.81 \times 10^{-4}\ A\,cm^{-2}$ and $E_{corr} = -0.94\ V$ *vs.* MSE, which corresponds to the corrosion rate of 3.27 $mm\,year^{-1}$.

$$\text{Cathodic reaction:} \qquad 2\,H^+ + 2\,e^- \longrightarrow H_2 \tag{4.2}$$

$$\text{Anodic reaction:} \qquad Me \longrightarrow Me^{n+} + ne^- \tag{4.3}$$

LSV of 316 stainless steel in 0.1 $M$ $H_2SO_4$ yields different behaviour compared to carbon steel owing to alloying with passive film forming Cr. As the potential is swept in the positive direction to less noble values, current density increases in the active region following Tafel kinetics of metal oxidation. Upon reaching the passivation potential, $E_{pp}$, sufficient current

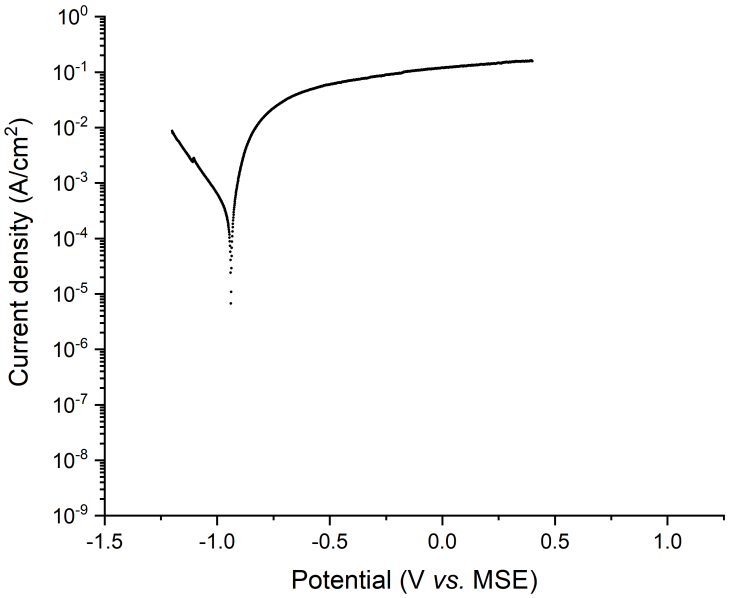


Figure 4.3: Linear scanning voltammogram of X65 carbon steel swept from -1.2 *V vs.* MSE to 0.4 *V vs.* MSE at room temperature in Ar-saturated 0.1 *M* $H_2SO_4$ aqueous solution at pH 1.0.

density is supplied to the system to enable the formation of the passive film. This current density is known as the critical current density, $i_{crit}$ [3]. Further increase of the potential leads to a decrease of the current density to the passivation current density, $i_{pass}$. The passive region in Figure 4.4 spans *ca.* $-0.7$ *V vs.* MSE to *ca.* 0.4 *V vs.* MSE. The small peak at *ca.* 0.1 *V vs.* MSE might be present due to dissolution of iron to iron oxy-hydroxides. Applying more positive overpotentials results in an increase in current density, which is associated with $Cr^{3+}$ to $Cr^{6+}$ oxidation followed by an oxygen evolution from the water electrolysis reaction (Equation 4.4) [4]. The polarisation graph agrees with those reported in the literature [5], [6].

$$2\,H_2O \longrightarrow O_2 + 4\,H^+ + 4\,e^- \tag{4.4}$$

SEM micrographs of X65 carbon steel and 316 stainless steel samples polarised in 0.1 *M* $H_2SO_4$ are presented in Figures 4.5a and 4.5b respectively. The oxide scale on X65 carbon steel was visible to the eye and could be recognised by its characteristic black colour, with SEM micrograph displaying a highly porous oxide structure. The presence of such porosity enables ion transport and can explain why the oxide scale formed is not protective in highly acidic solutions. The structure of the oxide scale formed *via* polarisation is widely reported in the literature [7], [8], [9] and is known to consist of iron oxy-hydroxides. Although, the surface of the 316 stainless steel sample polarised in pH 1 solution did not have any porous structures, the corrosion along the austenite grain boundaries was observed, along with occasional pits within

the grains and grain boundaries. This might occur due to the presence of various inclusions in austenitic stainless steels and their segregation at grain boundaries.

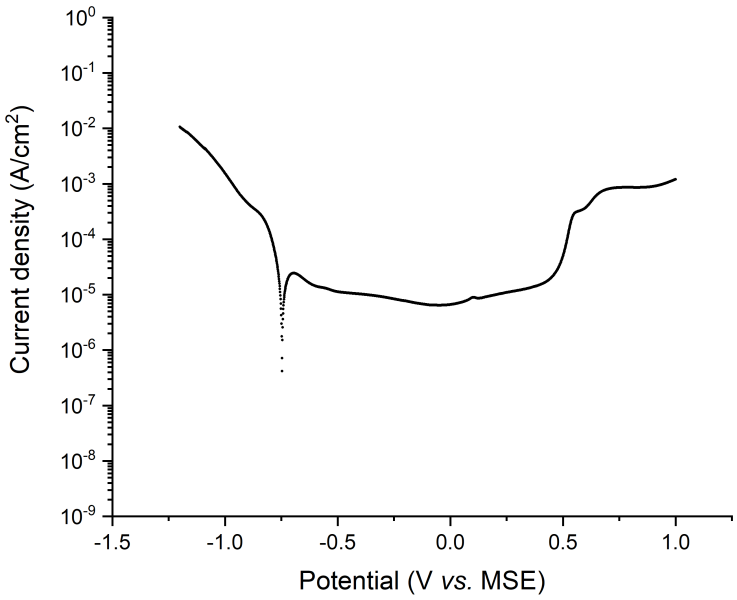


Figure 4.4: Linear scanning voltammogram of 316 stainless steel swept from -1.2 $V$ *vs.* MSE to 1.0 $V$ *vs.* MSE at room temperature in Ar-saturated 0.1 $M$ $H_2SO_4$ aqueous solution at pH 1.0.

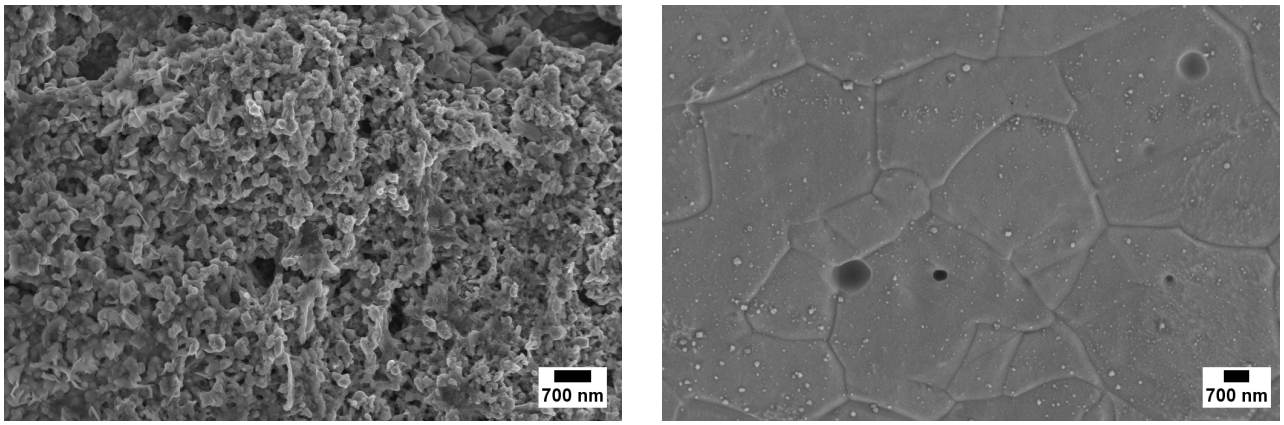


(a) (b)

Figure 4.5: SEM micrographs of a) X65 carbon steel after LSV in Ar-saturated 0.1 $M$ $H_2SO_4$ aqueous solution, from -1.2 $V$ *vs.* MSE to 0.9 $V$ *vs.* MSE and b) 316 stainless steel foil after LSV in $N_2$ saturated 0.1 $M$ $H_2SO_4$ aqueous solution, from -1.4 $V$ *vs.* MSE to 1.1 $V$ *vs.* MSE.

ToF-SIMS analysis was performed on X65 carbon steel polarised in 0.1 $M$ $H_2SO_4$ from $-1.2$ $V$ *vs.* MSE to 0.9 $V$ *vs.* MSE. Depth profiling of the porous oxide structure formed in sulphuric acid shows the presence of iron oxy-hydroxide anions (Figure 4.6b). The intensity of the anions is initially low, which can be correlated to the surface contamination present on

the top layers of the sample. However, once the contaminating species are sputtered away, the amount of oxide anions on the surface increases rapidly and remains constant throughout the oxide layer, indicative of a thick oxide scale produced *via* polarisation. The intensity of the cations (Figure 4.6a) also increases as the contaminants are sputtered away, followed by the continuous exponential decay of the signal. The signal decreases as the oxide is sputtered further.

Continuous sputtering of the surface down to the bare metal, past the oxide layer, should theoretically yield a decrease of oxide signal. This among other variables, is a function of the oxide layer thickness. Indeed, observation of the depth profile of the ions present at the surface of a metal that was not oxidized electrochemically but was rather exposed to air, showed the decrease of oxide intensity shortly after the surface oxide layer was sputtered away (Figure 4.7b). The thickness of the native oxide on carbon steel can be approximated as 1-3 $nm$ [10]. Thus, under similar sputtering conditions the slowest sputtering rate can be approximated as 1-3 $nm$ per 150 $s$. Using this, the oxide layer thickness on the electrochemically polarised sample is at least between 10 and 32 $nm$. Anion intensities are marked with several slope changes that correspond to previously mentioned layered structure of the oxides on carbon steels (See Chapter 2). As the specimen is sputtered, the oxide signal decreases due to the transition from oxygen rich haematite to oxygen depleted wüstite layer, eventually reaching the bare metal [11]. The intensity of positive ions decreases exponentially without initial increase, probably due to less contaminants (Figure 4.7a).

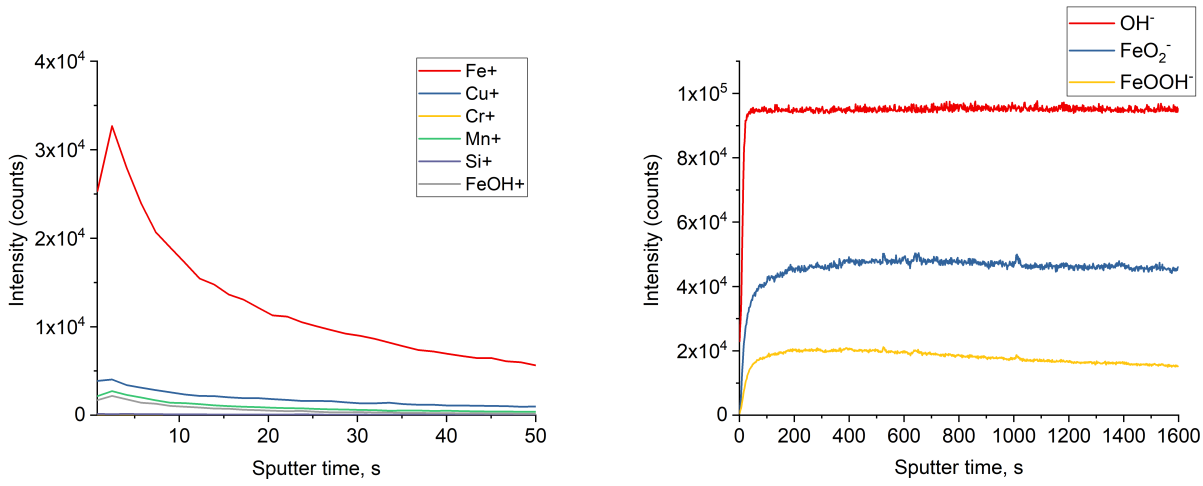


(a) (b)

Figure 4.6: ToF-SIMS depth profiles for X65 carbon steel collected with Cs sputter beam of 0.5 $kV$ from crater size of 500 x 500 $\mu m^2$. The sample was polarised from -1.2 $V$ *vs.* MSE to 0.9 $V$ *vs.* MSE at room temperature in Ar-saturated 0.1 $M$ $H_2SO_4$ aqueous solution at pH 1.0.

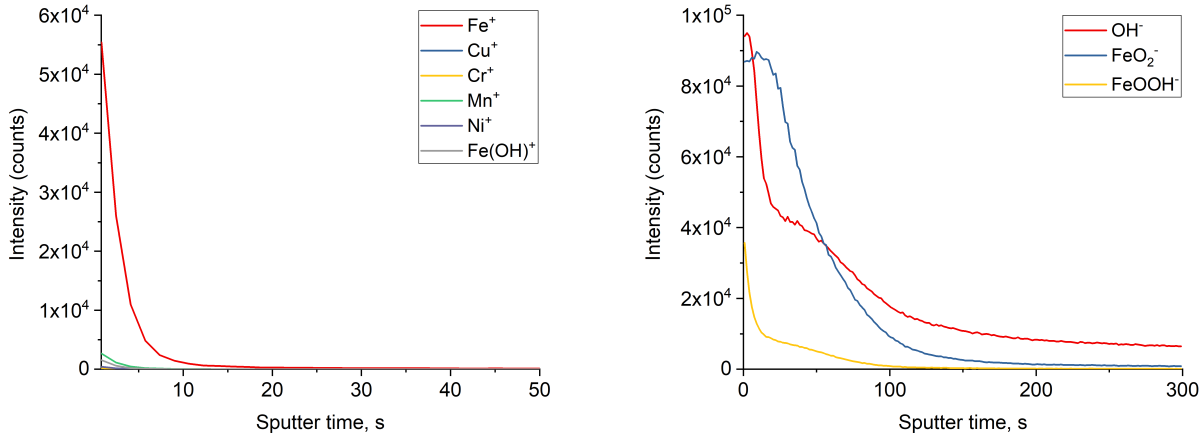


(a) (b)

Figure 4.7: Depth profiles for mirror polished X65 carbon steel collected with Cs sputter beam of 0.5 $kV$ from crater size of 500 x 500 $\mu m^2$

ToF-SIMS depth profiling was performed on an untreated, air exposed, mirror polished stainless steel sample. For such a steel a three-layered model is reported in the literature [12], which contains a chromium and iron enriched oxi-hydroxide outer layer that is depleted in nickel. Indeed, positive ion depth profiles are marked by apparent peaks of chromium as initial surface layers of the oxide are sputtered away, with a nickel depletion zone matching the chromium peak (Figure 4.8a). Observation of the negative depth profiles in Figure 4.8b supports the presence of a oxi-hydroxide layer on stainless steel. For the passive film formed in acidic solution, preferential dissolution of iron was reported, leading to a chromium enriched oxide layer located adjacent to the bare metal [13]. As the acidity of the solution decreases, the solubility of the chromium starts to increase, essentially leading to higher fractions of iron in the oxides. This behaviour is seen in Figure 4.8b, where the intensity of $FeO^-$ is higher than that of $CrO_2^-$. The thickness increase of the passive film takes place due to an increase in the oxide part, while hydroxide thickness remains unchanged. The plateau seen in Figure 4.8b supports this argument. ToF-SIMS results on 316 stainless steel agree with a study carried out by Wang *et al.* [6].

The absence of passivation zones in the LSV of X65 carbon steel in pH 1 solution means studies of the synergistic component of erosion-corrosion under such conditions would be irrelevant. Such high corrosion rates are not expected to be encountered in industrial applications without the use of corrosion protection. Hence, pH 1 solution can not be used for further study of fundamental electrochemical-mechanical corrosion interactions in X65 carbon steel. For oil and gas transportation applications, including pipelines, 316 stainless steel is normally used in

sections most prone to erosion-corrosion, such as elbows. Since both X65 carbon steel and 316 stainless steel are expected to be in the same environmental conditions, pH 1 solution also will not be used for erosion-corrosion study of 316 stainless steel within this work.

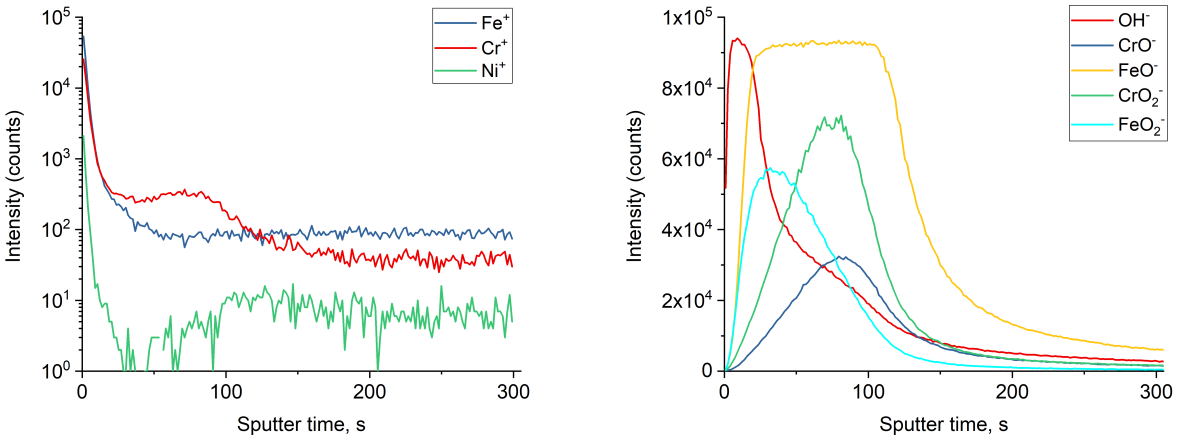


(a) (b)

Figure 4.8: Depth profiles for mirror polished air exposed 316L stainless steel treated Cs sputter beam of 0.5 $kV$ from crater size of 500 x 500 $\mu m^2$

### Potentiodynamic polarisation of steels in pH 4.0 KHP buffer electrolyte

LSV experiments were carried out in deaerated pH 4.0 KHP buffer electrolyte to evaluate corrosion of the studied samples. Figures 4.9 and 4.10 illustrate the difference in potentiodynamic polarisation of X65 carbon steel and 316 stainless steel electrodes in mildly acidic media. The decrease of solution acidity associated with the presence of less hydrogen ions, leads to lower overall maximum current densities being observed.

The X65 carbon steel electrode demonstrates a clear transition from cathodic to anodic behaviour at an equilibrium potential of -1.0 $V$ *vs.* MSE as expected for mild steels. The active anodic region continues up to 0.05 $V$ *vs.* MSE, after which the anodic current decreases rapidly and passivation is observed. This phenomena can be associated with salt film passivation, whereby dissolved iron forms a complex with electrolyte ions [14]. Extrapolating cathodic and anodic parts of the curve in Figure 4.9 gives $i_{corr} = 8.39 \times 10^{-5}\ A\,cm^{-2}$ and $E_{corr} = -1.09$ $V$ *vs.* MSE. Applying Equation 4.1 results in a corrosion rate of 0.98 $mm\,year^{-1}$ (see Table 4.2). The moderate corrosion rate of X65 carbon steel observed in pH 4.0 solution, with salt film passivation happening beyond a certain applied potential makes this environment useful to study individual components of erosion-corrosion. For example, scratching at passive potential could be helpful to mimic erosion-enhanced corrosion conditions, as one could measure

bare metal corrosion rates after removal of the passive layer. Additionally, 'sweet' conditions, defined by the presence of $CO_2$ gas, commonly encountered in oil and gas production and transportation have mildly acidic pH, hence making this environment an interesting one to study the fundamentals of erosion-corrosion. For reference, 'sour' conditions require presence of $H_2S$ gas above a certain ratio.

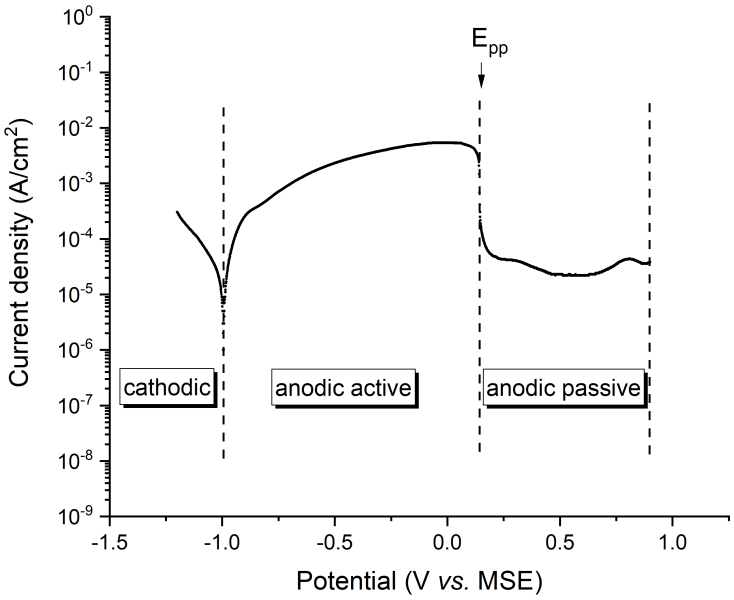


Figure 4.9: Linear scanning voltammogram of X65 carbon steel working electrode swept from -1.2 *V vs.* MSE to 0.9 *V vs.* MSE at room temperature in Ar-saturated aqueous KHP buffer solution at pH 4.0.

Polarisation of 316 stainless steel at pH 4.0 is characterised by a cathodic to passive transition at -0.86 *V vs.* MSE, which continues up to 0.82 *V vs.* MSE (Figure 4.10). For stainless steel widening of the passive zone and decrease of $i_{pass}$ is typical as the acidity of the electrolyte is decreased. Oxidation peaks can be observed at 0.22 *V vs.* MSE and 0.5 *V vs.* MSE within this region. These peaks correspond to transpassive oxidation of Cr and Mo oxides (Equation 4.5 and 4.6) [15], [16]. The oxygen evolution reaction is characterised by the sharp increase of current density at 0.83 *V vs.* MSE. Extrapolating anodic and passive regions of the LSV curve in Figure 4.10 around the equilibrium potential gives $i_{corr} = 1.88 \times 10^{-6}\ A\ cm^{-2}$ and $E_{corr} = -0.85\ V$ *vs.* MSE. Applying Equation 4.1 results in a corrosion rate of 0.02 $mm\ year^{-1}$. It should be noted that extrapolation overestimates the corrosion rate of the stainless steel due to the dynamic nature of the polarisation scanning - current transient measurements at the corrosion potential were much lower - but it is deemed acceptable for the purpose of this work.

$$Cr_2O_3 + 5\,H_2O \longrightarrow 2\,Cr_2O^{2-}_{4(aq.)} + 10\,H^+ + 6\,e^- \tag{4.5}$$

$$MoO_2 + 2\,H_2O \longrightarrow MoO^{2-}_{4(aq.)} + 4\,H^+ + 2\,e^- \tag{4.6}$$

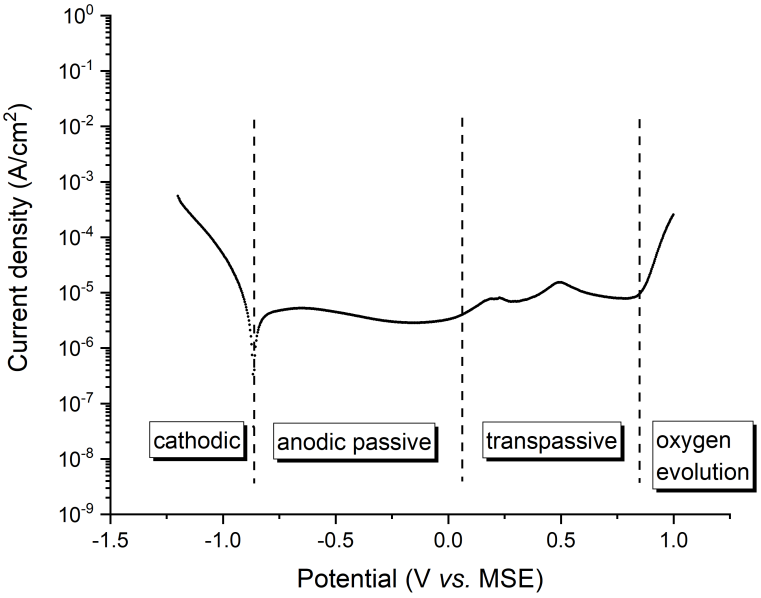


Figure 4.10: Linear scanning voltammograms of 316 stainless steel working electrode swept from -1.2 *V vs.* MSE to 1.0 *V vs.* MSE at room temperature in Ar-saturated aqueous KHP buffer solution at pH 4.0.

SEM micrographs of X65 carbon steel and 316 stainless steel samples polarised in deaerated pH 4.0 KHP electrolyte are presented in Figure 4.11. X65 carbon steel had occasional micron sized pits on the surface. However, the degree of degradation of the sample in pH 4 solution was lower compared to that polarised in the highly acidic solution of pH 1 (Figure 4.11a *vs.* Figure 4.5a). The decreased acidity of the solution and salt film passivation contributed to a lowered corrosion rate of X65 carbon steel at pH 4.0. 316 stainless steel had mostly smooth morphology, with occasional areas of dissolution near scratches that were artefacts left after polishing (Figure 4.11b).

### Potentiodynamic polarisation of steels in pH 8.3 borate buffer electrolyte

As the solution pH is increased to 8.3, X65 carbon steel shows an active to passive transition as seen in Figure 4.12. Passivation potential occurs at $E_{pp} = -0.96\ V$ *vs.* MSE with a critical current density equal to $4.3 \times 10^{-6}\ A\,cm^{-2}$. Iron shows passivity over wider potential ranges in near-neutral and basic solutions compared to acidic media as predicted by thermodynamics

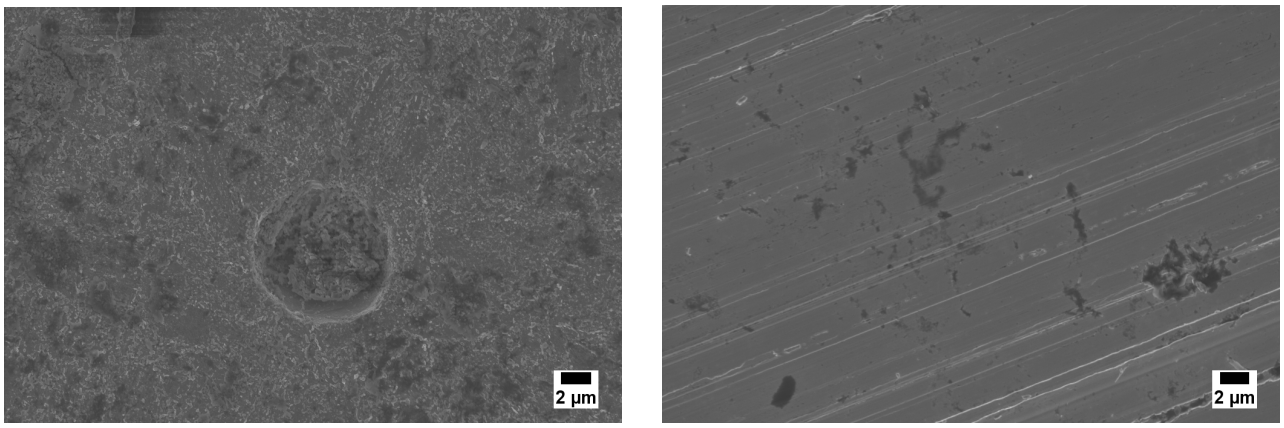


(a) (b)

Figure 4.11: SEM micrographs of a) X65 carbon steel coupon after LSV in $N_2$-saturated KHP solution at pH 4.0, from -1.2 *V vs.* MSE to 0.8*V vs.* MSE and b) 316 stainless steel coupon after LSV in $N_2$-saturated KHP solution at pH 4.0, from -1.2 *V vs.* MSE to 1.0 *V vs.* MSE.

[17]. The polarisation behaviour of X65 carbon steel in borate buffer reported here agrees with the literature [18]. Passivity of iron in alkaline electrolytes is achieved *via* iron dissolution at early stages of polarisation, followed by iron hydroxide precipitation once saturation is achieved (Equation 4.7) [19]. As the potential is increased further a current surge is seen due to the oxygen evolution reaction from 0.57 *V vs.* MSE onward.

$$Fe^{2+}(aq) + 2\,OH^{-}(aq) \longrightarrow Fe(OH)_2(s) \tag{4.7}$$

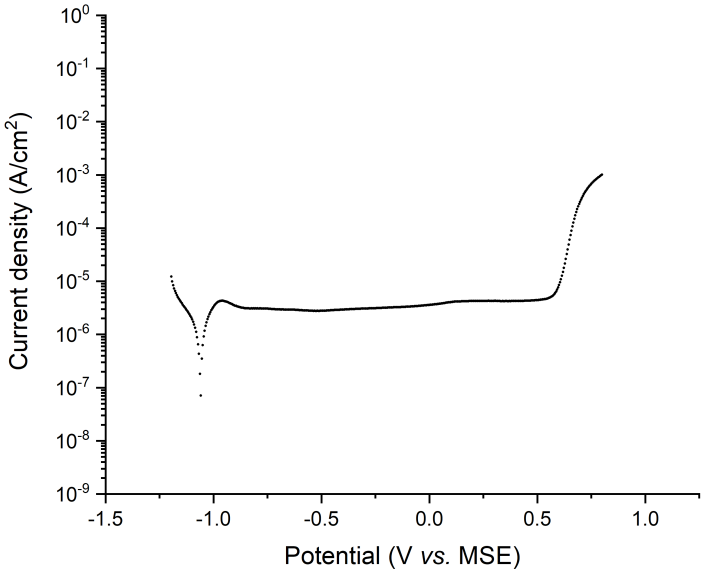


Figure 4.12: Linear scanning voltammogram of X65 carbon steel working electrode swept from -1.2 *V vs.* MSE to 0.9 *V vs.* MSE at room temperature in Ar-saturated aqueous borate buffer solution at pH 8.3.

316 stainless steel showed a lower corrosion rate in pH 8.3 borate buffer solution compared to the solutions tested above, owing to the superimposition of the passivity regions of both chromium and iron. Tafel extrapolation of the LSV shown in Figure 4.13 results in $i_{corr} = 2.02 \times 10^{-7}\ A\,cm^{-2}$ and $E_{corr} = -0.92\ V\ vs.$ MSE, with a corrosion rate as low as 0.002 $mm\ year^{-1}$. A peak corresponding to chromium (III) oxidation occurs at *ca.* 0.26 $V$ *vs.* MSE and the oxygen evolution reaction takes place from *ca.* 0.57 $V$ *vs.* MSE onward.

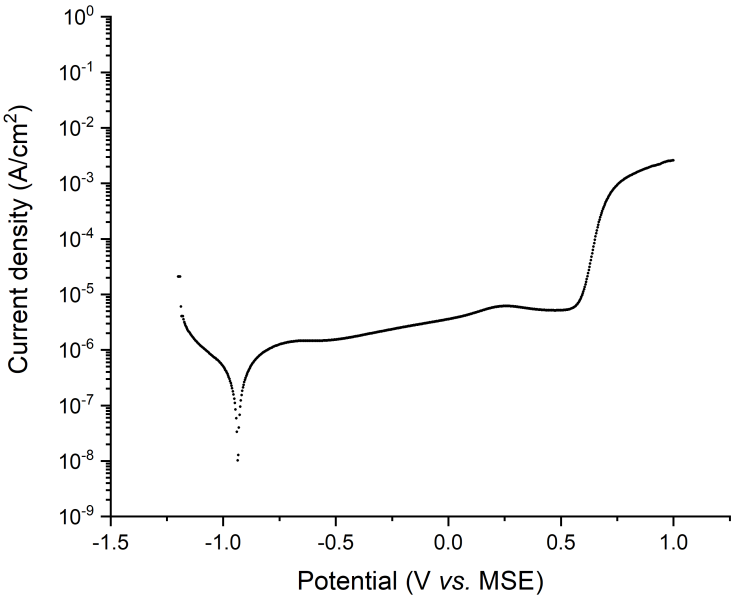


Figure 4.13: Linear scanning voltammograms of 316 stainless steel working electrode swept from -1.2 $V$ *vs.* MSE to 1.0 $V$ *vs.* MSE at room temperature in Ar-saturated aqueous borate buffer solution at pH 8.3.

SEM micrographs of X65 carbon steel and 316 stainless steel polarised in pH 8.3 deaerated borate buffer solution are presented in 4.14. The surfaces of the samples appear to be corrosion free owing to the passivity of both alloys in this solution as described above. Low corrosion rates reported here imply that the majority of the weight loss during erosion-corrosion will likely be dominated by the erosion component, as suggested by previous studies [20], [21]. Hence, this condition will not be used for further synergy studies using electrode scratching equipment.

The corrosion rates of X65 carbon steel and 316 stainless steel at all pHs studied were calculated from the above linear polarisation graphs and are presented in Table 4.2 and 4.3 respectively. It should be noted that these are estimates using Tafel extrapolation and involve certain approximations and human error.

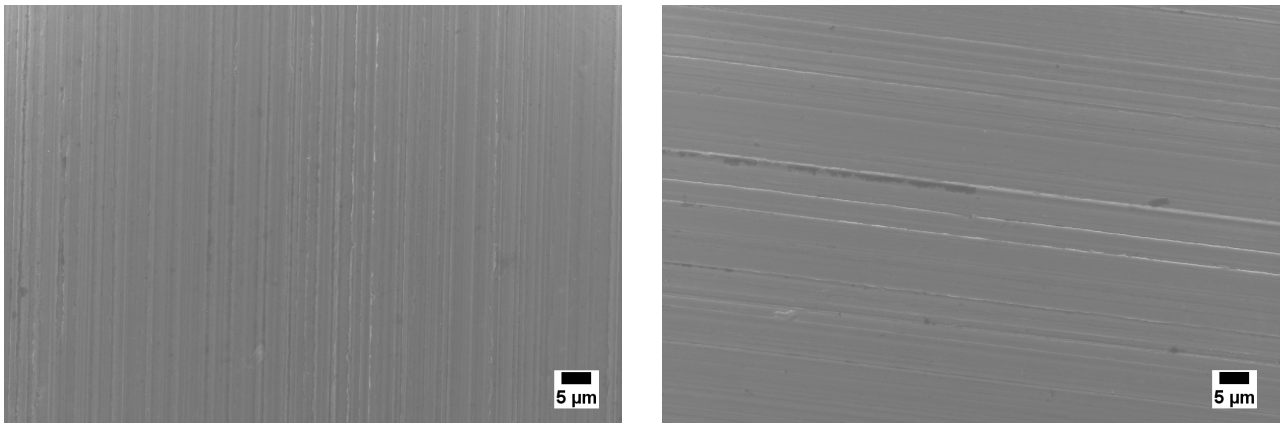


(a) (b)

Figure 4.14: SEM micrographs of a) X65 carbon steel coupon after LSV in $N_2$-saturated KHP solution at pH 4.0, from -1.2 *V vs.* MSE to 0.8*V vs.* MSE and b) 316 stainless steel coupon after LSV in $N_2$-saturated KHP solution at pH 4.0, from -1.2 *V vs.* MSE to 1.0 *V vs.* MSE.

Table 4.2: Corrosion rates of X65 carbon steel calculated using Tafel extrapolation method.

| Solution pH | $E_0$, *V vs.* MSE | $E_{corr}$, *V vs.* MSE | $\log(i_{corr})$ | $i_{corr}$, $A\,cm^{-2}$ | CR, $mm\,year^{-1}$ |
|---|---|---|---|---|---|
| 1.0 | -0.94 | -0.94 | -3.55 | $2.81 \times 10^{-4}$ | 3.27 |
| 4.0 | -1.00 | -1.09 | -4.08 | $8.39 \times 10^{-5}$ | 0.98 |
| 8.3 | -1.06 | -1.05 | -5.93 | $1.18 \times 10^{-6}$ | 0.014 |

Table 4.3: Corrosion rates of 316 stainless steel calculated using Tafel extrapolation method.

| Solution pH | $E_0$, *V vs.* MSE | $E_{corr}$, *V vs.* MSE | $\log(i_{corr})$ | $i_{corr}$, $A\,cm^{-2}$ | CR, $mm\,year^{-1}$ |
|---|---|---|---|---|---|
| 1.0 | -0.75 | -0.74 | -5.26 | $5.53 \times 10^{-6}$ | 0.057 |
| 4.0 | -0.86 | -0.85 | -5.73 | $1.88 \times 10^{-6}$ | 0.020 |
| 8.3 | -0.94 | -0.92 | -6.69 | $2.02 \times 10^{-7}$ | 0.002 |

### 4.3.2 Mechanical-electrochemical behaviour of steels

Electrochemical behaviour of X65 carbon steel and 316 stainless steel in various media concluded that pH 4.0 KHP buffer solution was a suitable media for studying erosion-corrosion of these alloys. Single and multiple scratching experiments that evaluate the fundamental electrochemical-mechanical behaviour of these steels are presented below.

#### Potentiostatic amperometry

Potentiostatic amperometry was implemented to observe fundamental mechanical-electrochemical behaviour of steels. The electrolyte of pH 4.05 was chosen as it had a pH comparable to the

'sweet' conditions encountered during oil and gas transportation. The applied potentials for X65 carbon steel and SS316 were chosen based on linear scanning voltammograms depicted in Figures 4.9 and 4.10 respectively. Table 4.4 lists the set potentials chosen for amperometry. As mentioned in section 4.3.1, 316 stainless steel has a passive film at anodic potentials, hence no amperometry was carried out at active anodic potentials.

Table 4.4: Potentials applied to X65 carbon steel and 316 stainless steel working electrodes during amperometry.

| Metal | Potential | | |
|---|---|---|---|
| | Cathodic | Active anodic | Passive anodic |
| X65 carbon steel | -1.1 *V vs.* MSE | -0.3 *V vs.* MSE | 0.6 *V vs.* MSE |
| 316 stainless steel | -1.1 *V vs.* MSE | n/a | 0 *V vs.* MSE |

### Scratching under cathodic potential

Figure 4.15 and Figure 4.16 present the results of potentiostatic amperometry of X65 carbon steel and 316 stainless steel at cathodic potentials. Application of cathodic potential drives the hydrogen reduction reaction at the working electrode.

For a X65 carbon steel electrode, evolution of hydrogen gas bubbles on the surface of the electrode slightly reduces overall cathodic current by blocking the active surface area (Figure 4.15). Scratching at -1.1 *V vs.* MSE influences the current density (red circle). Upon contact of the scratching tip with the electrode, the bare metal area is increased, therefore increasing sites for hydrogen reduction and hence the cathodic current density. This locally higher cathodic current tends to decrease due to tip interference and pick up once the tip is withdrawn (see the inset of Figure 4.15). SEM micrograph of the single scratched X65 carbon steel electrode in Figure 4.19 is free of corrosion products, with etching of the bulk metal happening around the scratch.

In Figure 4.16 a transient decay of cathodic current on 316 stainless steel working electrode can be seen. It can be attributed to the reduction of metal oxide. The passive layer on stainless steel does not fully reduce at applied potential of -1.1 *V vs.* MSE due to the reduction potential of chromium being much lower than this value. At the beginning of scratching (see Figure 4.16 inset) there is a current decrease from the disturbance of the tip and hydrogen evolution. As the tip leaves the electrode, current density increases due to an increase in surface area and the exposure of bare metal that may be more active for hydrogen reduction.

Single scratch experiments under cathodic potentials show increases of cathodic current

density for both X65 carbon steel and 316 stainless steel. Local transients during scratching tend to differ due to tip disturbance and the surface sensitivity of the hydrogen evolution reaction (HER) (Equations 4.8 – 4.10). The mechanism of HER involves an electrochemical hydrogen adsorption step, as well as electrochemical and/or chemical desorption of hydrogen step(s). The kinetics of HER depends heavily on the substrate and current densities can vary by as much as 10 orders of magnitude due to the first step of HER being hydrogen absorption, which is strongly influenced by the substrate chemistry.

$$H^+ + M + e^- \longrightarrow MH_{ads} \quad \text{Volmer equation} \tag{4.8}$$

$$MH + H^+ + e^- \longrightarrow M + H_2 \quad \text{Heyrovsky equation} \tag{4.9}$$

$$2\,MH \longrightarrow 2\,M + H_2 \quad \text{Tafel equation} \tag{4.10}$$

Although deconvoluting the mechanisms of HER on carbon and stainless steel scratched electrodes is outside the scope of this work, an important implication of the electrode scratching setup coupled with RDE is that it enables the changes in the cathodic current due to local surface changes to be probed.

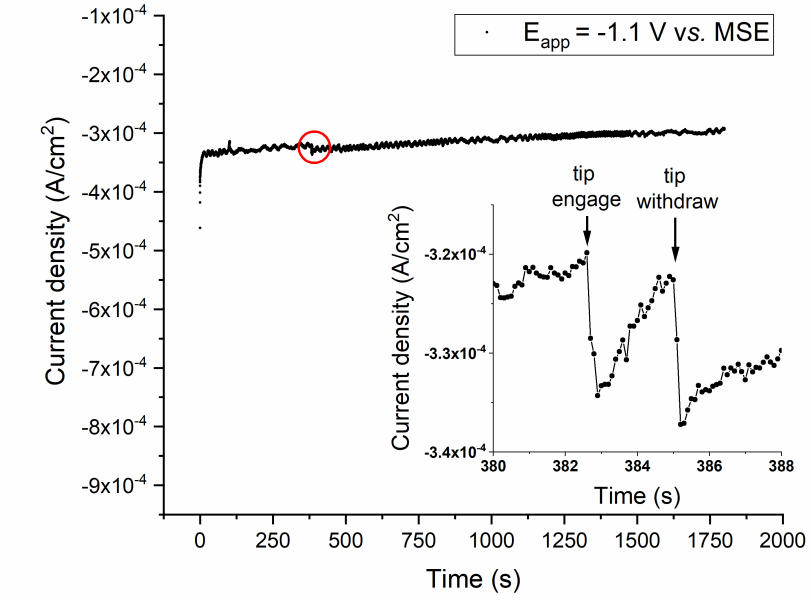


Figure 4.15: Current transient recorded from X65 carbon steel working electrode during single scratch experiment at applied potential of -1.1 *V vs.* MSE in pH 4.0 KHP solution deaerated with Ar. Inset: zoom in circled area - current transient showing the start and end of scratching.

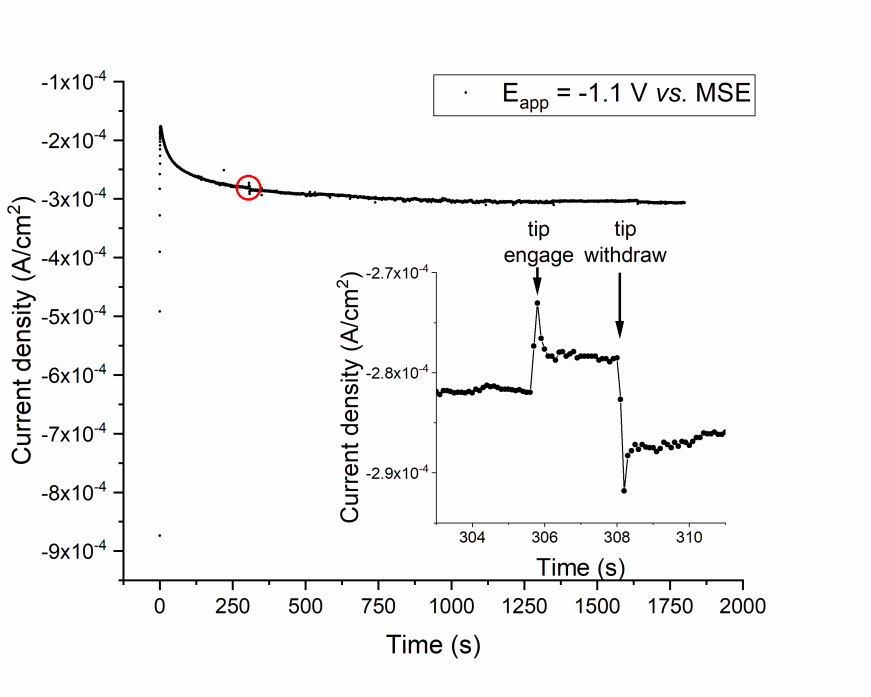


Figure 4.16: Current transient recorded from 316 stainless steel working electrode during single scratching at applied potential of -1.1 *V vs.* MSE in pH 4.0 KHP solution deaerated with Ar. Inset: zoom in circled area - current transient showing the beginning and the start and end of scratching.

During multiple scratching experiments at -1.1 *V vs.* MSE the cathodic current density increases with each successive scratch due to increase of bare metal area on both X65 carbon steel (Figure 4.17) and 316 stainless steel (Figure 4.18). Creation of each new scratch is accompanied by a current transients similar to those seen in Figures 4.15 and 4.16. Partial oxide reduction on 316 stainless steel can also be seen during multiple scratching of 316 stainless steel as evident from the decay of current transient (Figure 4.18). The decay is more pronounced due to the bare metal area increase with every consecutive scratch that creates new sites for proton reduction. As soon as scratching stops, around 1640 *s*, cathodic current density decreases on both metals. This could happen due to deactivation of the surface or bubble formation (once the scratching stops, the tip is not removing bubbles anymore). It should be noted that the final cathodic current values are still higher than the original current values.

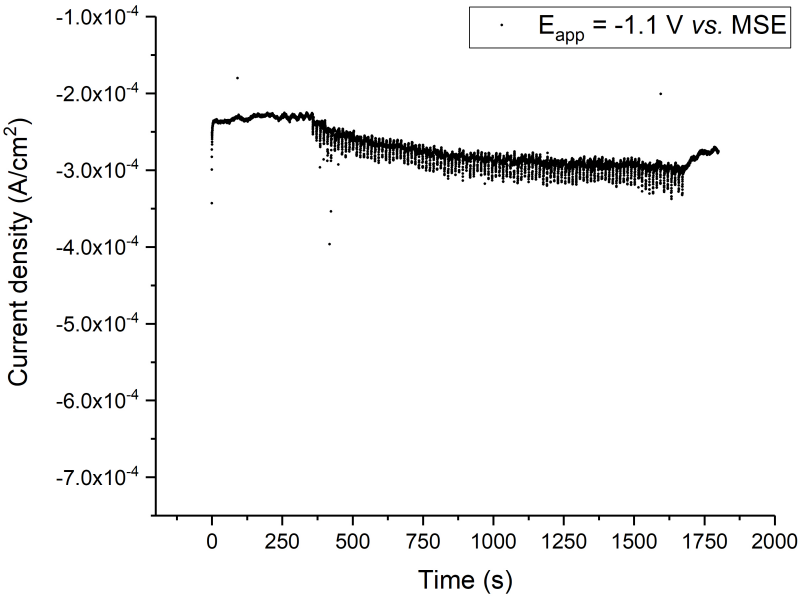


Figure 4.17: Current transient recorded from X65 carbon steel working electrode during multiple scratching at applied potential of -1.1 *V vs.* MSE. in pH 4.0 KHP solution deaerated with Ar.

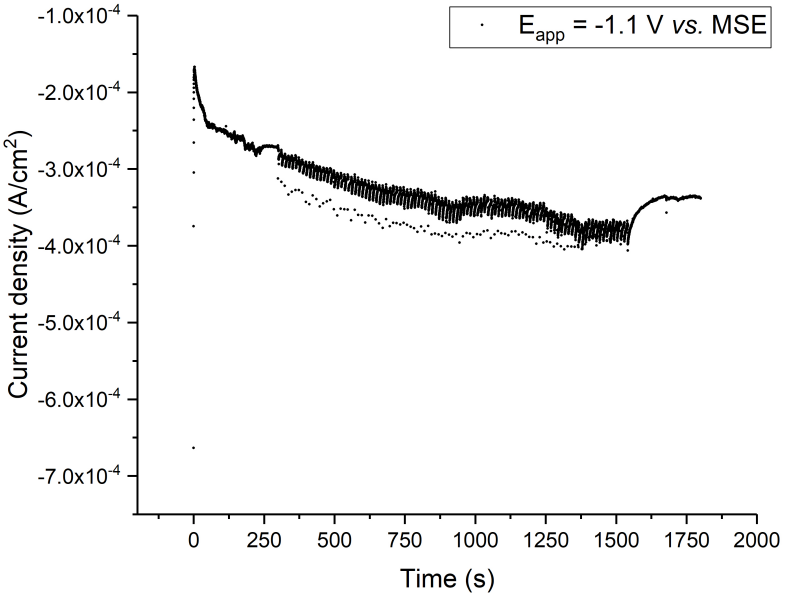


Figure 4.18: Current transient recorded from 316 stainless steel working electrode during multiple scratching at applied potential of -1.1 *V vs.* MSE. in pH 4.0 KHP solution deaerated with Ar.

An SEM micrograph of X65 carbon steel sample repeatedly scratched in pH 4.0 KHP buffer electrode at -1.1 *V vs.* MSE is presented in Figure 4.20. The scratches were created at the same location, which allows the study of multiple erosion-corrosion events. These erosion-corrosion

events are easy to quantify unlike erosion-corrosion experiments involving sand particles, where the collisions are random. The micrograph appears to be corrosion product free, with the bulk of the metal appearing as etched surface. EDS analysis of X65 carbon steel samples was conducted both on single and multiple scratched samples. Signal was collected both from the bottom of the scratch and the bulk metal (Table 4.5). The chemical composition was uniform within these regions and no oxygen signal was picked up by the detector.

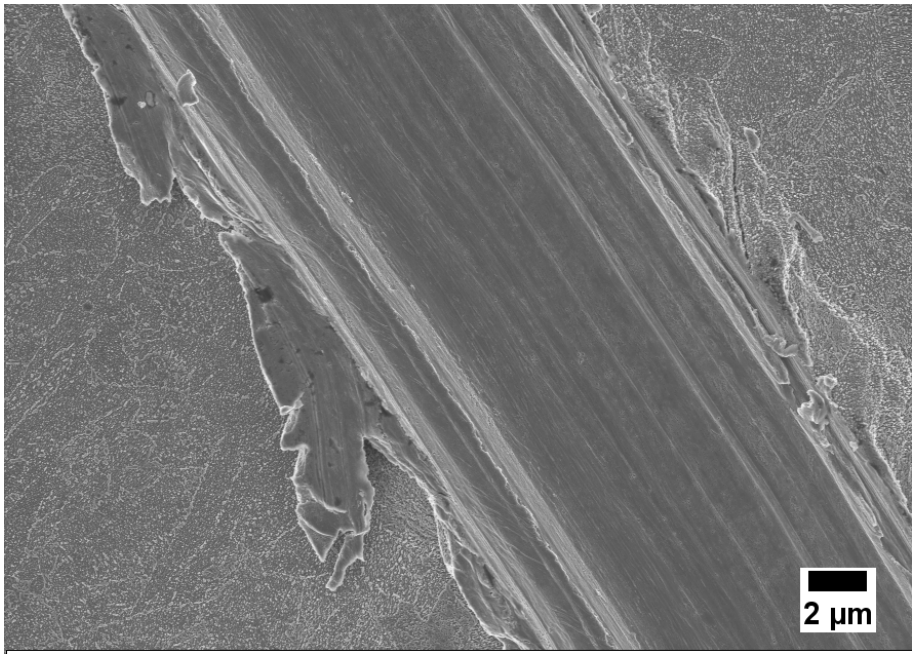


Figure 4.19: SEM micrograph of single-scratched X65 carbon steel electrode at applied potential of -1.1 *V vs.* MSE in pH 4.0 KHP solution deaerated with Ar.

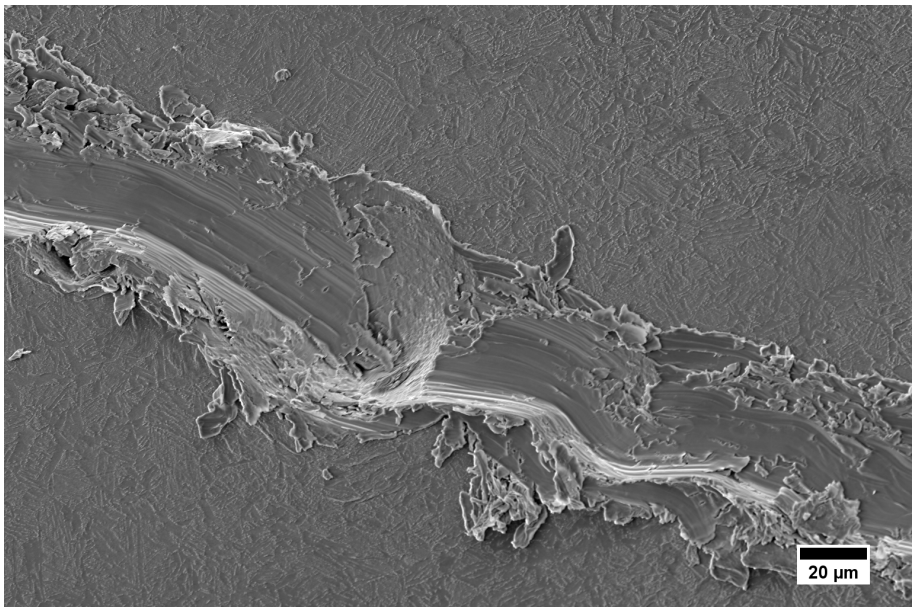


Figure 4.20: SEM micrograph of carbon steel scratched 100 times at applied potential of -1.1 *V vs.* MSE in pH 4.0 KHP solution deaerated with Ar.

Table 4.5: EDS analysis of X65 carbon steel samples after scratching at applied voltage of -1.1 *V vs.* MSE in pH 4.0 KHP solutions.

| No. of scratches | $E_{app}$,V *vs.MSE* | Bottom of the scratch, *wt.*% | | | Bulk of the metal, *wt.*% | | |
|---|---|---|---|---|---|---|---|
| | | Fe | Mn | Si | Fe | Mn | Si |
| 3 | -1.1 | 98.55 | 1.04 | 0.41 | 98.36 | 1.18 | 0.46 |
| 100 | -1.1 | 98.39 | 1.2 | 0.41 | 98.36 | 1.23 | 0.41 |

Both single and multiple scratching of electrodes under cathodic conditions demonstrated the absence of anodic current. Under this condition both metals are cathodically protected, preventing the metal from corrosion. Therefore, scratching under cathodic potentials can be used to decouple pure erosion rate of the metal by estimating mass/volume loss of the electrode. Additionally, this method allows the effects of cathodic protection, during which negative potentials to that of equilibrium potential are normally applied to the metal in order to protect it from corroding to be investigated. An interesting surface activation phenomenon influencing HER rates was shown due to scratching. However, both are beyond the scope of the current work but could be of interest for future research.

### Scratching at anodic potentials

Figure 4.21 and 4.22 present current transients recorded during single and multiple scratching of X65 carbon steel electrodes at -0.3 *V vs.* MSE. Since 316 stainless steel spontaneously forms a passive layer, no active region exists.

At -0.3 *V vs.* MSE X65 carbon steel is actively corroding, with the anodic current density reaching as high as $10^{-2} A\, cm^{-2}$ in the first few seconds in which a potential is applied. The current drops once iron oxi-hydroxides precipitate on the surface. Once the tip approaches the surface of the electrode at *ca.* 300 *s*, the current density drops due to the interference of the tip. As soon as the tip is retracted, the current density returns to its original value (Figure 4.21 inset). A similar variation of local current is observed during multiple scratching experiments (Figure 4.22) . Repetition of scratching does not affect the overall current density, *i.e.* presence of erosion does not seem to accelerate corrosion at an applied potential of -0.3 *V vs.* MSE. This agrees with previous research [22], which concluded that at very high corrosion rates erosion does not significantly affect corrosion under high current density active dissolution conditions.

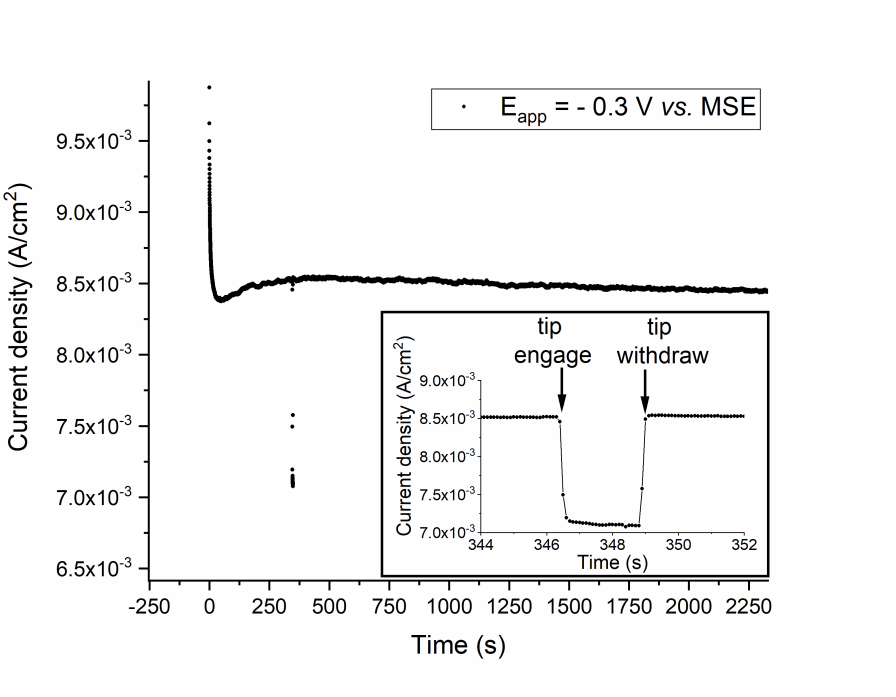


Figure 4.21: Current transient recorded from X65 carbon steel working electrode during single scratch experiments at applied potential of -0.3 $V$ *vs.* MSE in pH 4.0 KHP solution deaerated with Ar. Inset: zoom into current transient showing the start and the end of scratching.

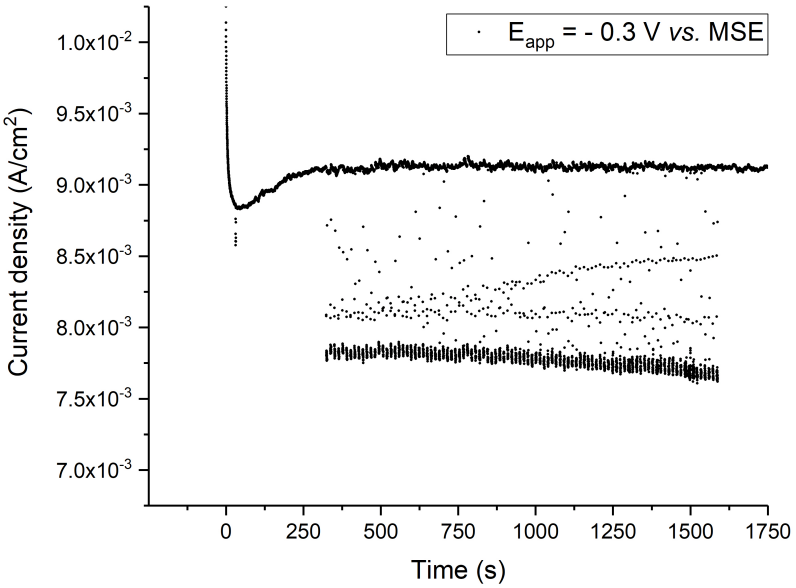


Figure 4.22: Current transient recorded from X65 carbon steel working electrode during multiple scratching at applied potential of -0.3 $V$ *vs.* MSE in pH 4.0 KHP solution deaerated with Ar.

An SEM micrograph of single scratched X65 carbon steel is given in Figure 4.23. The sample appears to be heavily corroded, and the scratch track is barely visible due to the build up of corrosion products along it. Figure 4.24 and 4.25 present SEM micrographs of multiple

scratched X65 carbon steel sample. In line with the high anodic currents recorded during scratching at -0.3 *V vs.* MSE, the sample is characterised by the presence of corrosion products in the bulk of the sample, as well as on the walls of the scratch. Cracks perpendicular to the scratching direction can be noticed inside the scratch track, along with occasional pits in the vicinity of the scratch consistent with the recorded high anodic currents.

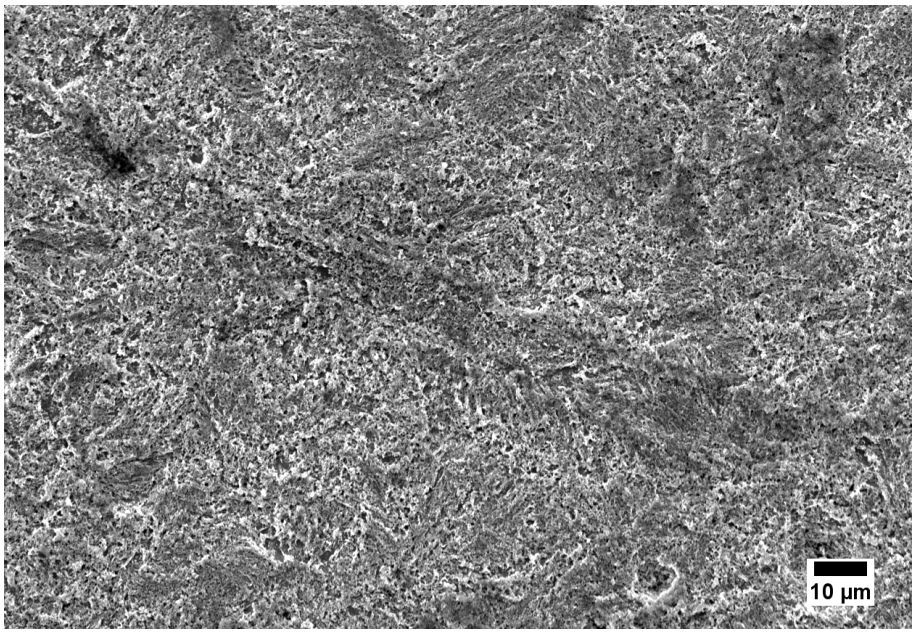


Figure 4.23: SEM micrograph of single-scratched X65 carbon steel at applied potential of -0.3 *V vs.* MSE in pH 4.0 KHP solution deaerated with Ar.


Figure 4.24: SEM micrograph of multiple-scratched X65 carbon steel at applied potential of -0.3 *V vs.* MSE in pH 4.0 KHP solution deaerated with Ar.

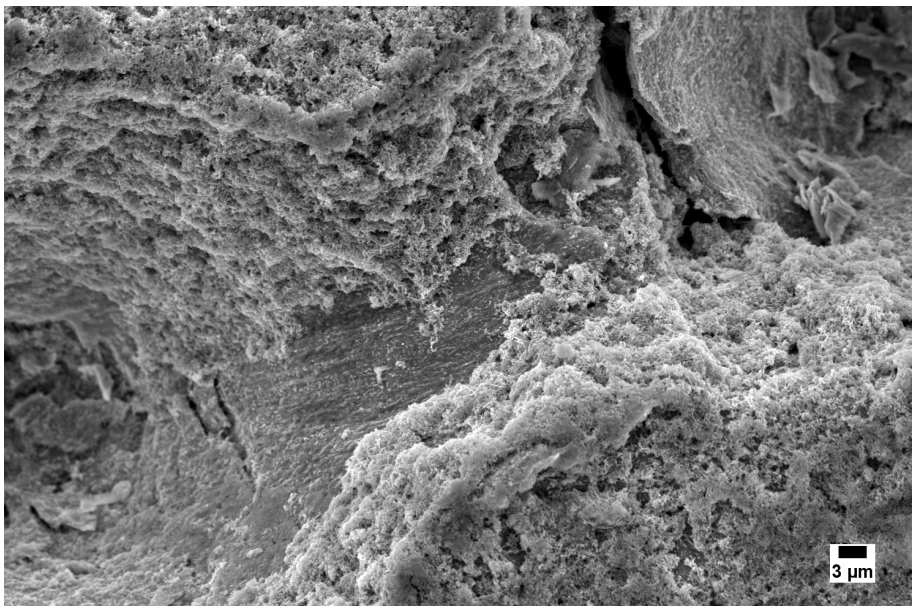


Figure 4.25: Close-up SEM micrograph of multiple-scratched X65 carbon steel at applied potential of -0.3 $V$ *vs.* MSE in pH 4.0 KHP solution deaerated with Ar: corrosion products build up on scratch walls.

Data show that under an applied potential of -0.3 $V$ *vs.* MSE there is no significant synergistic effects, hence this condition is not chosen for further study of the erosion-corrosion synergy of X65 carbon steel.

### Scratching under passive anodic potential

Application of a passive potential of 0.6 $V$ *vs.* MSE on a X65 carbon steel working electrode is characterised by a passivating current transient in the first few seconds (Figure 4.28). An oxide layer precipitates on the surface of X65 carbon steel protecting it from dissolution. The resultant constant current is called the base current of the electrode. Upon scratching, *via* the release of solenoid at *ca.* 300 $s$, some oxide film on the metal electrode is removed, exposing fresh unprotected bare metal to the solution. A sharp increase of the current density is recorded as the solenoid bounces off the surface of the rotating working electrode for a fraction of a second, after which the tip is fully in contact with the electrode (Figure 4.26). At this point the current plateaus out and is defined as bare metal current. Once the tip leaves the metal surface, the current peaks again before passivation takes place to give a new base current. Maximum peak currents recorded on X65 carbon steel working electrode due to scratching have values between $5.0 \times 10^{-5}$ and $1.0 \times 10^{-4} A\, cm^{-2}$. In fact, this value would be much larger if the area of the scratch was used instead of the total working electrode area for the current density calculation.

316 stainless steel behaves similar to X65 carbon steel when scratched under a passivating potential of 0.0 $V$ *vs.* MSE. The current density decays within the first few seconds of the

experiment, reaching a base current as the passive layer thickens (Figure 4.29). This passive layer is removed upon scratching, resulting in a current increase (Figure 4.26). The maximum peak current values generated by scratching 316 stainless steel working electrodes are an order of magnitude lower compared to those on X65 carbon steel and are between $5.0 \times 10^{-6}$ and $2.5 \times 10^{-5} A\, cm^{-2}$. 316 stainless steel has a thin passive oxide film (2-10 nm) and hence does not require as much charge as carbon steel to passivate. Refer to supplementary information in section 4.5 for passivation fits for 316 stainless steel.

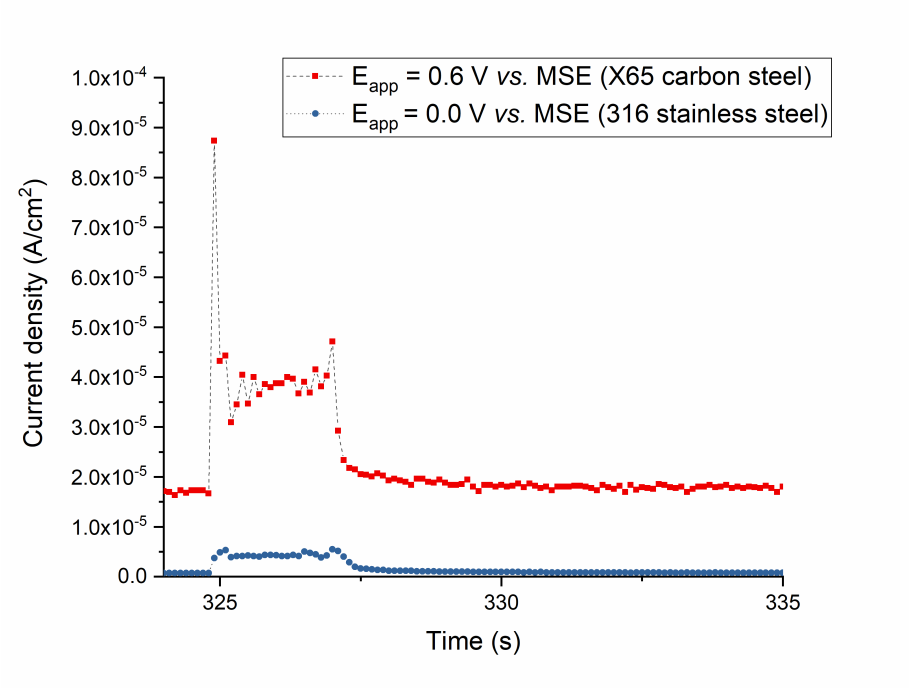


Figure 4.26: Typical repassivation peak for scratched X65 carbon steel and 316 stainless steel electrodes in pH 4.0 KHP solution. Base currents are $i_b$ (X65 carbon steel) $= 1.72 \times 10^{-5} A\, cm^{-2}$, $i_b$(316 stainless steel) $= 6.98 \times 10^{-7} A\, cm^{-2}$.

Normalising repassivation transients to peak currents recorded after tip removal allows comparison of how quickly repassivation happens on the different metal electrodes (Figure 4.27). As such, X65 carbon steel is characterised by a slower repassivation rate compared to 316 stainless steel, evident from the smaller slope of current *versus* time graph. Integrating each of the current transients over time allows calculation of the charge required to repassivate a single scratch. This can be plotted as charge density *versus* scratch number, as well as cumulative charge density *versus* scratch number (Figure 4.32 and Figure 4.34).

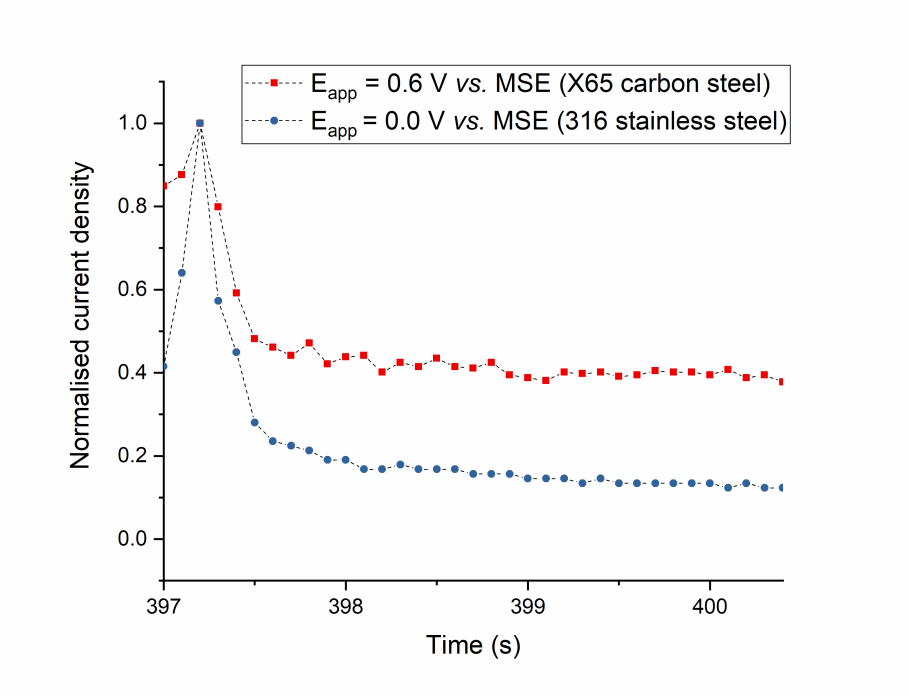


Figure 4.27: Current decay region normalised to peak current density value for scratched X65 carbon steel and 316 stainless steel electrodes in pH 4.0 KHP solution (See section 4.5 for the fits of 316 stainless steel passivation curves.)

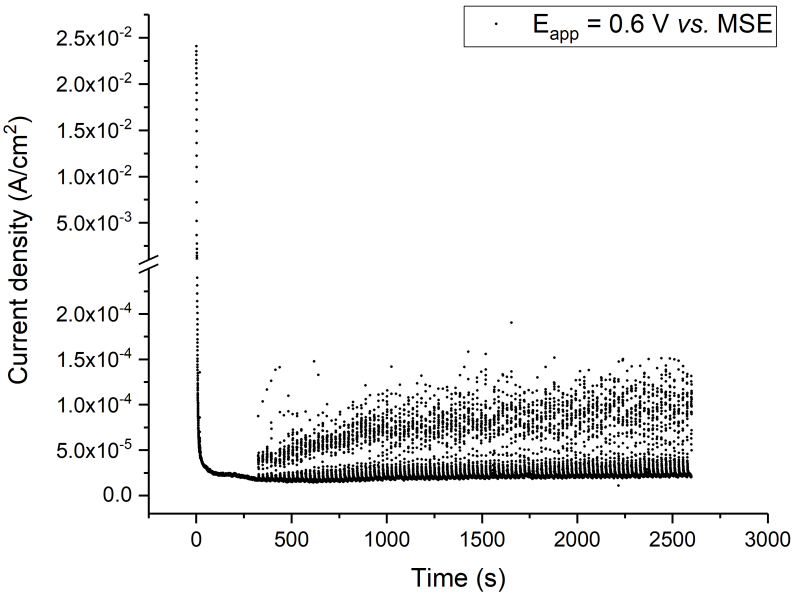


Figure 4.28: Current transients recorded from X65 carbon steel working electrode at applied potential of 0.6 *V vs.* MSE during a multiple scratching experiment. Note the difference in scales with Figure 4.29.

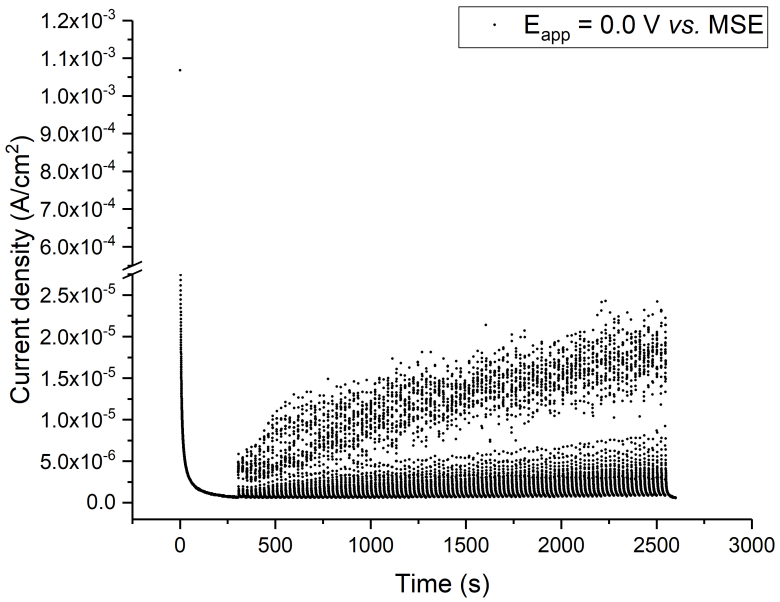


Figure 4.29: Current transients recorded from 316 stainless steel working electrode at applied potential of 0.0 *V vs.* MSE during multiple scratching experiments. Note the difference in scales with Figure 4.28.

An SEM micrograph of X65 carbon steel scratched 3 times at 0.6 *V vs.* MSE is presented in Figure 4.30. At this potential X65 carbon steel is passive — as expected the surface of the sample in SEM micrograph appears free of corrosion product. An SEM micrograph of X65 carbon steel scratched 100 times at the same potential is presented in Figure 4.31. The surface of the sample appears to be corrosion free with some etched areas present in the bulk of the sample. The circular features along the scratch track were created during the initial bouncing of the scratching tip, before full contact was established. Continuous scratching experiments can be used to avoid the interference from the tip bouncing. Table 4.6 contains the results of EDS analysis of these samples. The chemical composition of the samples as identified by SEM EDS is similar across the scratch and the bulk of the material. Unlike in samples scratched at -1.1 *V vs.* MSE (Table 4.5), some chromium signal was picked up from samples scratched at 0.6 *V vs.* MSE.

Table 4.6: EDS analysis of X65 carbon steel samples after scratching at applied voltage of 0.6 *V vs.* MSE in pH 4.0 KHP solutions.

| No. of scratches | Eapp, *V vs.* MSE | Bottom of the scratch, *wt.*% | | | | Bulk of the metal, *wt.*% | | | |
|---|---|---|---|---|---|---|---|---|---|
| | | Fe | Mn | Si | Cr | Fe | Mn | Si | Cr |
| 3 | 0.6 | 97.99 | 1.49 | 0.45 | 0.07 | 98.23 | 1.29 | 0.48 | 0 |
| 100 | 0.6 | 98.69 | 1.12 | 0.19 | 0 | 98.07 | 1.28 | 0.49 | 0.16 |

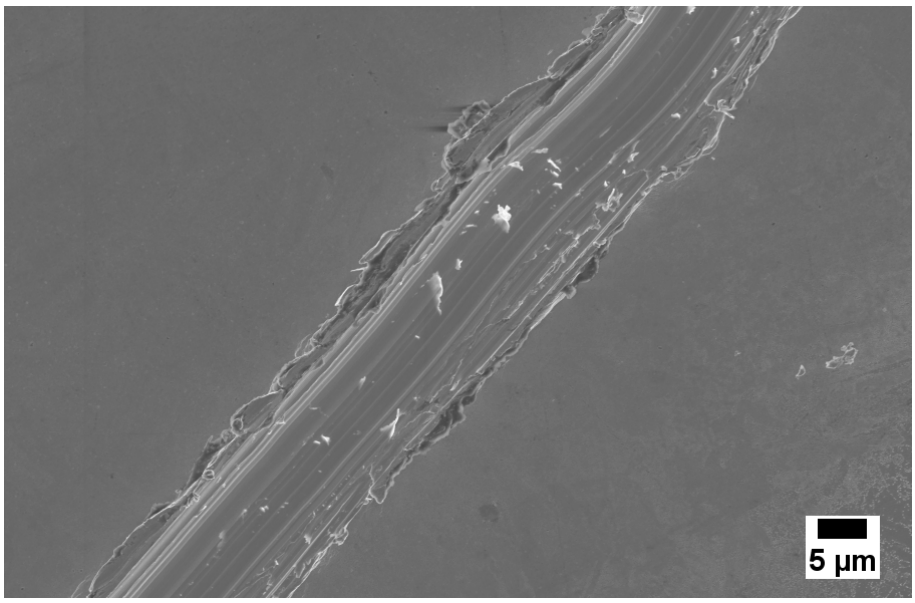


Figure 4.30: SEM micrograph of X65 carbon steel scratched 3 times at applied potential of 0.6 $V$ *vs.* MSE in pH 4.0 KHP solution deaerated with Ar.

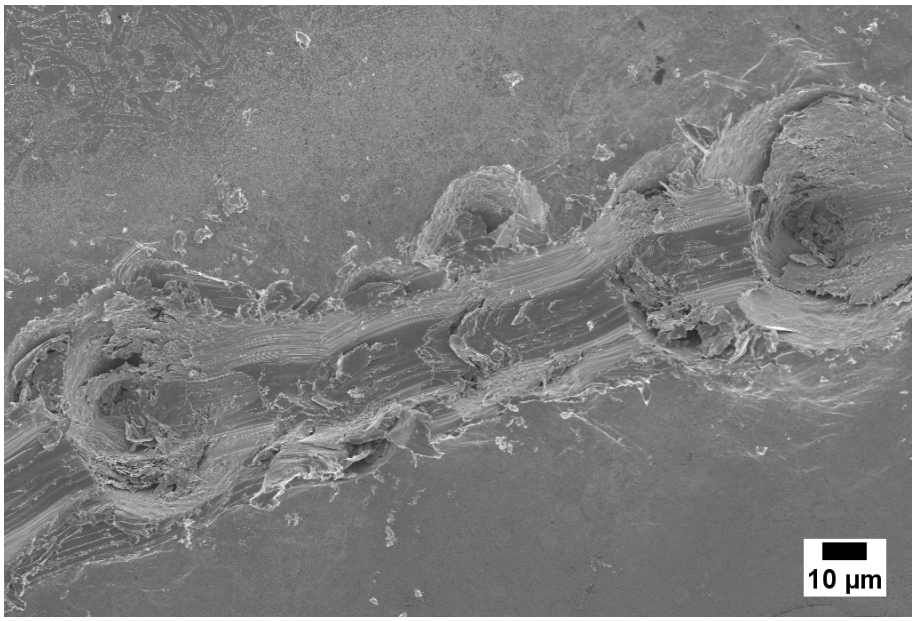


Figure 4.31: SEM micrograph of X65 carbon steel scratched *ca.* 100 times at 30 $RPM$ at applied potential of 0.6 $V$ *vs.* MSE in pH 4.0 KHP solution deaerated with Ar.

### Charge density *versus* scratch number

The charge density associated with each scratch is plotted *vs.* scratch number in Figure 4.32 (cumulative charge is discussed later). Charge density is related to mass loss and is approximately linear with scratch number until *ca.* the $40^{th}$ scratch, after which charge density plateaus out. This may indicate that as the same area is being scratched repeatedly, the material is undergoing a conditioning until after a period of time the same amount of material is removed with each scratch. The rate of mass loss inferred from cumulative charge density *vs.* scratch number

in Figure 4.33 shows that the predicted degradation rate is accelerated in the later scratches. This is evident from two different slopes obtained from linear extrapolation of charge density for the first 15 scratches and linear fit between scratch number 40 and 100. The charge density recorded during electrode scratching is a direct measurement of the erosion-enhanced corrosion ($c_e$) of a single scratching event. The fact that the mass loss rate does not have a uniform slope suggests that erosion-enhanced corrosion is time dependent. This is an important factor that needs to be considered for erosion-corrosion models. Time dependent mass loss might result from non-homogeneity of the polycrystalline alloy. Scanning electron microscope micrographs presented above confirmed the same location was repeatedly scratched. We speculate that the variation in mass loss with time is due to work hardening of the material. (Microstructural studies of alloys after scratching are discussed in Chapter 6). As more material is removed and the depth of the scratch is increased, the surface of the material changes, affecting the dissolution rates. Additionally, roughness affects the mass transfer coefficient and subsequent mass loss rates.

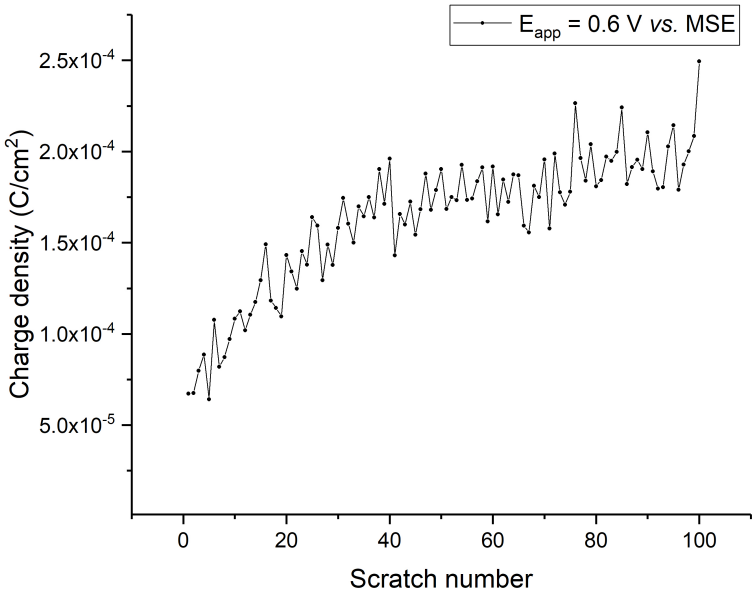


Figure 4.32: Charge density (total electrode area = 0.196 $cm^2$) *versus* scratch number recorded from X65 carbon steel working electrode during multiple scratching at applied potential of 0.6 $V$ *vs.* MSE at 30 $RPM$ rotating rate.

Figure 4.34 has the same y-axis scale as Figure 4.32. It is seen that charge density values associated with scratching 316 stainless steel electrode are much lower compared to those for X65 carbon steel. Charge density per scratched area agree with those reported in the literature [23], [24] and correspond to roughly 20–40 to 80–160 monolayers of oxide formed on stainless

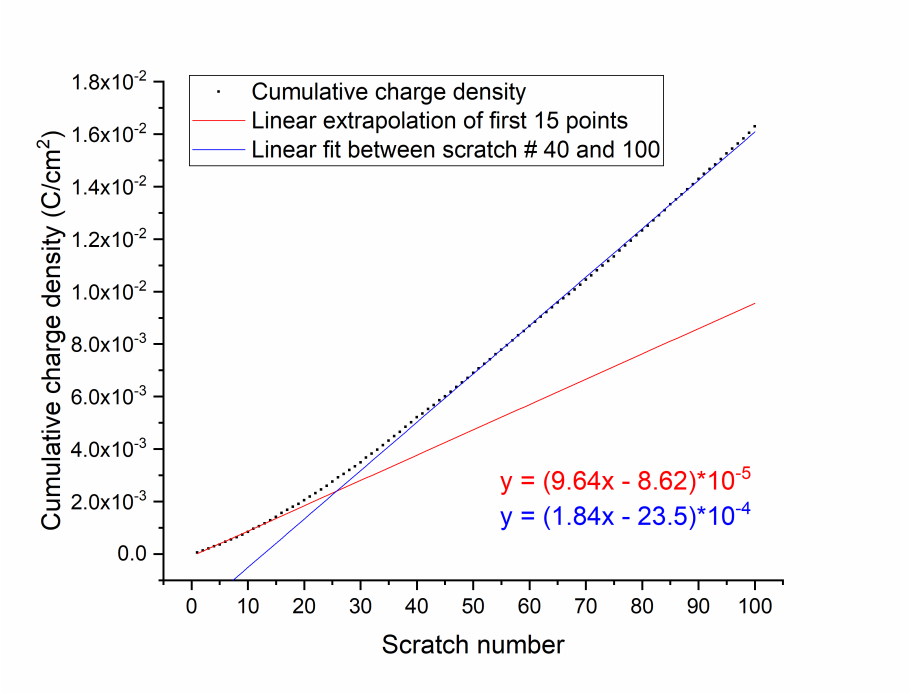


Figure 4.33: Cumulative charge density (total electrode area = 0.196 $cm^2$) *versus* scratch number recorded from X65 carbon steel during multiple scratching at applied potential of 0.6 $V$ *vs.* MSE.

steel during each scratch. In 316 stainless steel the charge density is approximately linear with number of scratches and there is no region of plateau observed within the studied number of scratches. This could either mean that at the 30 $RPM$ rotating rate no work hardening is taking place in 316 stainless steel samples during scratching, or all work hardened material is being removed. It is known that during passivation of austenitic stainless steels in acidic media, the oxide layer is enriched in chromium and some iron, while the layer between the bulk metal and the passive film is known to be nickel-enriched [12], [13]. This happens due to slower kinetics and higher thermodynamic stability of nickel compared to chromium and iron. It was shown that the passivating film formed on 316 stainless steel was less wear resistant compared to that on nickel [25]. Thus, the enrichment of the passive layer on 316 stainless steel with chromium and iron might contribute to an increase of charge density with scratch number. Additionally, time-dependency of mass loss can originate from the surface change and roughness variation as mentioned above. In general, it should be noted that the stainless steel and the passive film that forms on its surface change depending on the local conditions [13]. However, erosion-enhanced corrosion ($c_e$) is time-dependent on both carbon steel and stainless steel. Linear fit and extrapolation shows that the rate of $c_e$ on both metals is different. Synergy of erosion-corrosion is highly dependent on the substrate as multiple scratching experiments showed.

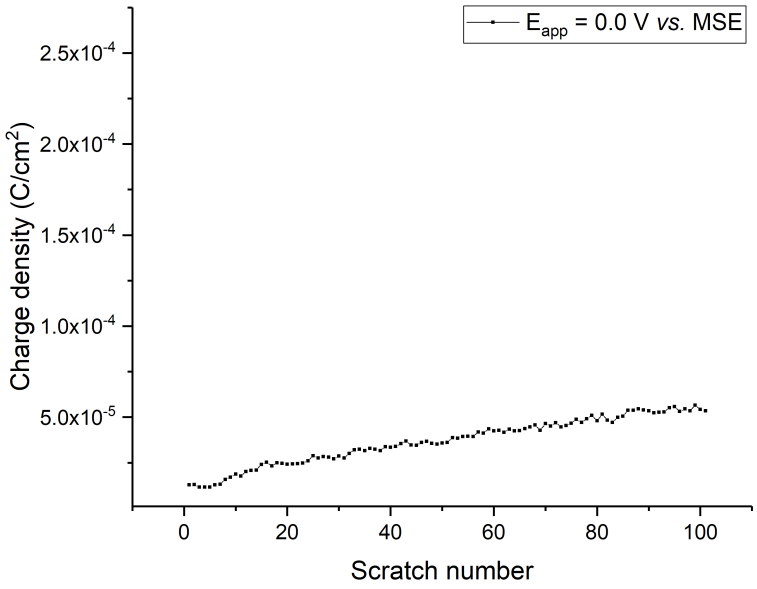


Figure 4.34: Charge density *versus* scratch number recorded from 316 stainless steel working electrode during multiple scratching at applied potential of 0.0 $V$ *vs.* MSE.

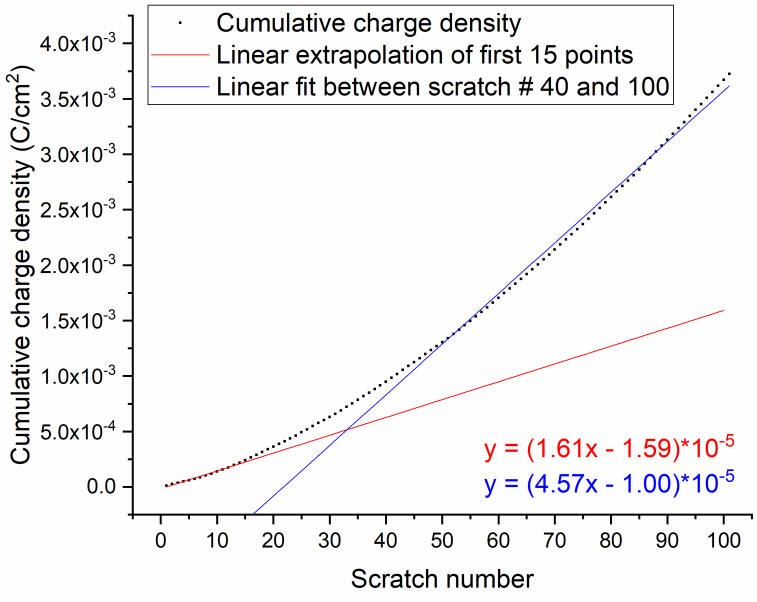


Figure 4.35: Cumulative charge density *versus* scratch number recorded from 316 stainless steel during multiple scratching at applied potential of 0.0 $V$ *vs.* MSE.

## 4.4 Summary

This chapter studied the fundamental electrochemical and mechanical-electrochemical behaviour of X65 carbon steel and 316 stainless steel. Linear scanning voltammetry of both alloys were conducted in aqueous solutions of pH 1.0, 4.0 and 8.3. The results of these studies agree with literature reported behaviour of the alloys. Time-dependent erosion-corrosion synergy was directly observed and quantified for the first time.

As expected, in pH 1 0.1 $M$ $H_2SO_4$ solution X65 carbon steel corroded actively, and no passivation zones were observed in LSV graphs due to the high solubility of iron oxy-hydroxides at this pH. 316 stainless steel in the same electrolyte showed an active to passive transition with corrosion rates as low as 0.06 $mm\ year^{-1}$. ToF-SIMS study of the polished 316 stainless steel samples confirmed the passive film consisted of oxy-hydroxide layers. Absence of passivation zones for X65 carbon steel in pH 1 solution means that it is irrelevant to study the synergistic component of erosion-corrosion, further these harsh conditions would not be expected in industrial applications without the use of corrosion protection. In pH 8.3 solutions both X65 carbon steel and 316 stainless steel are passive due to overlap of the passivity regions of iron and chromium metals that constitute the alloys. Low corrosion rates under these conditions imply that the majority of weight loss will be dominated by erosion, as suggested by previous studies [20], [21].

On the other hand, at pH 4.0 the LSV graph of X65 carbon steel showed an active to passive transition, most probably due to salt film passivation. This makes it an interesting environment to study erosion-corrosion synergy using an electrode scratching technique. Additionally, sweet conditions encountered in oil and gas industry have mildly acidic pH as well, making pH 4.0 KHP buffer an interesting environment to study the mechanisms of erosion-corrosion phenomena.

Following this, the fundamental mechanical-electrochemical behaviour of alloys was studied using the electrode scratching technique in pH 4.0 KHP electrolyte at a 30 $RPM$ rotation rate. The electrode scratching setup was coupled with an Arduino microcontroller to scratch X65 carbon steel and 316 stainless steel electrodes reproducibly. Both single and multiple scratching experiments were performed to confirm that the *same location was being repeatedly scratched.*

No net anodic current was recorded during multiple scratching of electrodes at cathodic potentials, making this a suitable condition for further calculation of pure erosion rates of materials. Additionally, an interesting phenomena of surface activation that led to an increase in HER rates was reported. Electrode scratching under cathodic conditions can also shine some

light on hydrogen embrittlement of steels, however it is beyond the scope of current thesis.

Repeated scratching of X65 carbon steel under active anodic conditions did not accelerate corrosion rates, while at passive anodic conditions, the erosion-enhanced corrosion rates of both X65 carbon steel and 316 stainless steel were found to be time-dependent. The scratching setup enabled assessment of the metals' tendency to passivate, and 316 stainless steel was found to passivate quicker than X65 carbon steel.

Bouncing of the scratching tip was sometimes found to be problematic, as it is expected to give erroneous data on degradation rate estimations. It was suggested that continuous scratching experiments, without retracting the solenoid tip should be used , see the next chapter, where decoupling erosion-corrosion components using electrode scratching technique will be demonstrated.

# Bibliography


[1] S. Fearn. *An Introduction to Time-of-Flight Secondary Ion Mass Spectrometry (ToF-SIMS) and its Application to Materials Science*. 2015.

[2] ASTM International. Making Potentiodynamic Anodic Standard Reference Test Method for Making Potentiodynamic Anodic Polarization Measurements (G5-14), 2014.

[3] B. N. Popov. Chapter 5 - Basics of Corrosion Measurements. In B. N. Popov, editor, *Corrosion Engineering*, pages 181–237. Elsevier, Amsterdam, 2015.

[4] E. McCafferty. *Introduction to corrosion science*. Springer International Publishing, 2010.

[5] S. Gao, C. Dong, H. Luo, K. Xiao, and X. Li. Electrochemical Behavior and Nonlinear Mott-Schottky Characterization of a Stainless Steel Passive Film. *Analytical Letters*, 47(7):1162–1181, 2014.

[6] Z. Wang, E. M. Paschalidou, A. Seyeux, S. Zanna, V. Maurice, and P. Marcus. Mechanisms of Cr and Mo Enrichments in the Passive Oxide Film on 316L Austenitic Stainless Steel. *Frontiers in Materials*, 6(September):1–12, 2019.

[7] S. Garber. Structure of scale on plain carbon steels. *Nature*, pages 1387–1388, 1959.

[8] S. Larose and R. Rapp. Review of low-temperature oxidation of carbon steels and low-alloy steels for use as high-level radioactive waste package materials. Technical report, Center for Nuclear Waste Regulatory Analyses, San Antonio, Texas, 1997.

[9] Y. Zhou, L. Guo, S. Zhang, S. Kaya, X. Luo, and B. Xiang. Corrosion control of mild steel in 0.1 M $H_2SO_4$ solution by benzimidazole and its derivatives: An experimental and theoretical study. *RSC Advances*, 7(39):23961–23969, 2017.

[10] G. Chan-Rosado and M. A. Pech-Canul. Influence of native oxide film age on the passivation of carbon steel in neutral aqueous solutions with a dicarboxylic acid. *Corrosion Science*, 153(March):19–31, 2019.

[11] S. Birosca, D. Dingley, and R. L. Higginson. Microstructural and microtextural characterization of oxide scale on steel using electron backscatter diffraction. *Journal of Microscopy*, 213(3):235–240, 2004.

[12] I. Olefjord and B. Elfstrom. The Composition of the Surface during Passivation of Stainless Steels. *Corrosion*, 38(1):46–52, 1982.

[13] C. Olsson and D. Landolt. Passive films on stainless steels - Chemistry, structure and growth. *Electrochimica Acta*, 48(9 SPEC.):1093–1104, 2003.

[14] T. R. Beck. Formation of Salt Films during Passivation of Iron. *Journal of The Electrochemical Society*, 129(11):2412, 1982.

[15] D. Zagidulin, X. Zhang, J. Zhou, J. J. Noël, and D. W. Shoesmith. Characterization of surface composition on Alloy 22 in neutral chloride solutions. *Surface and Interface Analysis*, 45(6):1014–1019, 2013.

[16] A. K. Mishra and D. W. Shoesmith. The activation/depassivation of nickel-chromium-molybdenum alloys: An oxyanion or a pH effect - Part II. *Electrochimica Acta*, 2013.

[17] E. D. Verink Jr. *Simplified Procedure for Constructing Pourbaix Diagrams*, chapter 7, pages 93–101. John Wiley  Sons, Ltd, 2011.

[18] L. Cáceres, A. Soliz, and T. Vargas. Potentiodynamic behavior of carbon steel in borate buffer solutions under different hydrodynamic conditions. *Journal of The Electrochemical Society*, 163(5):C171–C183, 2016.

[19] I. Dıez-Pérez, P. Gorostiza, F. Sanz, and C. Müller. First Stages of Electrochemical Growth of the Passive Film on Iron. *Journal of The Electrochemical Society*, 148(8):B307, 2001.

[20] B. D. Jana and M. M. Stack. Modelling impact angle effects on erosion-corrosion of pure metals: Construction of materials performance maps. *Wear*, 259(1-6):243–255, 2005.

[21] M. M. Stack. Bridging the gap between tribology and corrosion: From wear maps to Pourbaix diagrams. *International Materials Reviews*, 50(1):1–17, 2005.

[22] H. Guo. *Synergism in Erosion-Corrosion Caused by Interaction of Electrochemical and Mechanical Factors*. PhD thesis, 2006.

[23] G. T. Burstein and D. H. Davies. The Electrochemical Behavior of Scratched Iron Surfaces in Aqueous Solutions. *Journal of The Electrochemical Society*, 128(1):33, 1981.

[24] P. I. Marshall and G. T. Burstein. The effects of pH on the repassivation of 304L stainless steel. *Corrosion Science*, 23(11):1219–1228, 1983.

[25] P. Henry, J. Takadoum, and P. Berçot. Depassivation of some metals by sliding friction. *Corrosion Science*, 53(1):320–328, 2011.

## 4.5 Supplementary information

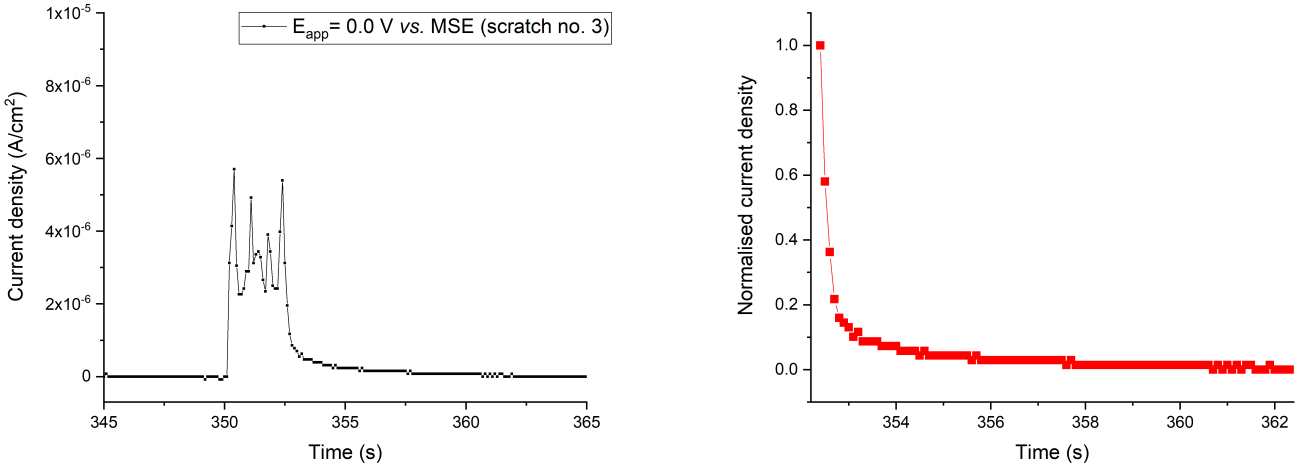


(a) (b)

Figure 4.36: a) A repassivation peak for scratched 316 stainless steel in pH 4.0 KHP solution for scratch number 3 and b) a current decay region normalised to peak current density value for the same scratch. Base current of $6.98 \times 10^{-7}$ $A\,cm^{-2}$ was subtracted from the total current density.

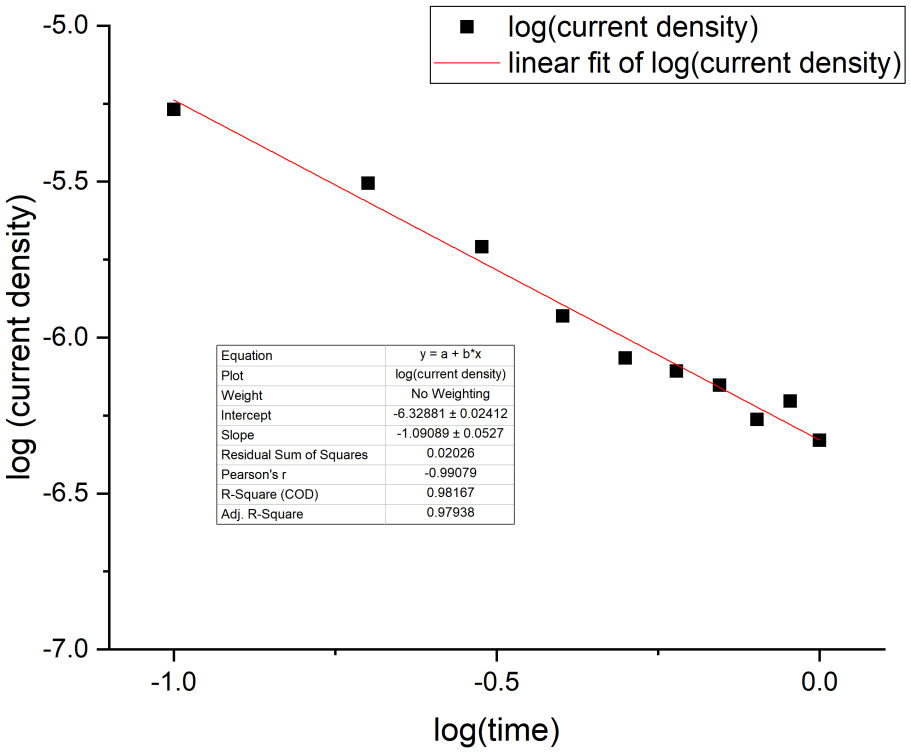


Figure 4.37: Current decay on scratched 316 stainless steel in pH 4.0 KHP solution at a potential of 0.0 V vs. MSE for the scratch number 3. $\Delta log(\text{current density})/\Delta log(\text{time}) = -1.09 \pm 0.05$

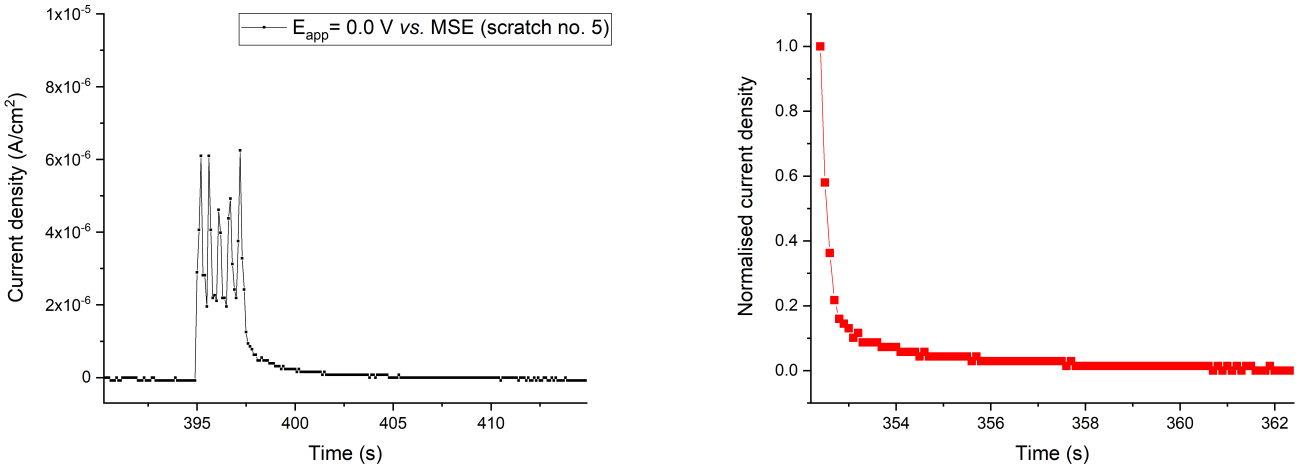


(a) (b)

Figure 4.38: A repassivation peak for scratched 316 stainless steel in pH 4.0 KHP solution for scratch number 5 and b) a current decay region normalised to peak current density value for the same scratch. Base current of $6.98 \times 10^{-7}$ $A\,cm^{-2}$ was subtracted from the total current density.

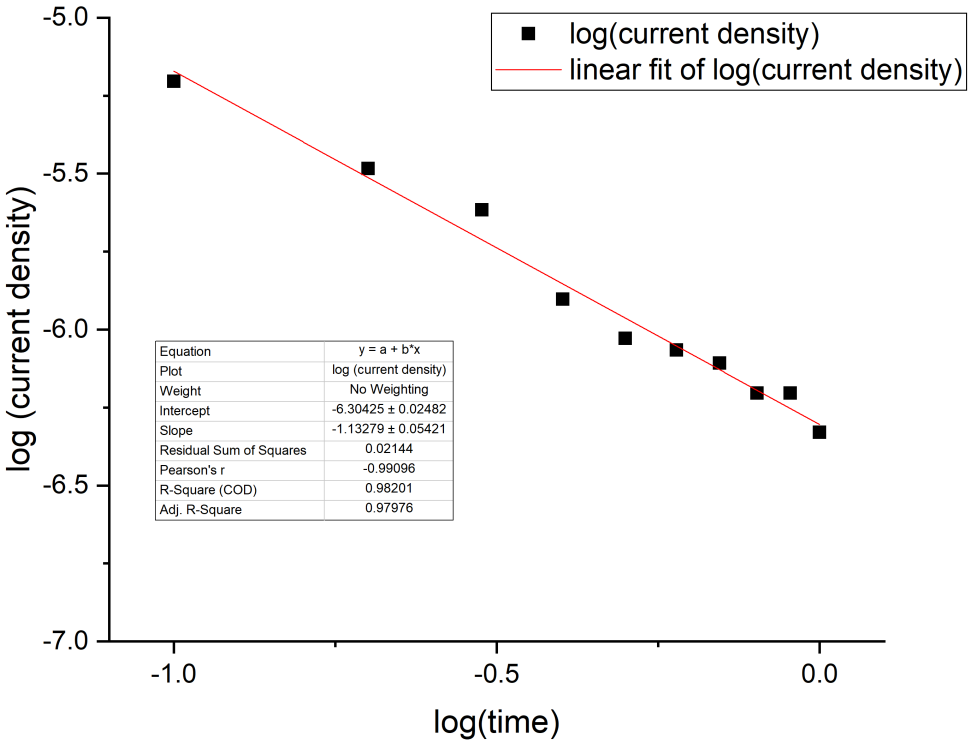


Figure 4.39: Current decay on scratched 316 stainless steel in pH 4.0 KHP solution at a potential of 0.0 V vs. MSE for the scratch number 5. $\Delta log(\text{current density})/\Delta log(\text{time}) = -1.13 \pm 0.05$.

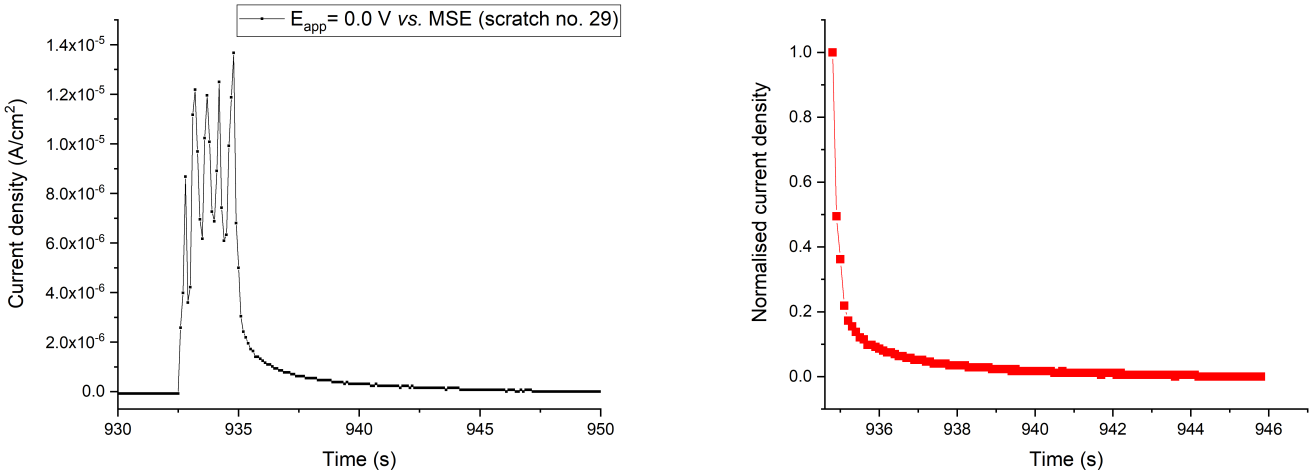


(a) (b)

Figure 4.40: A repassivation peak for scratched 316 stainless steel in pH 4.0 KHP solution for scratch number 29 and b) a current decay region normalised to peak current density value for the same scratch. Base current of $6.98 \times 10^{-7}$ $A\,cm^{-2}$ was subtracted from the total current density.

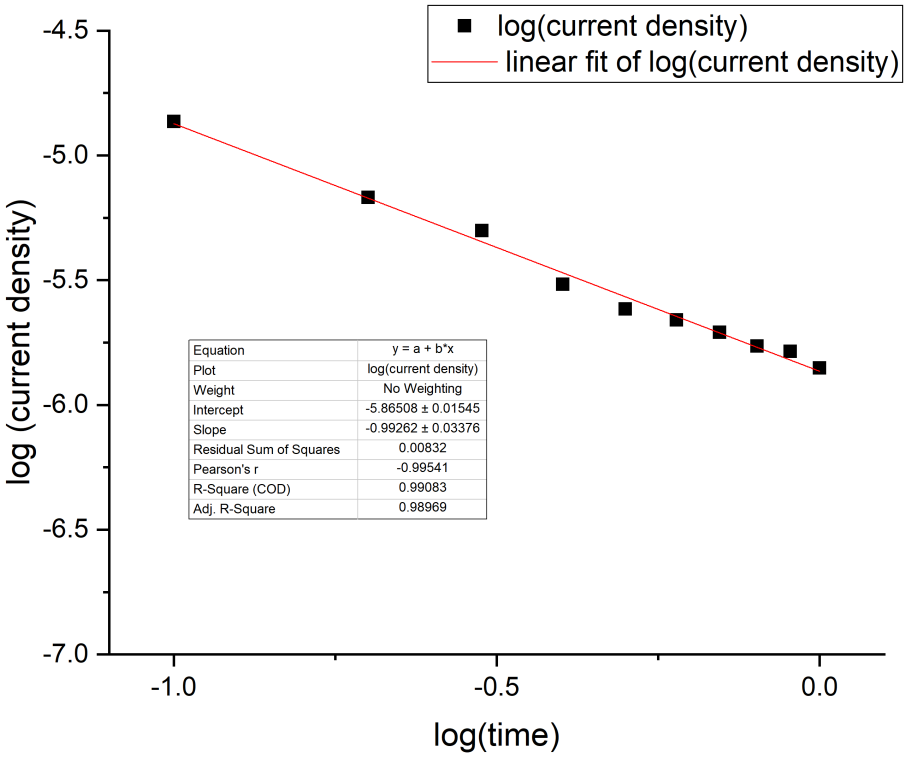


Figure 4.41: Current decay on scratched 316 stainless steel in pH 4.0 KHP solution at a potential of 0.0 V vs. MSE for the scratch number 29. $\Delta log(\text{current density})/\Delta log(\text{time}) = -0.99 \pm 0.03$.

# Chapter 5

# The electrode scratching technique as a robust way to decouple erosion-corrosion components

## 5.1 Overview

In this chapter the use of an electrode scratching technique to decouple erosion-corrosion components is demonstrated. Specifically, the effect of flow velocity on each component of mechanical-electrochemical corrosion of X65 carbon steel and 316 stainless steel was studied. Continuous scratching experiments were deemed most suitable for decoupling erosion-corrosion, as the tip bouncing effect seen in repeated scratching experiments was avoided. High frequency data collection experiments confirmed that keeping the rotation rate below 150 $RPM$ allowed repassivation of the scratched surface before the next scratch in continuous scratching experiments. For this purpose rotation rates of 25, 50 and 100 $RPM$ were chosen for decoupling erosion-corrosion components.

Pure corrosion rates of steels were calculated using Tafel extrapolation and linear polarisation resistance techniques. Wear volume measurement of samples scratched under cathodic protection conditions were used to calculate pure erosion rates, while erosion-enhanced corrosion and total erosion-corrosion rates were evaluated from charge calculations and volume loss measurements at passive anodic potentials. Corrosion-enhanced erosion was then found from the difference between total erosion-corrosion and sum of pure erosion, pure corrosion and erosion-enhanced corrosion rates (See Table 5.2).

These experiments showed the majority of the weight loss in X65 carbon steel took place

due to erosion, including both pure erosion and corrosion-enhanced erosion. 316 stainless steel electrode showed consistently lower erosion-corrosion rates compared to X65 carbon steel in agreement with the literature. Along with the quicker passivation rates of stainless steel, surface hardening of the alloy might have contributed to the lower erosion-corrosion rates. Microstructural and micro-mechanical analysis of these sample steels will form the basis of the next chapter.

Coupling the electrode scratching technique under potentiostatic control with volume loss measurements using white light interferometry allowed successful decoupling of the individual components of erosion-corrosion. The electrode scratching technique allows the parameters such as scratching tip size, electrolyte and scratching frequency to be easily changed, which makes the technique robust. The technique can further be applied to study the repassivation and erosion-corrosion fundamentals of other alloys.

Additional to continuous scratching experiments, repeated scratching of X65 carbon steel samples at higher rotation rates of 100, 400 and 900 $RPM$ are presented in this chapter. Repeated scratching of X65 carbon steel electrodes under passive anodic conditions allowed the time-dependency of erosion-enhanced corrosion to be studied. It was shown that at high rotation rates of the electrode not enough time was left for repassivation, resulting in lower charge per revolution compared to continuous experiments carried out at 25, 50 and 100 $RPM$. While continuous scratching experiments introduced insight to erosion-corrosion at high erosive conditions, the repeated scratching showed the importance of taking into account changes of erosion-enhanced corrosion rates with time under less erosive conditions.

Synergy during mechanical-electrochemical corrosion phenomena has been extensively studied using a variety of setups, including flow loops [1], jet impingement apparatus [2], slurry erosion-corrosion testers [3] and scratching techniques [4, 5, 6]. Out of these techniques scratching can be performed on an electrode, therefore allowing a potentiostatic selection of different modes of erosion-corrosion. Scratching techniques use either stationary electrodes with scratching tips sliding on the surface of the sample [5, 6] or rotating electrodes coupled to an external scratching arm [4]. In both modes, single scratches are created on the surface of the metal. However, across industry one would expect multiple impingement events to take place at the same spot. Performing multiple scratching experiments presents the advantage of potentiostatic control of the samples along with studying the time dependent evolution of erosion-corrosion components.

Unlike other erosion-corrosion testing systems (flow loops, jet impingement, and slurry pot tester), where repeated impact of particles on the same location is rather cumbersome to predict,

the electrode scratching technique allows a straightforward way of producing multiple scratches exactly at the same location. Rotation rate of the electrode, contact time of the tip, scratching frequency, as well as the potential of tested samples are easily controllable.

The aim of this chapter is to demonstrate the application of an electrode scratching technique coupled with white light interferometry to obtain improved understanding of synergy in erosion-corrosion for both X65 carbon steel and 316 stainless steels in deoxygenated, mildly acidic environment.

## 5.2 Experimental

### 5.2.1 Electrolyte

Potassium hydrogen phthalate (KHP) with molecular formula $C_6H_4 \cdot COOH \cdot COOK$ and molecular weight 204.22 $g\ mol^{-1}$ was used as an electrolyte. The electrolyte was made from analytical grade chemical dissolved in ultra-pure deionised (DI) water. 10.211 $g$ of potassium hydrogen phthalate (VWR Chemicals, ≥99.5% AnalaR NORMAPUR®) was dissolved in 500 $mL$ of DI water, 13 $mL$ of 0.1 $M$ NaOH and DI water was added to yield a 1 $L$ solution. The resultant pH of this buffer solution was 4.05±0.05. This electrolyte pH was chosen to reflect the 'sweet' conditions encountered during oil and gas transportation.

### 5.2.2 Materials

API X65 carbon steel and AISI 316L stainless steel presented in experimental section of Chapter 4, section 4.2.2 were used as working electrodes in the RDE assembly. Samples surface preparation and finish was identical to the one described earlier.

### 5.2.3 Electrochemical measurements

Electrochemical measurements were performed on a three-electrode system controlled *via* an Ivium CompacStat potentiostat. The solutions were deaerated prior to the experiment with high purity argon for 1 hour. Bubbling was maintained throughout the measurements to sustain an oxygen free environment in the cell, in addition to the argon blanket above the solution.

Pure corrosion rates of 316 stainless steel were estimated using Tafel extrapolation from linear polarisation graphs. The potential was swept at 1 $mV\ s^{-1}$ from cathodic to anodic regions. It was important that the cathodic region was linear for at least one decade for extrapolation.

For the anodic region the passivation current was used for extrapolation due to absence of linearity for a decade in logarithmic current *vs.* potential graphs. It is understood that this method may overestimate the corrosion rates, as confirmed by potentiostatic measurements at open circuit potential. Nevertheless, it is acceptable for the purposes of this work.

Pure corrosion rates of X65 carbon steel samples were estimated using linear polarisation resistance technique. The equilibrium potential of the samples was recorded prior to polarisation with threshold value of potential change rate of 0.01 $mV\ min^{-1}$. The potential was swept from $-$ 30 $mV$ to 30 $mV$ *versus* the open circuit potential determined before each polarisation. The sweeping rate was equal to 1 $mV\ s^{-1}$. Samples were polarised every 5 minutes during a 1-hour period. The corrosion current density of X65 carbon steel was estimated using linear polarisation resistance *via* equation 5.1.

$$\frac{\Delta E}{\Delta I} = \frac{\beta_a \beta_c}{2.3(\beta_a + \beta_c) i_{corr} \times A} \tag{5.1}$$

where $\frac{\Delta E}{\Delta I}$ is the slope of the line (*i.e.* polarisation resistance), $\beta_a$ and $\beta_c$ are anodic and cathodic Tafel constants derived from linear scanning voltammograms, $i_{corr}$ is the corrosion current density, and $A$ is the area of the electrode.

Corrosion current density of metal electrodes can then be used to identify the corrosion rates in $mm\ year^{-1}$ (Equation 5.2).

$$CR = \frac{3272 \times i_{corr} \times Eq.wt}{\rho} \tag{5.2}$$

where $Eq.wt$ is the equivalent weight and $\rho$ is the density of the working electrode. Equivalent weights were calculated as 27.93 $g$ for X65 carbon steel and 25.35 $g$ for 316 stainless steel, densities were equal to 7.85 $g\ cm^{-3}$ and 8.02 $g\ cm^{-3}$ respectively.

### Decoupling erosion-corrosion components

A rotating electrode scratching setup presented in Chapter 3, section 3.2.3 was used for decoupling individual components of erosion-corrosion. Table 5.2 summarises methods used to determine volumetric degradation rates of erosion-corrosion. A continuous electrode scratching protocol was implemented. During these experiments the chosen potential was applied for the duration of the experiment. After the sample has been polarised for *ca.* 300 $s$, the electromagnetic solenoid was released, and the continuous scratching began. Scratching time was chosen based on the time required for 100 rotations at 25$\pm$2, 50$\pm$2 and 100$\pm$2 $RPM$ and was equal to 240, 120 and 60 $s$ respectively.

The main rationale behind choosing continuous scratching for decoupling was to avoid the mass loss effect due to the bouncing of the tip during initial contact with the working electrode. Scratching experiments with high data collection frequency showed that the passivation time to reach 80% of base current was *ca.* 0.4 $s$. The highest rotation rate used for these experiments (100 $RPM$) corresponds to 0.6 $s$ per revolution. Hence, at passivating conditions the oxide layer is assumed to be fully recovered before the next scratch. This is an important assumption. Table 5.1 summarises experimental parameters set for continuous scratching experiments in this chapter.

Table 5.1: Experimental parameters used for continuous scratching tests in Chapter 5. Both X65 carbon steel and 316 stainless steel were tested in pH 4.0 KHP solution.

| Rotation rate, $RPM$ | $t_c$, $s$ | No. of scr. | $t_c$ per revolution, $s$ | $\omega$, $rad/s$ | Re | Flow regime |
|---|---|---|---|---|---|---|
| 25 | 240 | 100 | 2.4 | 2.62 | 147 | laminar |
| 50 | 120 | 100 | 1.2 | 5.24 | 294 | laminar |
| 100 | 60 | 100 | 0.6 | 10.47 | 588 | laminar |

The scratching tip was checked for integrity after each experiment and was found intact due to its superior hardness compared to that of metal samples. The cathodic potential to determine $\dot{c_0}$ was equal to -1.5 $V$ *vs.* MSE to minimize the anodic component of the current as much as possible, while passive anodic currents were recorded at potentials of equal to 0.6 $V$ *vs.* MSE for X65 carbon steel (Figure 4.9) and 0.0 $V$ *vs.* MSE for 316 stainless steel (Figure 4.10).

Table 5.2: Methods used to estimate degradation rates of erosion-corrosion components.

| Erosion-corrosion component | Method | Volumetric degradation rate, $mm^3\ s^{-1}$ |
|---|---|---|
| Pure erosion, $\dot{e_0}$ | Direct wear volume measurements of samples scratched at cathodic potential using white light interferometry | $$\dot{e_0} = \frac{V_{e_0}}{t_c}$$ where $V_{e_0}$ is the total volume of the scratch produced at cathodic potentials, and $t_c$ is the contact time of the tip |
| Pure corrosion, $\dot{c_0}$ | Faraday's law using corrosion current density identified *via* Tafel extrapolation or linear polarisation resistance | $$\dot{c_0} = \frac{V_{c_0}}{t_c} = \frac{i_{corr} \times 2\pi ry \times Eq.wt}{\rho \times F}$$ where $i_{corr}$ is the corrosion current density based on total area of WE, $r$ is the distance of the scratch to the centre of rotation, $y$ is the width of the scratch created under passivating potential, $Eq.wt$ is the equivalent weight of WE, $\rho$ is the density of WE, $F$ is the Faraday constant |
| Erosion-enhanced corrosion, $\dot{c_e}$ | Faraday's law using charge evolved during continuous scratching under passive potentials | $$\dot{c_e} = \frac{V_{c_e}}{t_c} = \frac{Q \times Eq.wt}{\rho \times F \times t_c} = \frac{\int_0^{t_c}[I(t) - I_b]dt}{\rho \times F \times t_c}$$ |
| Total erosion-corrosion rate, $\dot{w}$ | Direct wear volume measurements of samples scratched at passive potential using white light interferometry | $$\dot{w} = \frac{V_w}{t_c}$$ where $V_w$ is the total volume of the scratch produced at passive potentials |
| Corrosion-enhanced erosion rate, $\dot{e_c}$ | N/A | $$\dot{e_c} = \dot{w} - (\dot{e_0} + \dot{c_0} + \dot{c_e})$$ |

**Repeated scratching of X65 carbon steel at angular velocities beyond 100 RPM**

To demonstrate the electrochemical-mechanical interactions at rotation rates higher than 100 $RPM$ repeated scratching experiments were done in the range of 100 – 900 $RPM$ angular velocities. The protocol for these multiple scratching experiments was similar to those described in Chapter 4. A X65 carbon steel working electrode was potentiostatically polarised to 0.6 $V$ *vs.* MSE for the duration of the experiment. After 300 $s$ of polarisation, the scratching tip was released repeatedly 100 times with contact time of *ca.* 1 $s$. The time between the solenoid releases was equal to 60 $s$.

The charge per each release of solenoid was calculated by integration of the obtained current transients recorded during scratching. Integration of the current over time was carried out using the base current (the current flowing from the electrode before the scratch, $I_b$) as a baseline for each solenoid release, which is referred to as a scratch number for ease of interpretation. In reality, however, the number of scratches over the same area for 100 successive releases of solenoid with contact time of 1 $s$ corresponds to a total of 167, 667 and 1500 scratches made at the same location at rotation rates of 100 $RPM$, 400 $RPM$, and 900 $RPM$ respectively. Dividing the cumulative charge resulting from scratching by the total number of scratches can then be used to identify the average charge per revolution. See Table 5.3 for the summary of the experimental parameters.

Table 5.3: Experimental parameters set for the repeated scratching experiments carried out in Chapter 5. X65 carbon steel samples were scratched under applied potential of 0.6 $V$ *vs.* MSE in pH 4.0 KHP solution.

| Rotation rate, RPM | $t_c$, $s$ | No. of scratches | $\omega$, $rad/s$ | Re | Flow regime |
|---|---|---|---|---|---|
| 100 | 1 | 167 | 10.47 | 588 | laminar |
| 400 | 1 | 667 | 41.89 | 2351 | laminar |
| 900 | 1 | 1500 | 94.25 | 5289 | laminar |

### 5.2.4 ICP-OES

The iron concentration in KHP electrolytes after multiple scratching experiments at 100, 400 and 900 $RPM$ was determined using the ICP-OES technique. The Thermo Scientific iCAP 6000 series ICP Emission Spectrometer connected to an autosampler was used in conjuction with iTEVA iCAP software. Reference samples were prepared in 50 $mL$ Falcon tubes with 20.0 $mL$ of final solution containing 0, 0.25, 0.5, 1, and 5 $ppm$ Fe. A Sigma-Aldrich® 1000 $ppm$ iron standard for ICP stock solution was diluted with ultra pure deionised 18 $M\Omega.cm$ water to

a desired reference concentration. Fresh and used KHP electrolyte samples of 10.000 $mL$ were filtered with 0.2 $\mu m$ syringe filters prior to analysis and placed in 15 $mL$ Falcon tubes. The signal intensity *vs.* concentration calibration curve from reference samples (Figure 5.1) was used to identify the concentration of samples. The reported final concentration is the sample concentration minus the background concentration identified from fresh KHP electrolyte.

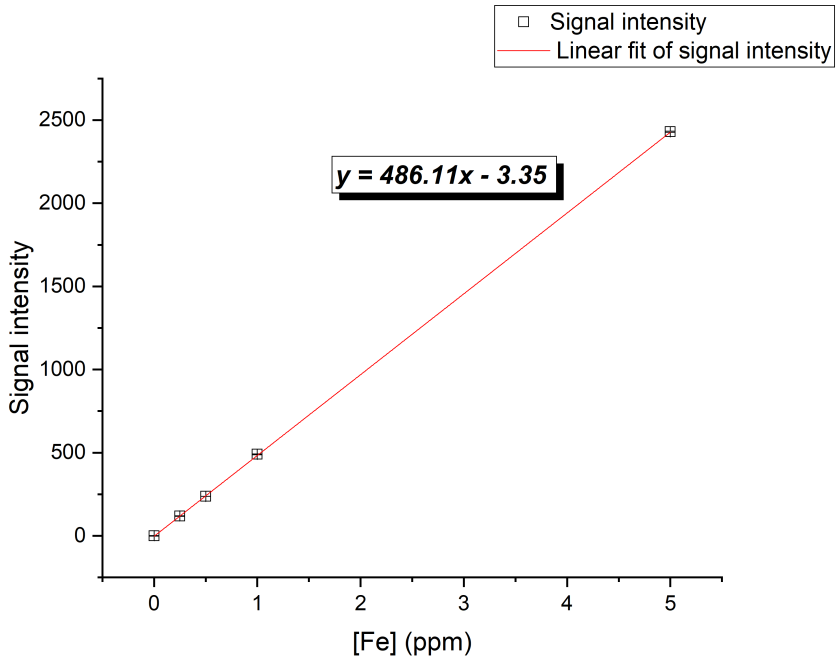


Figure 5.1: A typical calibration curve obtained using Fe reference standard samples. In the given graph the standard deviation error bars are smaller than the marker size, hence are not clearly visible at this scale.

### 5.2.5 White light interferometry

A Zygo New View 7000 series optical profilometer was used to perform non-contact, three-dimensional scanning white light interferometry of the scratched samples. White light interferometers use the interference of the light originating from the difference in travel distance of the reference and the measurement beam reflecting off the sample surface to measure the variations in height. The samples were automatically tilt-corrected prior to measurements. A 2.5× objective at 2× zoom was used to collect 3D wear profiles with a sampling size of 437.31 $\mu m$ × 437.31 $\mu m$ (See Figure 5.2a). Recorded data were analysed on Vision software. 3D volume data analysis was carried out and volume loss during scratching was recorded as the negative volume between the zero and sub-zero planes. 2D profiles of scratches were analysed using the same data, with the width of the scratch being defined as the average distance from peak to peak (See Figure 5.2b).

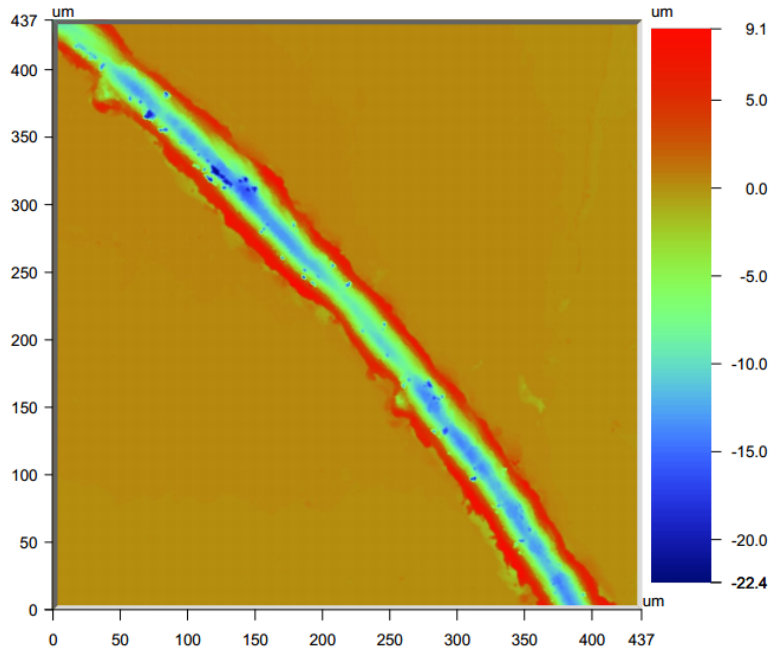


(a)

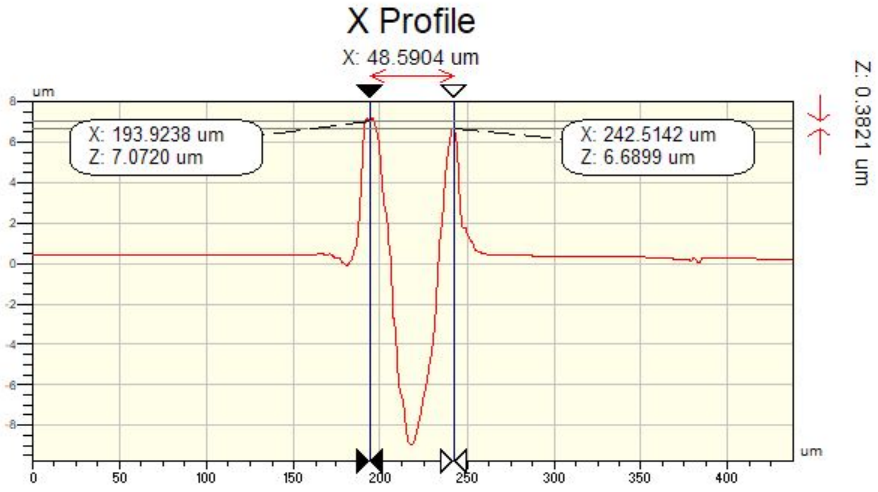


(b)

Figure 5.2: a) Typical surface plot and b) 2D scratch profile showing peak to peak distance recorded using Zygo white light interferometer. The peak to peak distance was used to determine the width of the scratch.

## 5.3 Results and discussion

### 5.3.1 Pure erosion ($\dot{e_0}$) *vs.* angular velocity

Erosion-corrosion components were decoupled using the methods described in Table 5.2. Current transients recorded from X65 carbon steel and 316 stainless steel electrodes at rotation rates of 25, 50 and 100 $RPM$ under cathodic potential are presented in Figure 5.3 and 5.4 respectively.

The cathodic current density (calculated as per the total electrode area) increases with rotation rate due to a faster supply of fresh electrolyte to the working electrodes, *i.e.* it is mass transport controlled. Consequently, a higher rate of proton reduction can take place. As was mentioned in Chapter 4, HER is highly surface sensitive, and the exchange current density can span several orders of magnitude on different substrates. In this case, the recorded current density of 316 stainless steel was about 2 times higher than that of X65 carbon steel, which can be attributed to local physicochemical variations of the different substrates. Note that there was no current decay observed at the 316 stainless steel electrode when a potential of -1.5 $V$ *vs.* MSE was applied. Overall, cathodic current densities recorded on both metals decreased with time owing to a reduction of working electrode area due to bubble formation from the hydrogen reduction reaction. To demonstrate this, in 316 stainless steel at 25 $RPM$ the rotation rate was rapidly increased at *ca.* 175 $s$ to remove the bubbles (Figure 5.4). This was followed by an increased cathodic current rate. Higher cathodic current densities recorded once the scratching is finished can be attributed to removal of hydrogen bubbles *via* the tip and absence of tip disturbance, as well as a surface change of the electrode after scratching that affects the HER rate.

Volumetric loss rates due to pure erosion *vs.* rotation rate are presented in Figure 5.5. Pure erosion rates of both alloys are proportional to the rotation rates of the electrodes. The volumetric erosion rate of X65 carbon steel is consistently higher than that of 316 stainless steel. Approximate Vickers hardness of the alloys are 200 $H_v$ and 160 $H_v$ respectively, from which *higher* erosion rates for stainless steel can be expected. However, the relationship between the hardness of alloys and their erosion rate is not straightforward. For example, Levy suggested that the ductility of the alloy allows the redistribution of the kinetic energy *via* plastic deformation resulting in lower erosion rates [7, 8]. Additionally, the hydrogen embrittlement of carbon steel due to cathodic charging may result in higher erosion rates. Since the passive oxide and film was constantly removed, it is assumed that they do not affect the pure erosion rate.

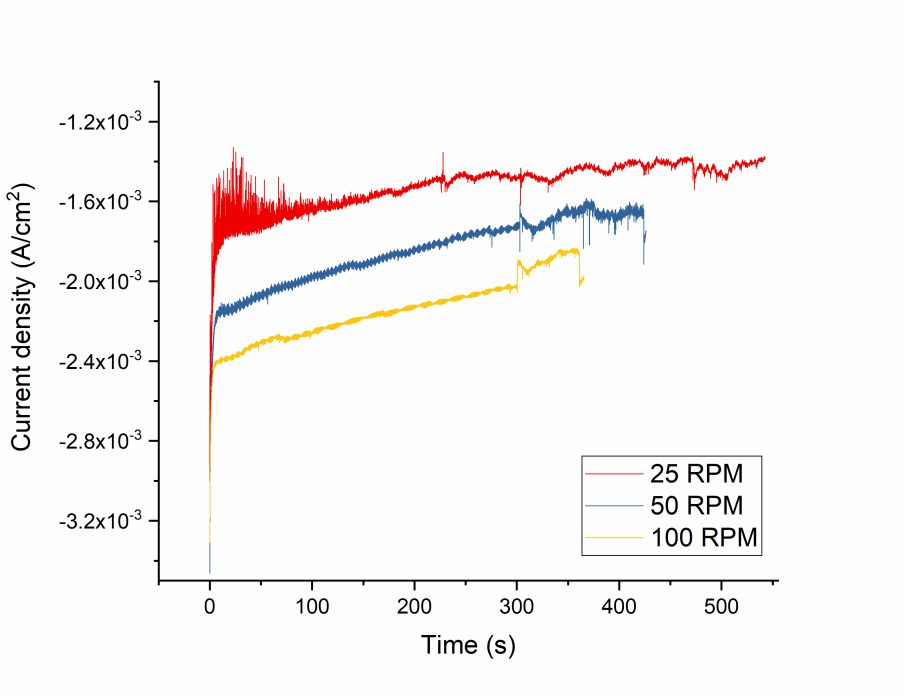


Figure 5.3: Current evolving at X65 carbon steel working electrode during continuous scratching at rotation rates of 25, 50 and 100 $RPM$ under applied cathodic potential of -1.5 $V$ *vs.* MSE in pH 4.0 KHP electrolyte. Scratching begins *ca.* 300 $s$.

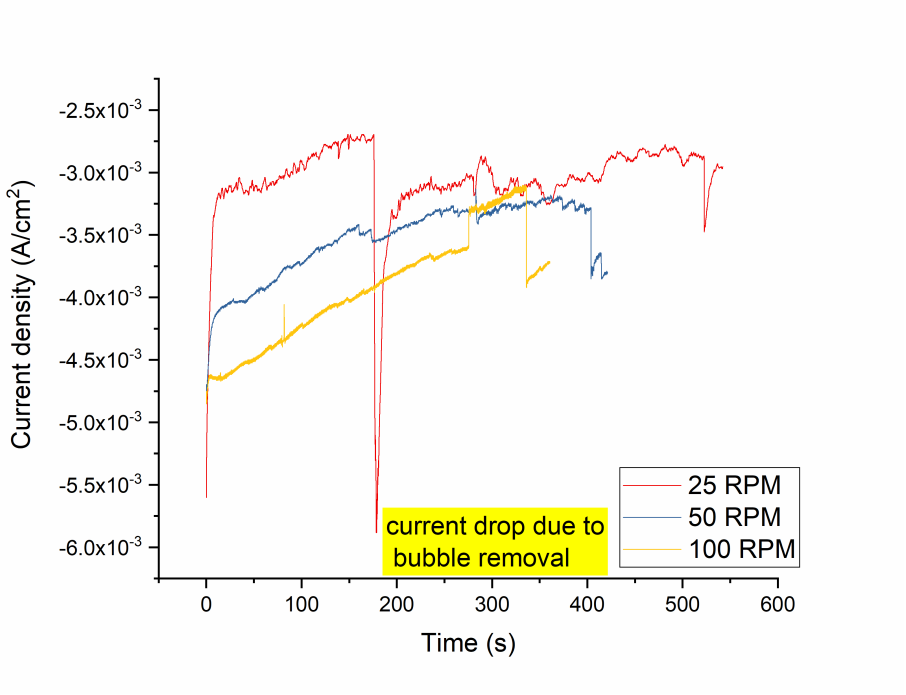


Figure 5.4: Current evolving at 316 stainless steel working electrode during continuous scratching at rotation rates of 25, 50 and 100 $RPM$ under applied cathodic potential of -1.5 $V$ *vs.* MSE in pH 4.0 KHP electrolyte. Scratching begins *ca.* 300 $s$.

There are numerous erosion models developed for different wear modes [8], however, it is generally accepted that pure erosion *vs.* particle velocity dependence follows a power law, with n being between 1.6 and 2.6:

$$\dot{e}_0 \propto KV^n \tag{5.3}$$

Within the studied conditions, erosion changes linearly with rotation rate and is a function of kinetic energy. The author acknowledges that given the limited data, any fitting would be inconclusive. However, judging from the line fits presented in Figure 5.5, it can be approximated that $n$ is smaller than 1.6, suggesting a deviation of erosion rates from the power law. This results in lower erosion rates than expected at higher rotation rates, one possible reason for which could be the work hardening of the surface.

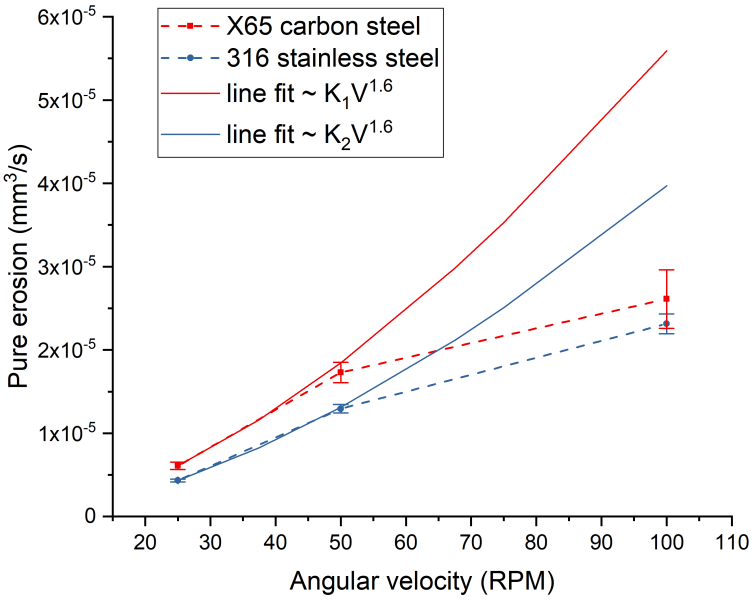


Figure 5.5: Volumetric pure erosion rates of X65 carbon and 316 stainless steel as a function of rotation rate. Line fits following the power law in Equation 5.3 are shown for comparison. Volumetric losses were estimated by Zygo white light interferometer, magnification 1.0 X, sampling size 437.31 $\mu m$.

### 5.3.2 Erosion-enhanced corrosion ($\dot{c}_e$) *vs.* angular velocity

Figure 5.6 and 5.7 present current transients evolved during continuous electrode scratching under passive anodic potentials for X65 carbon steel and 316 stainless steel working electrodes respectively. The integrated current density recorded over tip contact-time allows determination of mass loss and hence volume loss using Faraday's law. As mentioned in Table 5.2, scratching at passive anodic potentials allows the measurement of erosion-enhanced corrosion rates. Volumetric loss rates corresponding to this erosion-corrosion component are presented in Figure 5.8 as a function of rotation rate.

It can be seen that the anodic current evolving on the studied metals due to continuous scratching, *i.e.* erosion-enhanced corrosion $\dot{c}_e$, is directly proportional to the angular velocity. Higher shear stress values lead to more material removal, hence higher overall current densities are recorded at higher angular velocities. Additionally, mass transfer is accelerated at higher velocities. On X65 carbon steel the current density increases linearly with scratching time, which means that $\dot{c}_e$ is also time-dependent (Figure 5.6). This can happen due to surface deterioration with scratching, and acceleration of corrosion-enhanced erosion $\dot{c}_e$ with time. There is an interesting trend recorded on the 316 stainless steel working electrodes, whereby the current density initially decreases with time, as shown in Figures 5.7 and 5.9. This can be attributed to the preferential dissolution of chromium and iron, coupled with the work hardening of the surface as mentioned in section 4.3.2 page 117.

Despite variations of current density with time on 316 stainless steel, Figure 5.8 demonstrates a linear relationship between erosion-enhanced corrosion and rotation rate both for X65 carbon steel and 316 stainless steel working electrodes. The change is more pronounced in X65 carbon steel, where current evolves due to both protective oxide formation and dissolution, while 316 stainless steel spontaneously passivates after the surface is scratched as shown earlier in Figure 4.27.

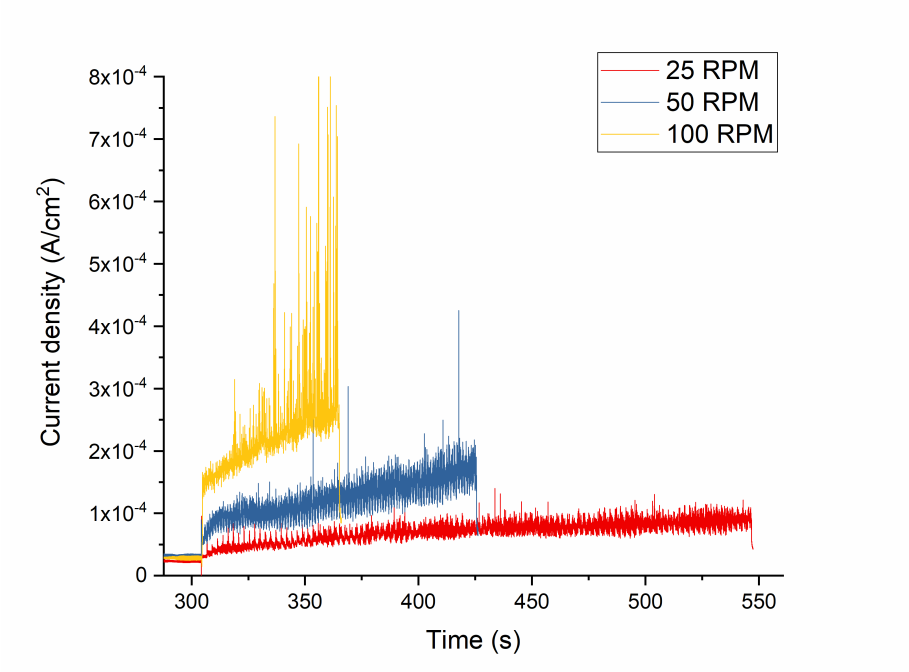


Figure 5.6: Current evolving during scratching X65 carbon steel working electrode at anodic potential of 0.6 $V$ *vs.* MSE in pH 4.0 KHP electrolyte. Scratching begins *ca.* 300 $s$.

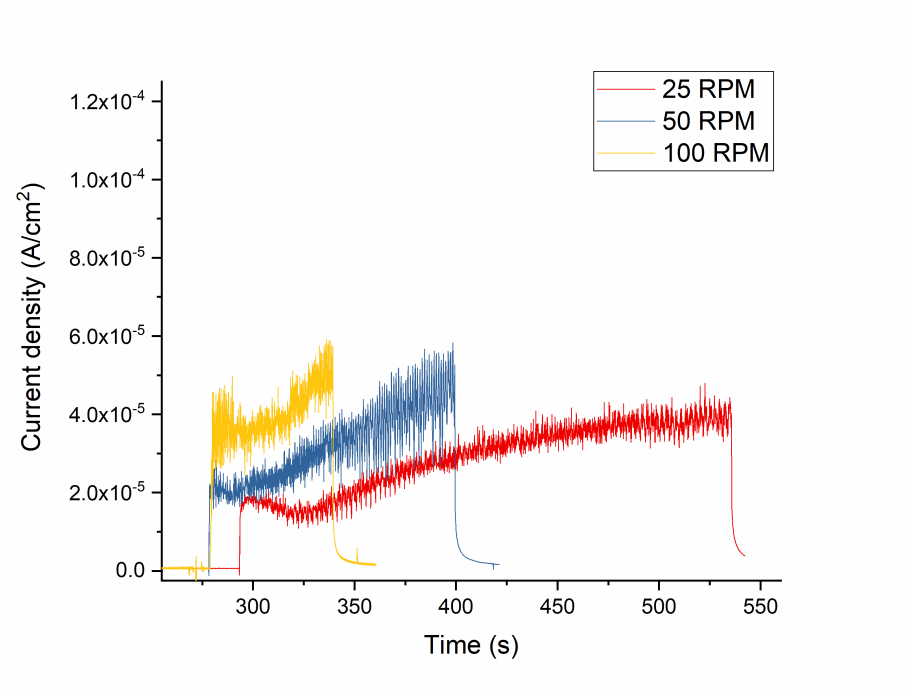


Figure 5.7: Current evolving during scratching 316 stainless steel working electrode at anodic potential of 0.0 $V$ *vs.* MSE in pH 4.0 KHP electrolyte. Scratching begins *ca.* 300 $s$.

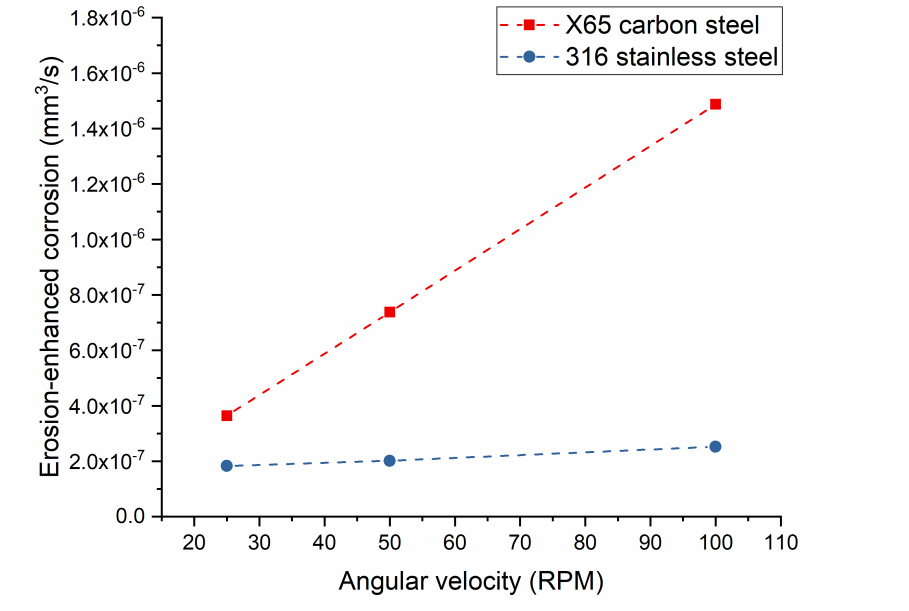


Figure 5.8: Volumetric erosion-enhanced corrosion rate of X65 carbon and 316 stainless steel calculated from Faraday's law *via* integrating the area under the lines shown in Figure 5.7

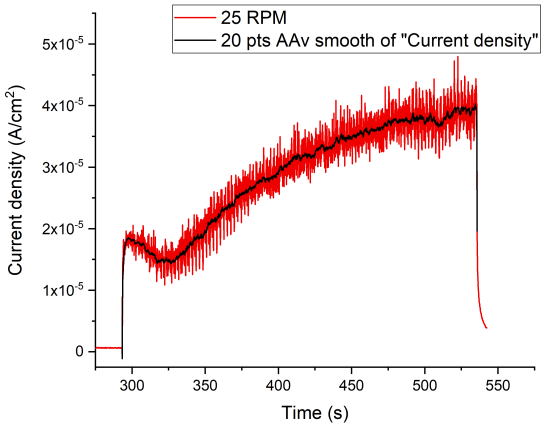


(a)

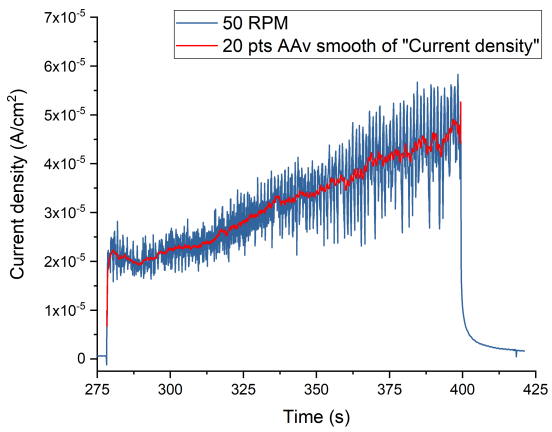


(b)

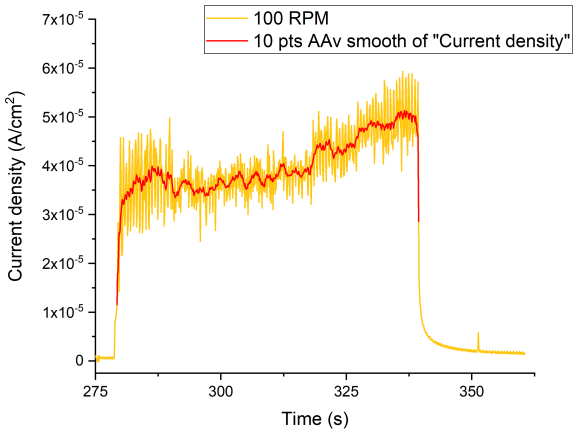


(c)

Figure 5.9: Current transients shown in Figure 5.7 and the adjacent-averaged data for a) 25 $RPM$, b) 50 $RPM$ and c) 100 $RPM$.

### Variation of current density at rotation rates higher than 100 RPM

As mentioned earlier, during non-continuous repeated scratches bouncing of the scratching tip was noticed before the initial contact was established. From scratching experiments with high time resolution the passivation time to reach 80% of base current was equal to *ca.* 0.4 $s$ (See Figure 5.14), which justifies doing continuous scratching experiments at rotation rates of 100 $RPM$ and less. Prior to continuous scratching, multiple repeated scratching experiments were performed at rotation rates of 100 $RPM$, 400 $RPM$ and 900 $RPM$ to study the repassivation behaviour at higher velocities. The results of potentiostatic amperometry are presented along with the current transients over time. The charge density per release of the solenoid at varying velocities is presented to offer a glimpse into the time-dependency of erosion-enhanced corrosion. Additionally, the charge passed per rotation during repeated scratching experiments

is compared with charge per rotation from continuous scratching experiments. ICP-OES results for the electrolytes sampled at the end of the experiments are presented along with the cumulative charge calculations.

The current transients recorded from X65 carbon steel working electrodes during repeated scratching experiments at an applied potential of 0.6 $V$ *vs.* MSE at rotation rates of 100, 400, 900 $RPM$ are presented in Figures 5.10, 5.11 and 5.12 respectively. As the contact time of the tip with the working electrode is constant (*ca.* 1 $s$) the total number of revolutions made during each experiment are proportional to the set rotation rate. The general behaviour of the current density is similar to the one presented in Chapter 4 with high instantaneous current densities being recorded upon application of potential followed by a rapid current decay due to passivation. Once the solenoid is released at *ca.* 300 $s$, bare metal is oxidised and current densities increase proportionally to the rotation rate of the electrode. As soon as the scratching tip leaves the surface of the electrode, the current decays due to repassivation of X65 carbon steel electrode. Magnified current transients showing repassivation at varying rotation rates are presented in Figure 5.13. Both the base currents and peak currents are found to be proportional to the rotation rates. Peak current, *i.e.* the highest current registered right before the tip left the electrode surface can be used to compare the passivation tendency of the X65 carbon steel electrode at different velocities. Current transient decay curves normalised to the peak currents are presented in Figure 5.14. The decay transients completely overlap, indicating that within studied rotation rates repassivation of X65 carbon steel at applied potential of 0.6 $V$ *vs.* MSE is independent of transport phenomena. It is rather unexpected, but quite an important observation with respect to the field, which shows that mechanistic understanding of synergy is crucial for developing accurate models.

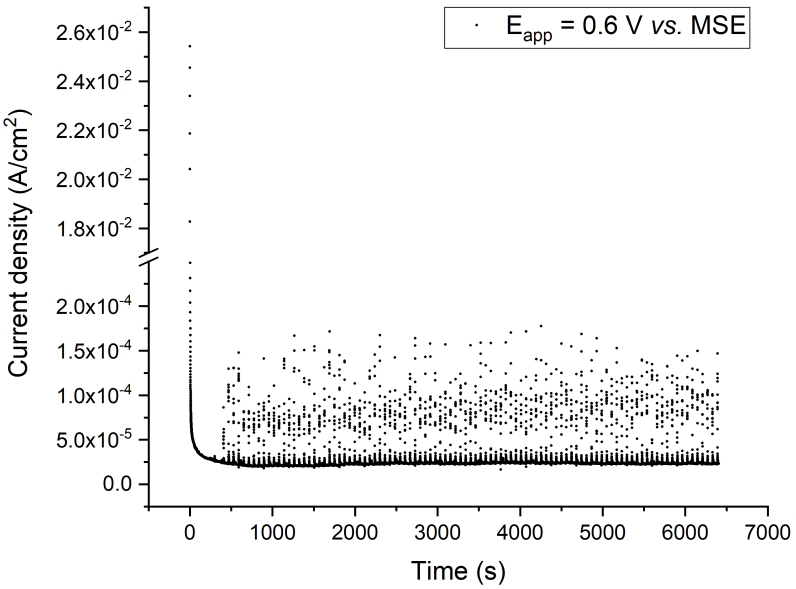


Figure 5.10: Current transients recorded from X65 carbon steel working electrode at applied potential of 0.6 $V$ *vs.* MSE during a multiple scratching experiment at 100 $RPM$ rotation rate.

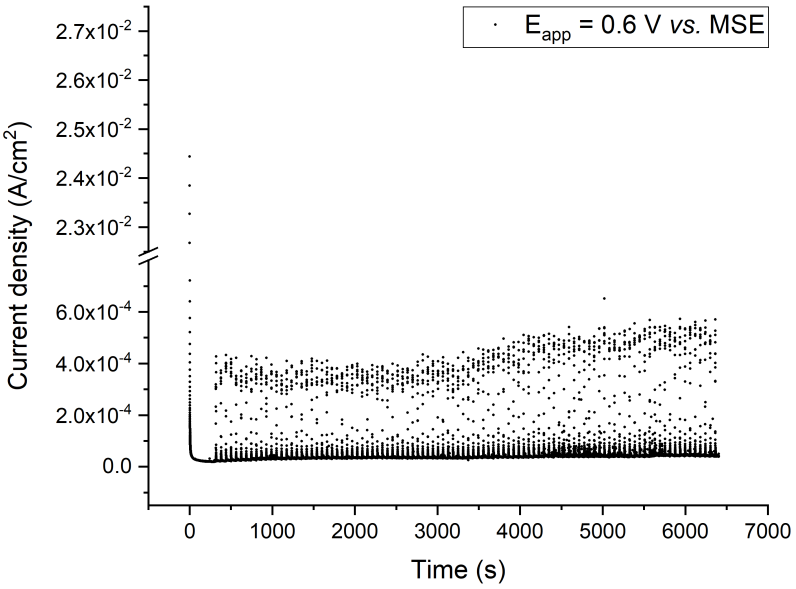


Figure 5.11: Current transients recorded from X65 carbon steel working electrode at applied potential of 0.6 $V$ *vs.* MSE during a multiple scratching experiment at 400 $RPM$ rotation rate.

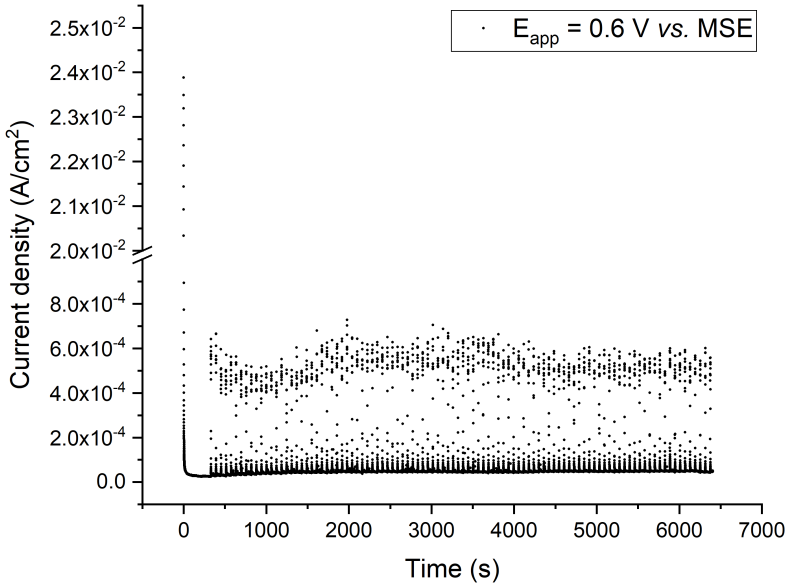


Figure 5.12: Current transients recorded from X65 carbon steel working electrode at applied potential of 0.6 $V$ *vs.* MSE during a multiple scratching experiment at 900 $RPM$ rotation rate.

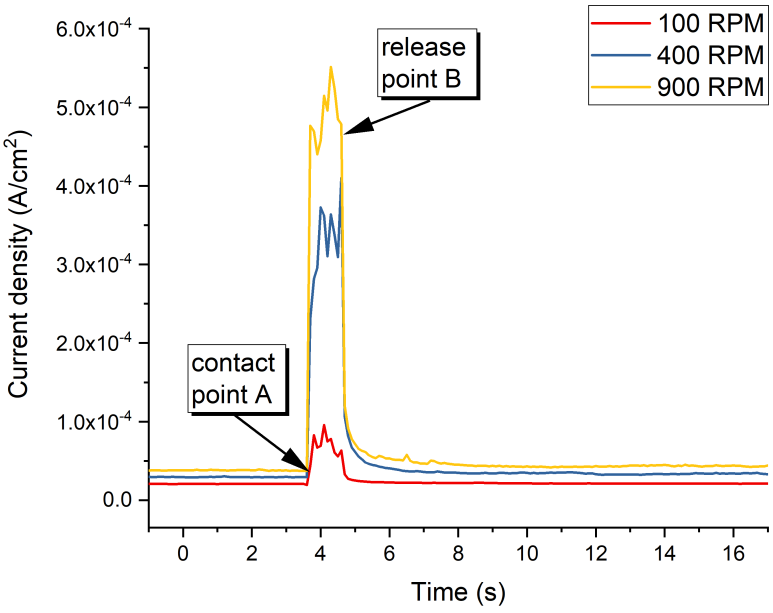


Figure 5.13: Current transients showing repassivation peaks recorded from X65 carbon steel working electrode at applied potential of 0.6 $V$ *vs.* MSE during scratching experiments at 100, 400 and 900 $RPM$ rotation rates.

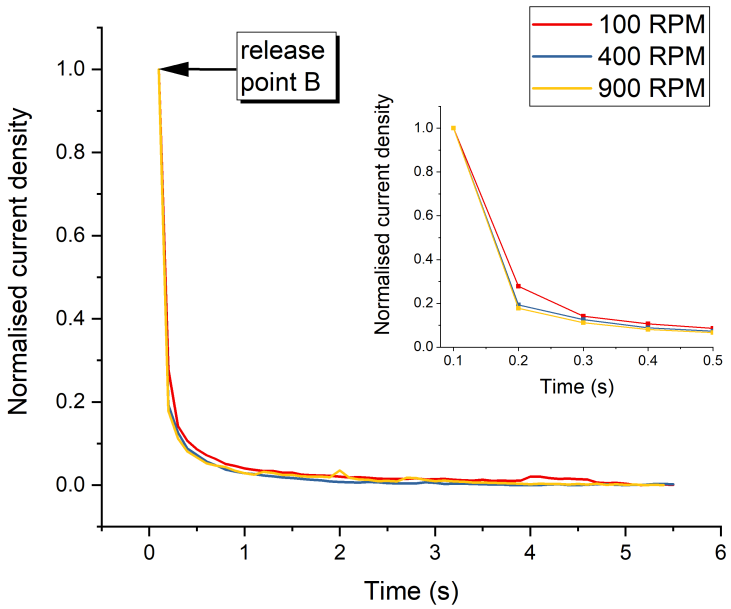


Figure 5.14: Current transient decay region shown in Figure 5.13 normalised to peak current density value for X65 carbon steel electrode in pH 4.0 KHP solution at 100, 400 and 900 $RPM$ rotation rates. Inset: zoomed in transient showing the consistency of the decay.

The charge density per solenoid release was calculated *via* current transient integration and is presented in Figure 5.15. At 100 $RPM$ the charge density per release of the solenoid is independent of the scratch number, indicative of a negligible time-dependency within the experimental time frames. As the rotation rate increases to 400 $RPM$, an interesting phenomenon is observed, where the charge density increases with scratch number. It can also be seen from the cumulative charge density *versus* scratch number graph, where the slope of the 400 $RPM$ line changes midway (Figure 5.16). This result was repeated three times to eliminate human error due to integration, and in all cases the current density was seen to increase with the number of scratches. This could happen due to the deterioration of the surface due to erosion-enhanced corrosion or other synergistic effects. The scatter of the charge density is more substantial at 900 $RPM$ compared to 100 $RPM$. Higher standard deviation at 900 $RPM$ suggests the scratching process is getting less reproducible at higher rotation rates. This is related to the surface changes of the metal as well as the decreased time for the surface recovery.

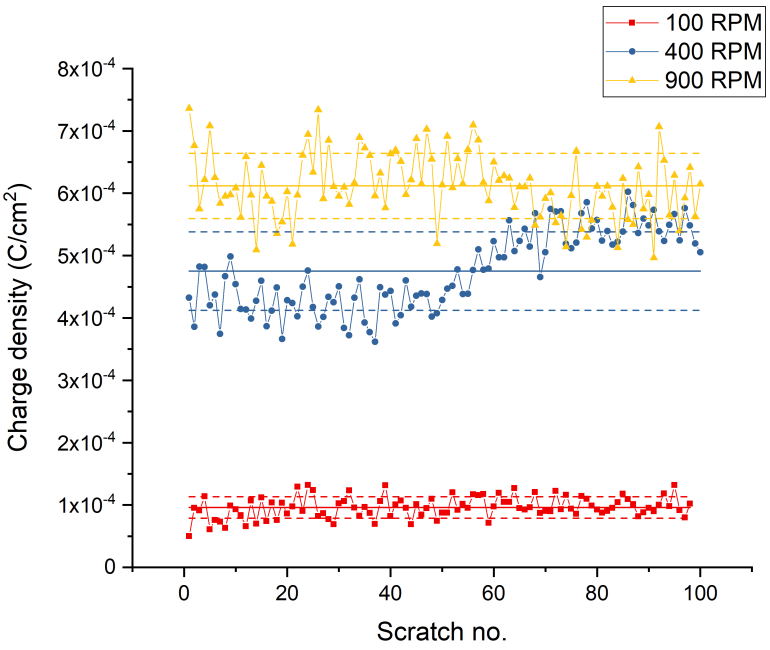


Figure 5.15: Charge density per total electrode area *vs.* scratch number for X65 carbon steel at rotation rates of 100, 400 and 900 $RPM$. Average charge density with the standard deviation is shown.

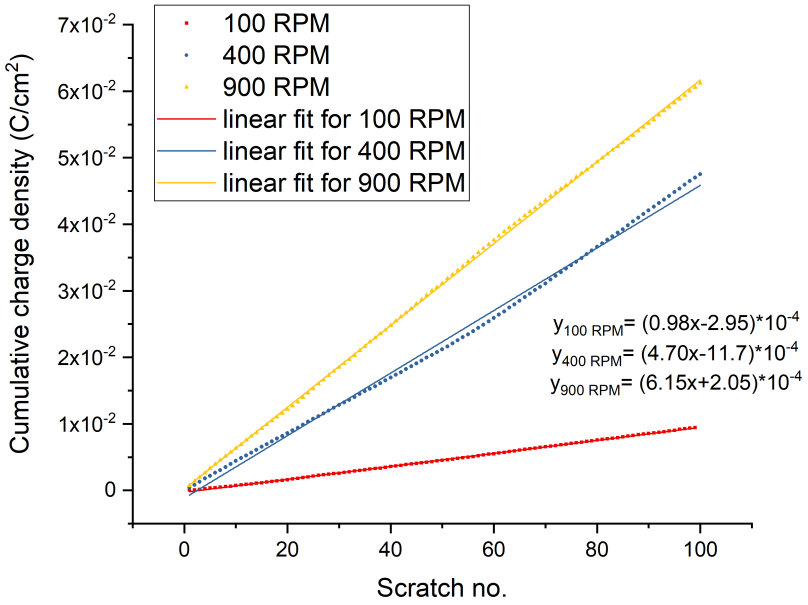


Figure 5.16: Cumulative charge density per total electrode area *vs.* scratch number for X65 carbon steel at rotation rates of 100, 400 and 900 $RPM$ with the linear fits. Note the inflection at scratch number *ca.* 55 for the 400 $RPM$ sample.

As seen from charge density variations per solenoid release, time-dependency is an important factor that needs to be taken into account in gaining a mechanistic understanding of erosion-corrosion. Whereby the same location is subject to erosion-corrosion, the time between

the repeated mechanical impacts becomes another important parameter to consider. This is illustrated in Figure 5.17, which presents charge per revolution against rotation rate at 25, 50, 100, 400 and 900 $RPM$. During continuous scratching experiments, the time between repeated scratches was equal to 2.4, 1.2 and 0.6 $s$ at rotation rates of 25, 50 and 100 $RPM$ respectively. With 0.4 $s$ being enough to reach 80% of base current during passivation, scratching at low velocities ensured that the scratched metal area was largely passivated before the next scratch. In the absence of transport related passivation this results in constant charge per revolution at rotation rates of 25, 50 and 100 $RPM$ as seen in Figure 5.17. Hence, given that enough time is allowed between the successive erosion events, the charge associated with each scratch, which is directly related to erosion-enhanced corrosion, will be *independent* of the rotation rate.

For repeated scratching experiments the contact time was equal to 1 $s$, which corresponds to 1.67, 6.67 and 15 revolutions per solenoid release at rotation rates of 100, 400 and 900 $RPM$. Although the same amount of time passed between successive scratches at 100 $RPM$ in repeated and continuous scratching experiments, the bouncing of the tip that happened during repeated scratching resulted in up to 25% lower charge per revolution. At 400 and 900 $RPM$ the same location was scratched multiple times within this 1 $s$, not allowing the X65 carbon electrode to fully repassivate between the erosion events. This is reflected in the lower charge per revolution calculated for repeated scratching experiments as presented in Figure 5.17. Charge per revolution calculated at 900 $RPM$ is much lower than that at 400 $RPM$ since time between successive scratches is inversely proportional to the rotation rate.

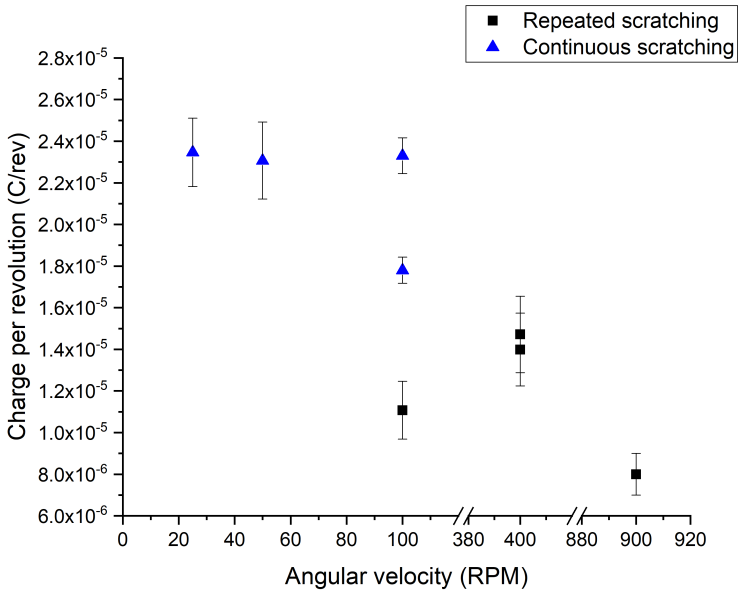


Figure 5.17: Calculated charge per revolution *vs.* rotation rate for X65 carbon steel in repeated scratching and continuous scratching experiments.

To validate the current integration calculations presented above, ICP-OES of electrolytes was carried out after multiple scratching experiments at 100, 400 and 900 $RPM$ rotating rates. The concentration of iron in the solutions is presented in Figure 5.18. The smallest Fe concentration corresponded to the repeated scratching experiment at 100 $RPM$ and was equal to 0.066 $ppm$. The literature value of instrument detection limit for iron using ICP-OES is around 2 $ppb$ [9], while experimental values of $3\sigma$ were equal to 0.023 $ppm$, which gives confidence in the data down to the lowest levels observed here.

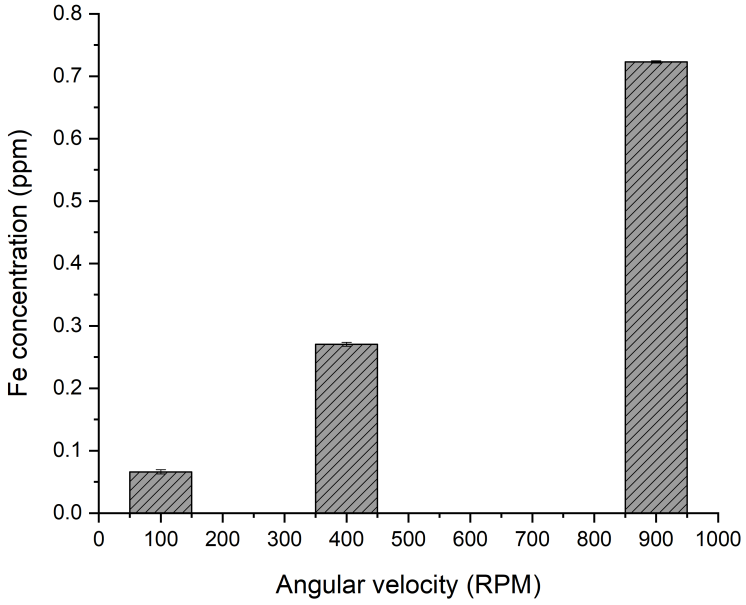


Figure 5.18: Fe concentration in $ppm$ measured from solutions after multiple scratching experiments at 100, 400 and 900 $RPM$.

Measured Fe concentrations can be converted to mass, which in turn can be used to calculate the related charge using Faraday's law of electrolysis. These results, along with the charge measured using potentiostatic amperometry are presented in Table 5.4. In the potentiostatic amperometry results both charge generated from scratching the electrode and total charge measured from beginning to the end of the experiment are presented. As mentioned earlier, the charge from scratching was calculated using the Equation 3.21 *via* integration. The integration was carried out from the base current, $I_b$, to the current $I(t)$ over the scratching time to calculate the charge from scratching. For calculating the total charge, the limit of integration was set between 0 and $I(t)$, and the time was equal to the length of the experiment.

Charge values calculated both from ICP-OES and amperometry are proportional to angular velocities (Figure 5.19). Charge values from ICP-OES are consistently higher than the total charge from amperometry results. This is not surprising if one thinks about the debris

that forms during scratching experiments. Those debris might lose contact with the working electrode during the experiment, hence current from their oxidation are not recorded by amperometry. The debris oxidise and corrode under open circuit conditions, increasing the concentration of iron ions in the solution. This also acidifies the solution. Although the solutions were filtered prior to ICP-OES, some time elapsed between the scratching experiments and the ICP-OES analysis due to instrument availability issues. Hence, the charge calculated from the measured ICP-OES includes not only the erosion-enhanced corrosion component, but also some pure erosion component due to reflection of debris oxidation in the solution.

Table 5.4: A comparison of charge generated by electrolysis of iron measured *via* ICP-OES and potentiostatic amperometry.

| Rotation rate, $RPM$ | ICP-OES | | | Potentiostatic amperometry | |
|---|---|---|---|---|---|
| | [Fe], $ppm$ | $m_{Fe}$, $mg$ | Q, C | Q (scratch repassiv-n), C | Q(total), C |
| 100 | 0.066 | 0.030 | 0.103 | 0.00185 | 0.0374 |
| 400 | 0.270 | 0.122 | 0.420 | 0.00933 | 0.0568 |
| 900 | 0.723 | 0.325 | 1.124 | 0.01238 | 0.0737 |

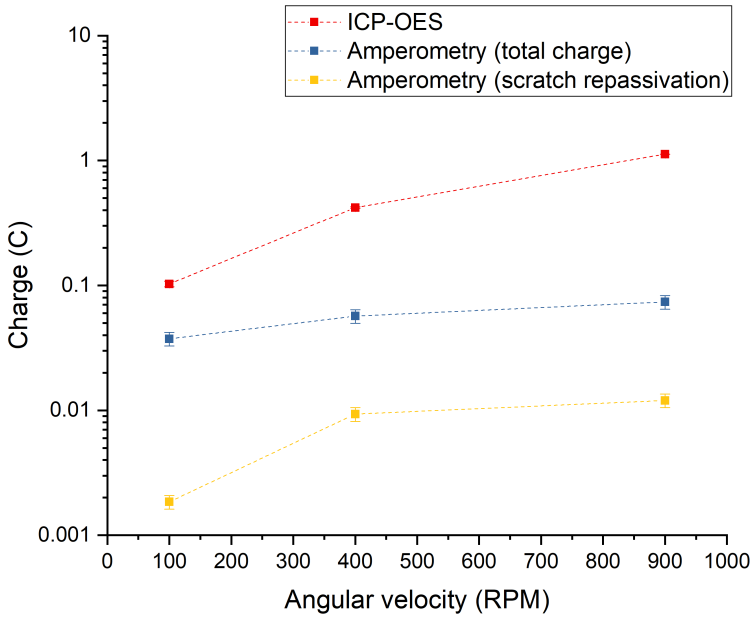


Figure 5.19: A comparison of charge associated with iron dissolution as calculated from the measured ICP-OES and potentiostatic amperometry results using X65 carbon steel samples.

### 5.3.3 Total erosion-corrosion ($\dot{w}$) *vs.* angular velocity

The total erosion-corrosion rate as a function of angular velocity of X65 and 316 stainless steel electrodes measured by WLI is presented in Figure 5.20. Volumetric erosion-corrosion rate, $\dot{w}$ is proportional to the angular velocity. The difference in erosion-corrosion rates of both X65 carbon steel and 316 stainless steel increases with angular velocity.

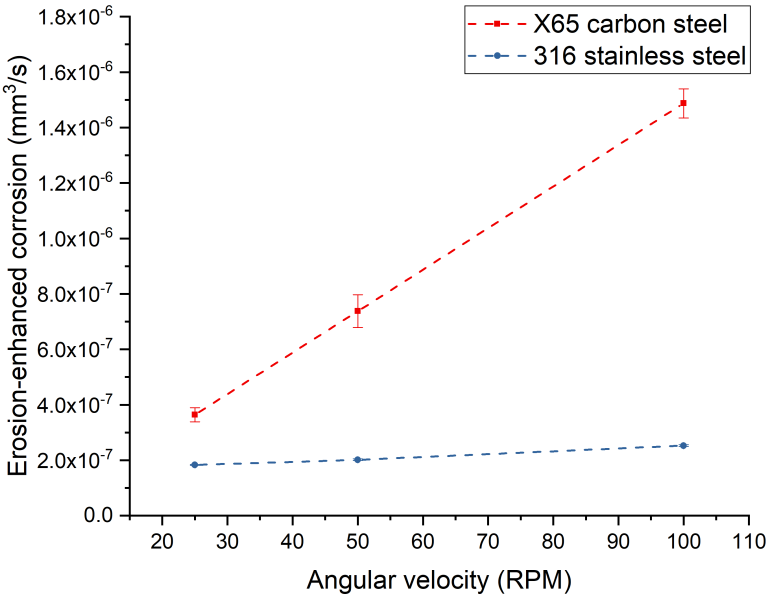


Figure 5.20: Volumetric total erosion-corrosion rates of X65 carbon and 316 stainless steel as a function of rotation rate. Volumetric losses were estimated by Zygo white light interferometer, magnification 1.0 X, sampling size 437.31 $\mu m$.

### 5.3.4 Decoupling erosion-corrosion components

Calculating pure corrosion and corrosion-enhanced erosion as shown in Table 5.2 allows decoupling all the components of erosion-corrosion. Figure 5.21 and 5.22 present variation of erosion-corrosion components of X65 carbon steel and 316 stainless steel as a function of rotation rate in pH 4 electrolyte respectively. Data are given in Tables 5.5 and 5.6. As corrosion-enhanced erosion, $\dot{e}_c$, is found indirectly *via* calculation from other erosion-corrosion components its value at 25 $RPM$ is below zero. This could be the effect of the individual components of erosion-corrosion and the errors in them. It also suggests that the value of $\dot{e}_c$ is quite small.

For the X65 carbon steel electrode most of erosion-corrosion takes place due to pure erosion at 25 and 50 $RPM$, and due to corrosion-enhanced erosion at 100 $RPM$ (Figure 5.21). The important takeaway from this result is that even at passive anodic conditions, corrosion deteriorates the surface leading to more pronounced corrosion-enhanced erosion rates as the

angular velocity is increased. In 316 stainless steel, most of the mass loss happens due to pure erosion, with corrosion-enhanced erosion also contributing to erosion-corrosion (Figure 5.22). Overall, 316 stainless steel has lower erosion-corrosion rates as angular velocity increases, owing to spontaneous passive film formation compared to X65 carbon steel and the possible effect of work hardening. Indeed, austenitic steel was reported to undergo phase transition from austenite to martensite due to a deformation-induced transition at room temperature [10]. Using the slurry pot test rig, researchers subjected 316 stainless steel samples to erosion-corrosion in distilled water and 3.5% NaCl solutions with 1 $wt.\%$ silica sand loading at the velocity of 7 $m\ s^{-1}$ for erosion and erosion-corrosion dominated tests respectively. Samples exhibited a refined nanoscale subsurface: martensitic transformation was pronounced in samples subject to erosion-dominated conditions, while it was suggested that the preferential dissolution of martensitic phase happened in the corrosive solution. Detailed microstructural characterisation and micro-mechanical analysis of samples subject to erosion-corrosion will be presented in Chapter 6.

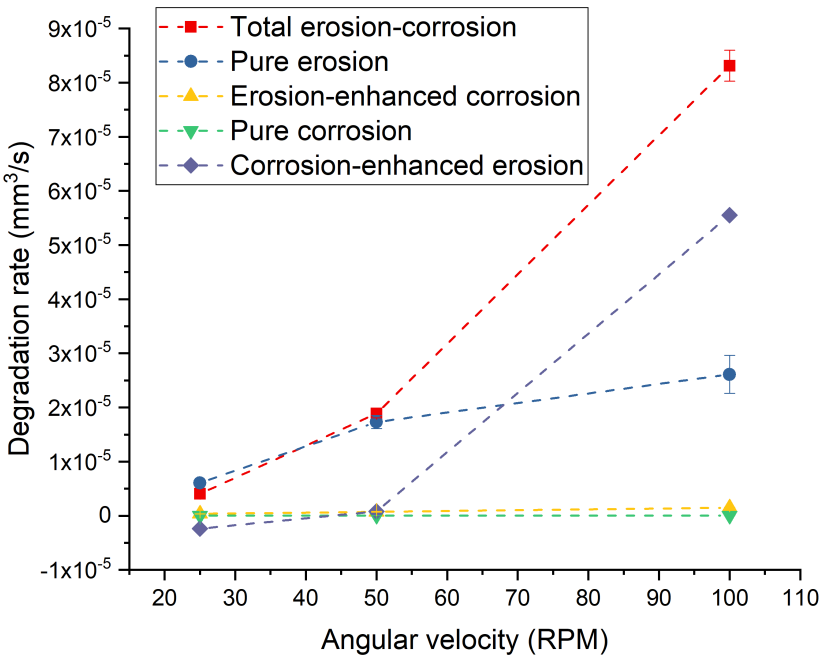


Figure 5.21: Degradation rate of X65 carbon steel working electrodes *vs.* angular velocity showing erosion-corrosion components recorded during continuous scratching in pH 4.0 KHP electrolyte. The vertical axis reflects the surface area of the scratch.

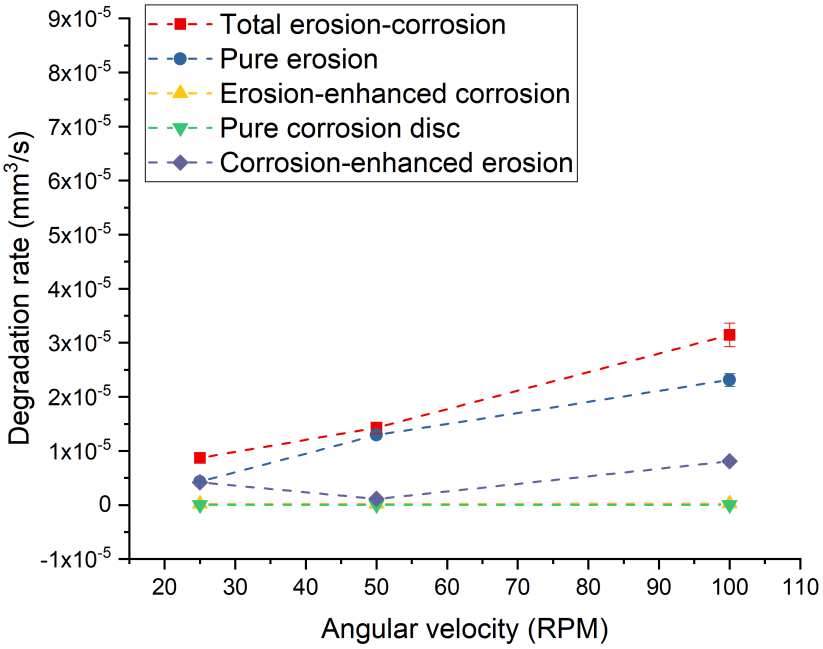


Figure 5.22: Degradation rate of 316 stainless steel working electrodes *vs.* angular velocity showing erosion-corrosion components recorded during continuous scratching in pH 4.0 KHP electrolyte. The vertical axis reflects the surface area of the scratch.

Table 5.5: Pure erosion, $\dot{e}_0$, pure corrosion, $\dot{c}_0$, erosion-enhanced corrosion, $\dot{c}_e$, total erosion-corrosion, $\dot{w}$, and corrosion-enhanced erosion, $\dot{e}_c$, rates of X65 carbon steel electrode at varying rotation rates.

| Rotation rate, $RPM$ | $\dot{e}_0$, x$10^{-6}$ $mm^3\ s^{-1}$ | $\dot{c}_0$, x$10^{-8}$ $mm^3\ s^{-1}$ | $\dot{c}_e$, x$10^{-7}$ $mm^3\ s^{-1}$ | $\dot{w}$, x$10^{-6}$ $mm^3\ s^{-1}$ | $\dot{e}_c$*, x$10^{-6}$ $mm^3\ s^{-1}$ |
|---|---|---|---|---|---|
| 25 | $6.08 \pm 0.44$ | $1.37 \pm 0.01$ | $3.64 \pm 0.14$ | $4.08 \pm 0.26$ | $-2.39$ |
| 50 | $17.3 \pm 1.22$ | $2.37 \pm 0.02$ | $7.38 \pm 0.24$ | $18.9 \pm 0.80$ | 0.80 |
| 100 | $26.1 \pm 3.50$ | $3.55 \pm 0.02$ | $14.9 \pm 0.35$ | $83.1 \pm 2.87$ | 55.5 |

Table 5.6: Pure erosion, $\dot{e}_0$, pure corrosion, $\dot{c}_0$, erosion-enhanced corrosion, $\dot{c}_e$, total erosion-corrosion, $\dot{w}$, and corrosion-enhanced erosion, $\dot{e}_c$, rates of 316 stainless steel electrode at varying rotation rates.

| Rotation rate, $RPM$ | $\dot{e}_0$, x$10^{-6}$ $mm^3\ s^{-1}$ | $\dot{c}_0$, x$10^{-10}$ $mm^3\ s^{-1}$ | $\dot{c}_e$, x$10^{-7}$ $mm^3\ s^{-1}$ | $\dot{w}$, x$10^{-6}$ $mm^3\ s^{-1}$ | $\dot{e}_c$*, x$10^{-6}$ $mm^3\ s^{-1}$ |
|---|---|---|---|---|---|
| 25 | $4.32 \pm 0.18$ | 2.29 | 1.83 | $8.70 \pm 0.35$ | 4.20 |
| 50 | $12.9 \pm 0.50$ | 2.75 | 2.02 | $14.3 \pm 1.04$ | 1.12 |
| 100 | $23.1 \pm 1.18$ | 2.62 | 2.52 | $31.5 \pm 2.17$ | 8.08 |

## 5.4 Summary

This chapter has demonstrated application of the electrode scratching technique for decoupling individual components of erosion-corrosion. Both X65 carbon steel and 316 stainless steel were studied in a pH 4.0 KHP buffer electrolyte. A continuous scratching technique was implemented at rotation rates of 25, 50 and 100 $RPM$.

Building upon the results presented in Chapter 4, volumetric pure erosion rates were measured from samples scratched under cathodic potential using white light interferometry. Pure corrosion rates were estimated using Tafel extrapolation and linear polarisation techniques, while scratching under passive anodic conditions was used to calculate erosion-enhanced corrosion rates. Measuring volumetric loss of samples scratched at passive anodic conditions was used to estimate total erosion-corrosion rates. Finally, the corrosion-enhanced erosion rate was indirectly obtained from the difference of total erosion-corrosion rate and sum of pure corrosion, pure erosion and erosion-enhanced corrosion rates.

Scratching under cathodic protection showed increased cathodic current densities with rotation rate across both alloys. The hydrogen evolution reaction rates were roughly two times higher on 316 stainless steel due to local physicochemical differences of the working electrodes. Within the studied conditions pure erosion rates calculated for X65 carbon steel were slightly higher than erosion rates of 316 stainless steel. The effect of local, surface induced microstructural changes happening due to erosion component will be presented in Chapter 6. Interesting phenomena where higher cathodic currents were measured after the solenoid tip left the surface of the electrode was noticed. This might have taken place due to surface activation after scratching, as well as removal of the scratching tip.

Continuous scratching experiments at passive anodic conditions showed acceleration of corrosion rates with time in X65 carbon steel electrode, while current densities recorded from 316 stainless steel initially decreased with time followed by an increase. Erosion-enhanced corrosion rates recorded from X65 carbon steel are substantially higher than those of 316 stainless steel. This can be attributed to the fact that passive oxide forming stainless steel passivates spontaneously, while current on carbon steel evolves both due to dissolution and protective oxide formation. Furthermore, in the tested solutions the critical current, *i.e.* the charge passed for passivation to occur is several orders of magnitude lower for the stainless steel compared to carbon steel.

The results of decoupling erosion-corrosion components showed that in X65 carbon steel most of the mass loss happened due to pure erosion at 25 and 50 $RPM$, and due to corrosion-

enhanced erosion at 100 $RPM$. In 316 stainless steel, both pure erosion and corrosion-enhanced erosion contributed to total erosion-corrosion rate. 316 stainless steel exhibited lower erosion-corrosion rates at higher angular velocities, due to faster repassivation kinetics and possible work hardening. This will be explored in detail in the next chapter.

Overall, the electrode scratching setup allowed measurement of the individual components of erosion-corrosion under well controlled conditions and is reported as a useful technique for studying the fundamental mechanisms of electrochemical-mechanical corrosion phenomena. The effect of varying the rotation rate on those components were reported in this chapter. Future research can be focused on decoupling the erosion-corrosion components under less erosive conditions. While the tip bouncing effect was avoided using continuous scratching, it did mean that imposed erosion-corrosion conditions had a rather high erosive component. The conditions reported here could be relevant for slurry transportation and wellhead start-up operations, as well as other settings, where there is not sufficient time for full repassivation of the surfaces. Improving the damping system of the electrode scratching is also suggested for future research. In principle, the scratching setup can be easily used to explore erosion-corrosion of other metals and alloys. It can also be used as a screening tool for candidate alloys before the commencement of expensive flow loop testing experiments. Due to ease of introduction of additional components to the system, erosion-corrosion in the presence of corrosive and scale forming gases such as $CO_2$ or $H_2S$ can also be studied. Another use of the scratching electrode technique is inhibitor screening, which is presented in Chapter 7.

# Bibliography


[1] H. E. Rincon. *Testing and prediction of erosion-corrosion for corrosion resistant alloys used in the oil and gas production industry.* PhD thesis, 2008.

[2] H. Xu and A. Neville. An electrochemical and microstructural assessment of erosion-corrosion of austenitic cast iron for marine applications. *Materials and Corrosion*, 53(1):5–12, 2002.

[3] T. J. Harvey, J. A. Wharton, and R. J. K. Wood. Development of synergy model for erosion–corrosion of carbon steel in a slurry pot. *Tribology*, 1(1):33–47, 2007.

[4] T. A. Adler and R. P. Walters. Corrosion and wear of 304 stainless steel using a scratch test. *Corrosion Science*, 33(12):1855–1876, 1992.

[5] H. X. Guo, B. T. Lu, and J. L. Luo. Interaction of mechanical and electrochemical factors in erosion-corrosion of carbon steel. *Electrochimica Acta*, 51(2):315–323, 2005.

[6] X.Y. Wang and D.Y. Li. Application of an electrochemical scratch technique to evaluate contributions of mechanical and electrochemical attacks to corrosive wear of materials. *Wear*, 259(7-12), 2005.

[7] A. Levy and G. Hickey. Surface degradation of metals in simulated synthetic fuels plant environments. *NACE - International Corrosion Conference Series*, pages 1–36, 1982.

[8] M. Parsi, K. Najmi, F. Najafifard, S. Hassani, B. S. McLaury, and S. A. Shirazi. A comprehensive review of solid particle erosion modeling for oil and gas wells and pipelines applications. *Journal of Natural Gas Science and Engineering*, 21:850–873, 2014.

[9] C. B. Boss and K. J. Fredeen. *Concepts, Instrumentation and techniques in ICP-OES.* 2004.

[10] R. J. K. Wood, J. C. Walker, T. J. Harvey, S. Wang, and S. S. Rajahram. Influence of microstructure on the erosion and erosion-corrosion characteristics of 316 stainless steel. *Wear*, 306(1-2):254–262, 2013.

# Chapter 6

# Mechanistic understanding of synergy in steels via microstructural and micro-mechanical analysis

## 6.1 Overview

In this chapter the influence of the erosion-corrosion on the microstructure of X65 carbon steel and 316 stainless steel is presented. The samples subject to the electrode scratching experiments presented earlier in Chapters 4 and 5 were analysed using the Focused Ion Beam milling - Scanning Electron Microscopy (FIB-SEM), *in-situ* micro-indentation and Transmission Electron Microscopy with Energy-dispersive X-Ray Spectroscopy (TEM-EDS). This allowed the observation of grain refinement that resulted from the scratching. *In-situ* micro-indentation experiments were carried out at the scratch cross sections to assess the potential work hardening induced by scratching. The influence of the applied cathodic and passive anodic potentials on the local sample hardness was compared. Finally, TEM was carried out to observe whether any phase transformation happened due to the erosion-corrosion. Localised chemical analysis of X65 carbon steel and 316 stainless steel samples was obtained using the EDS technique.

In addition to this, jet impingement erosion-corrosion experiments were carried out at the national Centre for Advanced Tribology at the University of Southampton (nCATS) to benchmark erosion-corrosion mechanisms. Both X65 carbon steel and 316 stainless steel samples were subject to the jet impingement. SEM and TEM analysis of these samples was carried out along with the mass loss measurements to compare the erosion-corrosion mechanism observed during electrode scratching to that in the jet impingement experiments.

## 6.2 Experimental

### 6.2.1 Cross section investigation

Scratch cross sections were investigated using optical and scanning electron microscopy. The steel working electrodes were cut in half using a precision saw, embedded in Bakelite resin, ground and polished to 1 $\mu m$ finish prior to imaging.

A Zeiss Auriga Cross Beam was also used to investigate if any microstructural change occurred due to the scratching. Cross sections of the steel electrodes were milled away using a $Ga^+$ ion beam. Samples were cut in half in the transverse direction to expedite the milling process. A rectangular area was drawn across the scratch and milled for depth at 30 $kV$ voltage. The milling current was reduced from 2-5 $nA$ during coarse milling to 100-500 $pA$ during medium polish mode, all the way to 50 $pA$ in fine polish mode (Refer to Figure 6.1). Secondary electron imaging was then used to observe the resultant polished cross sections.

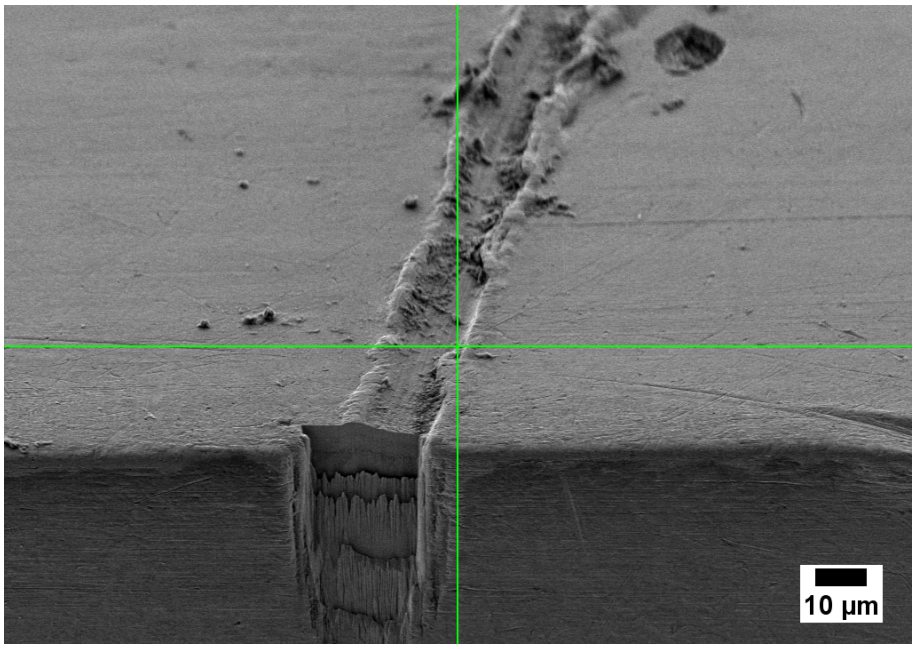


Figure 6.1: SEM micrograph showing FIB milling in stages to reveal the cross section for microstructural investigation.

### 6.2.2 Lamella preparation using focused ion beam milling

The FEI Helios NanoLab 600 Focussed Ion Beam Scanning Electron Microscope (FIB-SEM) was used for Transmission Electron Microscopy (TEM) sample preparation. The Helios FIB-SEM enables locating, milling and lifting out a sample lamella from a specific location using a $Ga^+$ ion beam coupled with an Omniprobe micromanipulator. The lamella can then be placed

onto a Cu TEM grid and thinned in stages until the sample is electron transparent. Figure 6.2 (a-f) demonstrates the stages of sample preparation.

Initially Pt is deposited at 0° over 15×2 $\mu m^2$ area of interest (for scratched samples it is usually along or across the scratch, depending on the wear size) at 3 $\mu m$ thickness using an electron beam. This Pt layer is then used to set the Eucentric height when the sample is tilted to 5°, 30° and finally to 52°. With the sample at 52° more Pt is deposited using an ion beam at 30 $kV$ and 0.46 $nA$ (See Figure 6.2a). Then two rough cross sections are milled away from the bulk sample either sides of the Pt strip using an ion beam at 30 $kV$ and 21 $nA$. The size of each trench is 25 $\mu m$ × 10 $\mu m$ × 10 $\mu m$. The cross sections are subsequently cleaned using a smaller current of 6.5 $nA$ at 55° and 49° tilt (Figure 6.2b).

The sample is then tilted to 7° and a side and the bottom part of the rectangular lamella is cut at 30 $kV$ and 6.5 $nA$. With the sample tilted to 0° the tungsten Omniprobe is inserted and aligned with the lamella. A Pt layer is deposited over the aligned area with 0.5 $\mu m$ thickness at 30 $kV$ and 93 $pA$ ion beam. The lamella is welded to the Omniprobe and the third side of the rectangle can be cut. The lamella is lifted out of the trench and transferred to the TEM grid using the Omniprobe micromanipulator (See Figure 6.2c). It is is then attached to a Cu grid using Pt deposition at 30 $kV$ and 93 $pA$ at 0° (Figure 6.2d).

The final steps of the TEM sample preparation require thinning the attached lamella at around 52° sample tilt with consequently decreasing $Ga^+$ beam currents. The lamella is milled at 30 $kV$ and 0.46 $nA$ current at ±1.5° to *ca.* 1.4 $\mu m$ sample thickness, 30 $kV$ and 93 $pA$ at ±1.2° to *ca.* 0.7 $\mu m$ sample thickness, and 5 $kV$ and 47 $pA$ at ±2.5° until the Pt layer is sufficiently reduced. Finally, the lamella is cleaned at ±7° at 2 $kV$ and 28 $pA$. The sample thickness at this point is approximately 80–120 $nm$ and should be ready for TEM imaging (See Figures 6.2e and 6.2f).

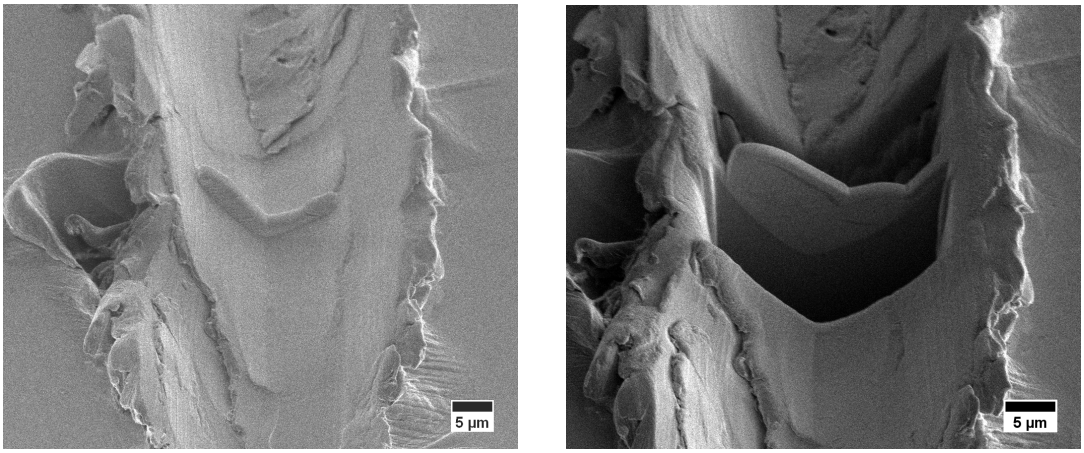


(a) (b)

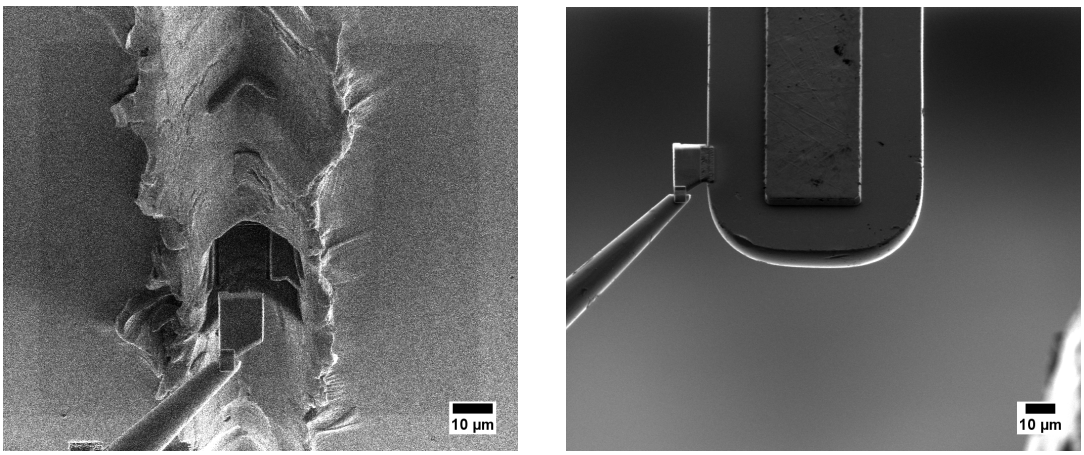


(c) (d)

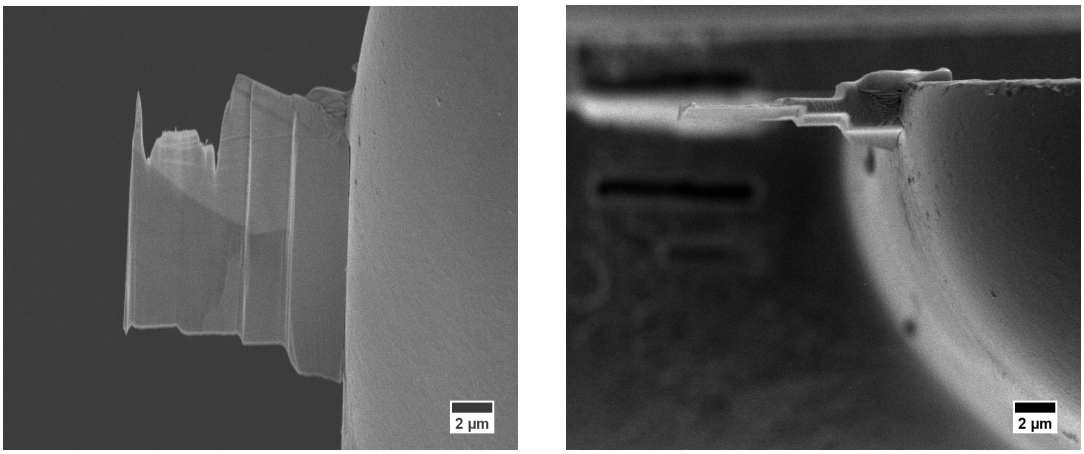


(e) (f)

Figure 6.2: Secondary electron and ion beam images demonstrating FIB lift-out technique: a) Deposition of Pt protective layer inside the scratched area of interest. b) Trenches milled away from the bulk sample. c) Lifting out the cut lamella with the Omniprobe micromanipulator. d) Attaching the lamella to Cu TEM grid with Pt deposition. e) Lamella midway through thinning steps. f) Top view of the lamella on TEM grid.

### 6.2.3 Transmission electron microscopy

Samples were characterised using a JEOL 2100Plus $LaB_6$ source and a JEOL JEM-2100F FEG source transmission electron microscopes. Bright field imaging was carried out in the former instrument, while chemical analysis using an Oxford Instruments INCA/AZtec EDS detector system with STEM was mainly performed on the latter instrument. The accelerating voltage was equal to 200 $kV$.

Selected area electron diffraction (SAED) was performed using both TEM instruments. The crystal planes giving rise to the diffraction patterns can be assigned by first identifying allowed reflections for the crystal structure and the applying Bragg's equation 6.1.

$$d = \frac{\lambda L}{R} \tag{6.1}$$

where $d$ is the interplanar spacing, $\lambda$ is the wavelength of the electrons at accelerating voltage of 200 $kV$, $L$ is the camera length, and $R$ is the distance between the direct and diffracted beam.

At least two diffraction patterns were collected at different camera lengths to confirm the camera constant ($\lambda L$). In this study, a TEM plugin of Fiji image processing software was used to calculate the d-spacing [1]. Since the d-spacing values obtained using the software were comparable to the ones obtained from a manual calculation, the image processing software results were used.

### 6.2.4 Micro-indentation experiments using Alemnis

Microhardness of the scratched samples was measured using the Alemnis nano- and micro-indenter mounted *in-situ* FEI Quanta FEG 650 SEM. The Alemnis Standard Assembly (ASA) was mounted on the SEM stage at 30° horizontal angle. The assembly consists of a piezo actuated displacement head integrated with a displacement sensor (maximum displacement 40 $\mu m$), an indenter tip, a sample stage fit for a standard SEM stub, and a load cell (maximum load 500 $mN$). The piezo stack can be moved in the z-direction to enable tip approach, while the load cell is placed on an x,y-stage for sample navigation (Figure 6.3). The sample is positioned below the electron beam and the image view is rotated 180° for an *in-situ* observation of the indentation by a cube corner diamond tip indenter (Synton-MDP). The three sides of the indenter are axisymmetric and at 120° to each other and 35.26° to the primary axis.

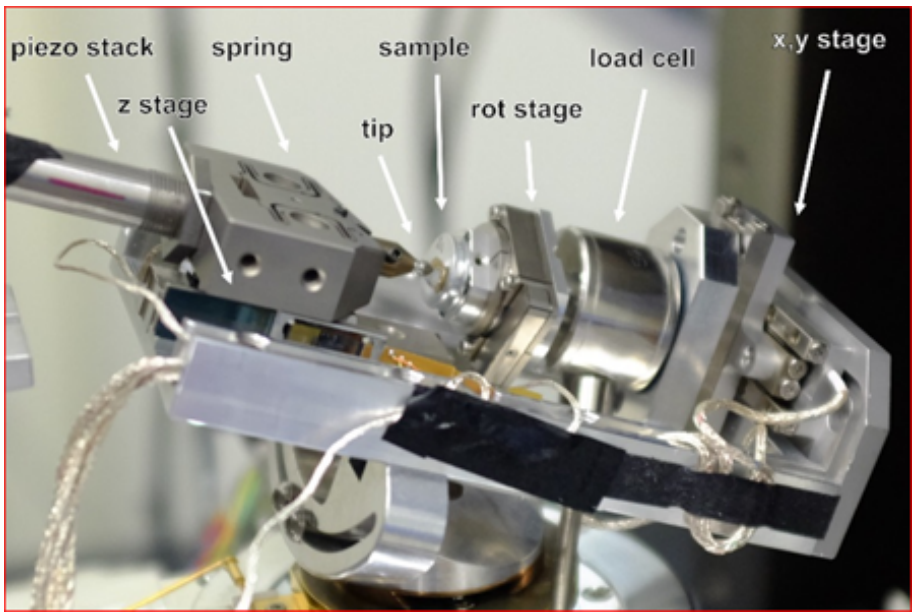


Figure 6.3: Image showing the Alemnis Standard Assembly (Please note rotation stage was not used in this work. Image courtesy of Dr Giorgio Sernicola.)

The disc electrode sample was cut in half using EDM and polished to 1 $\mu m$ finish (Figure 6.4a). The convex side of the half-discs was flattened *via* polishing in order to increase the contact area with the sample stub. The sample was glued to the stub using quick drying Ag paste and care was taken to minimize the amount of paste seeping under the sample (Figure 6.4b).

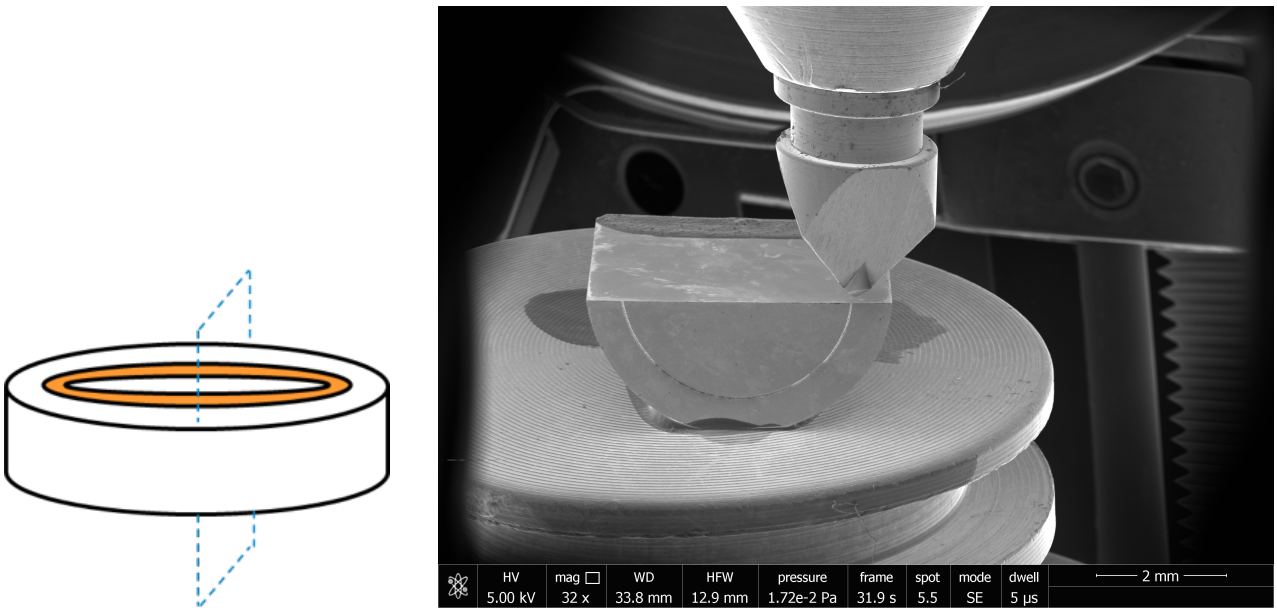


(a) (b)

Figure 6.4: a) An illustration showing the scratched sample and the direction of cutting. b) A low magnification SEM micrograph showing the sample on a stub with the cube corner tip at close proximity to the surface.

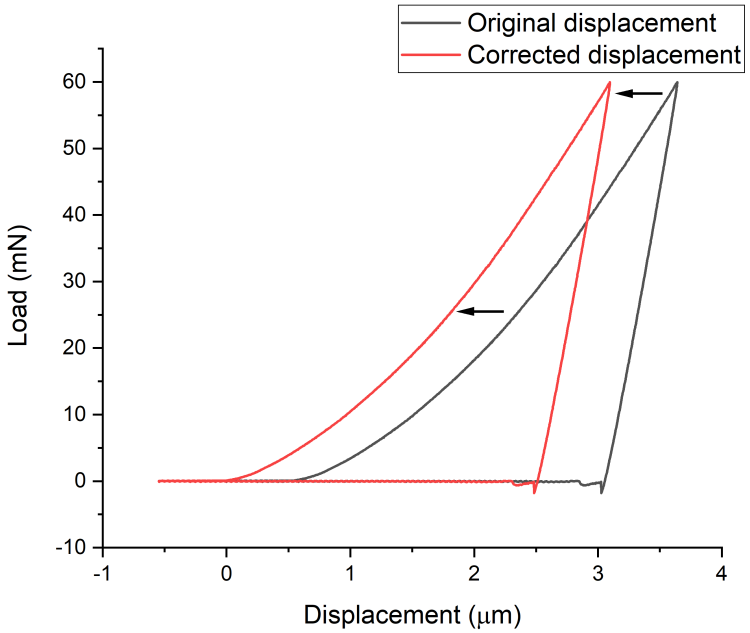


Figure 6.5: Example of load displacement graphs showing the original and corrected displacements at 60 $mN$ load.

A series of micro-indentation tests were carried out at increasing distances from the wear scratch. The projected distance between the scratch and the indent was measured from the deepest point of the scratch to the center of the triangular indent impression. The actual distance was found by dividing the measured distance by cos(30°) due to the equipment setup. The indents were large enough to be imaged post indentation using a standard SEM at 0° horizontal and the measurements confirmed. The microhardness experiments were set up using the AMICS software. A displacement control with load target mode was used. A series of tests with target loads between 10-100 $mN$ showed the lowest load at which hardness plateaued was equal to 60 $mN$ for both X65 carbon steel and 316 stainless steel. Hence all tests were done with the load target of 60 $mN$. The displacement rate was set to 0.05 $\mu m\ s^{-1}$ and the tip was retracted immediately after achieving the target load.

Prior to loading the indenter was moved as close as possible to the area of interest to avoid crashing with the surface. Due to the tip not being in contact with the sample at the beginning of the test, the displacement had to be corrected during data analysis. To do so, the value of the displacement after which the load started constantly increasing was identified. A corrected displacement was then found by subtracting this value from the original displacement. An example of this is shown in Figure 6.5. All load *vs.* displacement curves shown in this work refer to the corrected displacement values.

The microhardness of the sample was found by dividing the maximum load over the contact

area under the load (Equation 6.2). Oliver and Pharr pioneered the method for the hardness measurement using an instrumental indentation. Following their method, the contact area under the load could be identified from the unloading portion of the load-displacement graph [2, 3]. This method, however, was difficult to implement in this study across large numbers of samples due to the slight variations in sample preparation. Furthermore, the indents formed at 60 $mN$ could easily be viewed using an SEM, so the contact area was measured using imaging. There is a possibility that the area under the load is larger than the area of the residual hardness impression. However this is the case for the materials with very small $E/H$ values, where significant elastic recovery takes place during the unloading [3]. Hence, it was assumed that the contact area under the max load is equal to the residual area.

$$H = \frac{P_{max}}{A_c} \tag{6.2}$$

### 6.2.5 Jet impingement testing

Jet impingement testing was carried out at the national Centre for Advanced Tribology at Southampton. A slurry jet impingement tester enables circulating water with sand using positive displacement pump. The capacity of the tank is 200 $L$. The flow rate was set to 2.5 $m^3\,h^{-1}$ and 6 $mm$ nozzle was used for the tests. This resulted in the jet velocity of $24 \pm 1$ $m\,s^{-1}$. The duration of the tests was equal to 1 hour. Note that the solution was allowed to circulate until the development of the desired velocity (usually under a minute) and sand was added afterwards. The beginning of the test was set at the moment of addition of sand. The jet erosion tester and the view of the chamber is presented in Figure 6.6.

The slurry was prepared *via* mixing 18 $L$ of tap water, 180 $g$ of sand (50–70 mesh/210–297 $\mu m$), 183.8 $g$ KHP and 11.7 $mL$ 2 $M$ NaOH to result in pH of *ca.* 4.0. The concentration of sand was equal to *ca.* 1 $wt.\%$. Due to substantial amount of water required, tap water was used as a solvent instead of de-ionised water. The presence of certain ions, especially chlorides, along with higher conductivity of the tap water will have a deleterious impact on the corrosion rate of samples. These factors need to be taken into account.

X65 carbon steel and 316L stainless steel plates of $5\,cm \times 5\,cm \times 3\,mm$ were used as the samples. The samples were ground to P1200 grit size prior to the tests. A total of 4 jet impingement tests were done for each material: two at 30°, two at 90° angles to the vertical. The mass of the samples before and after the testing was measured using a high precision 5 decimal place analytical balance. Samples were dried in the oven at 40° $C$ for 4 hours after the tests prior to weighing. Wear scars were imaged using optical, scanning and transmission

electron microscopes.

Mass loss recorded in 1 $h$ period was converted to the erosion-corrosion rate (ECR) in $mm/year$ using Equation 6.3.

$$ECR = \Delta\dot{h} = \frac{\Delta h}{t} = \frac{\Delta m}{\rho A t} \tag{6.3}$$

where $\Delta h$ is the thickness loss of the material, $t$ is the jet impingement time (1 $h = \frac{1}{8766} year$), $\Delta m$ is the mass loss, $A$ is the area of the sample (25 $cm^2$) and $\rho$ is the sample density (7.85 $g\,cm^{-3}$ for X65 carbon steel, 8.02 $g\,cm^{-3}$ for 316 stainless steel).

(a) (b)

Figure 6.6: a) The jet impingement tester at nCATS. b) An image of the chamber interior showing the nozzle and the sample at an angle mounted on a sample holder.

## 6.3 Results and discussion

### 6.3.1 Cross section investigation

Figure 6.7 presents the optical and scanning electron micrographs of the X65 carbon steel electrode scratched 3 times at 30 $RPM$ under passive anodic conditions, with the applied potential of 0.6 $V$ *vs.* MSE. The optical micrograph does not provide enough information on the possible microstructural refinement. There are local variations in the carbon content with the interference bands indicating possible carbon-rich areas along the top of the micrograph in Figure 6.7a. The SEM micrograph shown in Figure 6.7b, on the other hand, shows a small crack at the bottom of the scratch. Figure 6.8 is an SEM micrograph of the same sample. Not only can the crack be seen at the left hand side of the scratch but also a region of densely packed material is found at the right hand side of the micrograph. To gain further understanding of the microstructural changes, finer cross section analysis was carried out. This was achieved using FIB-SEM cross section analysis of the X65 carbon steel.

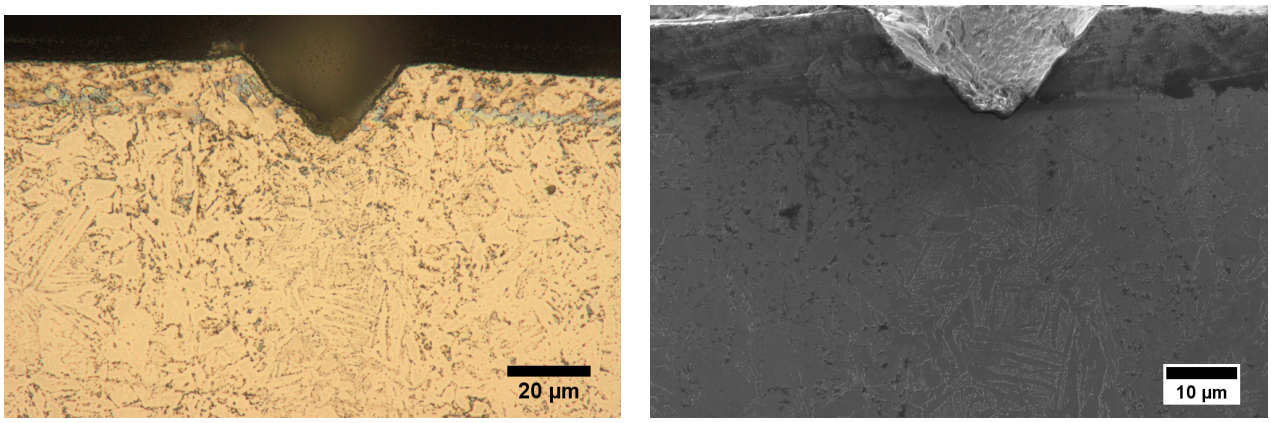


(a) (b)

Figure 6.7: a) Optical and b) SEM micrographs showing the cross section of the X65 sample repeatedly scratched 3 times at applied potential of 0.6 $V$ *vs.* MSE.

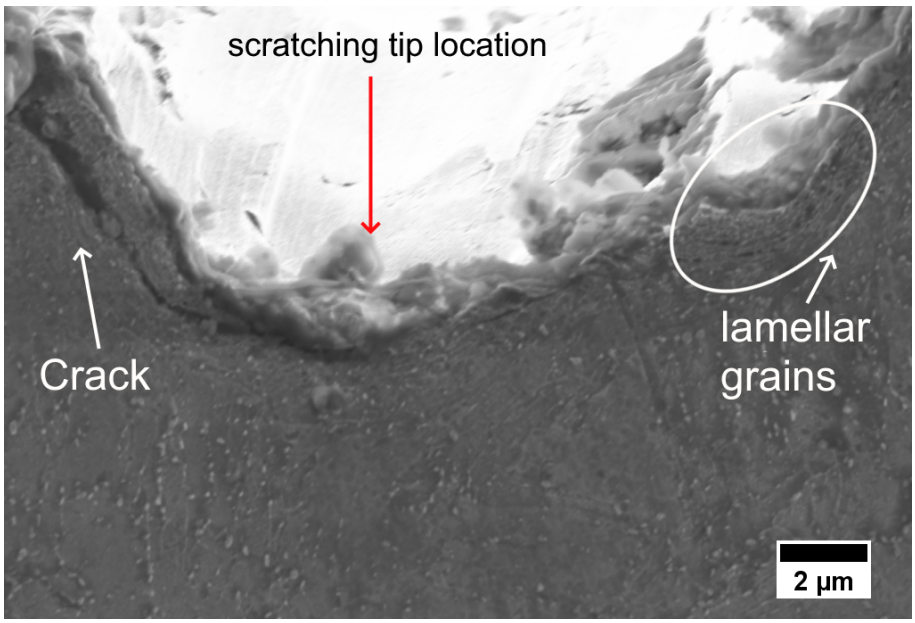


Figure 6.8: SEM micrograph showing the cracks and the densely packed areas in the X65 carbon steel sample scratched under the passive anodic potential.

Figure 6.9 is the cross section of the X65 carbon steel sample that was repeatedly scratched 3 times at passive anodic potential of 0.6 $V$ *vs.* MSE in pH 4.0 KHP solution. The region directly under the scratch is characterised by the grain refinement. These changes are observable up to 3 $\mu m$ below the surface. This observation suggests that nanoscale lamellar grains are formed as a result of the mechanical scratching process. The width of these lamellae is *ca.* 100 $nm$, and a higher resolution technique such as the TEM is required to approximate it better (Refer to section 6.3.3). The original microstructure with larger grains is seen to the both sides of the deformed area. The microstructure of the transition region is presented in Figure 6.10. Scratching the metal caused the grain refinement in a half-circular region evident from the flow of the material shown in the micrograph.

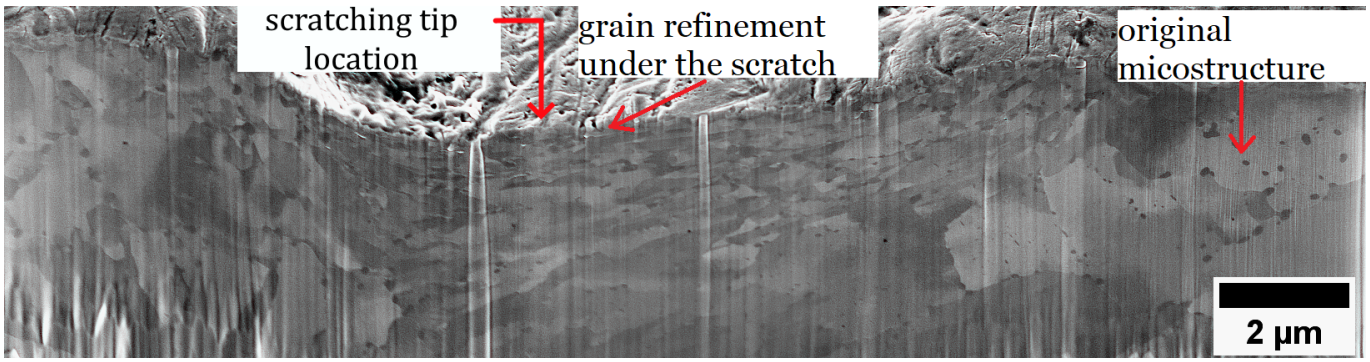


Figure 6.9: SEM micrograph showing the scratch cross section of the X65 carbon steel sample repeatedly scratched 3 times at 30 $RPM$ in pH 4.0 KHP solution.

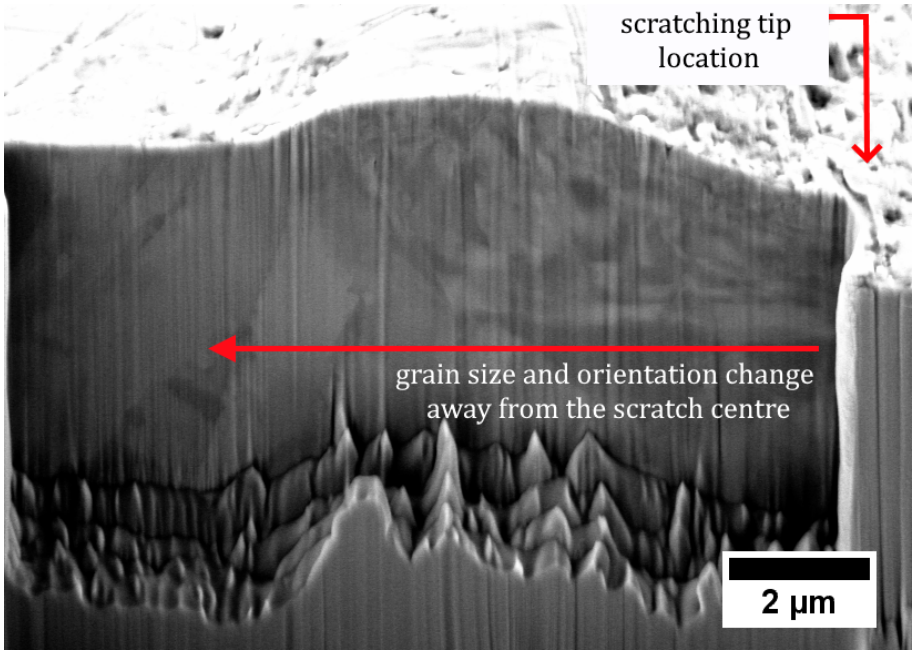


Figure 6.10: SEM micrograph showing the cross section of the left hand side of the scratch: a transition from refined to original microstructure can be seen.

### 6.3.2 Local hardness measurements using micro-indentation

This section presents the results of the local hardness measurements that were carried out using *in-situ* micro-indentation. First, the load-displacement graphs of the X65 carbon steel samples *before* scratching experiments are presented. This is followed by the hardness measurements of the X65 carbon steel samples repeatedly scratched under passive anodic potential at rotation rates of 100, 400 and 900 $RPM$. Finally, the hardness of the continuously scratched X65 carbon steel and 316 stainless steel samples are presented. Samples scratched at 25, 50 and 100 $RPM$ under both cathodic and passive anodic potential are compared.

#### Bare surface hardness measurements

Figure 6.11 presents typical indents formed after the indentation of the unscratched bare X65 carbon steel samples at 60 $mN$ load. Assuming there was not a significant elastic recovery during the unloading, the area of the triangular impressions was measured from the SEM micrographs. This resulted in average microhardness of 3.62±0.03 $GPa$ measured from the total of 8 indents. All load-displacement curves overlapped and the typical graphs recorded during the microindentation are presented in Figure 6.12. Owen *et al.* [4] reported Vickers hardness $H_v$ of 202±9 (1.98±9 $GPa$) for X65 steel using 4.9 $N$ load. Guo [5] reported hardness of *ca.* 3 $GPa$ for A1045 carbon steel using nanoindenter at a 2 $mN$ load. It is known that small scale indentation experiments tend to overestimate the hardness of the material. This phenomenon is

known as an indentation size effect (ISE), where the hardness of the material increases at small depths of penetration, usually of the order a few micrometers and less [6]. The Nix-Gao model describes ISE such that geometrically necessary dislocations (GNDs) occur along with statistically stored dislocations (SSDs) that appear from uniform straining, contributing to extra hardening component that increases with the decreasing indentation depth [6]. The equation describing the hardness $H$ at depth $h$ using the Nix-Gao model is given in Equation 6.4.

$$H = H_0 \times \sqrt{1 + \frac{h^*}{h}} \tag{6.4}$$

where $H_0$ is the bulk metal hardness, *i.e.* hardness approached asymptotically at large hardness impressions, $h^*$ is the characteristic depth below which GNDs start to take effect. The characteristic depth can then be found out from a slope of the plot of $H^2$ *vs.* $\frac{1}{h}$ along with the bulk hardness $H_0$ at the intercept.

Although current research did not estimate the characteristic depth for the X65 carbon steel, the literature value available for X52 [1] carbon steel and is *ca.* 2086 $nm$ [7]. Hence, it is possible that ISE was the reason for the higher bare surface hardness of X65 carbon steel. Alongside ISE, the surface finish of the sample is known to affect the characteristic depth of the material. The author also acknowledges that elastic recovery taking place during unloading would also reduce the projected area, therefore resulting in an overestimated hardness value. Nevertheless, the results of microhardness tests were deemed to be useful for qualitative comparison of the samples.

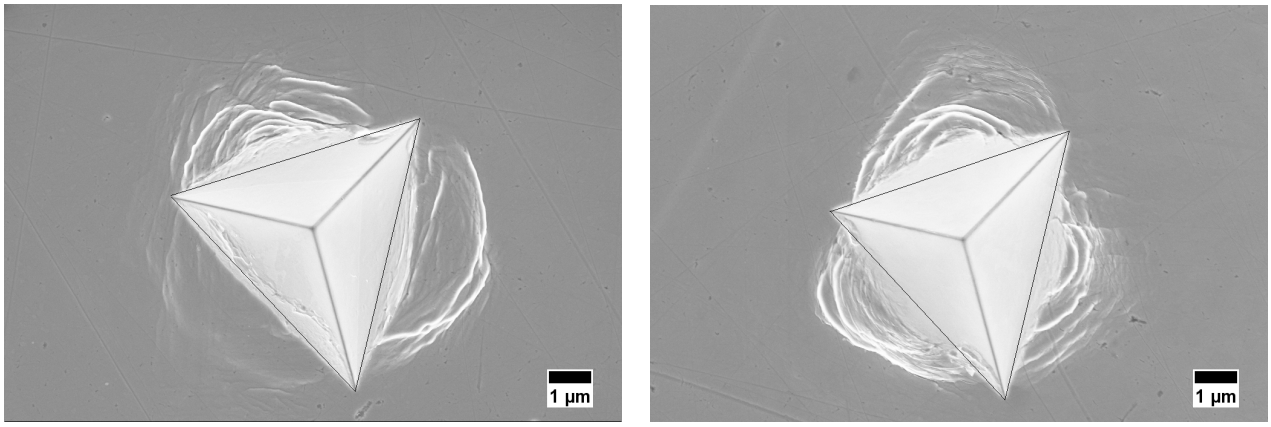


(a) (b)

Figure 6.11: Secondary electron micrographs of indents formed on bare X65 carbon steel subject to 60 $mN$ load. Total of 8 indents were made with hardness of $3.62 \pm 0.03$ $GPa$.

[1] The American Petroleum Institute (API) standards describe the minimum yield strength for X65 and X52 grades as 65000 pound-per-square-inch (*psi*) and 52000 *psi* respectively.

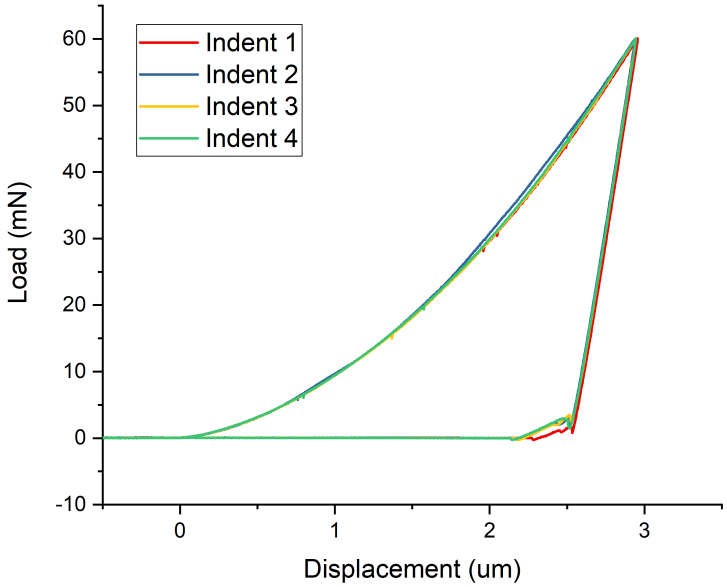


Figure 6.12: Load-displacement graphs recorded during a micro-indentation of the X65 carbon steel showing a consistency of the measurement.

### Cross section hardness measurements of the scratched samples

Repeatedly scratched samples

Samples scratched 100 times [2] under the passive anodic potential of 0.6 $V$ *vs.* MSE at 100, 400 and 900 $RPM$ were studied. The SEM micrograph showing the sample and the indenter after the tip retraction is presented in Figure 6.13. Some pile-up of the material can be noticed at the contact periphery. A total of 8 indents were created in two rows from the base of the scratch location to the bulk metal. The locations of the indents and their numbering are displayed in Figure 6.14. Figure 6.15 presents the hardness of X65 carbon steel samples *vs.* the distance from scratch. *All* samples show relative *local hardening* close to the scratch, *i.e.* the subsurface closest to the scratch tended to have the highest hardness value, and the hardness decreased further away from the scratch. Regarding the rotating rate of the disc electrode, the hardness of the samples repeatedly scratched at 900 $RPM$ had the highest value. This could be related to the increased amount of working hardening happening at high strain rates taking place at a high velocity. Surprisingly, the sample scratched at 100 $RPM$ had higher hardness compared to the one scratched at 400 $RPM$. Sample heterogeneity as well as the relationship between the material removal and work-hardening could explain this phenomenon. Further research is

[2]The number of scratches over the same area for 100 successive releases of solenoid with contact time of 1 s corresponds to a total of 167, 667 and 1500 scratches made at the same location at rotation rates of 100 RPM, 400 RPM, and 900 RPM respectively.

necessary to estimate the change of total erosion-corrosion rate as a function of work-hardening rate. Some additional indentations were carried out further away from the scratch at up to 2.5 $mm$ distance. The results are presented in Figure 6.16. The general trendline of the hardness *vs.* distance from scratch suggest that microhardness decreases away from the surface. This suggests work-hardening takes place most noticably on the samples scratched at 900 $RPM$.

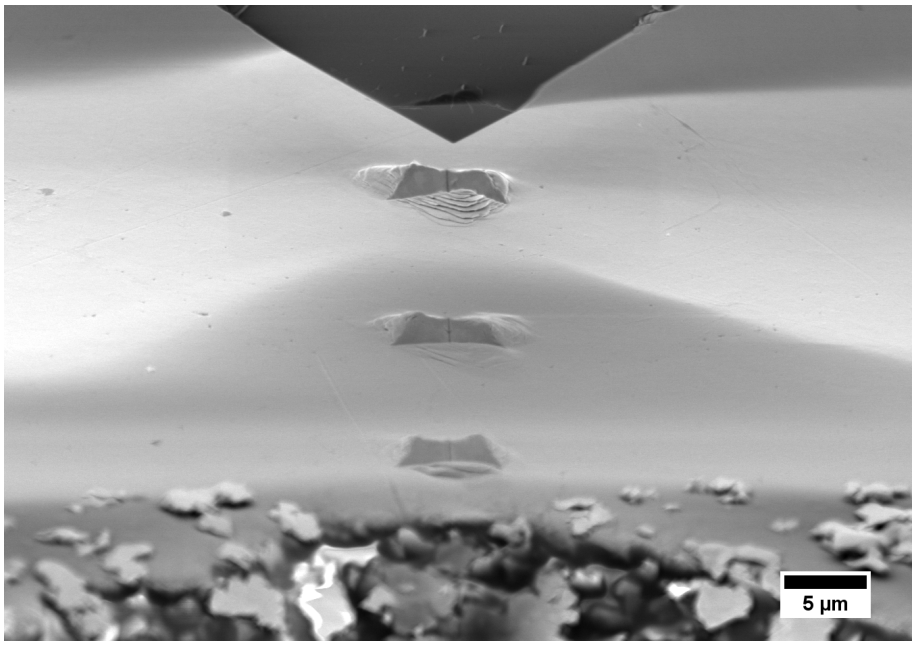


Figure 6.13: An SEM image showing the X65 carbon steel sample after the third indentation at 30°. The sample was repeatedly scratched at 400 $RPM$ at 0.6 $V$ *vs.* MSE applied voltage.

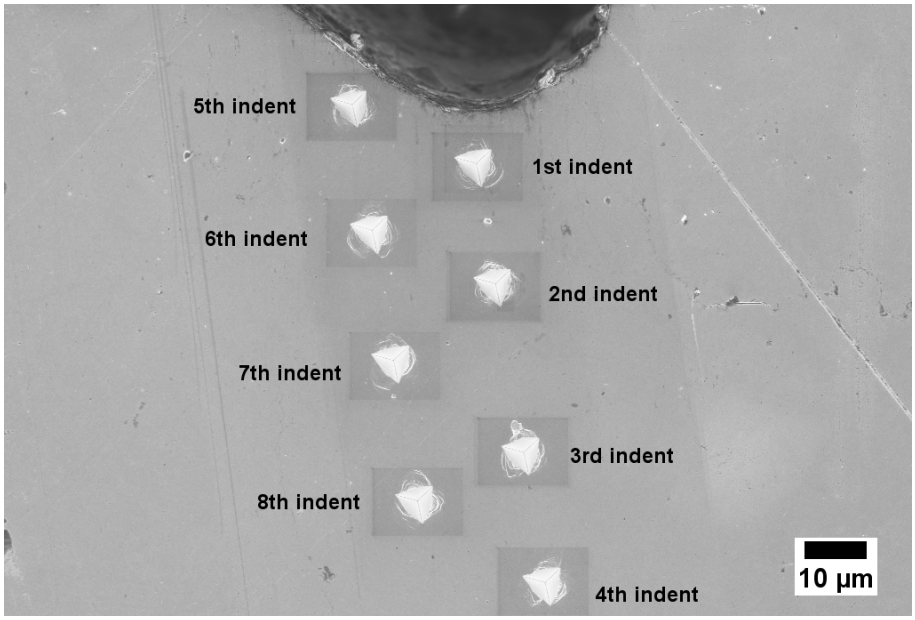


Figure 6.14: An SEM image showing the location of the indents in the sample scratched at 900 $RPM$. '0' distance from the scratch is set as the intersection between the scratch and the perpendicular to the centre of the indent.

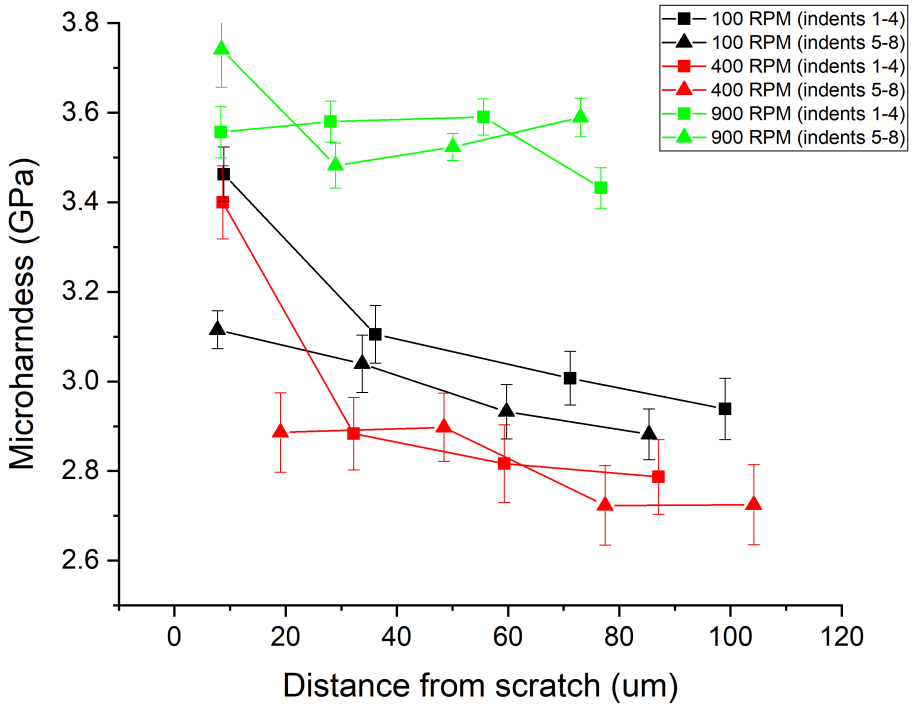


Figure 6.15: Hardness of X65 carbon steel electrodes repeatedly scratched at 100, 400 and 900 $RPM$ rotation rates, under applied potential of 0.6 $Vvs.$ MSE. The error bars represent the uncertainty in measuring the area of the indent impression.

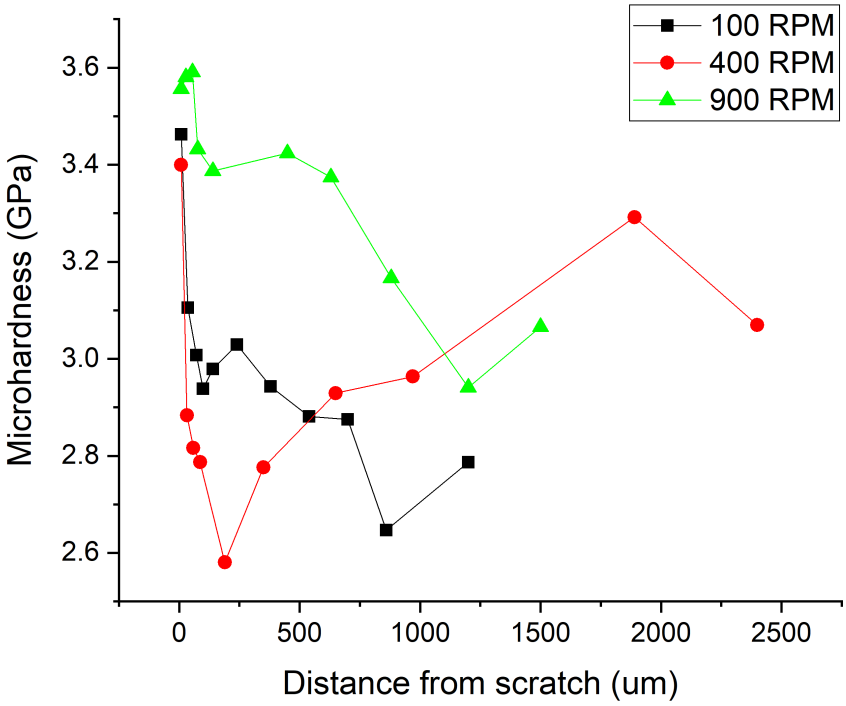


Figure 6.16: Hardness of X65 carbon steel electrodes repeatedly scratched at 100, 400 and 900 $RPM$ rotation rates, under applied potential of 0.6 $V$ *vs.* MSE presented in Figure 6.15 with additional indents created further away from the scratch.

Continuously scratched samples

X65 carbon steel and 316 stainless steel samples continuously scratched 100 times [3] at 25, 50 and 100 $RPM$ were cut in half in transverse direction across the scratch and the cross section hardness was measured as a function of the distance from the scratched area. A total of 8 indents were created and the locations of the indents are displayed in Figure 6.17.

The hardness values of the samples scratched at 25 $RPM$ in pH 4.0 KHP solution are presented in Figure 6.18. Among the studied conditions and materials the hardness of the samples increased in the following order at 25 $RPM$: 316 stainless steel scratched at 0.6 V, X65 carbon steel scratched at 0.6 $V$ and 316 stainless steel scratched at -1.5 $V$ *vs.* MSE. Across all three samples presented here, the highest hardness values were recorded closest to the location of the scratch. This suggests work hardening taking place during both erosion and erosion-corrosion in the scratch subsurface. However, in 316 stainless steel samples there is a significant difference in hardness values between the samples scratched under passive anodic and cathodic protection conditions, the latter having significantly higher hardness values. Research by Lu and

[3]Here the total rotations for the samples was equal to 100, with total contact time of 240, 120 and 60 $s$ for the rotation rates of 25, 50 and 100 $RPM$ respectively.

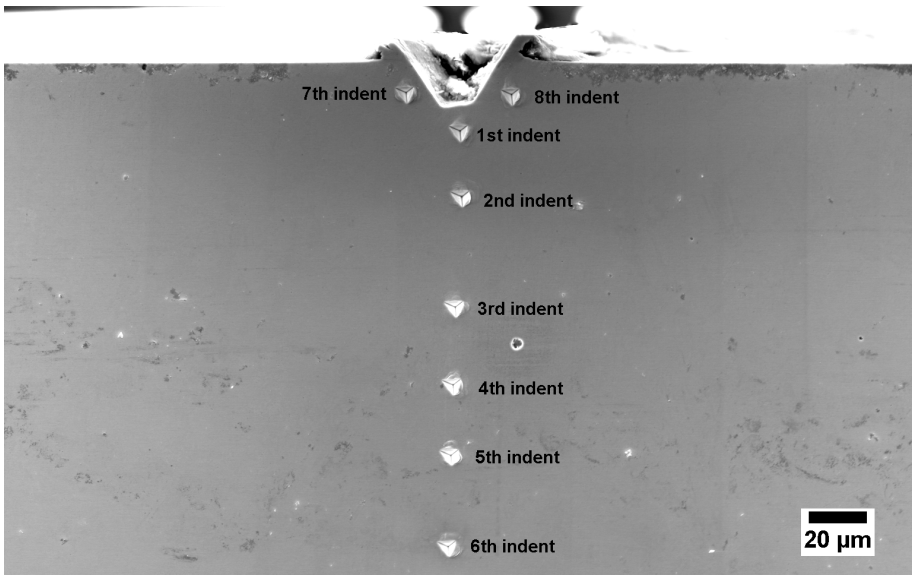


Figure 6.17: SEM image indicating the locations of the indentations for continuously scratched samples.

Luo [8] found that significant *in-situ* surface hardness degradation took place at anodic current densities of 1 $mA\,cm^{-2}$ in low carbon steels. Furthermore, the hardness increase and ductility reduction is known to take place under cathodic protection due to hydrogen embrittlement [9]. As samples subject to pure erosion conditions are held at cathodic potentials and are under cyclic strain due to scratching, it is possible that hydrogen embrittlement has occurred. Hydrogen emrbitllement susceptibility correlates positively with the strength of the material — high strength alloys such as X80 grade steels are known to be susceptible to hydrogen ingress [10]. Hardness increase with cathodic current density during charging, as well as hardness decrease due to hydrogen desorption after charging have been reported [11]. Further research under controlled conditions are necessary to elucidate the effects of anodic and cathodic current on microhardness of samples, including *in-situ* testing similar to those used by Guo [5].

As the rotation rate of the electrode was increased to 50 $RPM$ similar trends were observed (See Figure 6.19). Specifically, 316 stainless steel scratched under cathodic protection showed the highest hardness among the studied samples. 316 stainless steel scratched at passive potential of 0.0 $V$ *vs.* MSE showed considerably higher hardness close to the surface interface, suggesting work hardening. Similar trend was observed in the sample eroded under cathodic protection. Hardness values of X65 carbon steel samples, on the other hand, did not show a clear trend. However, all hardness values recorded at a similar distance from the interface were higher for the sample under cathodic protection both in stainless and carbon steels, suggesting possible hardness degradation due to anodic current or hydrogen embrittlement due to application of cathodic currents and local ingress of hydrogen facilitated by scratching.

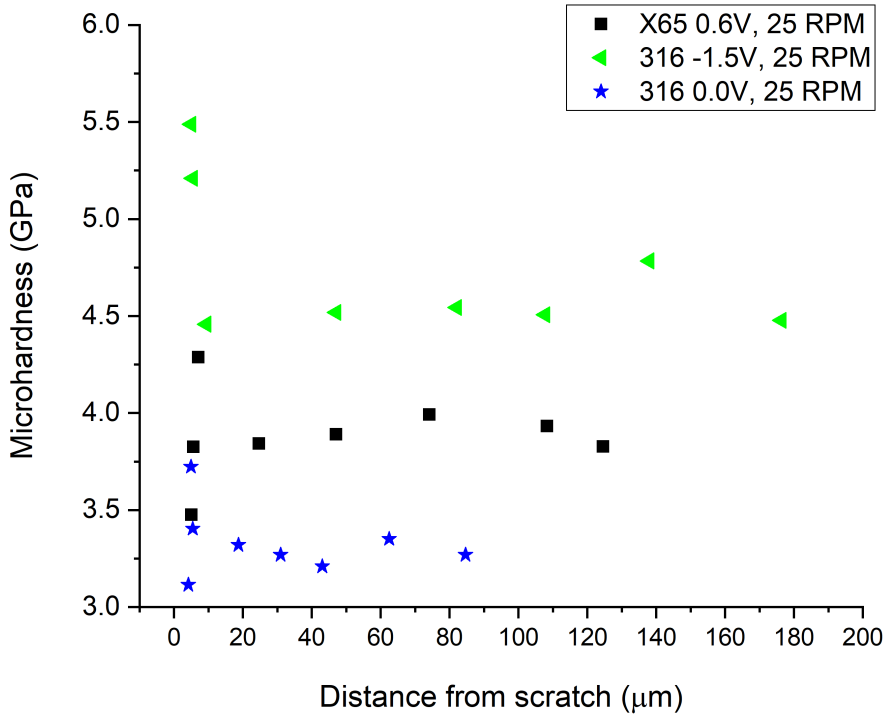


Figure 6.18: Microhardness of cross section of X65 carbon steel and 316 stainless steel samples continuously scratched at 25 $RPM$ *vs.* distance from the scratch.

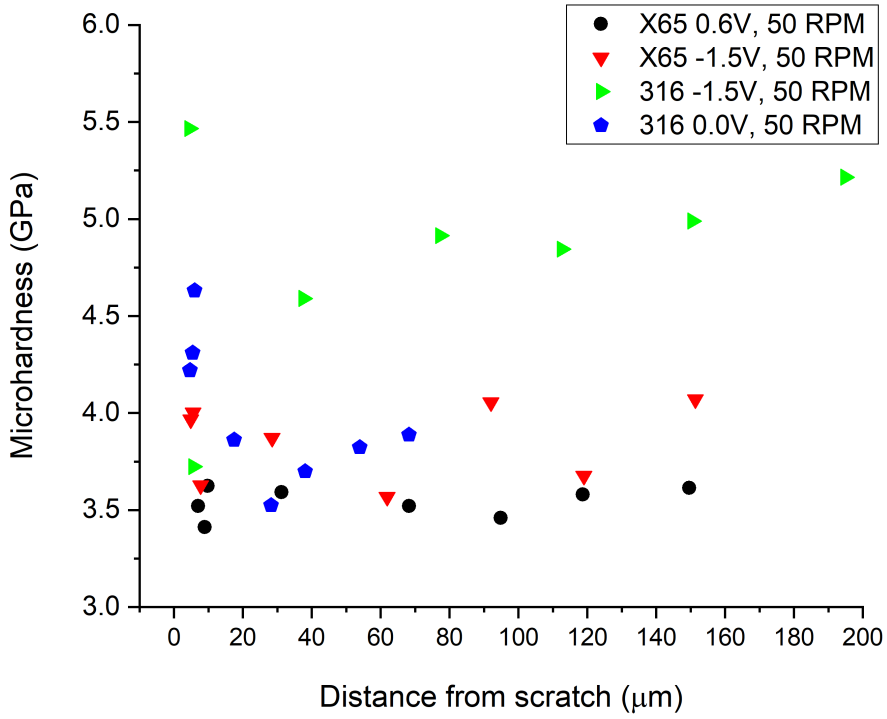


Figure 6.19: Microhardness of cross section of X65 carbon steel and 316 stainless steel samples continuously scratched at 50 $RPM$ *vs.* distance from the scratch.

Hardness values *vs.* the distance from the scratch recorded from the samples scratched at 100 $RPM$ are presented in Figure 6.20. Yet again, 316 stainless steel sample scratched under cathodic protection had the highest hardness values. The sample scratched under passive anodic potential had considerably higher hardness values close to the scratch compared to the bulk, indicative of the work hardening. The hardness values of X65 carbon steel scratched at -1.5 $V$ *vs.* MSE were generally higher than the ones scratched under passive anodic potential. The highest hardness of X65 carbon steel sample scratched at -1.5 $V$ *vs.* MSE was close to the scratched area, confirming the work hardening.

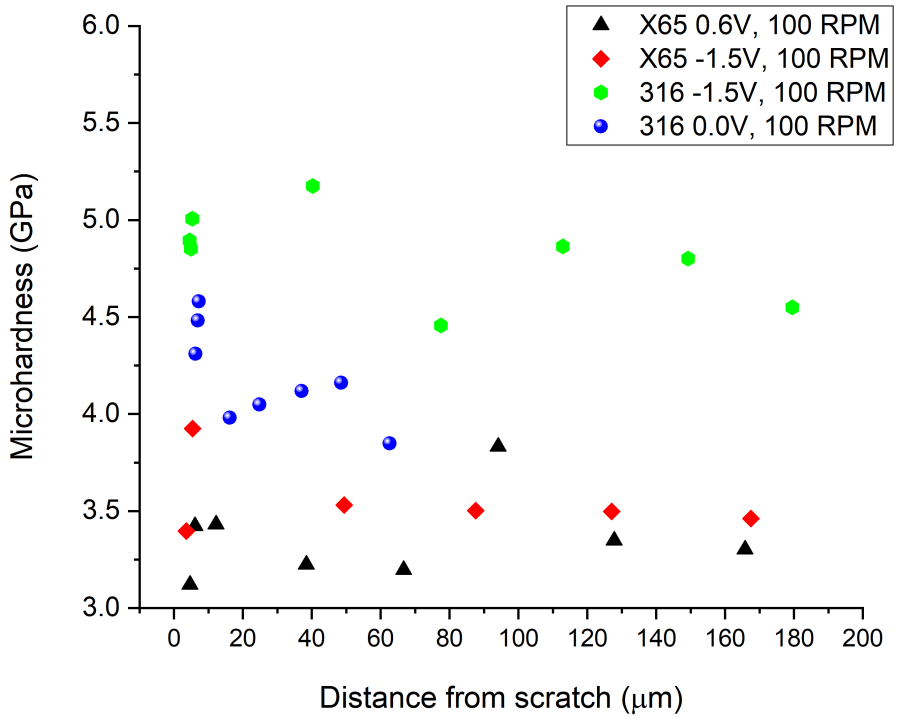


Figure 6.20: Microhardness of cross section of X65 carbon steel and 316 stainless steel samples continuously scratched at 100 $RPM$ *vs.* distance from the scratch.

*In-situ* microindentation experiments of X65 carbon steel suggest that a complex relationship exists between the work-hardening of this sample and material removal by scratching. X65 carbon steel repeatedly scratched under passive anodic potential at 100, 400 and 900 $RPM$ rotation rates revealed hardness that decreased away from the scratch interface, indicative of work hardened subsurface. However, the hardness values of these samples were lower than the bare sample hardness ($3.62 \pm 0.03\ GPa$). X65 carbon steel samples that were continuously scratched at 25, 50 and 100 $RPM$ under passive anodic potential had an average microhardness of $3.88 \pm 0.07\ GPa$, $3.54 \pm 0.03\ GPa$, and $3.36 \pm 0.07\ GPa$ respectively. For X65 carbon steel samples scratched under cathodic protection at 50 and 100 $RPM$, the average hardness was

equal to $3.86 \pm 0.07\ GPa$ and $3.56 \pm 0.06\ GPa$ respectively. It is apparent that the hardness decreased with increasing rotation rates, possibly due to an increased removal of the work hardened material at higher strain rates. Additionally, the average hardness of the X65 carbon steel scratched at the same rotation rate is higher for samples under cathodic protection compared to the passive anodic potential. To our knowledge, this is the first study when the cross section hardness of X65 carbon steel subject to pure erosion and erosion-corrosion was compared. However, it was shown in Lu and Luo's work that *in-situ* hardness degradation was recorded in various metals and steels subject to anodic polarisation. These tests involved galvanostatically polarising the electrode and immersing a hardness indenter into the solution. 200 $g$ load was applied on a variety of carbon steels [12], while nano-indentation experiments were done at a maximum 1.2 $mN$ load to assess bare hardness of pure iron [8]. The indentation tests under applied anodic current confirmed the relationship shown in Equation 6.5. While confirming an important connection between surface degradation and an anodic current, the main disadvantage of these studies was that the hardness of the samples subject to erosion-corrosion tests was not evaluated. Rather hardness degradation of the fresh samples immersed into a corrosive solution was identified. This degradation due to the electrochemical component can be defined as part of the corrosion-enhanced erosion.

$$\frac{\Delta H_v}{H_v} = -B\frac{i_A}{i_{th}} \tag{6.5}$$

where $\Delta H_v < 0$ is the reduction of hardness due to anodic current, $H_v$ is the hardness in a non-corrosive environment, $i_A$ is applied anodic current density, $i_{th}$ is the threshold current density that causes surface degradation, and $B$ is the constant encompassing the activation volume of dislocations and the test environment.

Unfortunately the bare surface hardness of 316 stainless steel was not measured in the present study using microindentation. However, there are some data on the microhardness of 304 stainless steel, which is quite similar to 316 stainless steel in composition and microstructure. 316 stainless steel contains more Ni and has added Mo for improved corrosion resistance and stabilization of the austenitic phase [13]. Wang and Li reported the microhardness at 50 $mN$ applied load of as received 304 stainless steel to be equal to 249.2 $H_v$ (2.44 $GPa$) [14]. Sasaki and Burstein reported the value to be 270 $H_v$ (2.65 $GPa$) [15]. The hardness of 316 stainless steel samples measured using a Vickers indenter at 1 $kg$ load in 10 $s$ resulted in 252 $H_v$ (2.47 $GPa$). The microhardness values of the 316 stainless steel samples measured in this study after the pure erosion and erosion-corrosion experiments exceeds these values. The aver-

age microhardness of the 316 stainless steel samples scratched at passive potential at 25, 50 and 100 $RPM$ was equal to $3.33 \pm 0.06$ $GPa$, $4.00 \pm 0.12$ $GPa$ and $4.19 \pm 0.08$ $GPa$ respectively. For samples under cathodic protection the average hardness was equal to $4.75 \pm 0.13$ $GPa$, $4.82 \pm 0.18$ $GPa$ and $4.83 \pm 0.08$ $GPa$ respectively. The author appreciates that overestimation of the hardness might have resulted due the nature of the microindentation method (ISE, elastic recovery, surface preparation mentioned earlier). Nevertheless, the results are deemed acceptable for qualitative comparison of the samples subject to erosion-corrosion. In addition to subsurface work hardening discussed above, these results suggest the following observations:

- Continuously scratching 316 stainless steel 100 times under both passive anodic and cathodic potentials resulted in much higher microhardness values compared to the bare surface hardness of 304 stainless steel [14, 15];
- The average hardness of 316 stainless steel samples scratched under passive anodic conditions is lower compared to the samples that were under cathodic protection. The hardness values increase with increasing rotation rates.
- Cathodically protected samples have similar average hardness values across all rotation rates.

These results suggest that 316 stainless steel samples underwent work hardening. Wang and Li [14] reported a considerable increase of the surface hardness of 304 stainless steel after sandblasting as determined by micro-indentation at 100 $mN$. In Figure 6.21 the maximum displacement depth is smaller for samples with sandblasted surface, suggesting larger resistance to deformation, hence higher hardness. Sandblasting was achieved *via* blasting the metal surface with 50-70 mesh silica particles for 10 $min$ at 200 $kPa$, which is similar to a dry erosion process. Hardness improvement was explained by the presence of the nanocrystalline surface and numerous dislocations.

Significant strain hardening in the plastic zone was measured after solid erosion at 129 $m\ s^{-1}$ of 316 stainless steel in Sundararajan's work [16]. Eroded samples were sectioned perpendicular to the eroded surface, similar to the present study. The microhardness values measured at 50 $g$ load decreased as a function of increasing distance from the eroded surface. The increase of hardness values due to scratching was reported in a few other studies too. Exponential increase of hardness with erosion test duration was reported [15, 17]. However, Sasaki and Burstein reported that after erosion-corrosion by 13.2 $wt.\%$ slurry in 0.6 $M$ NaCl solution the pitting potential, *i.e.* the potential at which pits become stable, decreased. This shows that while

increasing the hardness, erosion-corrosion caused an undesirable effect of pitting susceptibility in 304 stainless steel.

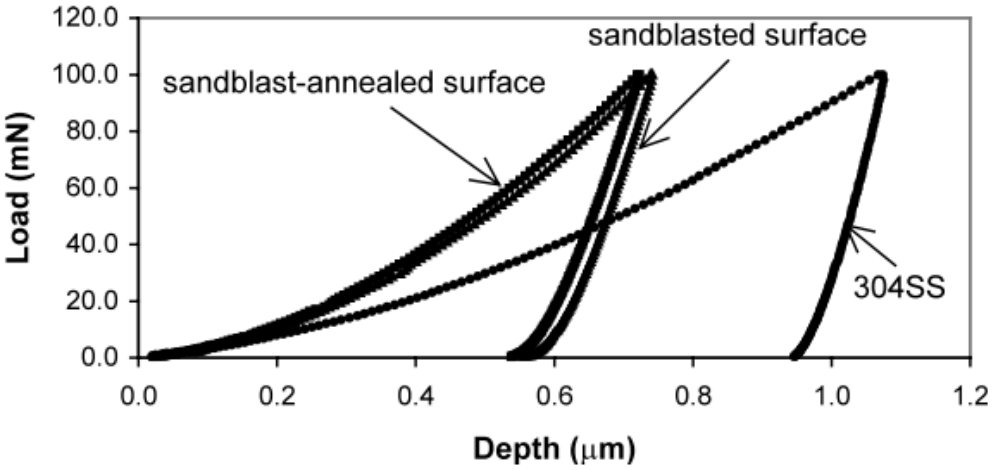


Figure 6.21: Load-displacement curves of as-received, sandblasted and sandblast-annealed 304 stainless steel samples. Reprinted from Wang and Li [14] with permission. Copyright (2002) Elsevier Science Ltd.

As was shown in Chapter 5, the degradation rate caused by total erosion-corrosion was higher than that of pure erosion rate (Figure 5.22). Rajahram *et al.* [18] showed increasing synergy of 316 stainless steel in aggressive solutions during erosion-corrosion experiments using a slurry pot erosion tester. In another experiment the same group reported reduced work hardening of 316 stainless steel samples under erosion-corrosion conditions with formation of lips at the impact crater edges that were susceptible to enhanced dissolution [19]. Adler and Walter [20, 21] concluded that for a single scratch experiments using a similar electrode scratching technique as in the present study, there was *no* dependence of wear volumes on applied potential. It should be noted that researchers used 2D surface profilometers and the error associated with this estimation is higher compared to 3D WLI used in this study. Moreover, in the present work, multiple scratches at the same place increase the degree of work hardening, hence 100 scratches at the same point are more likely to show a measurable difference.

To sum up, microstructural changes happening due to multiple scratching, including hardness variations, *and* the electrochemical conditions strongly impact the total material degradation rate. The next section will explore microstructural refinement taking place due to pure erosion and erosion-corrosion due to scratching using TEM.

### 6.3.3 TEM observations

This subsection presents the microstructural analysis of X65 carbon steel and 316 stainless steel samples using TEM. First, the results of X65 carbon steel are presented in order of a bare sample, the samples repeatedly scratched at 30 $RPM$, 400 $RPM$ and 900 $RPM$ at applied potential of 0.6 $V vs.$ MSE, followed by the samples continuously scratched at 100 $RPM$ at applied potentials of -1.5 V and 0.6 $V vs.$ MSE. Then, the TEM characterisation of 316 stain less steel samples continuously scratched at 100 $RPM$ at applied potentials of -1.5 V and 0.0 $V vs.$ MSE is presented.

#### X65 carbon steel

Undeformed sample

As mentioned in Chapter 4, X65 carbon steel has lower bainitic microstructure (See Figure 4.1). Bainite consists of a non-lamellar mixture of ferrite and carbides. The difference between the lower and upper bainite results from the transformation temperature. Lower bainite is obtained at lower temperatures, which results in lower bainite having precipitates both between and inside ferrite grains [22]. Figure 6.22a shows the bright field TEM image of an unscratched X65 carbon steel. A SAED pattern was obtained from this region and is presented in Figure 6.22b. This SAED pattern corresponds to that of $\alpha$-ferrite along [001] zone axis. The d-spacing was measured using TEM plugin of Fiji image processing software [1]. The measured d-spacing is 2.065 $\mathring{A}$ and is originating from {110} planes.

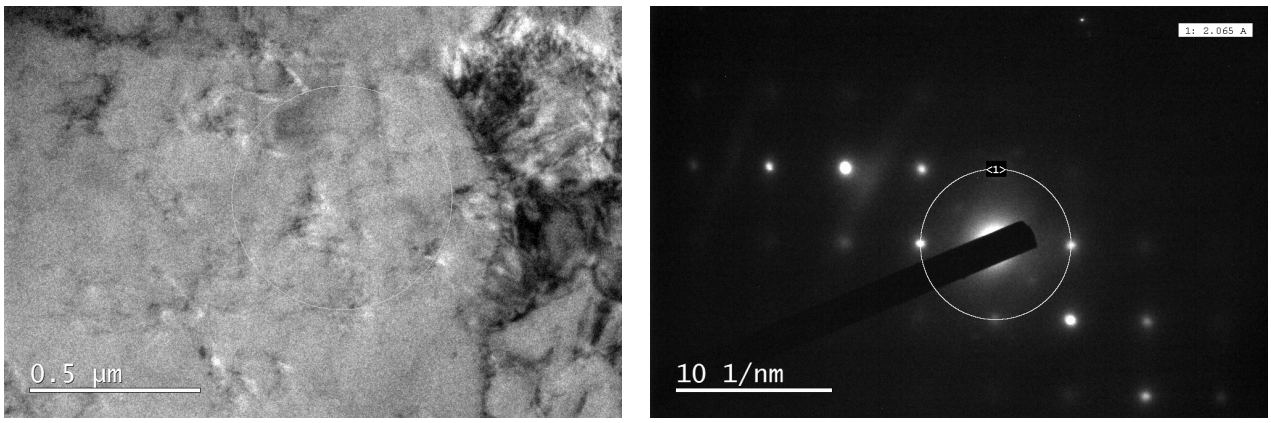


(a) (b)

Figure 6.22: a) A TEM bright field image of an undeformed X65 carbon steel sample showing the ferrite grain and b) SAED pattern recorded from the circled location.

Carbide precipitates are present both between and inside the ferrite grains in lower bainite. Figure 6.23a presents the bright field TEM image of unscratched X65 carbon steel with the precipitate visible in the middle of the micrograph. Figure 6.23b shows the SAED pattern recorded from the circled area in Figure 6.23a.

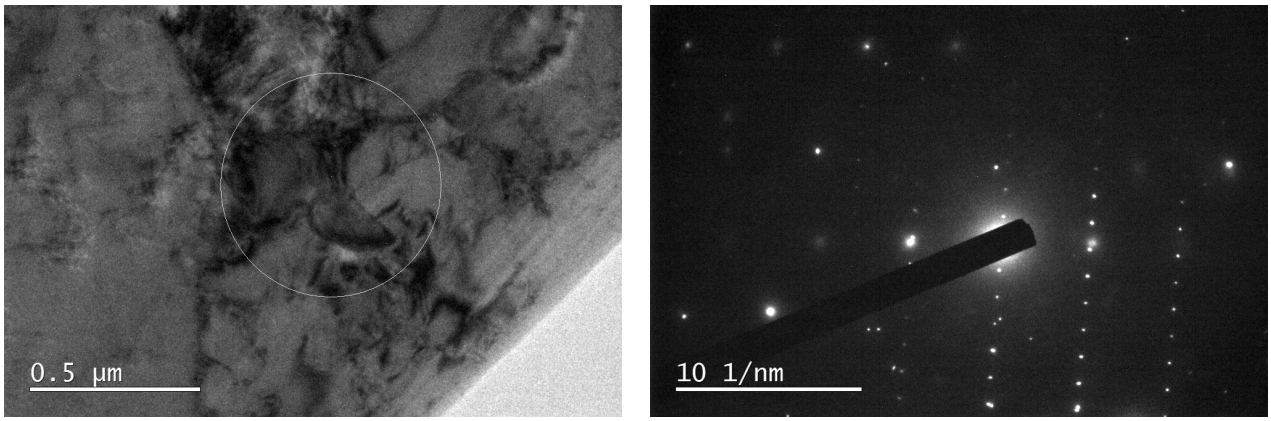


(a) (b)

Figure 6.23: a) A bright field TEM image of undeformed X65 carbon steel sample showing the precipitate and b) a SAED pattern recorded from the circled location.

Scanning Transmission Electron Microscopy (STEM) was carried out on an unscratched X65 carbon steel sample to show the ferrite grains and the carbide precipitates characteristic of lower bainitic microstructure. The contrast in STEM DF images, specifically the ones captured with an annular dark field detector originates mostly from the diffraction contrast and some mass-thickness contrast [23]. Figure 6.24 presents the STEM DF micrograph of the X65 carbon steel sample. The ferrite grains as well as the small carbide precipitates within and on the grain boundaries can be seen. An EDS map collected over the precipitates revealed an increased Mn, Cr and C signal indicating that these could be $M_xC_y$ particles, where M = Mn, Cr (see Figure 6.24).

Line spectrum EDS analysis was carried out at points shown in Figure 6.26. The chemical composition of the spectra in *wt.* % is presented in Table 6.1. Note that a Cu signal is recorded mostly from the TEM sample holder and a Ga signal is from the ion implantation due to FIB milling. The original sample only contained a small amount of Cu and did not have any Ga or Au, the chemical composition of the X65 carbon steel was recalculated by removing these elements in Table 6.2. The line spectrum 3 that was collected over the precipitate shows higher C and Mn signal compared to other spectra.

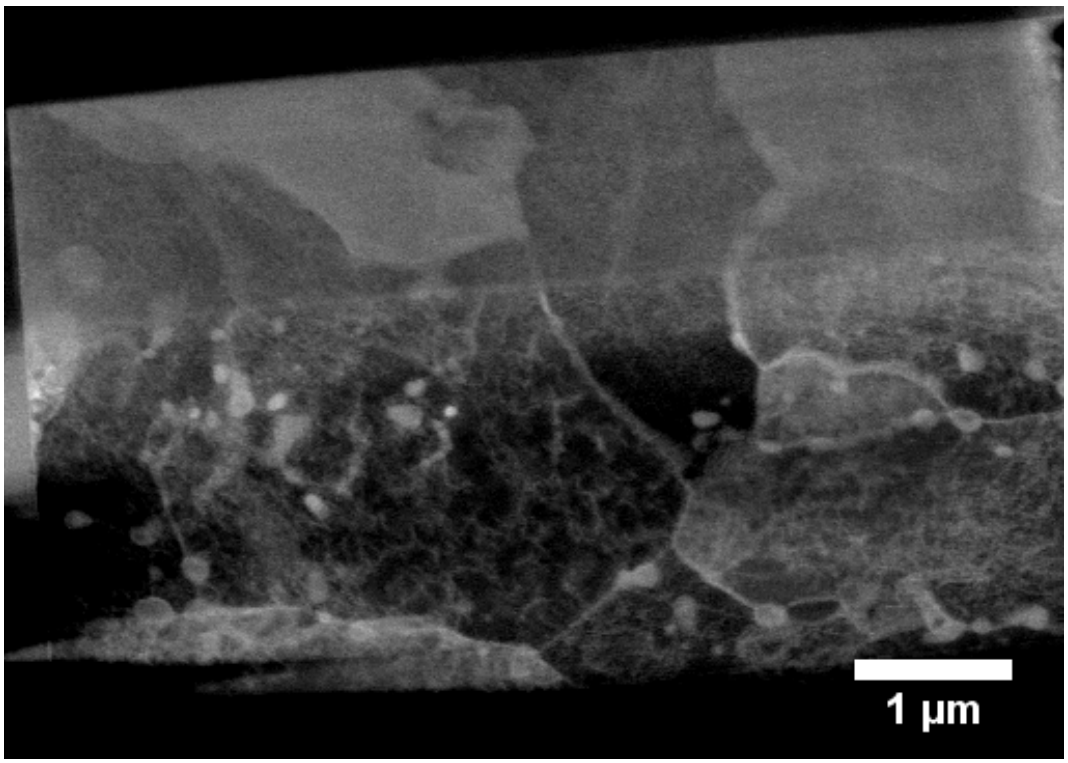


Figure 6.24: STEM DF image of the lamella lifted out from undeformed X65 carbon steel sample. Grain boundaries and precipitates appear bright on DF image.

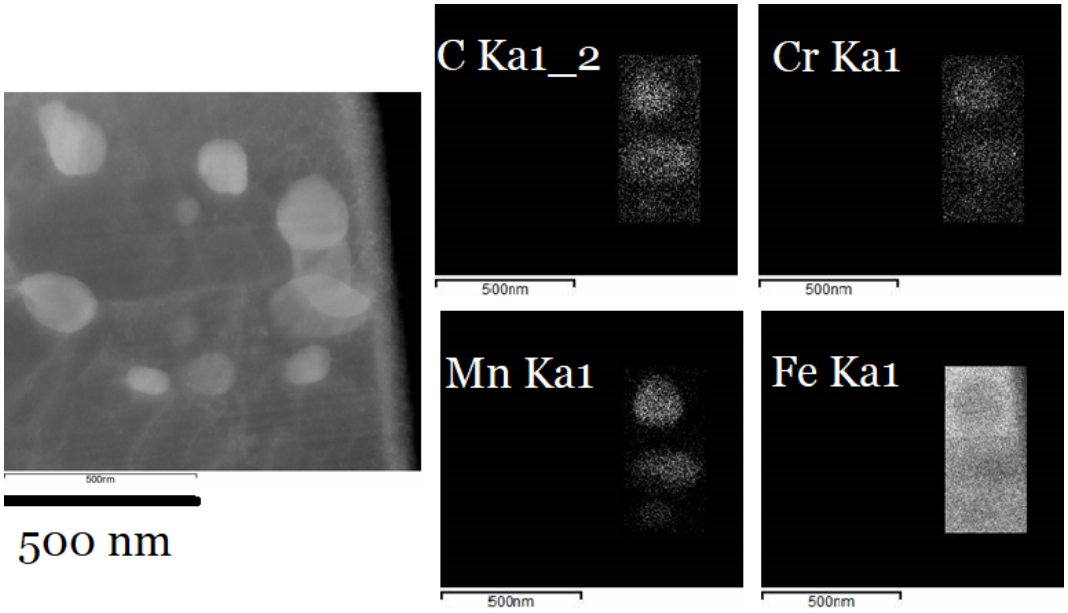


Figure 6.25: STEM BF image and EDX map over the precipitates.

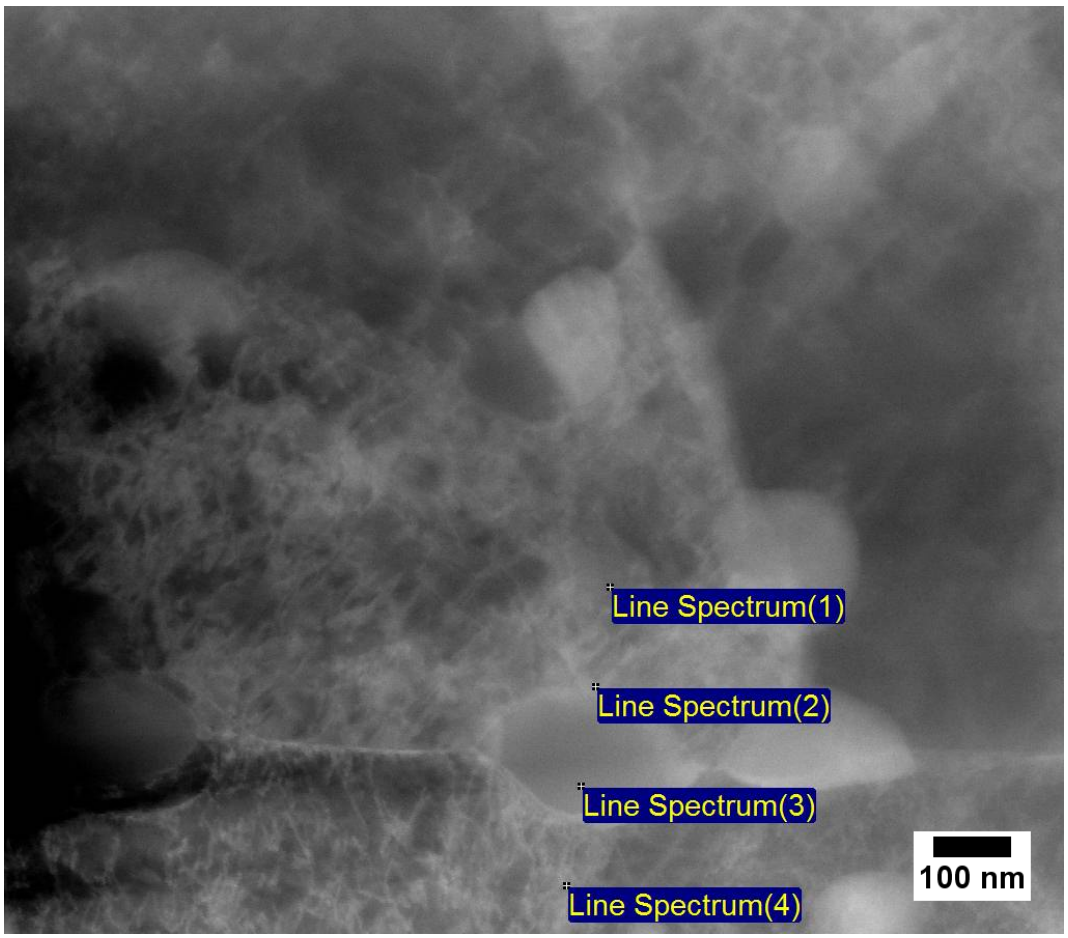


Figure 6.26: STEM DF image showing the location of the line spectra.

Table 6.1: EDS analysis of undeformed X65 carbon steel sample. All results are in *wt*. %.

| Spectrum | C | Si | V | Cr | Mn | Fe | Cu | Ga | Au | Total |
|---|---|---|---|---|---|---|---|---|---|---|
| Line Spectrum(1) | 1.0 | 0.4 | | 0.8 | 2.2 | 83.6 | 11.2 | 0.2 | 0.6 | 100.0 |
| Line Spectrum(2) | 1.2 | 0.4 | 0.2 | 0.9 | 2.9 | 82.8 | 10.8 | 0.1 | 0.7 | 100.0 |
| Line Spectrum(3) | 4.1 | 0.1 | 0.1 | 0.7 | 3.2 | 80.4 | 10.5 | | 0.9 | 100.0 |
| Line Spectrum(4) | 0.4 | 0.5 | | 0.4 | 0.5 | 87.2 | 10.3 | | 0.7 | 100.0 |

Table 6.2: EDS analysis of undeformed X65 carbon steel sample with Cu, Ga and Au signals removed. All results are shown in *wt*. %.

| Spectrum | C | Si | V | Cr | Mn | Fe | Total |
|---|---|---|---|---|---|---|---|
| Line Spectrum(1) | 1.1 | 0.5 | | 0.9 | 2.5 | 95.0 | 100.0 |
| Line Spectrum(2) | 1.3 | 0.4 | 0.2 | 1.1 | 3.3 | 93.7 | 100.0 |
| Line Spectrum(3) | 4.6 | 0.2 | 0.1 | 0.8 | 3.6 | 90.7 | 100.0 |
| Line Spectrum(4) | 0.5 | 0.5 | | 0.4 | 0.6 | 98.0 | 100.0 |

Repeatedly scratched samples

*30 RPM 0.6 V vs. MSE*

To understand the influence of erosion-corrosion on the microstructure of X65 carbon steel, samples scratched at 0.6 $V vs.$ MSE were studied using TEM.

Figure 6.27a presents a secondary electron SEM image of the X65 carbon steel repeatedly scratched 3 times at 30 $RPM$ in pH 4.0 KHP solution under an applied potential of 0.6 $V vs.$ MSE. The micrograph shows the TEM lamella taken across the scratch inside the trench. Figure 6.27b shows the lamella after the completion of thinning. A shiny appearance of the lamella is a good indication of the electron transparency of the sample due to increased efficiency of the secondary electrons collection from the thin sample.

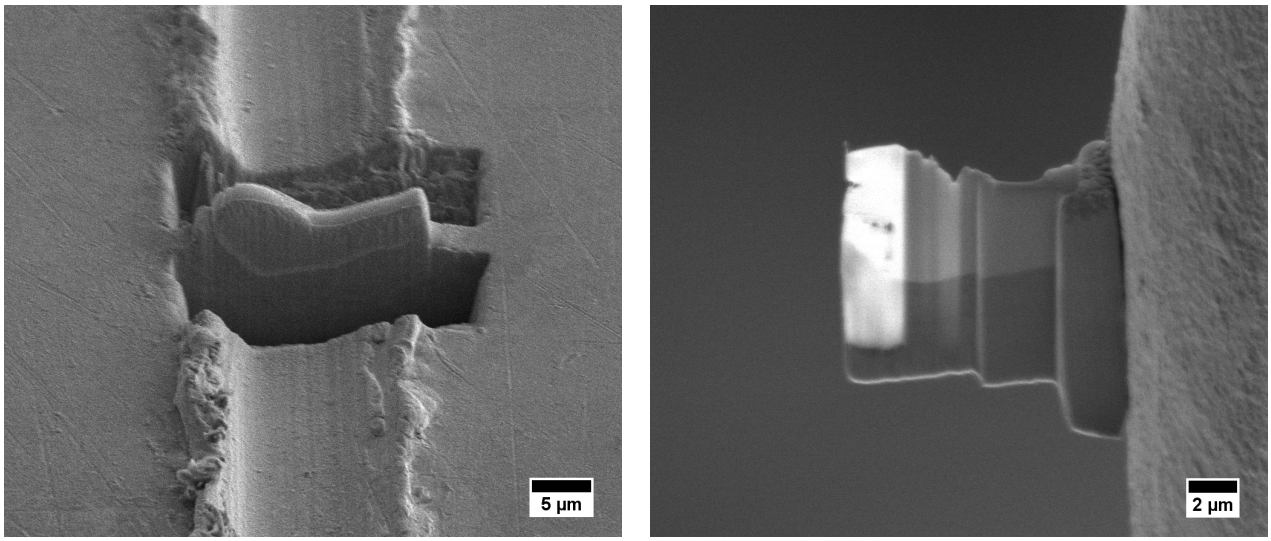


(a) (b)

Figure 6.27: SEM micrographs showing a) the location of the sample from where the TEM lamella was lifted out and b) the electron transparent lamella. This sample was lifted out and thinned by Dr Ecaterina Ware during FIB-SEM training.

Figure 6.28 is a bright field TEM micrograph of the lamella presented in Figure 6.27 above. The location of the Pt protective layer is labelled as 'Pt layer' on the micrograph, while 'metal' refers to the scratched X65 carbon steel. This lamella was lifted out from the same sample presented in Figure 6.9 earlier. Cross section analysis revealed grain refinement up to 3 $\mu m$ below the scratched surface and the formation of nano-sized lamellar grains. These lamellar grains can be clearly observed in Figure 6.28b. The size of the lamellar grains start from *ca.* 25 $nm$ and gradually increases to over 100 $nm$. It is believed that the size of the lamellae and the distance up to which they can be observed from the scratch surface depends on the material removal frequency, work hardening and the electrode rotation rate. Due to the size of these

nano-lamellae being comparable to the size of the carbide precipitates, it was hard to identify the precipitates within the region deformed due to erosion-corrosion. Only a few precipitates similar to those observed in the bare X65 carbon steel sample could be seen at the bottom of the TEM sample, *ca.* 4 $\mu m$ away from the surface.

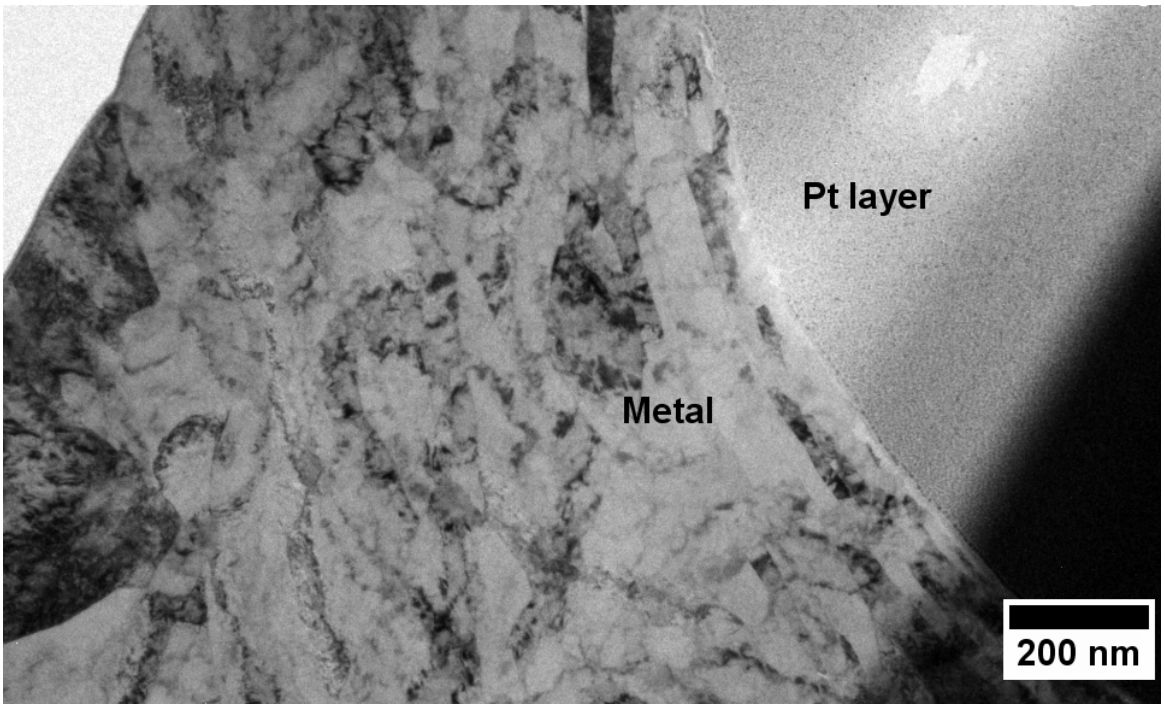


(a)

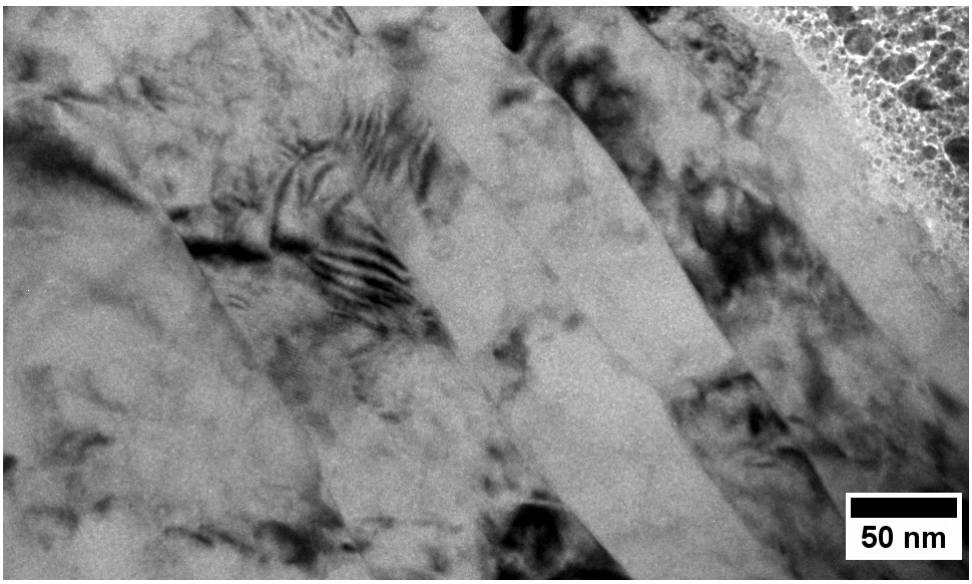


(b)

Figure 6.28: A bright field TEM images showing the X65 carbon steel sample scratched repeatedly 3 times in pH 4.0 KHP solution at applied potential of 0.6 $V$ *vs.* MSE and rotation rate of 30 $RPM$.

Selected area electron diffraction analysis was carried out at the locations indicated in Figure 6.29a. Closer to the scratched surface, grain refinement is evident from the polycrystalline electron diffraction pattern shown in Figure 6.29b. Diffraction spots closest to the central beam are similar to those originating from twinning. Twinning in bcc metals occurs when the material is strained at low temperatures or under high strain rates [24]. Further down the sample, away from the scratched region, the single crystal electron diffraction patterns were recorded and the planes were assigned as shown in Figures 6.29c and 6.29d. This confirms that grain size increases away from the surface subject to erosion-corrosion.

Grain refinement takes place in most erosion-corrosion tests, regardless of the setup used, including a submerged impinging jet using X65 carbon steel samples [4] and the slurry pot erosion tester using 316 stainless steel samples [19]. Owen *et al.* confirmed the grain size increased away from the surface using a FIB-SEM cross section analysis [4]. TEM micrographs of the samples presented in the present study can be used in erosion-corrosion models to predict asset lifetimes in industry.

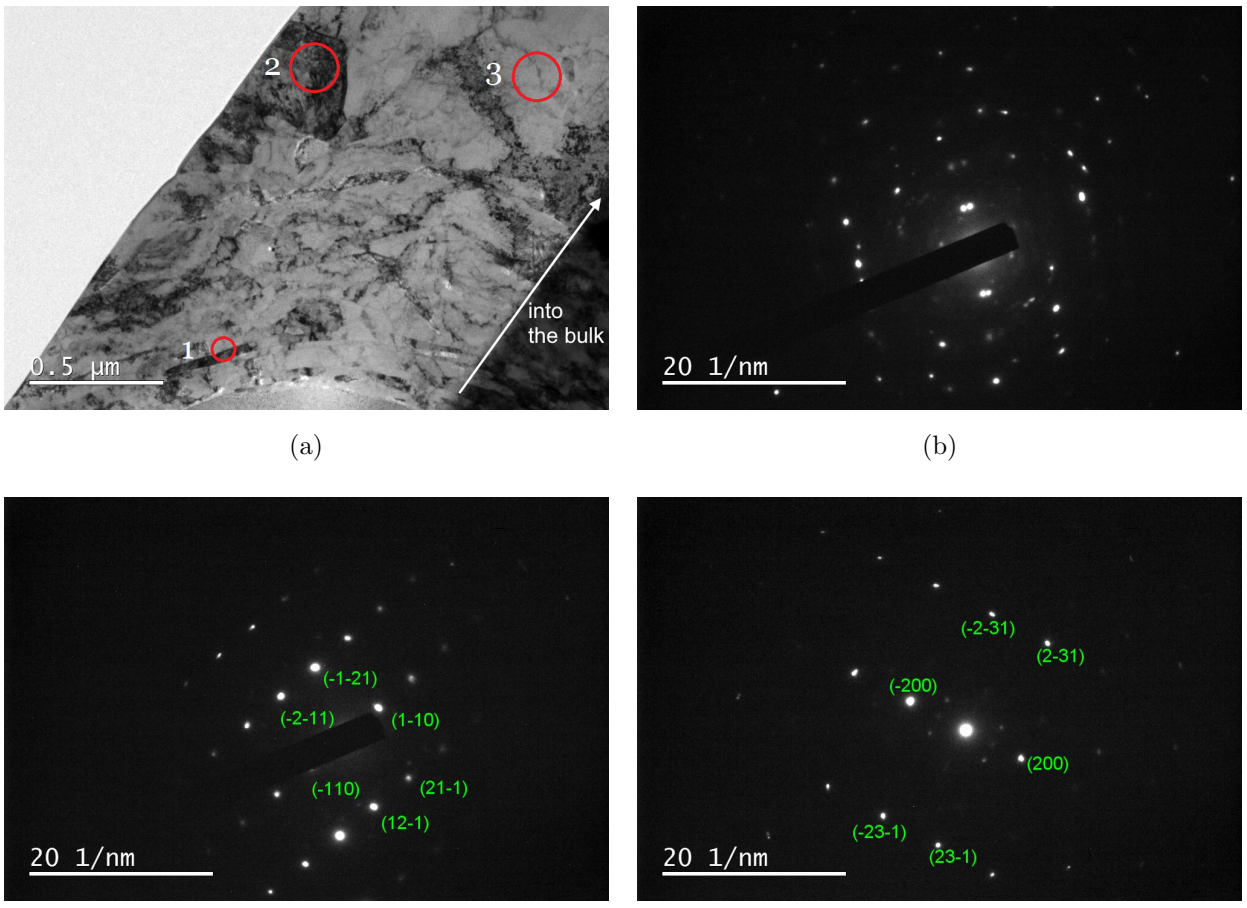


(a) (b)

(c) (d)

Figure 6.29: a) A bright field TEM image showing the specific locations used for the SAED, b) a SAED pattern from circle no.1, c) a SAED pattern from circle no.2, d) a SAED pattern from circle no.3.

Figure 6.30 presents the high angle annular dark field (HAADF) image of the X65 carbon steel sample scratched at 30 $RPM$. Although, HAADF imaging is normally used for enabling Z-contrast, the image resolution is quite high. Hence the deformation due to scratching can be observed in great detail.

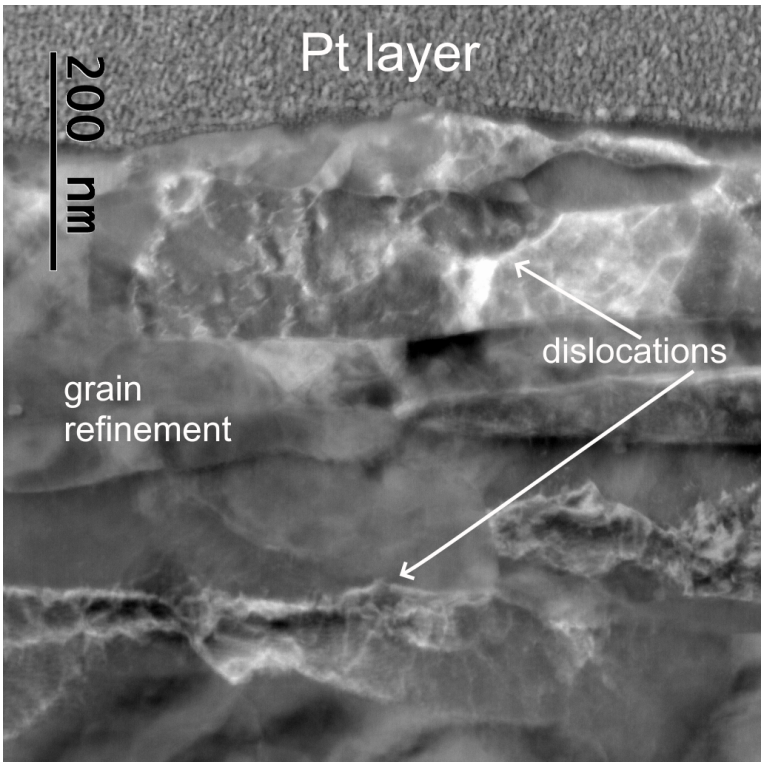


Figure 6.30: An STEM HAADF image highlighting the deformation and the grain refinement in the X65 carbon steel sample scratched repeatedly 3 times in pH 4.0 KHP solution at applied potential of 0.6 $V$ *vs.* MSE and rotation rate of 30 $RPM$.

Figure 6.31a presents the results of the EDS analysis carried out along the line indicated in Figure 6.31b. The chemical composition of the material based on $wt.$ % indicate that Pt-metal interface is enriched in O, Cr and is depleted in Fe. The O signal eventually levels off around 200 $nm$ away from the scratched surface. Cr-enrichment of the oxides on stainless steel is a known phenomena, and as indicated by EDS analysis in this study the enrichment also takes place in X65 carbon steel sample, which has less than 1% Cr by composition. The erosion-corrosion resistance was directly related to the Cr concentration owing to an increased corrosion resistance [5], similar to the results presented in Chapter 5, where X65 carbon steel had lower resistance to erosion-corrosion compared to 316 stainless steel. To identify whether small addition of Cr had an effect on overall erosion-corrosion rate, decoupling experiments similar to ones presented in this study can be carried out on low carbon steels containing varying content of chromium. Not only will the passivation behaviour be affected by the chromium content, but also it is believed that chromium enriched passivating films are thinner and more resistant to

mechanical deformation [25]. Hence, it an important observation that follows from this study and might be of interest for future research.

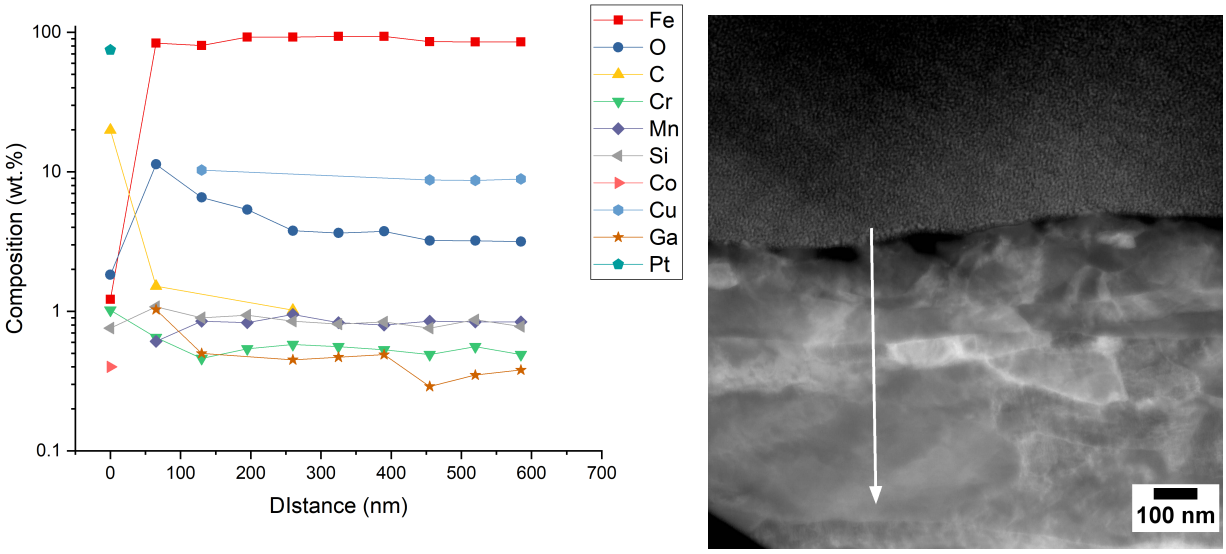


(a) (b)

Figure 6.31: a) An EDS analysis of X65 carbon steel that was repeatedly scratched 3 times at applied potential of 0.6 $V$ *vs.* MSE and rotation rate of 30 $RPM$ and b) STEM DF image showing the line along which the spectra was collected *ca.* every 65 $nm$.

### *400 RPM 0.6 V vs. MSE*

As the rotation rate of the electrode was increased to 400 $RPM$ and the surface was repeatedly scratched 100 times at a passive anodic potential, the depth of the scratch increased substantially. Due to this lamella could not be lifted across the scratch. Rather, it was lifted along the scratched direction as shown in Figure 6.32a. The X65 carbon steel sample scratched at 400 $RPM$ had lots of flakes and the lips were formed following the direction of the erodent, *i.e.* the scratching tip. The preferential dissolution of these lips is considered to be one of the factors contributing to the erosion-enhanced corrosion [19].

Similar to the X65 carbon steel scratched at 30 $RPM$, the sample scratched at 400 $RPM$ is characterised by grain refinement with formation of nano-sized lamellar grains. The Pt protective layer as well as the deformed metal are indicated in Figure 6.33. HAADF micrograph highlighting the lamellar grains is presented in Figure 6.34. The low magnification TEM micrograph in Figure 6.35 shows that the width of these lamellae, *i.e.* the size of the grains increases with the distance from the scratched surface. The decrease of the hardness away from the surface reported earlier in Figure 6.15 can be related to the apparent variation of the grain size observed.

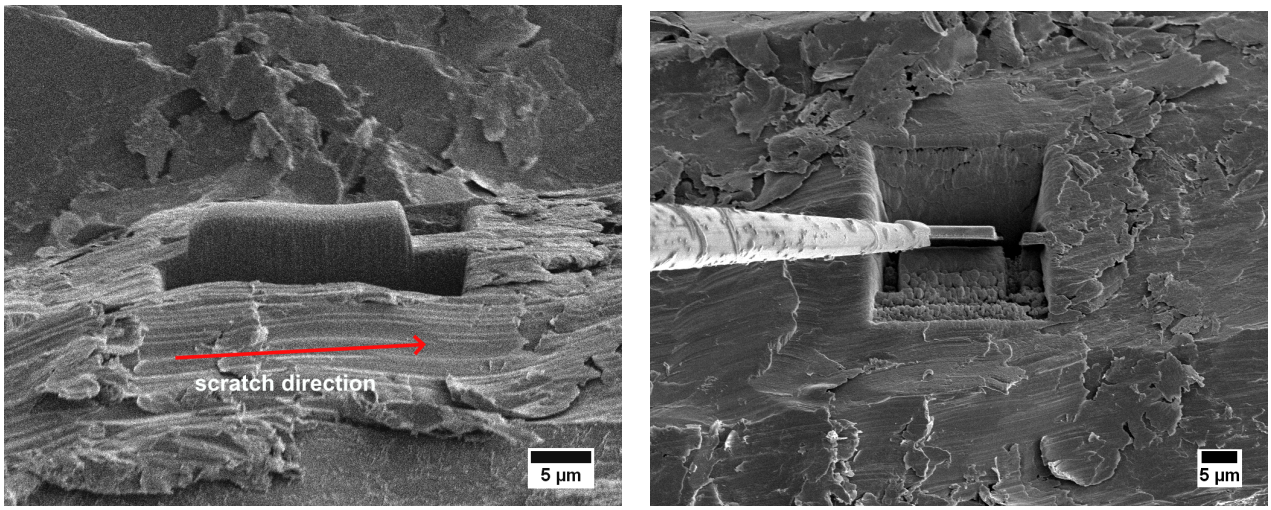


(a) (b)

Figure 6.32: SEM micrographs showing a) the location of the TEM lamella at stage tilt of 52° and b) the top view of the lamella attached to the Omniprobe micromanipulator. X65 carbon steel sample was repeatedly scratched 100 times at 400 $RPM$.

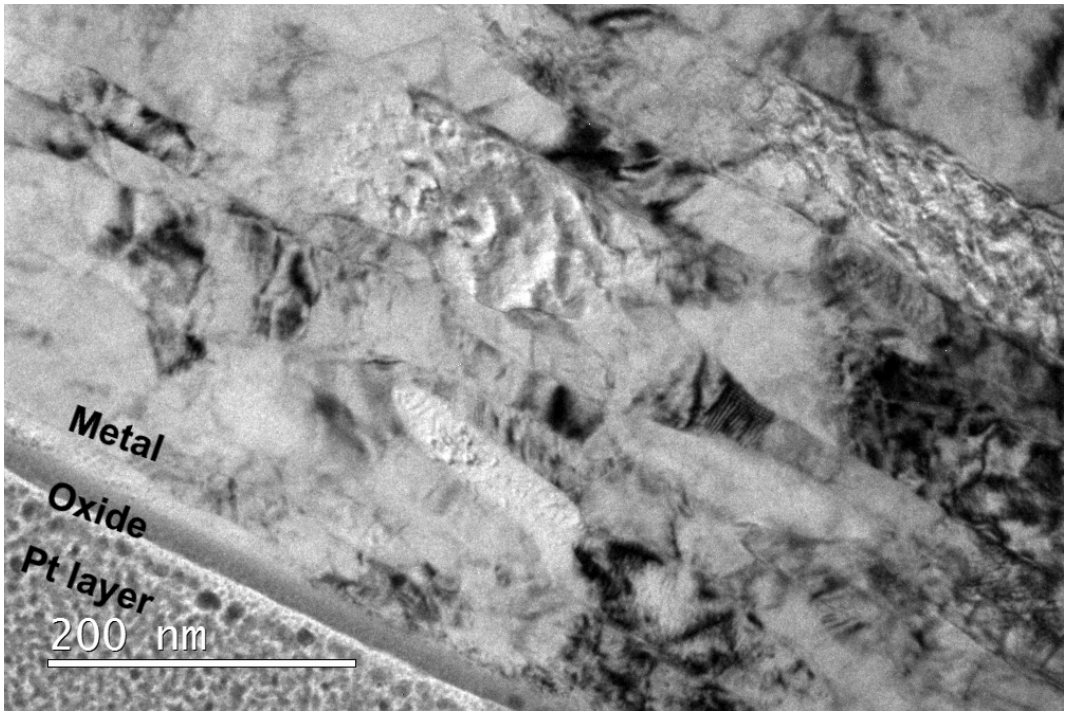


Figure 6.33: A bright field TEM micrograph showing the sample repeatedly scratched 100 times in pH 4.0 KHP solution at applied potential of 0.6 $V vs.$ MSE at rotation rate of 400 $RPM$.

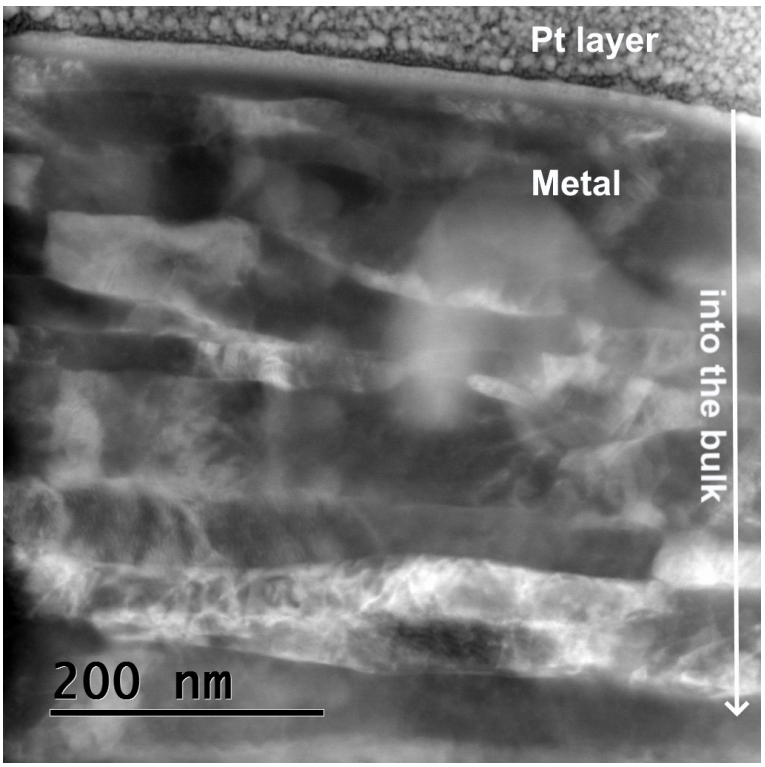


Figure 6.34: An STEM HAADF micrograph highlighting the deformation and formation of nano-sized lamellar grains in the viscinity of the scratched region.

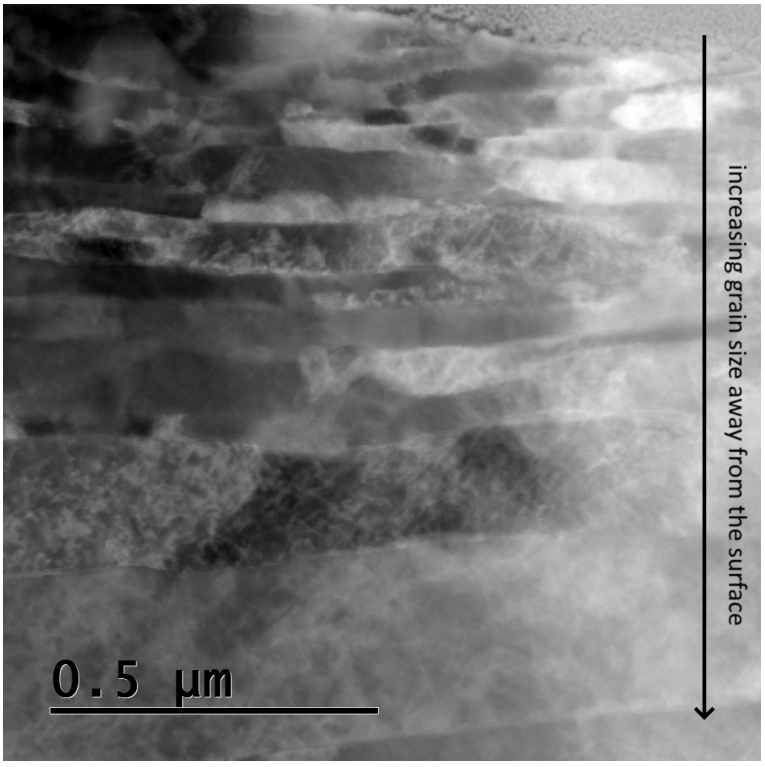


Figure 6.35: A low magnification STEM HAADF micrograph highlighting the change of grain size away from the Pt layer/scratch region.

*900 RPM 0.6 V vs. MSE*

It was quite challenging to lift out the lamella from X65 carbon steel sample scratched at 900 $RPM$. The material removal rate and the depth of the scratch increase with increasing rotation rate. *in-situ* lift out could not be performed across the scratch as the micromanipulator could not reach the lamella. To resolve this problem, the disc was carefully cut, using EDM, in half and the lamella was lifted out along the scratch.

Figure 6.36 presents the FIB micrographs of the X65 carbon steel cross sections along and perpendicular to the scratch. Both micrographs have distinct areas of grain refinement in the sample subsurface observable up to *ca.* 4 $\mu m$. The micrograph of the sample cross section taken along the scratch (Figure 6.36a) also shows grain orientation following the direction of the scratching within the milled region up to 11 $\mu m$. This is in agreement with Owen *et al.* who studied erosion-corrosion of X65 carbon steel in 2 $wt.\%$ NaCl, 1000 $mg\ L^{-1}$ sand particle aqueous solutions that were either $N_2$ or $CO_2$ saturated. FIB images of these samples are presented in Figure 6.37. Although the FIB cross-section images do correspond, it should be noted that while exploring the synergy of erosion-corrosion, the authors approximated experiments under $N_2$ flow as being pure erosion even though the solution contained significant amount of aggressive $Cl^-$ ions and so significant corrosion effects were likely not taken into account.

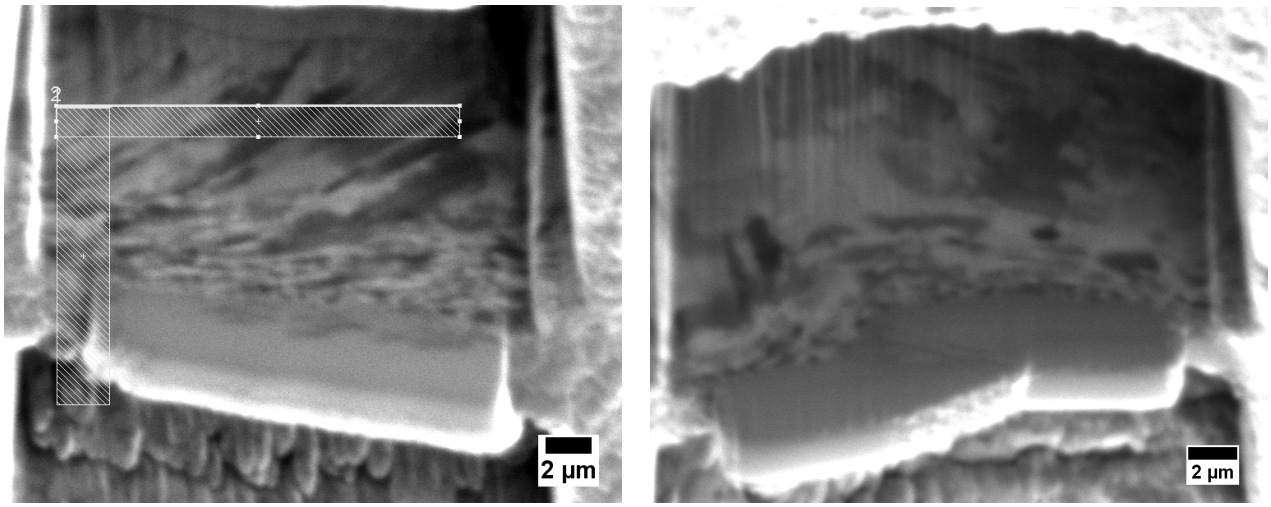


(a) (b)

Figure 6.36: FIB micrographs of the cross sections of X65 carbon steel samples scratched at 900 $RPM$ at applied potential of 0.6 $V vs.$ MSE in pH 4.0 KHP solution. a) Lamella lifted along the scratch and used for further TEM analysis. b) Cross section perpendicular to the scratch: this lamella could not be lifted out.

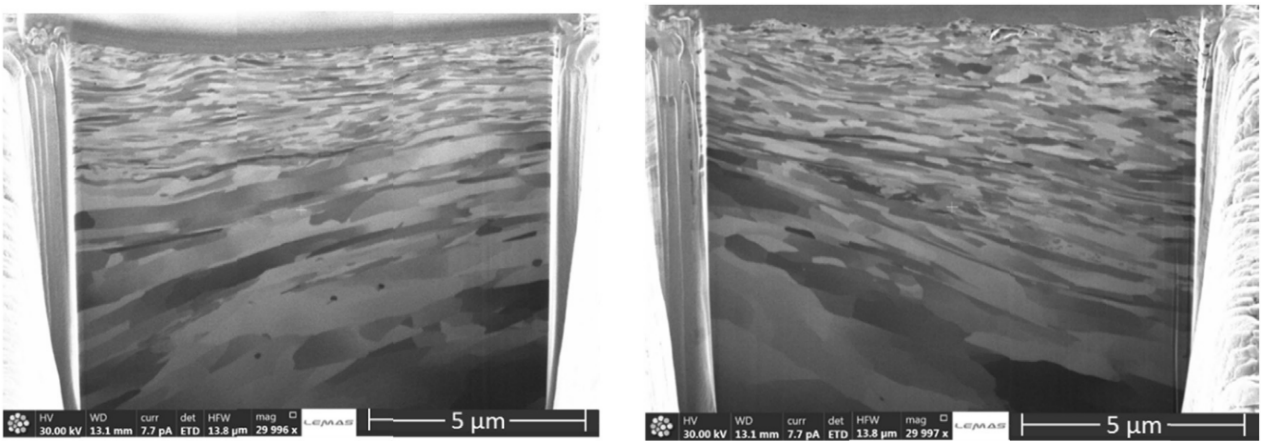


(a) (b)

Figure 6.37: FIB micrographs of X65 carbon steel cross sections after 30 minutes of a) erosion and b) erosion-corrosion tests using submerged jet impingement apparatus. Reprinted from Owen *et al.* [4] with permission. Copyright (2018) Elsevier B.V.

Figure 6.38 presents a bright field TEM micrograph of the X65 carbon steel sample repeatedly scratched 100 times at a rotation rate of 900 $RPM$ in pH 4.0 KHP solution at an applied potential of 0.6 $V$ *vs.* MSE. The image was stitched using a stitch plugin in Fiji image processing software [26]. A Pt protective layer and the X65 carbon steel are labelled on the micrograph. A bright layer between the Pt and the metal is the thick oxide layer formed due to EDM machining of the disc. A higher magnification image of the oxide is given in Figure 6.39a. The microstructural changes observed in the sample scratched at 900 $RPM$ are quite similar to the ones described above. Numerous nano-sized lamellar grains can be observed in the vicinity of the surface in Figure 6.39b. Typical strain induced deformation substructures including twins are observed too (Figure 6.40).

The EDS analysis of the sample was performed at 4 different locations at an increasing distance from the surface. The locations are presented and labelled 1–4 in Figure 6.41. The quantitative EDS results can be seen in Table 6.3. The considerable Zn signal recorded in spectrum 1 originates from the brass wire used in the electrical discharge machining used to cut the X65 carbon steel disc in half. It is also likely that EDM caused partial oxidation of the sample due to the presence of quite a thick oxide layer in the lamella, which was not observed in the samples presented previously.

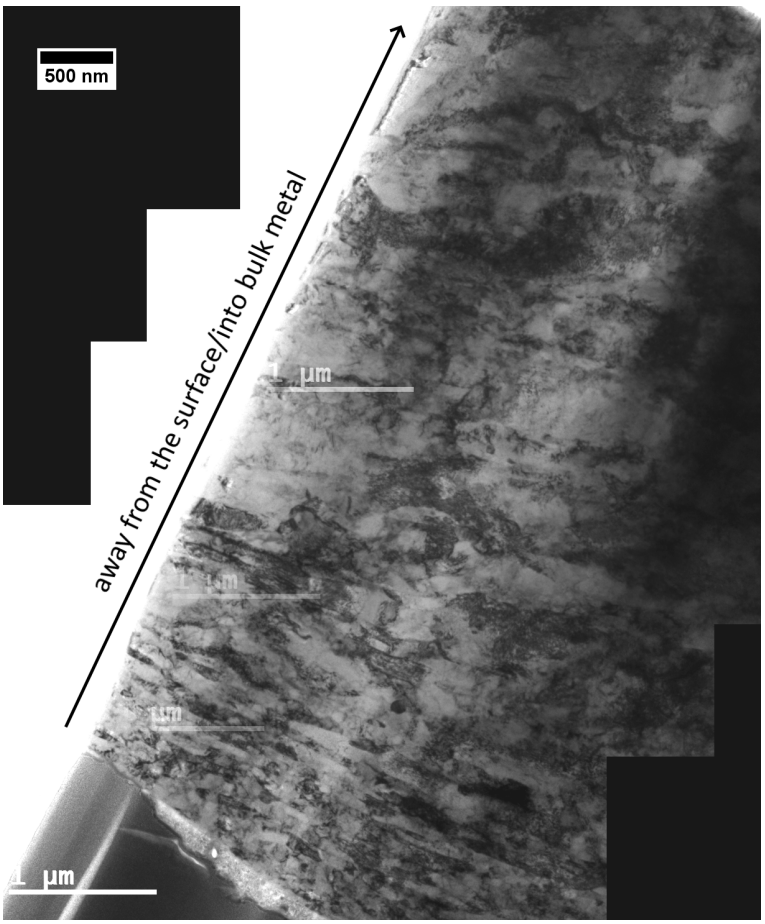


Figure 6.38: A low magnification BF TEM stitched image showing the extent of microstructural deformation in X65 carbon steel repeatedly scratched 100 times at 900 $RPM$.

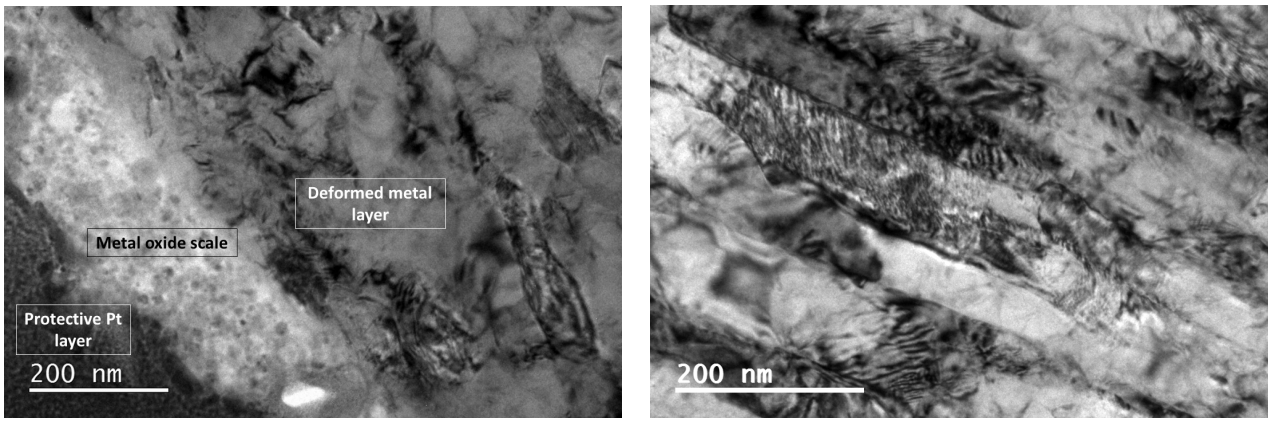


(a) (b)

Figure 6.39: A High magnification BF TEM micrographs showing a) the Pt-oxide-metal interface and b) the grain refinement occurring due to erosion-corrosion of the X65 carbon steel repeatedly scratched 100 times at 900 $RPM$.

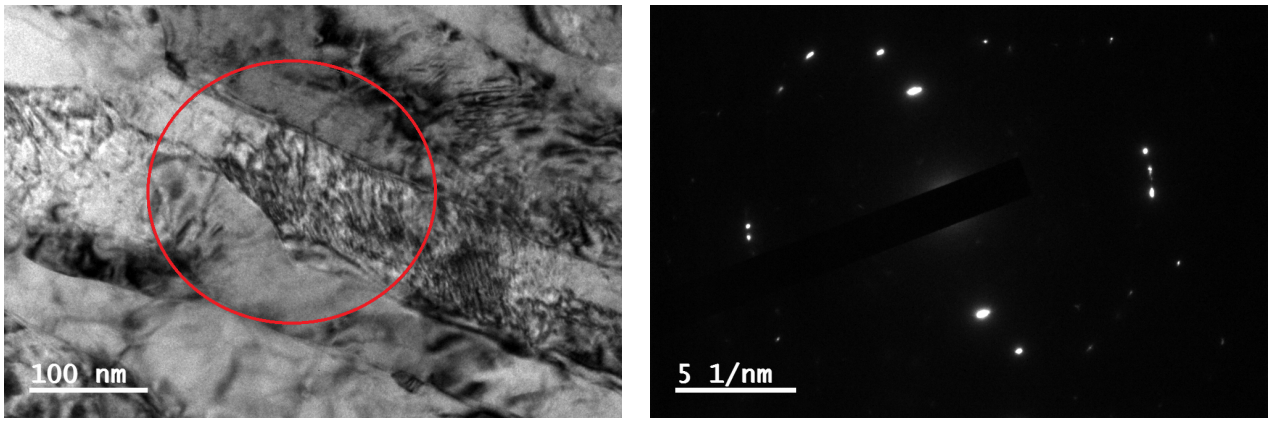


(a) (b)

Figure 6.40: a) A bright field TEM image showing nano-lamellar grains formed during repeated scratching at 900 $RPM$, b) the SAED pattern originating from that location, which indicates the presence of twinning.

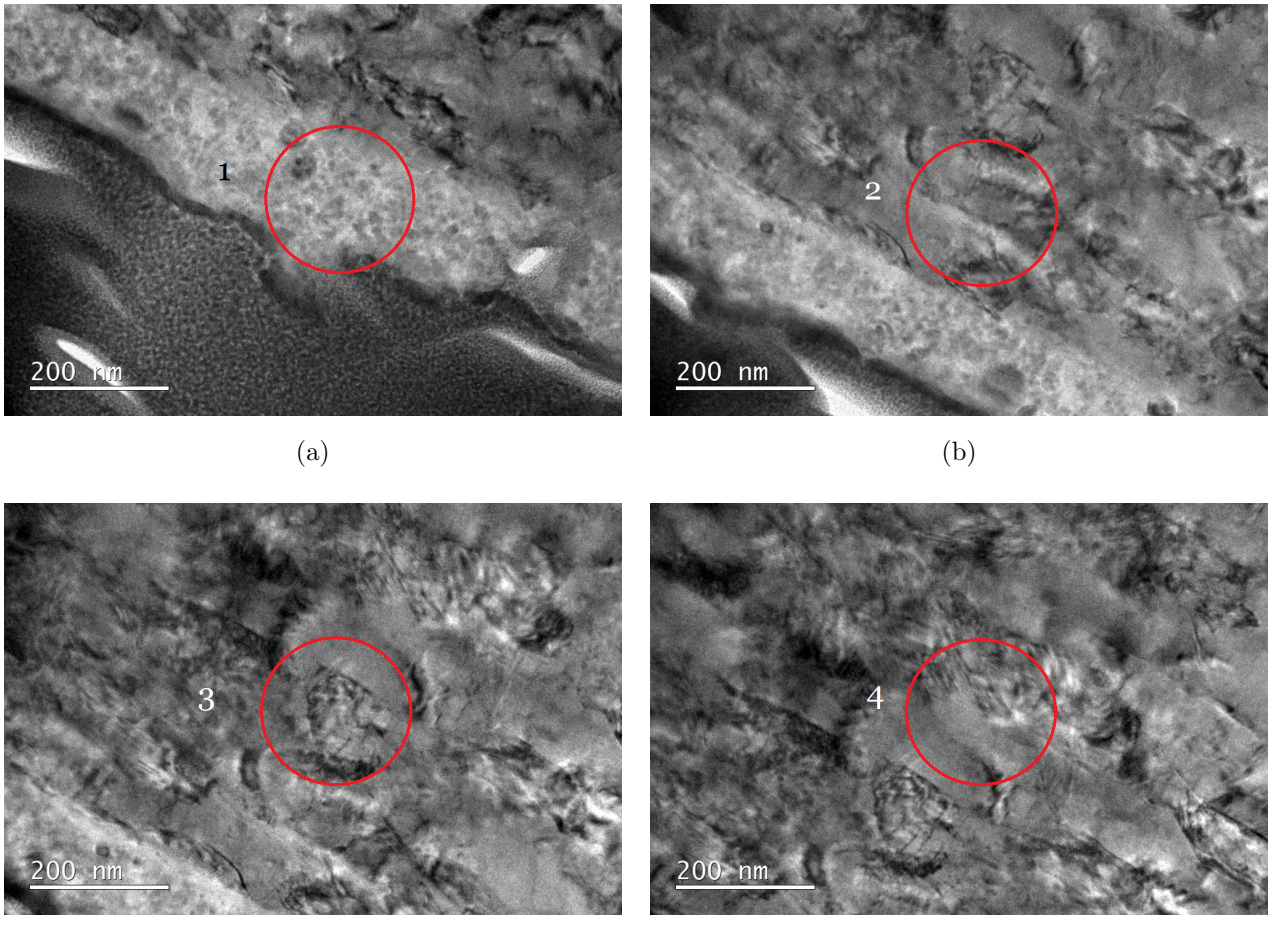


(a) (b)

(c) (d)

Figure 6.41: BF TEM images indicating the locations of EDS spectra presented in Table 6.3.

Table 6.3: An EDS analysis of the X65 carbon steel repeatedly scratched 100 times at 900 $RPM$. All results are in $wt.\%$.

| Spectrum | C | O | Si | Cr | Mn | Fe | Zn (EDM) | Ga | Pt |
|---|---|---|---|---|---|---|---|---|---|
| Spectrum 1 | 9.55 | 24.76 | 0.90 | 0.40 | 0.44 | 42.82 | 6.03 | 3.78 | 11.33 |
| Spectrum 2 | 1.77 | 5.97 | 0.93 | 0.46 | 0.83 | 89.63 | - | 0.41 | - |
| Spectrum 3 | 0.79 | 2.39 | 0.53 | 0.45 | 0.98 | 94.86 | - | - | - |
| Spectrum 4 | 1.90 | 2.32 | 0.61 | 0.47 | 0.92 | 93.78 | - | - | - |

Continuously scratched samples

*100 RPM -1.5V vs. MSE*

Continuously scratched X65 carbon steel samples were also studied using TEM analysis. Two samples scratched at 100 $RPM$ were chosen for TEM analysis: one scratched under a cathodic protection potential of -1.5 $V$ *vs.* MSE, another scratched under a passive anodic potential of 0.6 $V$ *vs.* MSE. Both samples were scratched 100 times at exactly the same location in pH 4.0 KHP solutions.

Figure 6.42 shows the location of the lamella that was lifted out from a X65 carbon steel sample scratched at -1.5 $V$ *vs.* MSE. Due to the smaller scratching depth formed at 100 $RPM$ compared to 400 and 900 $RPM$, the lamella could be lifted out across the scratch. A low magnification bright field TEM micrograph of this lamella is given in Figure 6.43. The Pt protective layer can be seen on the lower left hand side of the micrograph, with deformed metal located adjacent to it. Due to the lamella from this sample being quite thick, grain refinement was not observed. This could also happen due to less deformation taking place under cathodic protection, and a TEM analysis of additional cathodically protected samples are needed to confirm this. Nevertheless, the SAED pattern taken from a circular area with *ca.* 150 $nm$ radius adjacent to the surface shows a polycrystalline behaviour, albeit with fewer diffraction spots, as seen in Figure 6.44. Diffraction spots origianted from {110}, {002} and {121} bcc planes corresponding to measured interplanar spacings of 2.031 $\AA$, 1.454 $\AA$, 1.171 $\AA$ of $\alpha$-ferrite respectively.

Similar to the samples scratched under passive anodic conditions, strain induced deformation can be observed in the sample scratched under cathodic protection in Figure 6.45. EDS mapping was performed at the interface between high contrast areas labelled 'metal'. The exact location of the spectrum and the chemical maps collected for 30 minutes are presented in Figure 6.46. Increased O signal suggests that the bright stripe seen adjacent to the Pt protective layer in

Figure 6.45 is an iron oxide layer. Since this X65 carbon steel sample was under cathodic protection the oxide layer most probably formed after the potential was released and during sample immersion.

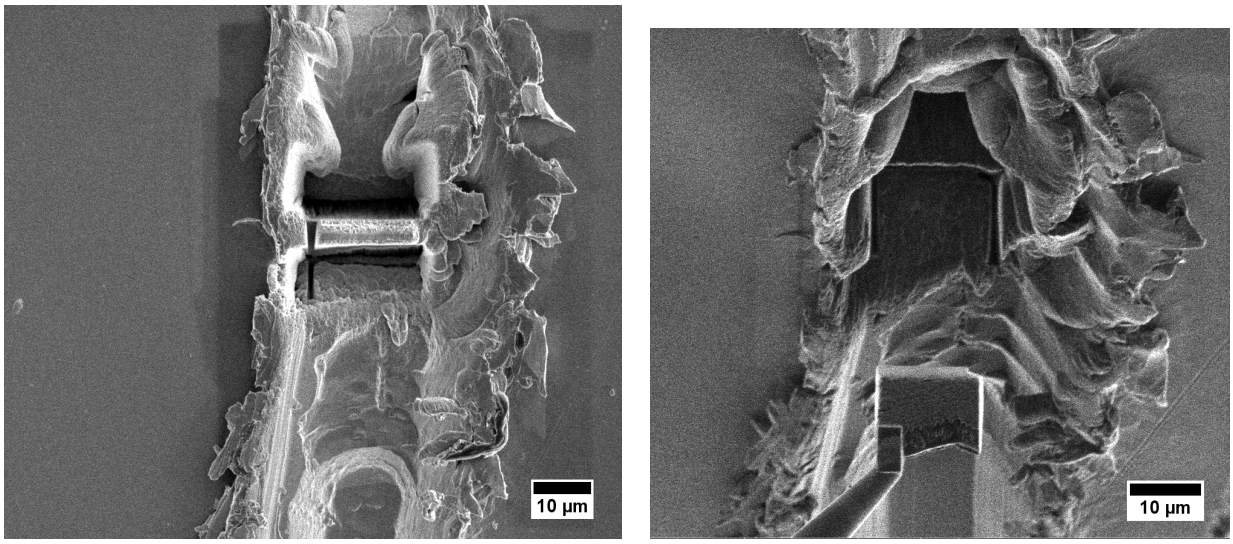


(a) (b)

Figure 6.42: a) An SEM micrograph showing the location of the lamella used for the TEM analysis and b) FIB micrograph showing the moment of *in-situ* lift out.

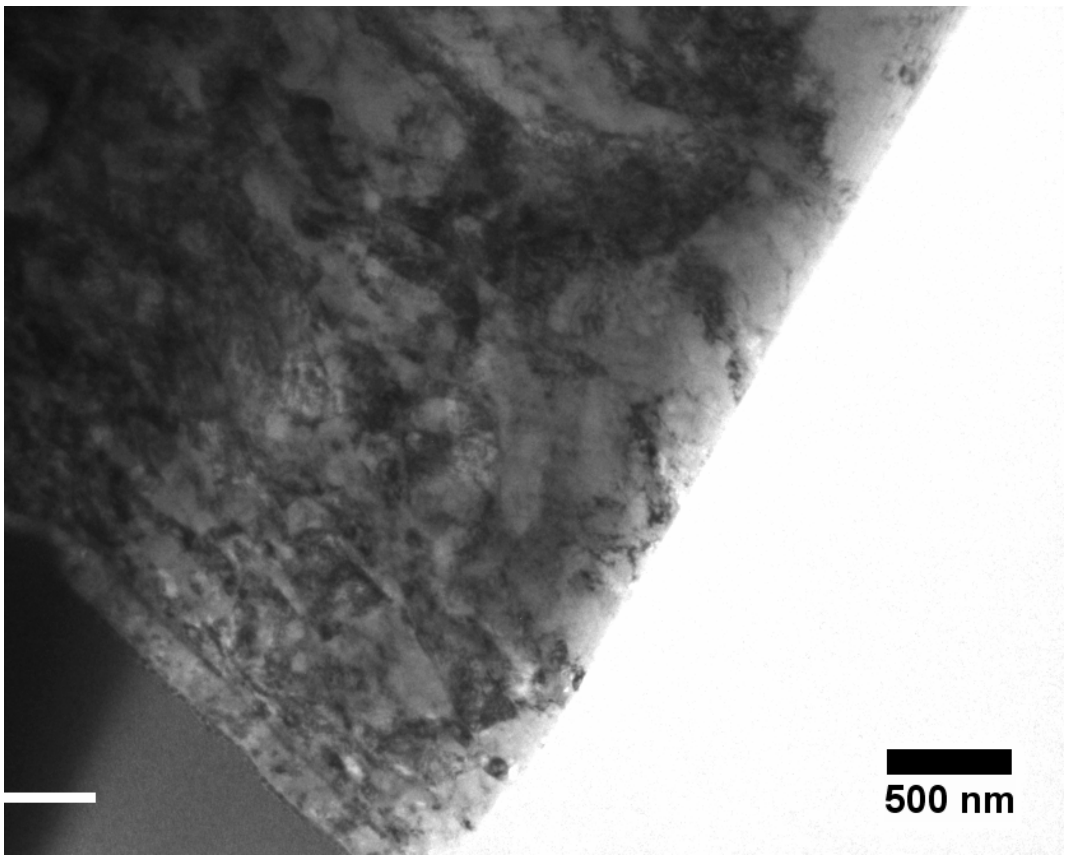


Figure 6.43: A low magnification bright field TEM micrograph showing the lamella from X65 carbon steel sample continuously scratched 100 times at applied potential of -1.5 *V vs.* MSE.

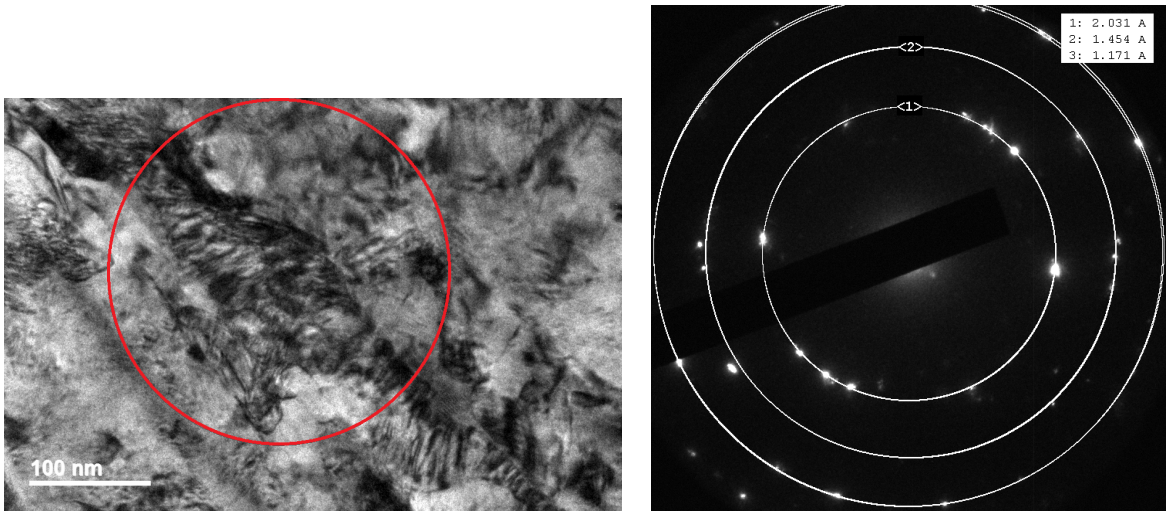


(a) (b)

Figure 6.44: a) A TEM micrograph showing the deformation and the location used for the diffraction and b) the SAED pattern originating from the circled area.

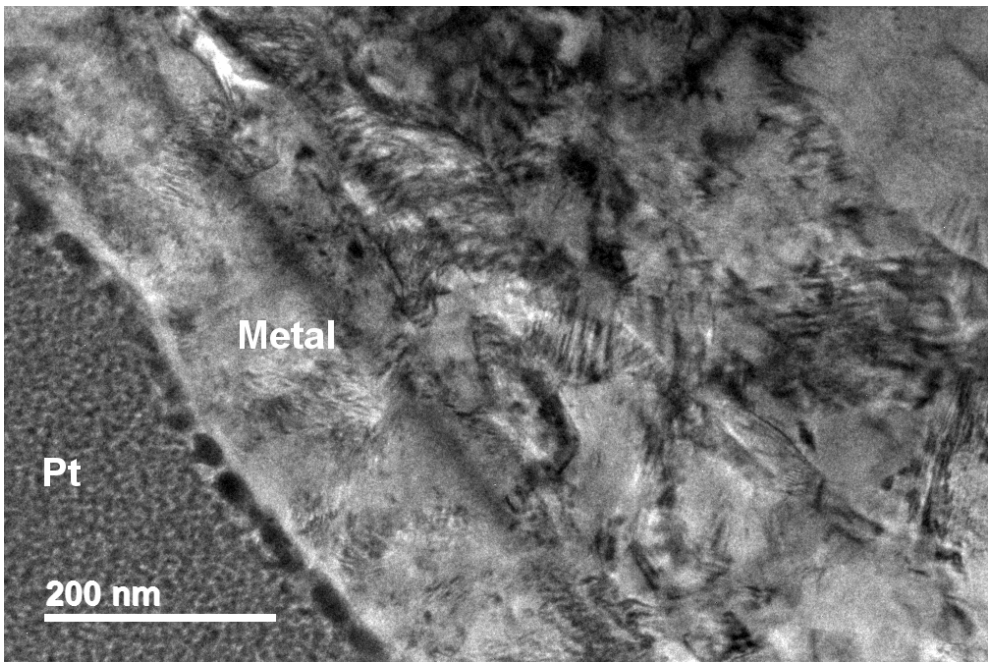


Figure 6.45: A bright field TEM micrograph showing the Pt – steel interface in the X65 carbon steel sample continuously scratched 100 times at applied potential of -1.5 $V$ *vs.* MSE.

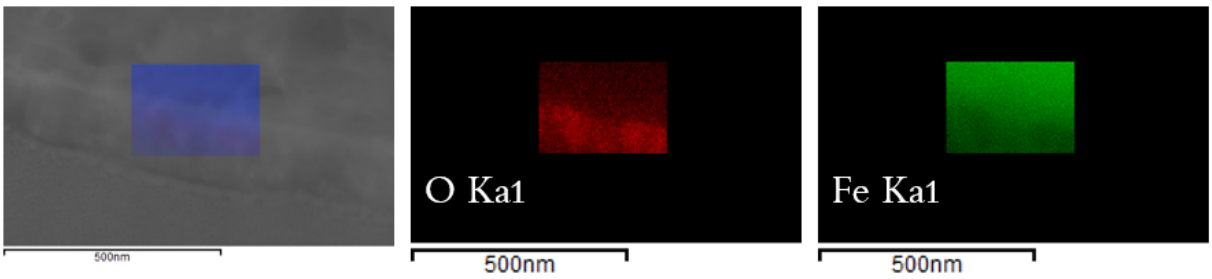


Figure 6.46: EDS maps showing O and Fe signal at the metal oxide – metal interface.

*100 RPM 0.6 V vs. MSE*

TEM lamella from a X65 carbon steel sample continuously scratched 100 times at 100 $RPM$ under an applied potential of 0.6 $V$ *vs.* MSE was lifted out using FIB. A FIB micrograph showing the location of the lamella is presented in Figure 6.47a. The SEM micrograph taken during lamella thinning process shows a microcrack at the subsurface in Figure 6.47b.

A low magnification bright field TEM image of the lamella is presented in Figure 6.48. Microstructure refinement *via* formation of nano-lamellar grains is again observed. The size of the lamellar grains increases with the distance from the surface. The crack is seen on the lower right hand side of the micrograph. A higher magnification image of the Pt-metal interface is presented in Figure 6.49. Regular deformation lines following the direction of the scratch can be seen. The lighter band between the Pt and deformed metal could be an oxide scale. Figure 6.50 shows the deformation of the X65 carbon steel and the polycrystalline SAED pattern recorded from the deformed area.

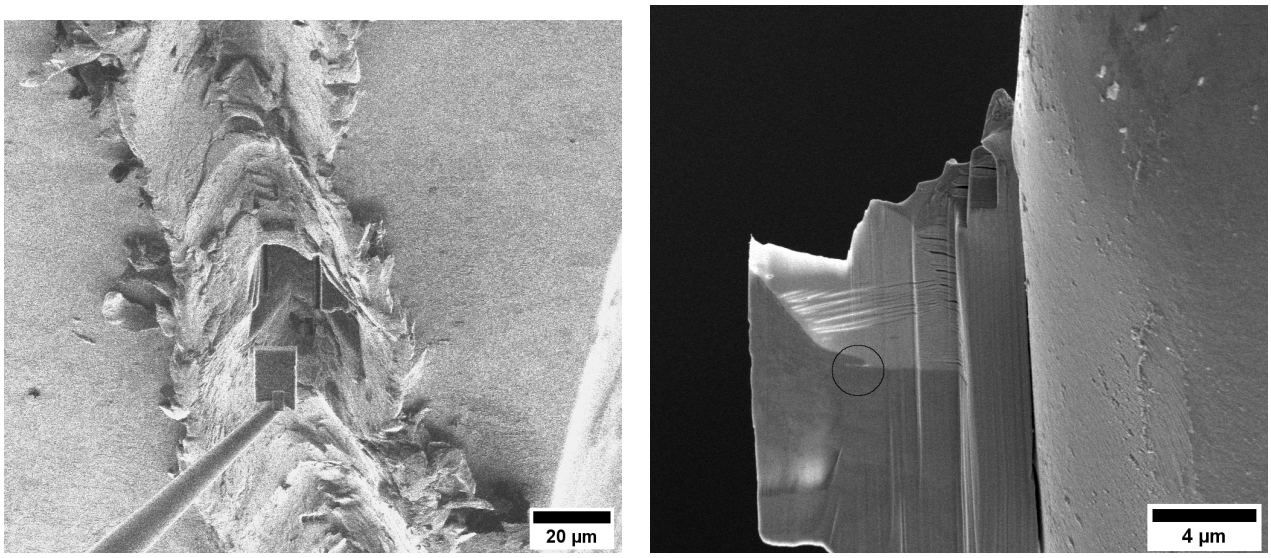


(a) (b)

Figure 6.47: a) FIB micrograph showing the TEM lamella being lifted out from the scratch track and b) SEM micrograph showing the lamella during thinning process. The circled area indicated the location of the crack.

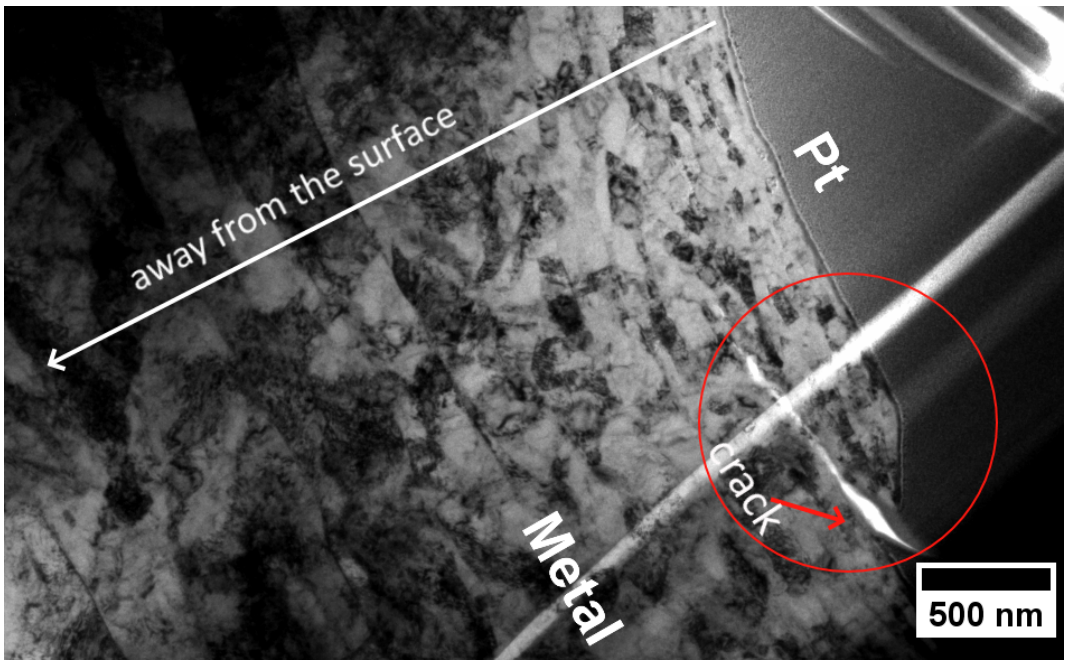


Figure 6.48: A low magnification bright field TEM micrograph showing the deformation in X65 carbon steel. The sample was continuously scratched at 100 $RPM$ under applied potential of 0.6 $V$ *vs.* MSE in pH 4.0 KHP solution.

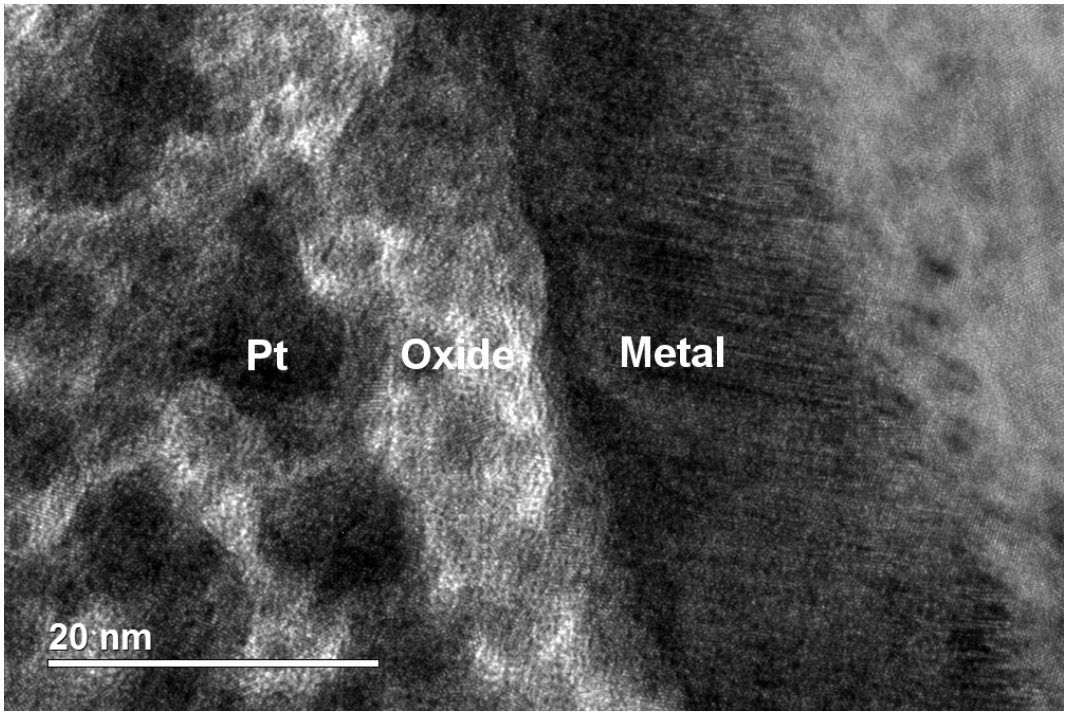


Figure 6.49: A bright field TEM image showing the interface between Pt protective layer, metal oxide and metal.

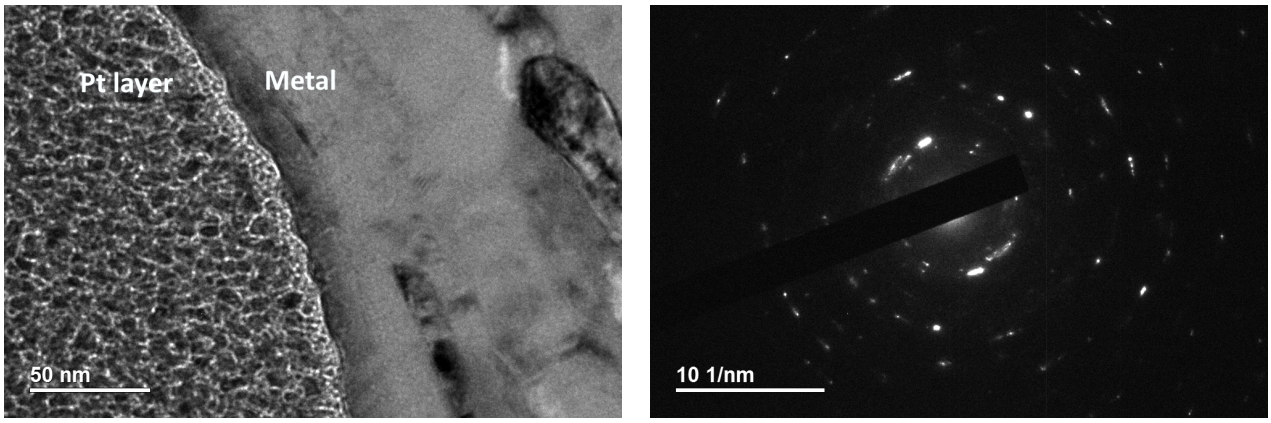


(a) (b)

Figure 6.50: a) A bright field TEM micrograph showing the deformation of the metal at the Pt-metal interface and b) a polycrystalline SAED pattern recorded from the deformed X65 carbon steel adjacent to the Pt protective layer.

To confirm the presence of an oxide layer EDS analysis across Pt-metal interface was attempted. The line along which spectra were collected every 9 *nm* is presented in Figure 6.51. The results in *wt.* % are given in Table 6.4. There was not a considerable increase in O signal across the interface. However, removing heavy elements that are not present in the X65 carbon steel and recalculating the *wt.* % compositions yields the results presented in Table 6.5, where the O and Cr signal are higher at the interface, suggesting the presence of the oxide scale that is Cr-enriched. The line along which data were collected is given in Figure 6.52. HRTEM experiments might be necessary to confirm this.

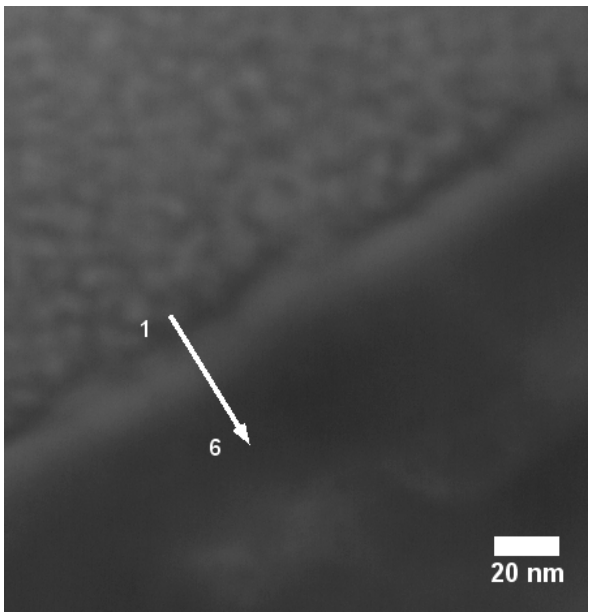


Figure 6.51: A dark field STEM image showing the line along which EDS spectra presented in Table 6.4 was taken. Signal was recorded *ca.* every 9 *nm*. The line begins at Pt protective layer and ends at the deformed metal site.

Table 6.4: An EDS analysis of the X65 carbon steel sample continuously scratched at 100 $RPM$ at applied potential of 0.6 $V$ *vs.* MSE. Spectra were collected across Pt-metal interface. All results are in $wt.\%$. Cr content of the bulk metal is 1.12 %.

| Spectrum | C | O | Si | Cr | Mn | Fe | Ga | Pt |
|---|---|---|---|---|---|---|---|---|
| Line Spectrum(1) | 7.17 | 3.12 | | 1.15 | 0.62 | 38.81 | | 49.12 |
| Line Spectrum(2) | 6.46 | 3.32 | | 1.04 | 0.59 | 43.5 | | 45.09 |
| Line Spectrum(3) | 5.04 | 3.45 | | 0.9 | 0.51 | 45.3 | 5.61 | 39.2 |
| Line Spectrum(4) | 3.73 | 4.04 | | 0.79 | 0.52 | 53.03 | 4.77 | 33.12 |
| Line Spectrum(5) | 3.04 | 4.6 | 0.4 | 0.67 | 0.72 | 65.01 | 3.83 | 21.74 |
| Line Spectrum(6) | 2.27 | 5.07 | 0.41 | 0.75 | 0.86 | 72.87 | 2.68 | 15.08 |


Figure 6.52: A dark field STEM image showing the line along which EDS spectra presented in Table 6.5 was taken. Signal was recorded *ca.* every 38 $nm$. The line begins at Pt protective layer and ends at the deformed metal site.

Table 6.5: An EDS analysis of the X65 carbon steel sample continuously scratched at 100 $RPM$ at applied potential of 0.6 $V$ *vs.* MSE. Spectra were collected across Pt-metal interface. Pt, Cu, Ga and Au signals were removed and the results in $wt.\%$ were recalculated.

| Spectrum | O | Si | Cr | Mn | Fe | Total |
|---|---|---|---|---|---|---|
| Line Spectrum(1) | 8.47 | 1.20 | 2.09 | 0.78 | 87.46 | 100.00 |
| Line Spectrum(2) | 7.65 | 0.83 | 1.28 | 0.85 | 89.38 | 100.00 |
| Line Spectrum(3) | 6.53 | 0.65 | 0.61 | 0.89 | 91.32 | 100.00 |
| Line Spectrum(4) | 6.24 | 0.62 | 0.54 | 0.92 | 91.68 | 100.00 |
| Line Spectrum(5) | 6.26 | 0.61 | 0.39 | 0.88 | 91.86 | 100.00 |

To sum up, X65 carbon steel samples showed grain refinement after the electrode scratching experiments. The grain refinement was similar to that reported in previous erosion-corrosion studies across different setups. This confirms the scratching setup is a viable alternative for obtaining the mechanistic understanding of erosion-corrosion in various metals.

Distinct nano-sized lamellar grains were observed in the X65 carbon steel samples scratched under passive anodic conditions at all tested rotation rates including 30, 100, 400 and 900 $RPM$. In the X65 carbon steel sample scratched under cathodic protection the grains were not as distinctive, either due to the thickness of the sample or decreased deformation. Strain induced deformation substructures could be still be observed in samples subject to both pure erosion and erosion-corrosion. The SAED patterns collected at the deformed subsurface confirmed polycrystalline structure. No phase change was recorded and diffraction pattern corresponded to that of the $\alpha$-ferrite. Continuous scratching under passive anodic conditions resulted in the formation of the crack near the surface. The interface was Cr enriched. Cracking could happen due to a combination of factors, including the embrittlement of the nano-sized grains in the subsurface, deleterious effect of the applied anodic current, low cycle fatigue [27, 4], and the non-uniformity of the oxide scale. Erosion-enhanced corrosion will take place in these areas due to disruption of the protective oxide.

**316 stainless steel**

Microstructural analysis of continuously scratched 316 stainless steel samples was performed. Two samples scratched at 100 $RPM$ in pH 4.0 KHP electrolyte under applied potentials of -1.5 V and 0.6 $V$ *vs.* MSE are presented next.

Continuously scratched samples

*100 RPM -1.5 V vs. MSE*

An SEM micrograph showing the scratch track formed due to continuously scratching the 316 stainless steel electrode 100 times under cathodic protection is presented in Figures 6.53a and 6.53b. Surface slip markings characteristic for austenitic stainless steel can be noticed to both sides of the scratch track in both FIB and SEM micrographs. Material spalling due to scratching can be seen at the Pt–metal interface in the TEM lamella (circled in red in Figure 6.53c).

The scratched samples were lightly polished with 1 $\mu m$ diamond suspension to remove the material piled up on the sides of the scratch. This allowed the observation of the slip markings. Figure 6.54 presents various slip bands formed by scratching 316 stainless steel samples at an applied potential of -1.5 $V$ *vs.* MSE, as well as indenting the same sample.

Slip can be defined as the process *via* which plastic deformation takes place during dislocation movement. The plane along which dislocations travel is termed the slip plane. Dislocations travel along the densest packed crystallographic planes along the most closely packed direction. The slip direction and the slip plane are known as the slip system, for an fcc material such as austenitic stainless steel there are 12 slip systems [28].

Brinckmann and Dehm [29] performed single-scratching experiments on austenitic stainless steel (1.5 % C, 2.3 % Si, 0.3 % Mn, 25 % Cr, 19 % Ni and Fe balance by weight) using a 5 $\mu m$ spherical nanoindenter. The authors observed surface slip markings resulting from plastic ploughing during a single scratching experiment. The plasticity was dominated by the crystal orientation of the material evident from non-symmetric pile-up on the sides of the scratch track. Cracks were found in the scratch track. As the indenter scratches the metal pile-up is formed ahead of the scratch. When the indenter continues its movement, previously sheared material is pushed under the indenter resulting in a crack driving force [29]. The depiction of the process is given in Figure 6.55. Indeed, in the present study the crack seen in the SEM image showing the lamella location and the crack observed in the lifted out lamella are aligned (Figures 6.53a and 6.53c).

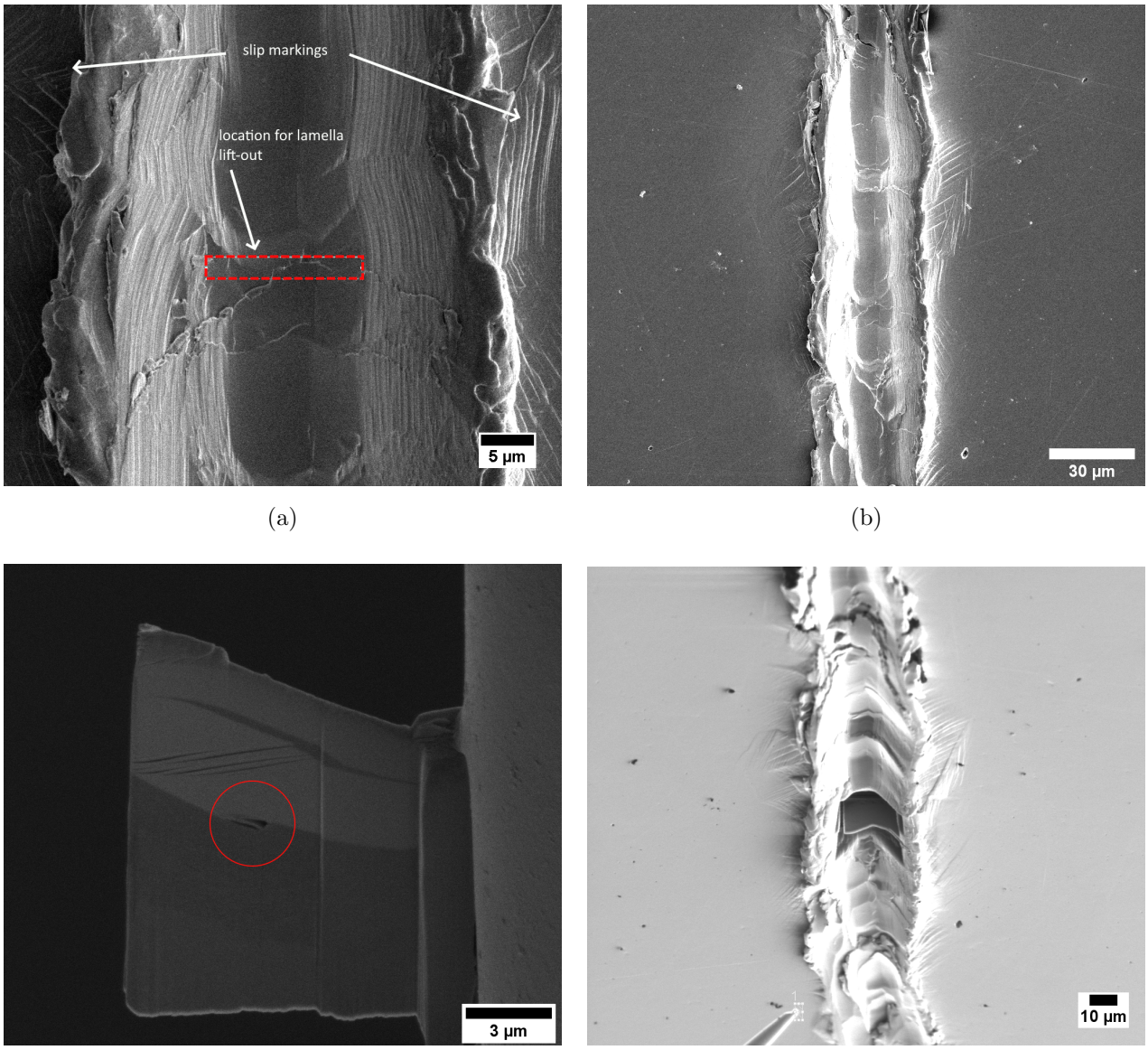


(a) (b)

(c) (d)

Figure 6.53: a) A high and b) low magnification SEM micrographs showing the location of the TEM lamella to be lifted from 316 stainless steel sample continuously scratched 100 times under applied potential of -1.5 $V$ *vs.* MSE at 100 $RPM$. c) SEM image of the crack in the lamella. d) FIB micrograph showing the scratch track and the lamella inside the trench that is ready to be attached to the Omniprobe micromanipulator.

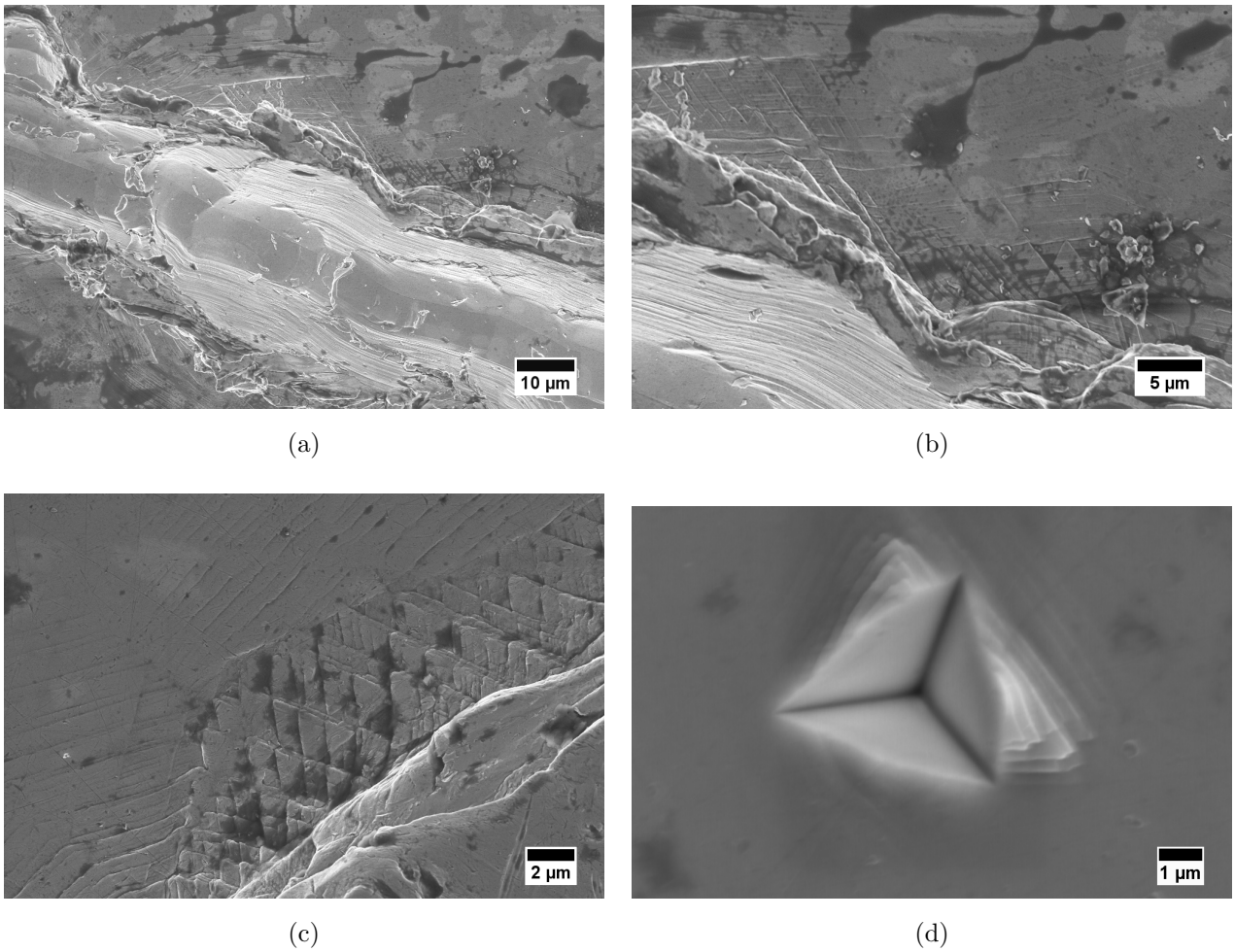


(a) (b)

(c) (d)

Figure 6.54: SEM micrographs of 316 stainless steel showing various slip markings due to deformation: a) – c) Slip bands formed due to continuously scratching the same place 100 times. The sample was lightly polished to remove the piled up material on the sides of the scratch. These images were captured by Dr Joseph Hadden[4]. d) The indent formed due to 60 $mN$ load.

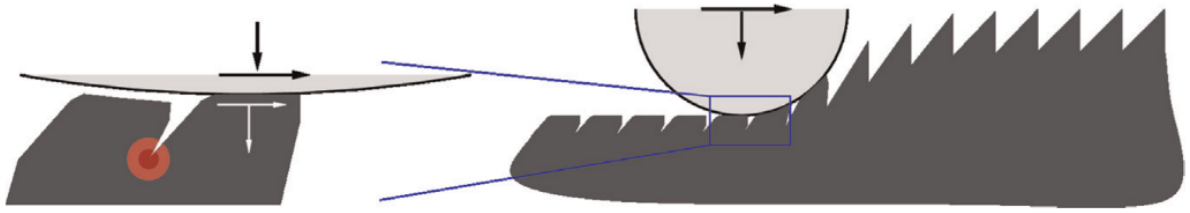

Figure 6.55: The illustration showing the indenter moving across the surface roughness forming the cracks. Reprinted from Brinckmann and Dehm [29] with permission. Copyright (2015) Elsevier B.V.

TEM micrographs of 316 stainless steel subject to pure erosion at -1.5 $V$ *vs.* MSE are presented in Figure 6.56. The lamella is quite thick for TEM imaging, however the deformation due to erosion is easily seen in Figure 6.56a. The interface between the Pt protective layer and

[4]Due to COVID-19 restrictions on access

the deformed 316 stainless steel is shown in Figure 6.56b. Grain refinement is observed in 316 stainless steel sample, with increasing grain size away from the subsurface. The deformation substructures showing the strained material can be seen in Figure 6.56b. However, the nano-sized lamellar grains were *not* as apparent in this sample, similar to the cathodically protected X65 carbon steel.

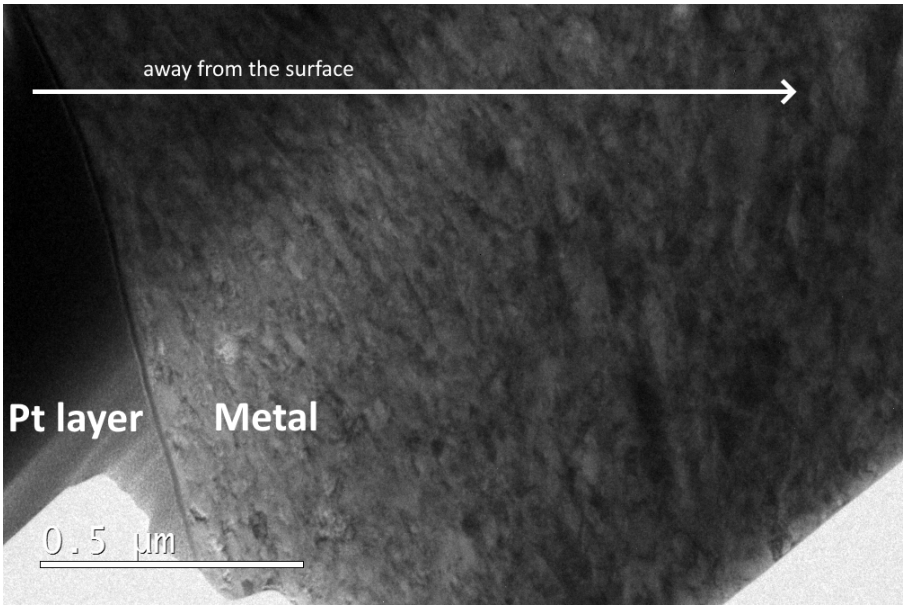


(a)

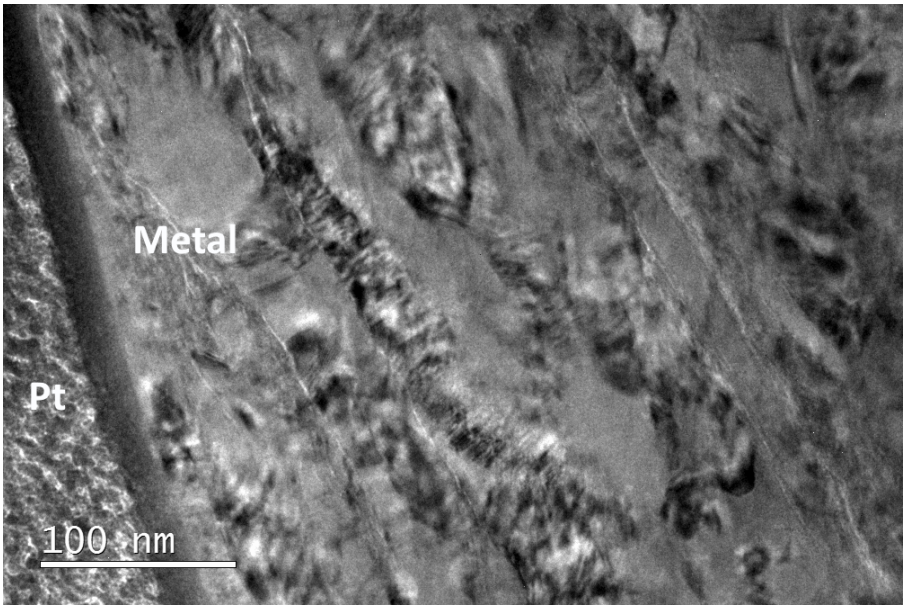


(b)

Figure 6.56: A bright field TEM images showing the deformation in 316 stainless steel sample continuously scratched 100 times under applied cathodic potential of -1.5 $V$ *vs.* MSE.

The selected area electron diffraction was carried out at the circular area indicated in Figure 6.57a. The d-spacings were measured using TEM plugin of Fiji software [1] and were equal to 2.043 $\mathring{A}$, 1.819 $\mathring{A}$, 1.530 $\mathring{A}$, 1.434 $\mathring{A}$, 1.261 $\mathring{A}$, 1.176 $\mathring{A}$, 1.079 $\mathring{A}$ and 1.010 $\mathring{A}$ (See Figure

6.57b). These diffraction spots can be assigned to crystal planes as following: {111} fcc and {110} bct, {200} fcc, unknown, {002} bct, {220} fcc, {121} bct, {113} fcc, {222} fcc and {022} bct. The presence of the diffraction spots corresponding to the bct crystal structure confirms partial transformation of austenite to martensitic steel due to erosion. This is in agreement with Wood *et al.* [19] and Majeed [17] who studied erosion-corrosion of 316 stainless steel.

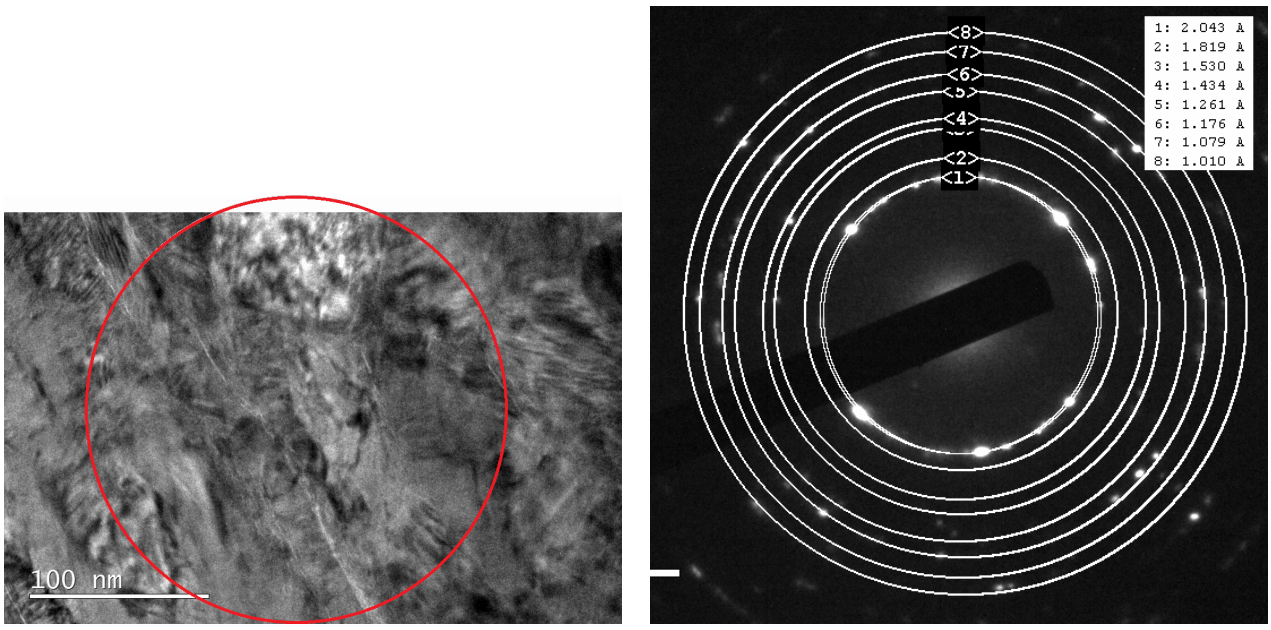


(a) (b)

Figure 6.57: a) TEM micrograph showing the location of the SAED aperture and b) the respective electron diffraction pattern with measured interplanar d-spacings.

*100 RPM 0.0 V vs. MSE*

Figure 6.58a shows the top view of the sample continuously scratched 100 times at 100 $RPM$ under passive anodic potential of 0.0 $V$ *vs.* MSE. A lamella ready for the lift-out is shown in Figure 6.58b. Grain refinement due to erosion-corrosion can be observed in the bright field TEM micrograph given in Figure 6.59. Nano-lamellar grains are formed similar to the X65 carbon steel samples scratched under passive anodic potential. The size of these lamellae start from *ca.* 15 $nm$ and gradually increase as a function of the distance from the surface. Due to multiple scratching, a formation of crack was observed in Figure 6.59c.

The selected area electron diffraction was performed at the area indicated in Figure 6.60a. d-spacings measured from the SAED pattern were equal to 2.082 $\AA$, 1.461 $\AA$, 1.205 $\AA$, 1.056 $\AA$ and 0.944 $\AA$. These d-spacings can be correlated to the {111} fcc and {110} bct, {002} bct, {220} fcc, {222}/{113} fcc and {022} bct, and {031} bct respectively. Similar to the 316 stainless steel sample scratched under cathodic protection, the one scratched under passive anodic potential

has some diffraction spots corresponding to the bct crystal structure, confirming partial phase transformation of austenite to martensite.

Martensitic stainless steel is harder compared to the austenite. As was shown in Figures 6.18, 6.19, and 6.20 presented above, significant microhardness increase of the 316 stainless steel samples was noticed in the subsurface after scratching under both pure erosion and erosion-corrosion conditions. This was likely caused by work hardening, partial phase transformation and grain refinement. The application of cathodic currents during pure erosion tests can also result in hydrogen embrittlement of corrosion-resistant alloys such as 316 stainless steel, albeit to a lesser extent compared to carbon steels due to the low diffusivity and high solubility of hydrogen in the fcc structures [30].

Although high hardness implies high resistance to localized plastic deformation including erosion, materials with high hardness are generally brittle and susceptible to cracking. The cracks in 316 stainless steel were mostly observed in the subsurface in the present study. Whether cracks developed due to the embrittlement of the material or the scratching tip pushing the previously ploughed material underneath the tip can not be discerned. However, it can be elaborated that the presence of the cracks disrupted the passive film on stainless steel contributing to erosion-enhanced corrosion component of erosion-corrosion.

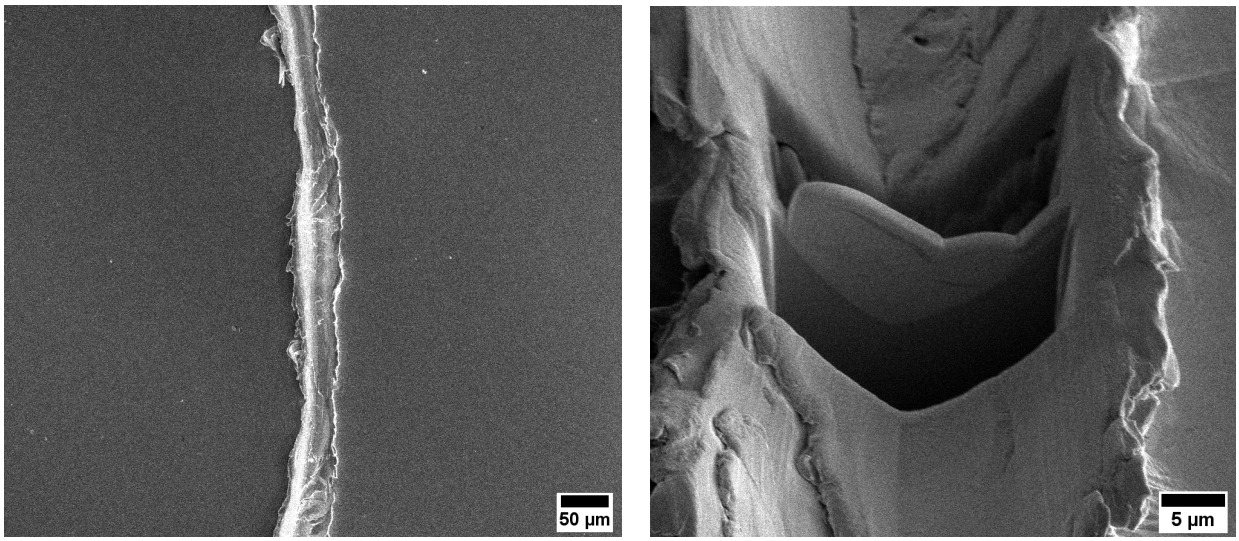


(a) (b)

Figure 6.58: SEM micrographs of the 316 stainless steel continuously scratched at 0.0 $V$ *vs.* MSE showing: a) top view of the scratch and b) a lamella inside the trench ready for the lift-out.

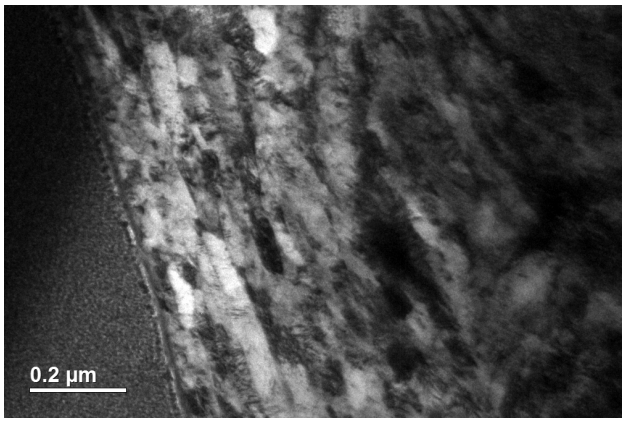


(a)

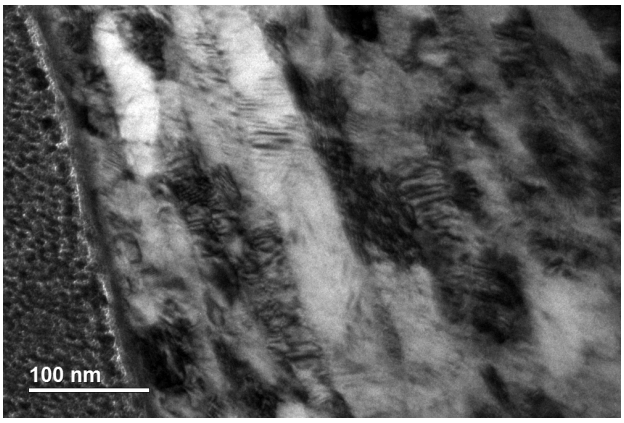


(b)

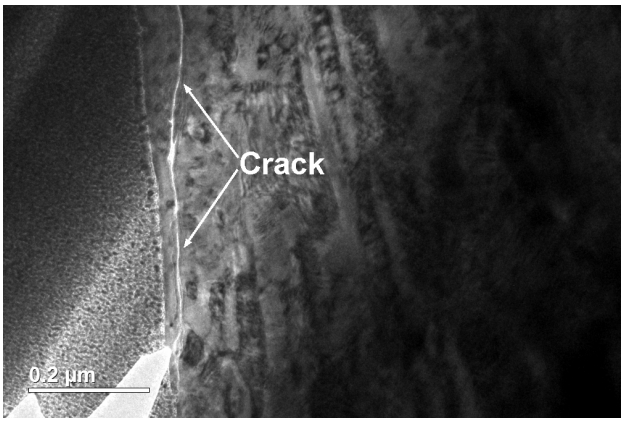


(c)

Figure 6.59: Bright field TEM micrographs of the 316 stainless steel sample continuously scratched at 100 $RPM$ under applied potential of 0.0 $V$ *vs.* MSE.

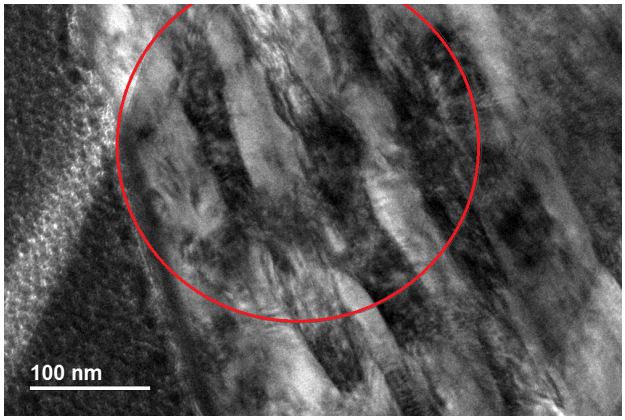


(a)

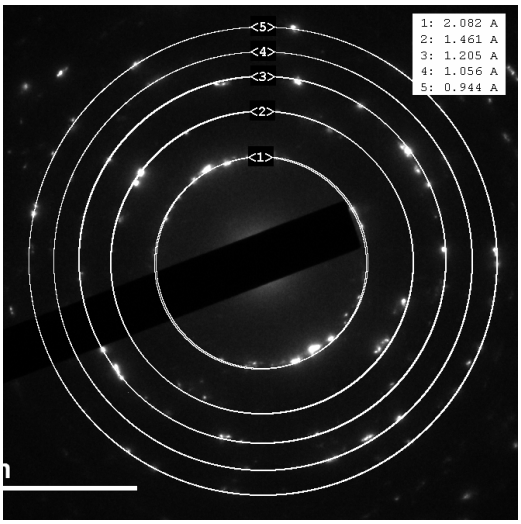


(b)

Figure 6.60: a) A bright field TEM image showing the location for the diffraction and b) the SAED pattern collected from that area with calculated interplanar spacings.

### 6.3.4 Erosion-corrosion due to jet impingement testing

The results of jet impingement testing of X65 carbon steel and 316L stainless steel samples at impingement angles of 30° and 90° are presented in this section. These experiments were completed in order to compare the microstructural changes taking place during jet impingement to scratching erosion-corrosion experiments.

#### Particle analysis

As mentioned in Chapter 2, erosion-corrosion rate is correlated to the particle size and shape. Usually larger (up to a certain size) and more angular particles result in higher erosion-corrosion rates. The size, sharpness and shape of the erodent can also change during the experiment.

Figure 6.61 presents optical micrographs of the silica particles before and after the jet impingement experiments. The particles were analysed using ImageJ software [31]. The circularity of the particles, which is defined as $4\pi \times area/perimeter^2$ with 1 indicating a perfect circle, did not change after the experiment. However, significant particle size reduction was observed. Specifically, the Feret's diameter (the longest distance between any two points of the shape) decreased from *ca.* 445 $\mu m$ to 156 $\mu m$. Erosion-corrosion models need to account for this time-dependency of particle size that ultimately affects the material wastage rate.

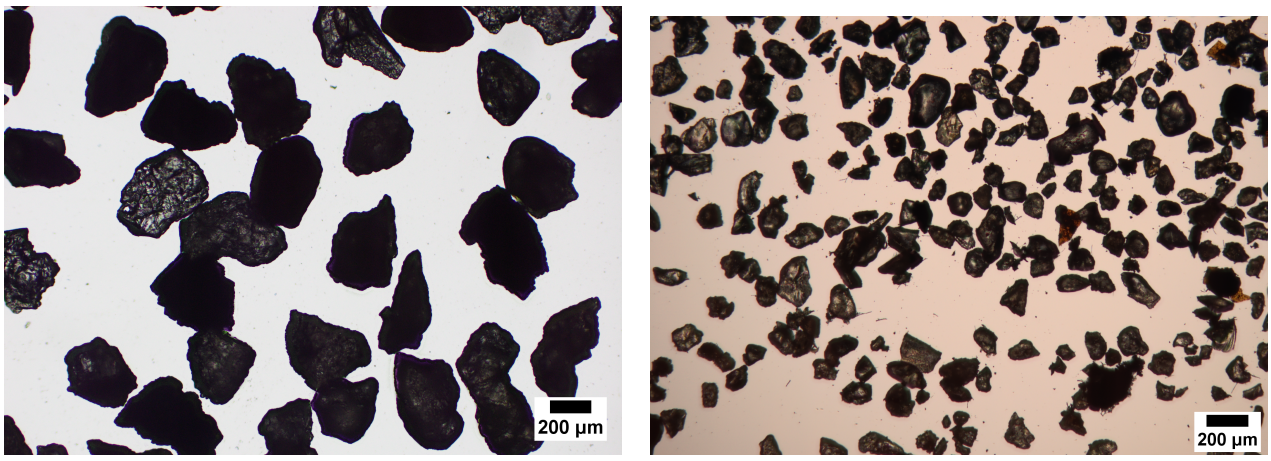


(a) (b)

Figure 6.61: Optical micrographs showing sand particles used for jet impingement a) before and b) after the experiment. 1 $h$ experiments were conducted at 2.5 $m^3\ h^{-1}$ flow rate and 24 $m\ s^{-1}$ jet velocity.

#### Mass loss analysis

The results of mass loss measurements for X65 carbon steel and 316L stainless steel samples after the jet impingement testing are presented in Tables 6.6 and 6.7. Annual erosion-corrosion

rates were calculated using Equation 6.3. In X65 carbon steel the erosion-corrosion rate was independent of the impingement angle. The data scatter implies a considerable component of the total erosion-corrosion happened due to corrosion. Because the sample was not coated, corrosion could occur on all sides of the sample, while erosion-corrosion only took place on the side facing the jet. Indeed, pitting corrosion was noticed at the back of certain X65 carbon steel samples, which is believed to have caused the large scatter of the calculated erosion-corrosion rates of X65 carbon steel sample. In principle, the erosion rate of the ductile materials including carbon steels is known to vary with angle as mentioned in Chapter 2, section 2.2.2. Hence, high erosion-corrosion rates seen for X65 carbon steel imply the mechanism is dominated by corrosion. For 316L stainless steel, on the other hand, a dependence of erosion-corrosion rate on the impingement angle was apparent. The material degradation rate was lower at 90° compared to that at 30°. This is in agreement with the study conducted on 304L stainless steel by Burstein and Sasaki [32], where higher erosion and erosion-corrosion rates were recorded at oblique angles. This happens due to platelet forming mechanism occurring during erosion, where platelets are removed easier at lower impact angles in ductile materials [33] (See Figure 2.9b). Erosion rate is usually the highest at 30° impact angle and tends to decrease towards 0° and 90° for many ductile materials [34, 33, 32].

Table 6.6: Mass loss of X65 carbon steel samples subject to 1 h jet impingement tests in pH 4.0 KHP solution at jet velocity of 24 ± 1 $m\ s^{-1}$. Mass loss was measured with a high precision 5 decimal place analytical balance.

| Material | Angle | m(before), g | m(after), g | Δ m, mg | 1 hr wall loss, mm | E-C Rate, $mm\ yr^{-1}$ |
|---|---|---|---|---|---|---|
| X65 carbon steel | 90° | 57.80222 | 57.72196 | 80.26 | 0.004090 | 35.83 |
| | | 57.58864 | 57.53335 | 55.29 | 0.002817 | 24.68 |
| | 30° | 57.62794 | 57.55961 | 68.33 | 0.003482 | 30.50 |
| | | 56.79611 | 56.73815 | 57.96 | 0.002953 | 25.87 |

Table 6.7: Mass loss of 316L stainless steel samples subject to 1 h jet impingement tests in pH 4.0 KHP solution at jet velocity of 24 ± 1 $m\ s^{-1}$. Mass loss was measured with a high precision 5 decimal place analytical balance.

| Material | Angle | m(before), g | m(after), g | Δ m, mg | 1 hr wall loss, mm | E-C Rate, $mm\ yr^{-1}$ |
|---|---|---|---|---|---|---|
| 316 stainless steel | 90° | 54.03176 | 54.02734 | 4.42 | $2.204\times10^{-4}$ | 1.931 |
| | | 54.03669 | 54.03056 | 6.13 | $3.057\times10^{-4}$ | 2.678 |
| | 30° | 54.01774 | 54.00187 | 15.87 | $7.915\times10^{-4}$ | 6.934 |
| | | 57.13681 | 57.12181 | 15.00 | $7.481\times10^{-4}$ | 6.554 |

### Surface deformation observed by SEM

The images of the samples after the jet impingement erosion-corrosion tests at 24 $m\,s^{-1}$ for 1 $h$ in pH 4.0 KHP solution are presented in Figure 6.62. The erosion-corrosion scars are circular for the samples impinged at 90° and elongated at 30°. The approximate 2D profiles of the samples impinged at 90° and 30° are shown in Figures 6.62c and 6.62f respectively. During direct impingement of the materials at 90° by two phase liquid-particle flow, CFD simulations indicated the presence of the stagnation region [4, 35]. The stagnation region can be described as the region in the vicinity of the target wall, where particles are decelerated by the flow [33]. In the direct impingement by the jet flow, the centre of the stagnation region is expected to have a lower erosion rate due to the smaller velocity of the jet. The 2D profile of the erosion-corrosion scar recorded after jet impingement at 90° corresponds well with this prediction, as the depth of the scar is smaller at the centre compared to the region around this stagnation point.

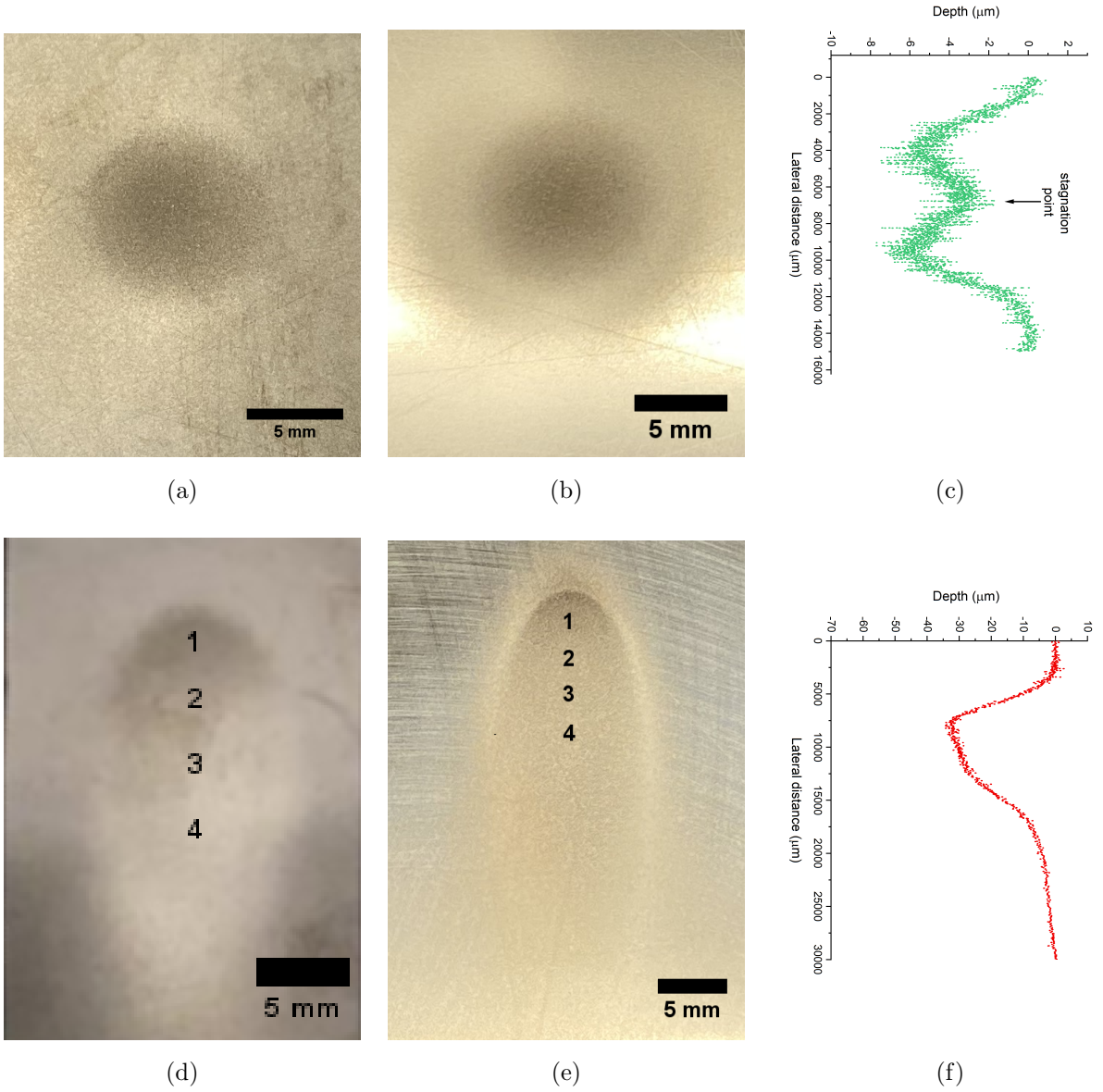


Figure 6.62: Photographs of the samples after 1 h jet erosion-corrosion experiments at 24 $m\ s^{-1}$ in pH 4 KHP solution: a) X65 carbon steel sample impinged at 90°, b) 316L stainless steel sample impinged at 90°, c) 2D profile of the sample impinged at 90°measured using Dektak profilometer, d) X65 carbon steel sample impinged at 30°, e) 316L stainless steel sample impinged at 30°, f) 2D profile of samples impinged at 30°measured using Dektak profilometer.

The surface morphology of the X65 carbon steel sample impinged at 90° to the vertical is presented in Figure 6.63. Surface roughening is observed due to erosion-corrosion with formation of platelets and craters at the centre of the scar. Towards the edge of the scar the platelets are more elongated and the direction of the jet flow can therefore be inferred (Figure 6.63c).

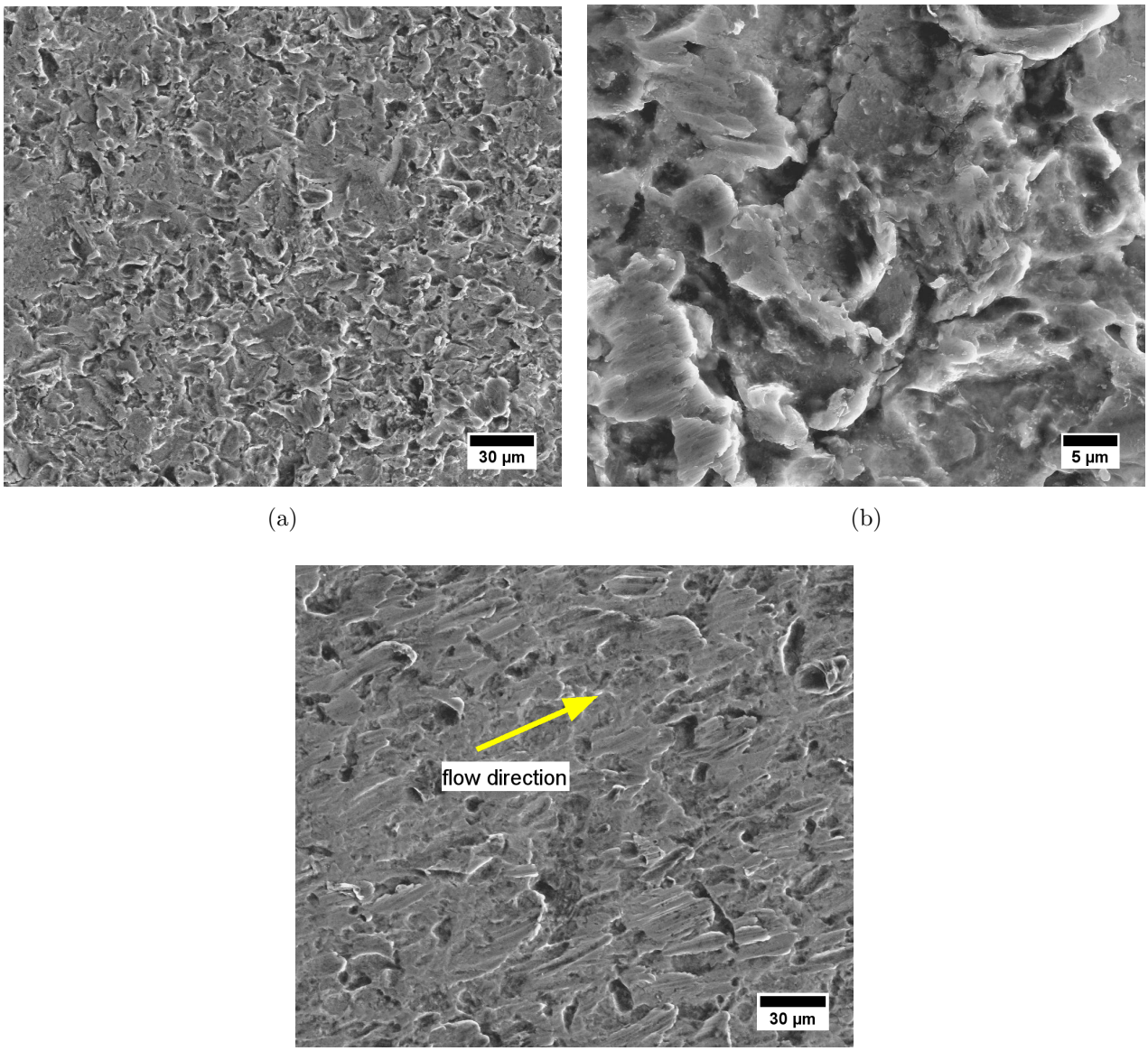


(a) (b)

(c)

Figure 6.63: SEM micrographs of the X65 carbon steel sample after the jet impingement experiment at 90° impact angle captured at: a), b) the centre and c) the edge of the erosion-corrosion scar shown in Figure 6.62a.

.

SEM micrographs of the X65 carbon steel sample impinged at 30° are presented in Figure 6.64. The locations used for SEM imaging are numbered in Figure 6.62d. The surface appears to be dominated with craters at locations 1 and 2 as shown in Figures 6.64a and 6.64b. The formation of the platelets/elongated lips is predominant at locations 3, 4 as seen in Figures 6.64c and 6.64d. This can be related to the velocity profile of the jet flow upon impingement and the particle trajectory. After initial impingement at point 1, particles slide off the surface with the flow towards point 4, forming elongated platelets. The incoming angle of the particles also changes with the distance from the centre of the nozzle [36].

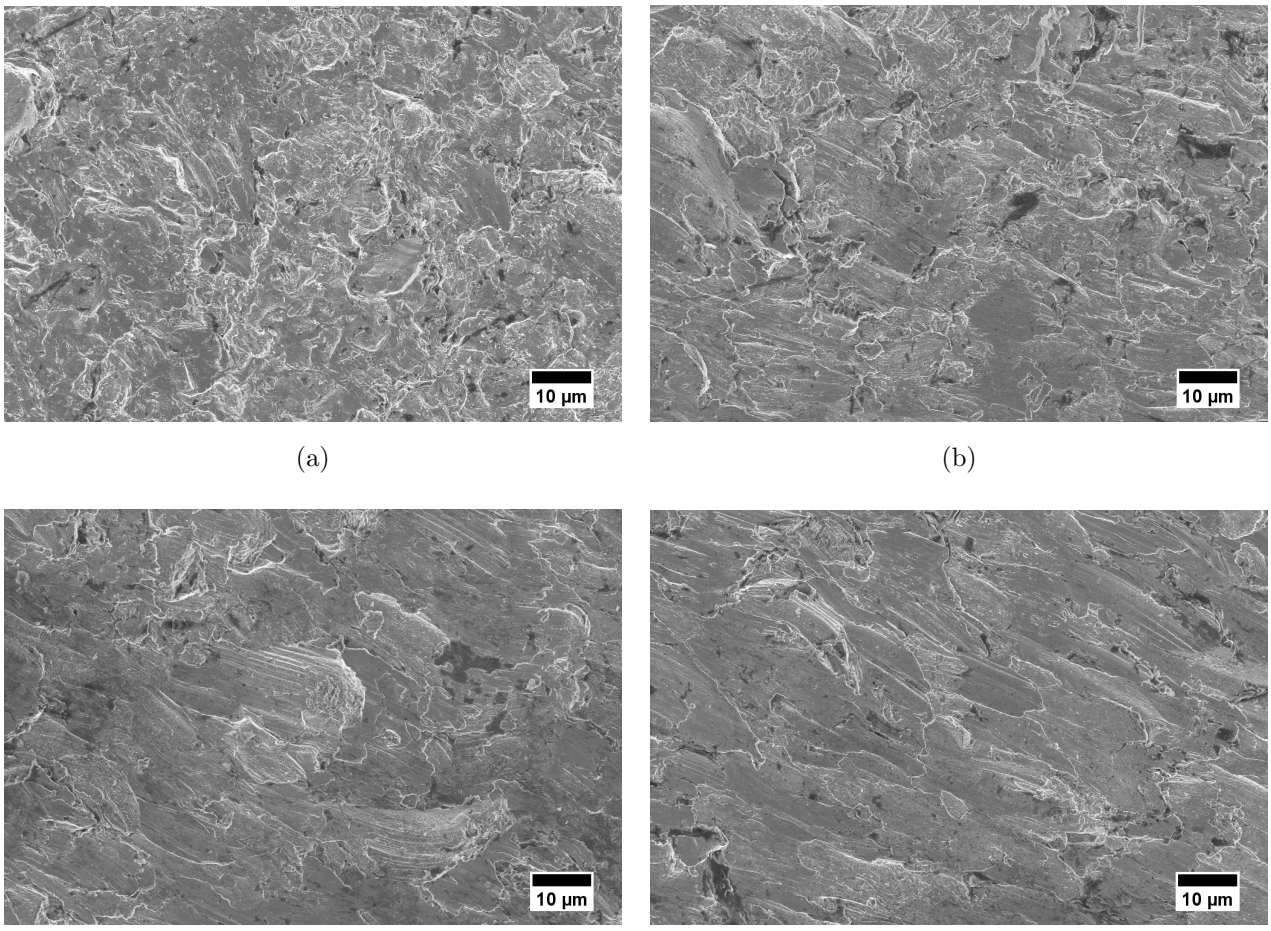


(a) (b)

(c) (d)

Figure 6.64: SEM images of X65 carbon steel impinged at 30° angle showing the deformation at locations a) 1, b) 2, c) 3 and d) 4 of the erosion-corrosion scar shown in Figure 6.62d. These micrographs were captured by Dr Joseph Hadden[5].

316L stainless steel samples impinged at 90° have prominent surface roughening as seen in Figure 6.65. The morphology of the sample that corresponds to the centre of the erosion-corrosion scar in Figures 6.65a and 6.65b has particle cuts and indents that appear due to cutting wear. Slip markings observed during scratching were also observed after the jet erosion impingement of the 316 stainless steel, see circled areas in Figure 6.65b. As briefly mentioned in page 60, slip markings were previously observed during erosion of austenitic steels [29] and fcc aluminium alloys [37]. It is thought that fatigue crack initiates around these surface slip markings [38]. Surface slip markings were formed during cyclic straining of 316L stainless steel samples. Deformation induced martensite formation was also observed in these samples [38]. Figures 6.65c and 6.65d show the surface roughening decreased at the edge of the scar, and is characterised by ploughing wear type mechanism, where material is displaced to both sides of the particle trajectory and grooves are formed.

[5]Due to COVID-19 restrictions on access

As previously mentioned, ductile materials have maximum erosion rates around 30° impact angle [33, 39]. Figure 6.66 presents the SEM micrographs of 316L stainless steel sample impinged at a 30° angle to the vertical. The sequence of micrographs clearly shows a transition from cutting to ploughing wear with the width of the platelets decreasing from point 1 to 4. It indicates decreased partial kinetic energy transfer to the material that result in lower wear rates further away from the first point of contact.

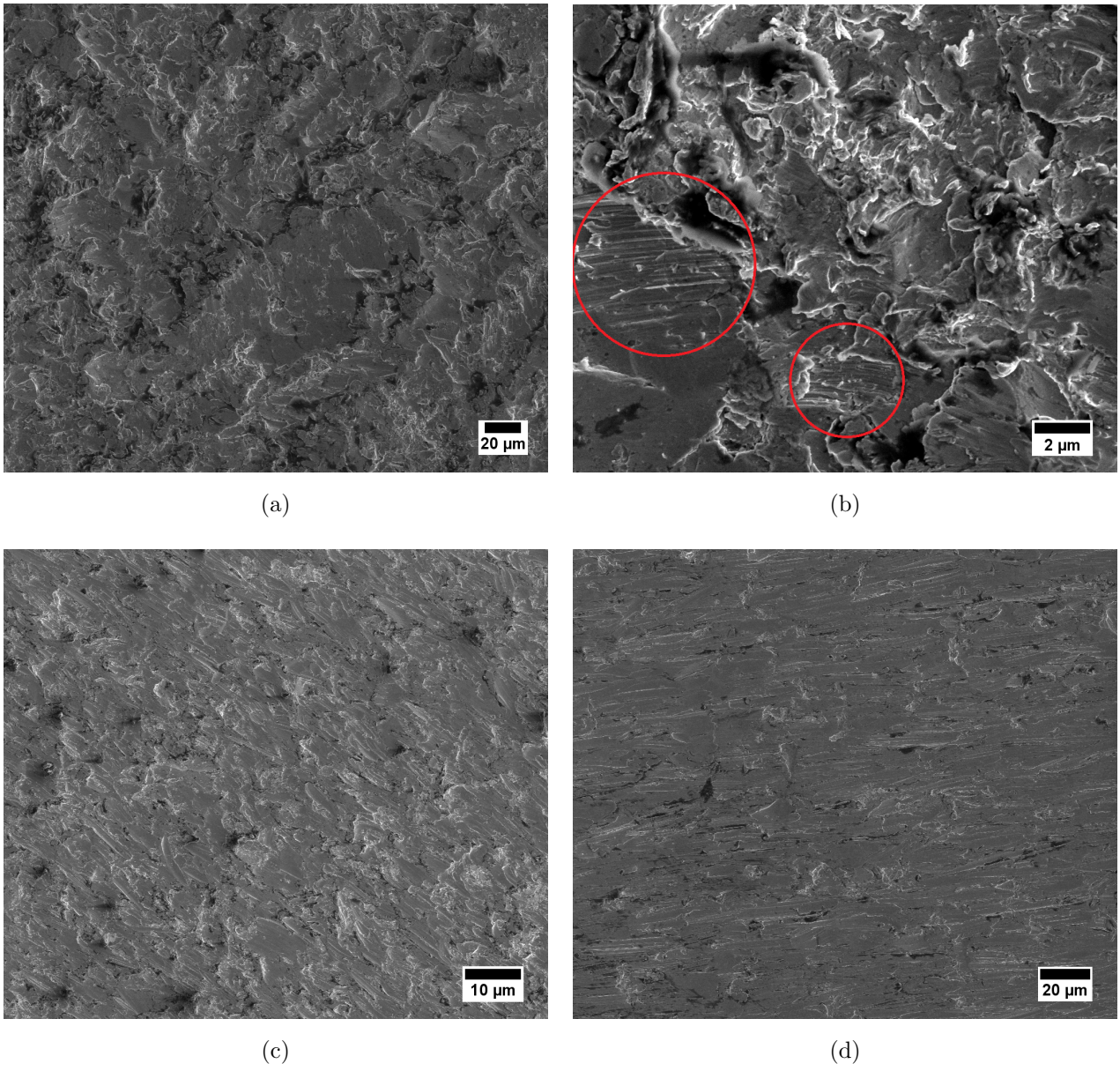


(a) (b)

(c) (d)

Figure 6.65: SEM images of 316L stainless steel impinged at 90° angle showing the deformation a, b) at the centre and c, d) at the edge of the erosion-corrosion scar presented in Figure 6.62b.

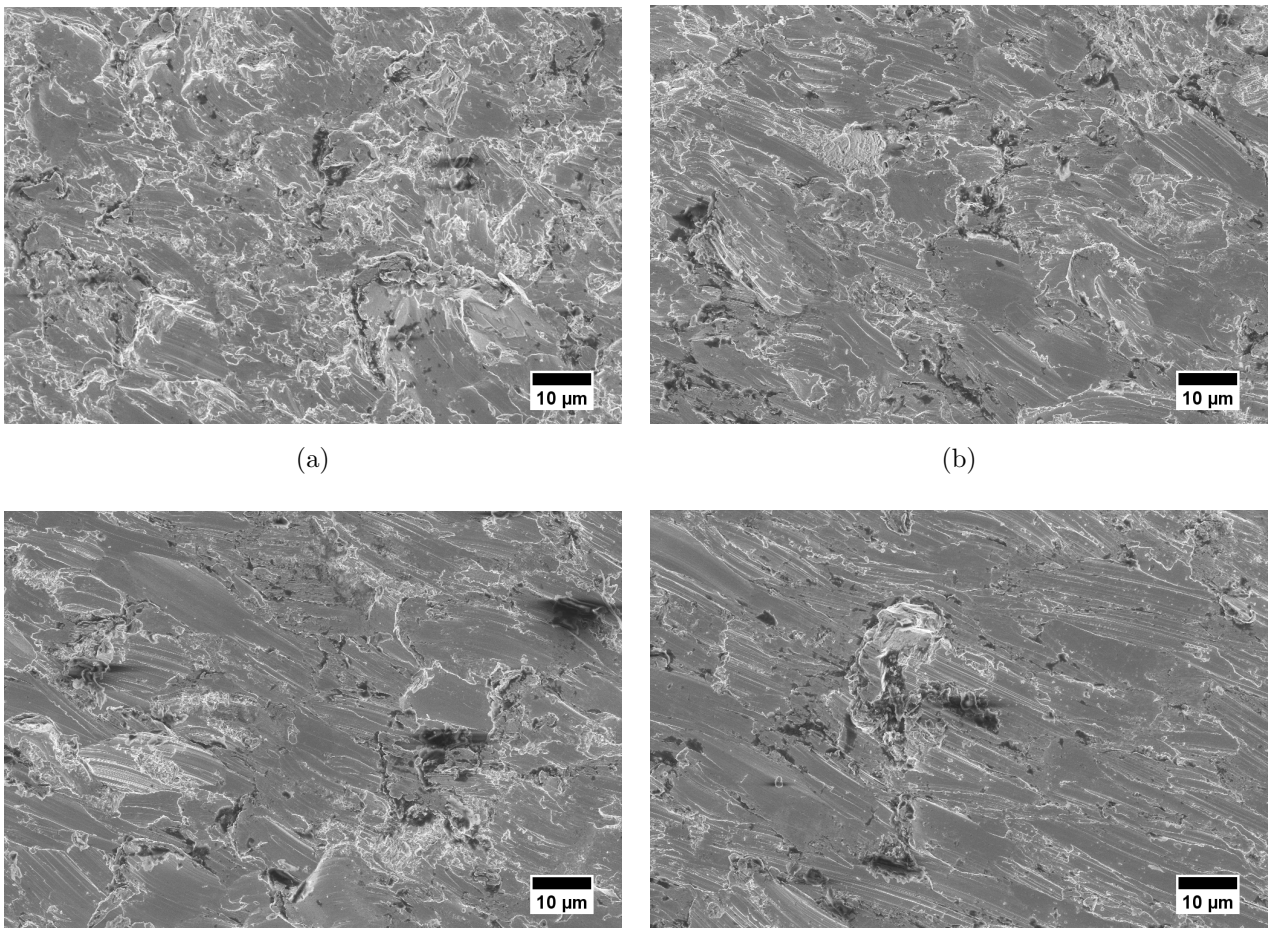


(a) (b)

(c) (d)

Figure 6.66: SEM images of 316L stainless steel impinged at 30° showing the deformation at locations a) 1, b) 2, c) 3 and d) 4 of the erosion-corrosion scar shown in Figure 6.62e. These micrographs were captured by Dr Joseph Hadden.

Cross section

Cross section analysis of 316L stainless steel sample subject to jet impingement erosion-corrosion at 90° angle was performed. Figure 6.67 presents the low magnification view of the cross section. Slip markings covered with Pt protective layer can be noticed at the top of the micrograph. The cross section reveals the presence of cracks and the micro-crack networks within 1 $\mu m$ of the impinged surface. These cracks have an important implication in terms of corrosion, pitting and fatigue cracking susceptibility [27]. The microstructural refinement observed within FIB milled area up to *ca.* 6 $\mu m$ below the surface is similar to the one in scratched samples presented earlier in Figures 6.56, 6.59 .

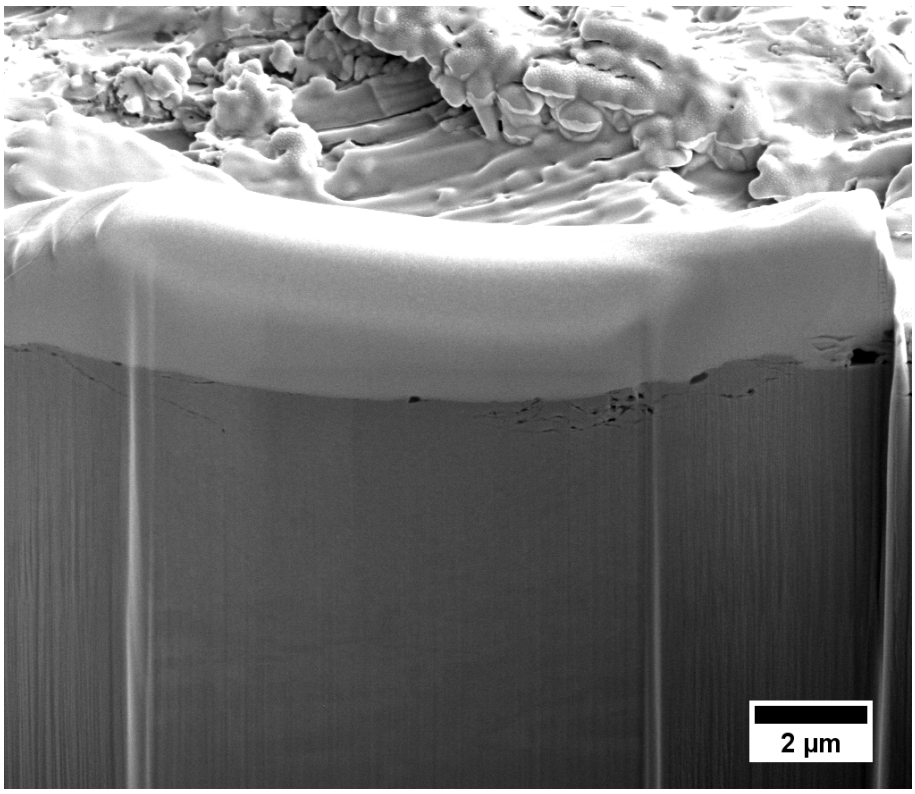


Figure 6.67: SEM image of the 316L stainless steel cross section after the jet impingement test at 90° impingement angle.

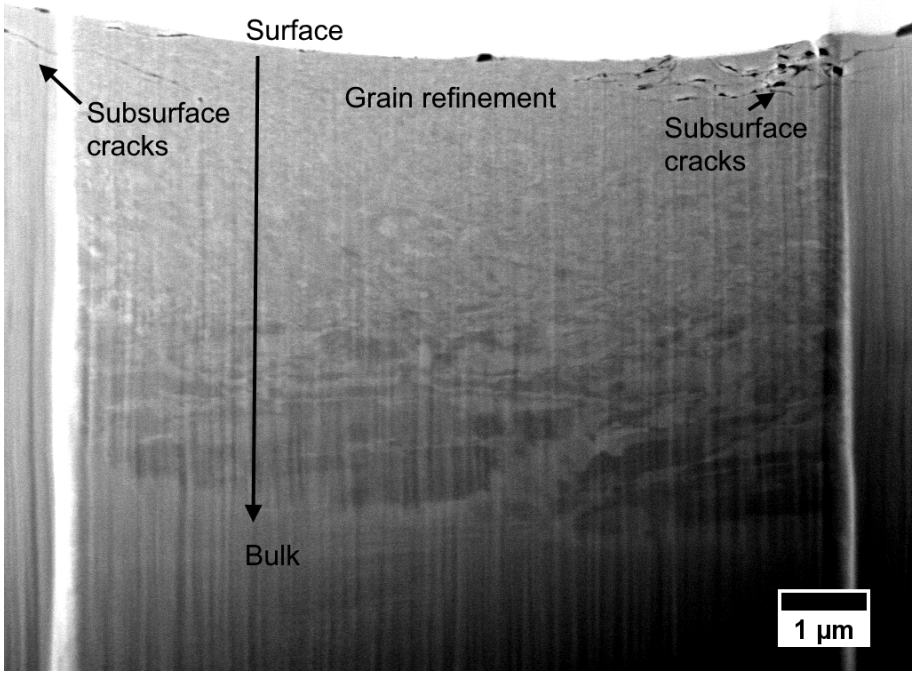


Figure 6.68: 316L stainless steel cross section after the jet impingement test at 90°. Adjusting the brightness and contrast of the image allows seeing the deformation of the material subject to jet impingement.

### Microstructural analysis using TEM

The microstructure of X65 carbon steel and 316L stainless steel samples impinged at 90° was studied using TEM and EDS techniques.

X65 carbon steel

SEM micrographs of the jet impinged X65 carbon steel showing the location of the lamella for *in-situ* lift out are shown in Figure 6.69. The Pt protective layer was applied over the ridge shown in Figure 6.69a. Grain refinement accompanied by a formation of nano-lamellar grains in the subsurface region is observed in the bright field TEM image in Figure 6.70. The SAED pattern was taken at the subsurface region and corresponds to that of bcc $\alpha$-ferrite. The SAED pattern is polycrystalline indicating the presence of several grains within the area used for diffraction.

Grain refinement at higher resolution can be observed in the dark field STEM micrograph in Figure 6.71. The size of the nano-lamellar grains begins from *ca.* 20 $nm$ and gradually increases away from the jet impinged region, similar to the scratched samples presented earlier in this chapter. There appears to be a layer between the protective Pt layer and the deformed X65 carbon steel. The EDS line analysis from the interface to the bulk material showed considerable O signal at the interface as seen in Figure 6.72. This implies there is a metal oxide layer between the Pt layer and the deformed metal. Increased Cr signal is also observed at the interface. The thickness of the oxide layer on jet impinged sample varies between *ca.* 35 and 100 $nm$. This oxide is much thicker than the one observed in X65 carbon steel samples scratched at 0.6 $V$ *vs.* MSE applied potential, where the thickness was equal *ca.* 20 $nm$ as measured from Figure 6.49.

It is known that the oxide scale on X65 carbon steel is formed due to precipitation in these conditions. Both bright field TEM (Figure 6.70) and dark field STEM (Figure 6.71) images indicate that the oxide scale was not compact at the erosion ridge/lip. Non-uniformity and disruption of the oxide scale due to erosion will contribute to the erosion-enhanced corrosion of the carbon steels. Furthermore, surface roughening was related to lower pitting potential of stainless steels [15] and increased corrosion rate of copper [40]. Hence, formation of the non-continuous oxide scale due to erosion-corrosion is an important consideration for erosion-corrosion models.

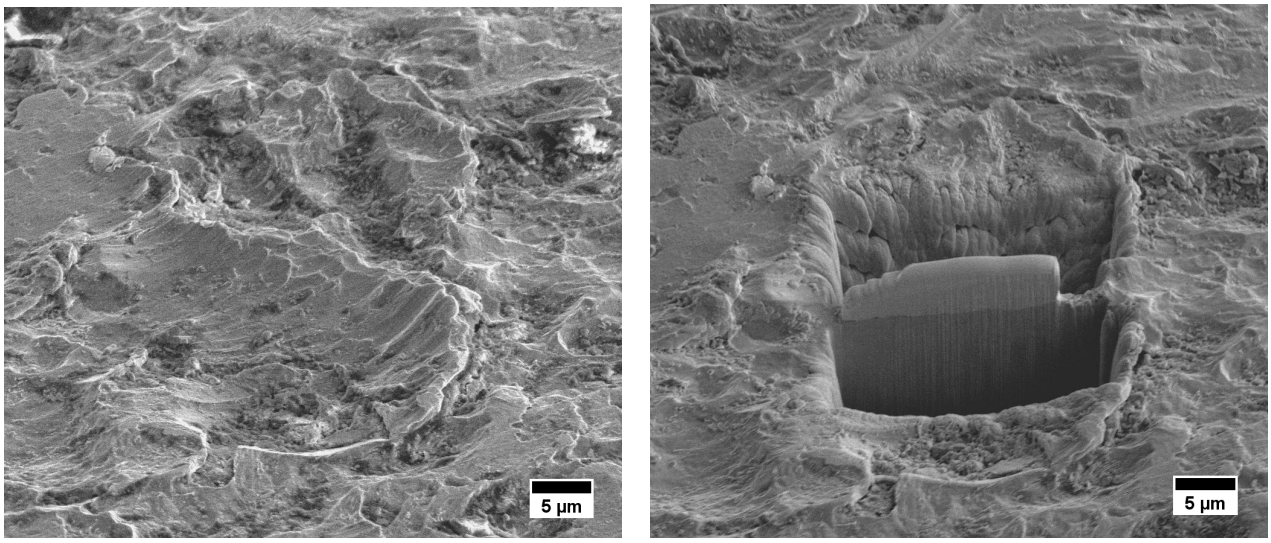


(a) (b)

Figure 6.69: SEM images captured at stage tilt of 52° showing the location of X65 carbon steel sample from where a TEM lamella was lifted out. The sample was subject to jet impingement at 90° angle at 24 $m\ s^{-1}$.

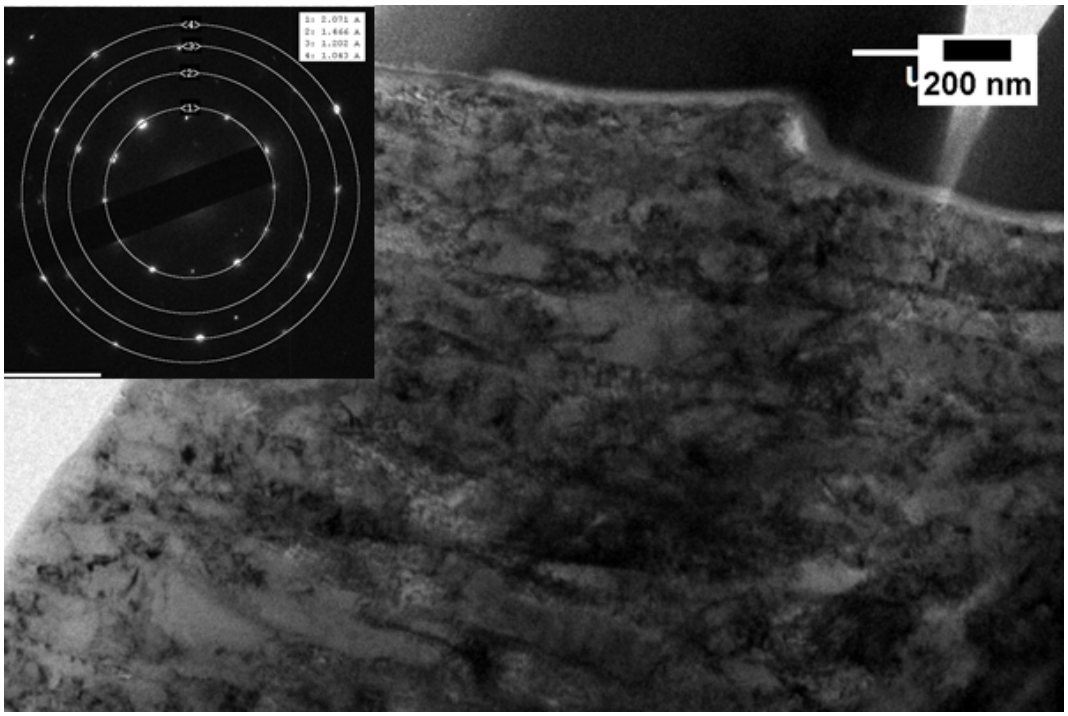


Figure 6.70: A bright field TEM image of the X65 carbon steel showing grain refinement. Inset: polycrystalline SAED pattern corresponding to {110}, {002}, {121} and {022} planes.

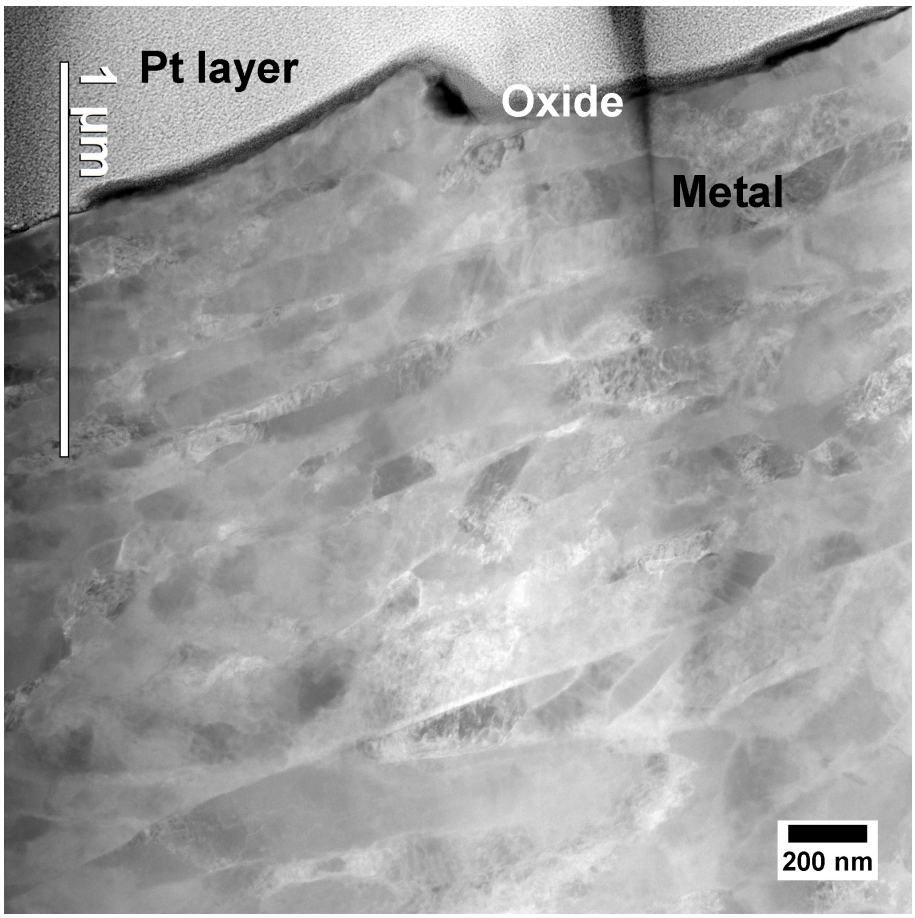


Figure 6.71: A dark field STEM image of the X65 carbon steel lamella showing the nanoscale grains formed due to jet impingement erosion-corrosion.

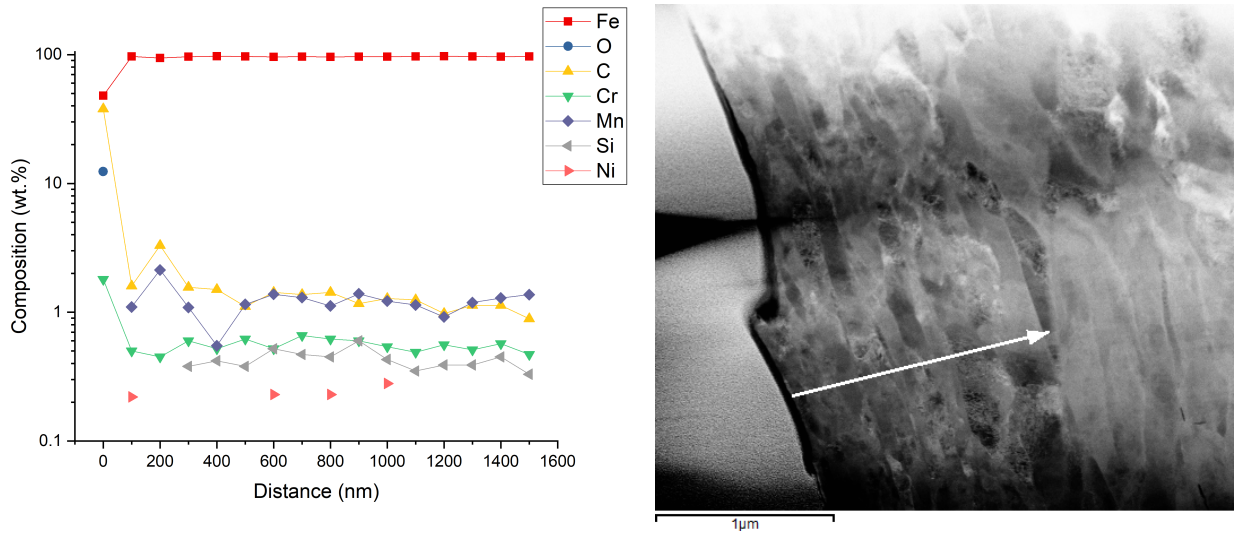


(a) (b)

Figure 6.72: a) An EDS analysis of the X65 carbon steel sample subject to jet impingement and b) a dark field STEM image showing the line along which spectra was recorded every 100 $nm$.

316L stainless steel

Figure 6.73a shows the topography of 316L stainless steel sample subject to jet impingement at 24 $m\ s^{-1}$ for 1 $h$. The SEM micrograph at 52° stage tilt with Pt layer applied can be seen in Figure 6.73b. Both cross section of the sample and the lamella show the cracks at the subsurfacen(Figure 6.73c and 6.73d).

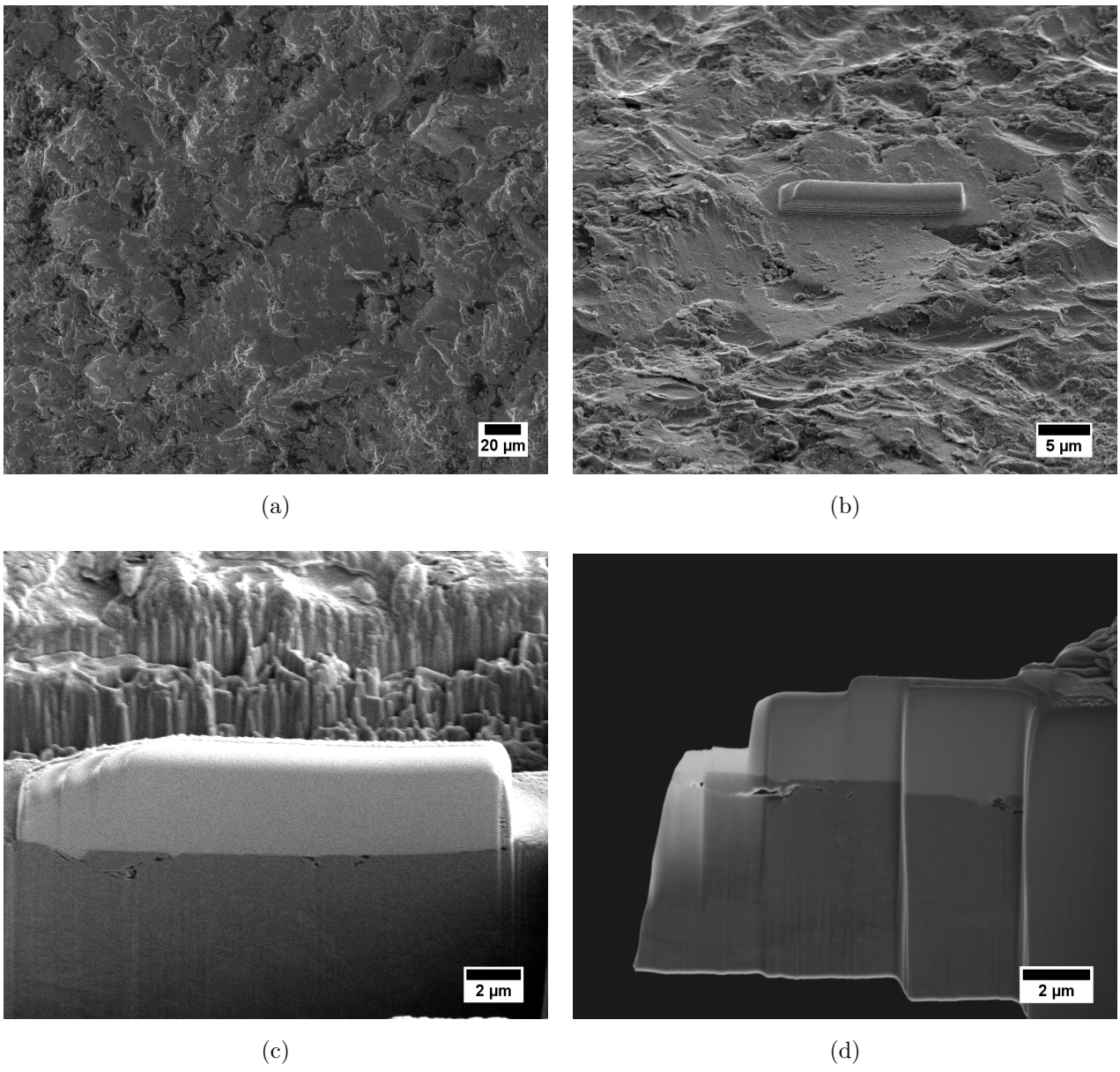


(a) (b)

(c) (d)

Figure 6.73: SEM images of the jet impinged 316L stainless steel sample showing: a) the sample at 0° stage tilt, b) the sample at 52° stage tilt, c) TEM lamella inside the trench with cracks at the subsurface, d) thinned lamella with cracks at the subsurface. The sample was subject to jet impingement at 90° angle at 24 $m\ s^{-1}$.

A low magnification bright field TEM image in Figure 6.74 shows the crack at the subsurface of the metal and the chipped metal ridge entrapped in the Pt layer. Substantial grain refinement is observed with nanoscale grains formation. Figure 6.75 shows higher magnification bright field TEM images of the damaged region next to the Pt layer. 316L stainless steel appears to be strained, as evidenced from the numerous fringes seen in Figure 6.75b. Similar fringes were observed in other studies involving erosion-corrosion of 316 stainless steel using a slurry pot erosion tester [19, 27].

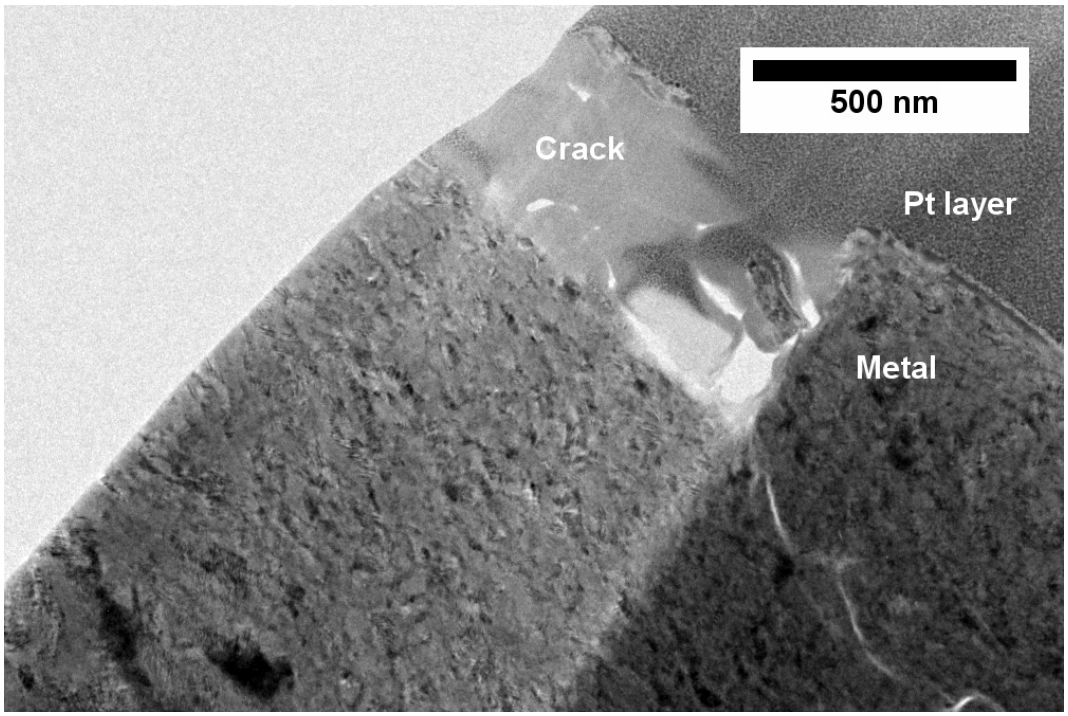


Figure 6.74: A bright field TEM image showing the lamella lifted out from 316L stainless steel sample subject to jet impingement at 90° angle at 24 $m\ s^{-1}$.

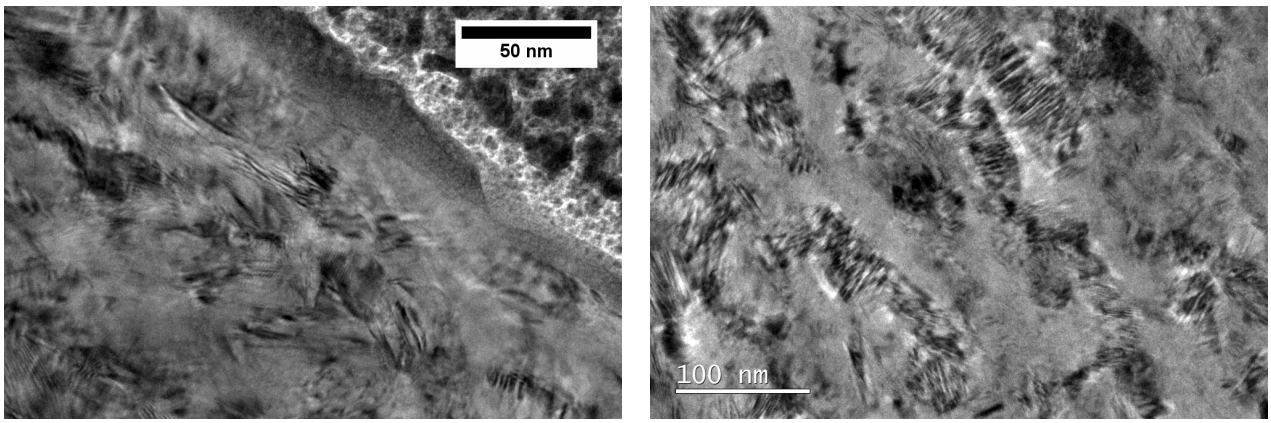


(a) (b)

Figure 6.75: Bright field TEM micrographs showing a) Pt-oxide-metal interface and b) multiple fringes found in the 316L stainless steel sample subject to jet impingement at 90°.

The SAED was performed on the area shown in Figure 6.76. Figure 6.77a shows the diffraction pattern with labelled d-spacings. The original diffraction pattern is given in Figure 6.77b. Table 6.8 shows possible lattice planes assigned to measured SAED patterns. Lattice cell parameters for austenite and ferrite were looked up from the website of Phase Transformations and Complex Properties Research Group led by Professor Sir Harry Bhadeshia [41]. Bct lattice parameters were then calculated assuming 0.03 $wt.\%$ C content in 316L stainless steels. Presence of bct planes confirms partial phase transformation of 316 austenitic stainless steel (fcc) to martensite. Similar results were obtained by other groups [27, 19]. The EDS line spectra collected shows slightly higher O composition up to 1.25 $\mu m$ into the sample suggesting possible oxide film embedment due to repeated impingement. The embedded oxides are expected to create pathways for further anodic dissolution contributing to the erosion-corrosion synergy [27].

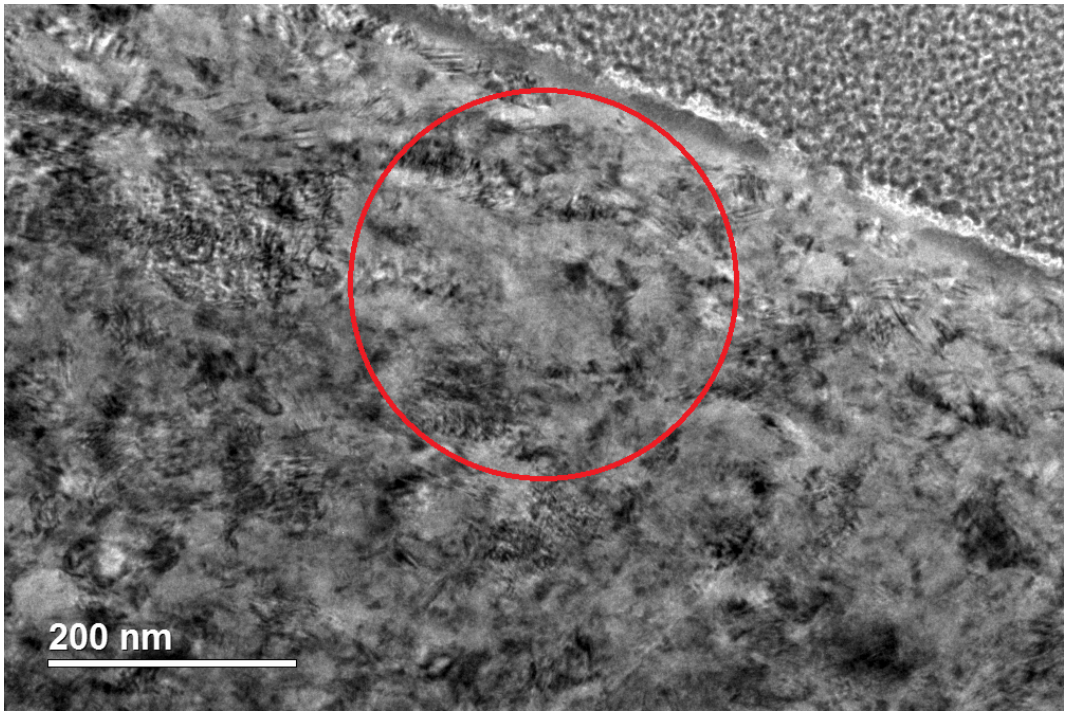


Figure 6.76: A bright field TEM image showing the location used for the SAED. The micrograph was taken by Dr Eleonora Cali [6].

[6]Due to COVID-19 restrictions on access

Table 6.8: Possible lattice planes assigned to measured SAED pattern shown in Figure 6.77

| Peak | measured d-spacing, $\mathring{A}$ | 2% error | fcc plane | theoretical d-spacing, $\mathring{A}$ | bct plane | theoretical d-spacing, $\mathring{A}$ |
|---|---|---|---|---|---|---|
| 2 | 2.015 | 0.040 | {111} | 2.05941 | {110} | 2.027275 |
| 3 | 1.667 | 0.033 | {200} | 1.78350 | | |
| 4 | 1.395 | 0.028 | | | {002} | 1.43545 |
| 5 | 1.214 | 0.024 | {220} | 1.26112 | | |
| 6 | 1.142 | 0.023 | | | {121} | 1.170713 |
| 7 | 1.000 | 0.020 | {222} | 1.02970 | {022} | 1.014326 |
| 8 | 0.907 | 0.018 | {004} | 0.89175 | {031} | 0.906748 |
| 9 | 0.813 | 0.016 | {313} | 0.81833 | {222} | 0.828006 |
| 10 | 0.756 | 0.015 | | | {312} | 0.766535 |

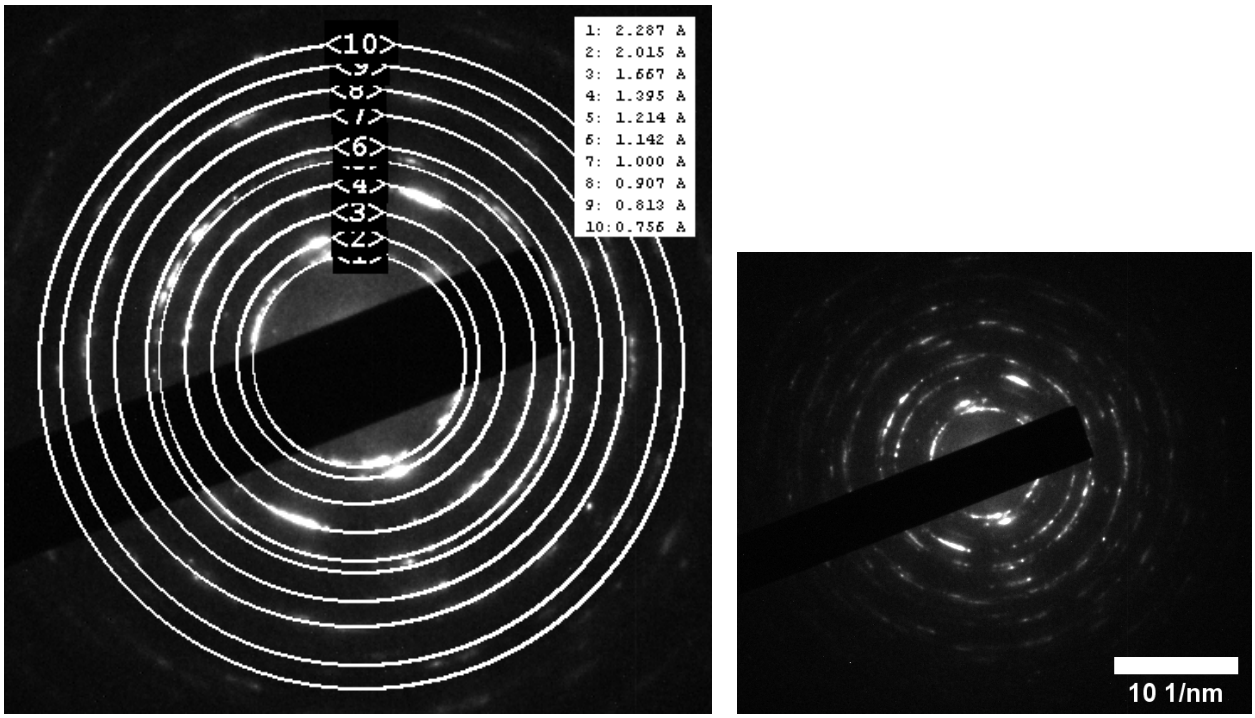


(a) (b)

Figure 6.77: a) The SAED pattern with assigned d-spacings taken from the area shown in Figure 6.76. b) The original image. The diffraction pattern was collected by Dr Eleonora Cali [7].

[7]Due to COVID-19 restrictions on access

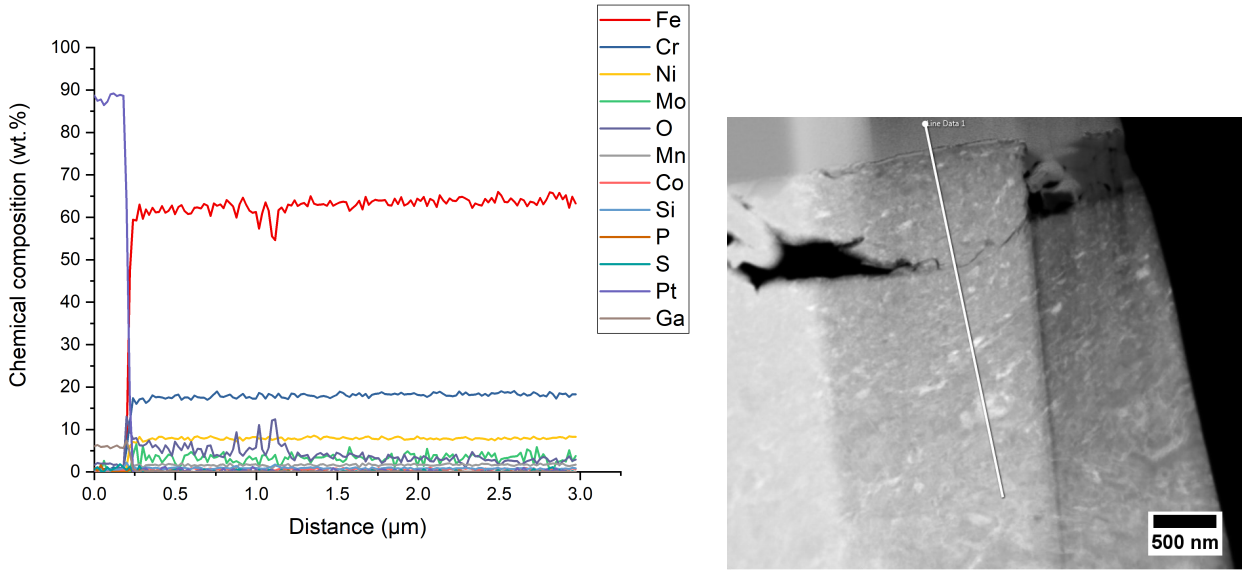


(a) (b)

Figure 6.78: a) An EDS line analysis of the 316L stainless steel sample subject to jet impingement and b) dark field STEM image showing the line along which spectra was recorded every 20 $nm$. These data were collected by Dr Eleonora Cali [8].

[8]Due to COVID-19 restrictions on access

## 6.4 Summary

Microstructural and micro-mechanical analysis of X65 carbon steel and 316 stainless steel samples was carried out in this chapter. The key results are summarised below:

- Cross section analysis of the scratched X65 carbon steel samples indicated the presence of densely packed areas and the cracks in the scratch trench. FIB-SEM analysis showed grain refinement takes place in the region directly under the scratch.

- X65 carbon steel samples repeatedly scratched 100 times at rotation rates of 100, 400 and 900 $RPM$ under passive anodic potential showed noticeably higher microhardness values near the scratched subsurface. Strain hardening as well as microstructural refinement in the scratched subsurface contributed to this. The hardness values decreased with increasing distance from the surface within 100 $\mu m$ and were lower compared to that of the bare metal microhardness. It is believed that this surface hardness degradation occurred due to application of anodic current densities [8].

- X65 carbon steel samples continuously scratched under cathodic potential had higher average hardness values compared to samples scratched under passive anodic potential. Average hardness also decreased with increasing rotation rates, possibly due to increased removal of the work hardened material at higher strain rates.

- In continuously scratched 316 stainless steel samples the highest hardness values were recorded closest to the scratch confirming work hardening. The average hardness values of the samples scratched under anodic conditions increased with increasing strain rates, but were all lower than the microhardness of the samples scratched under cathodic protection conditions suggesting possible hydrogen embrittlement or hardness degradation due to anodic current application. Further experiments are required to elucidate the exact mechanism, using techniques such as *in-situ* electrochemical nanoindentation [42].

- TEM analysis of the X65 carbon steel lamellae lifted out from scratch trenches confirmed grain refinement. Nano-sized lamellar grains formed after scratching and the size of these grains increased with increasing distance from the scratch in samples scratched under passive anodic potential. Strain induced deformation substructures were present in both pure erosion and erosion-corrosion samples. Cracks were present at the subsurface and are expected to provide pathways for erosion-enhanced corrosion.

- 316 stainless steel samples underwent strain induced partial phase transformation from austenite to martensite as confirmed by SAED analysis. Martensite could be responsible for the *in-situ* microhardness increase after scratching. The grain refinement and work hardening observed could also contribute to the hardness increase. Well defined slip markings were seen in the scratched 316 stainless steel samples. Fatigue crack nucleation takes place around the slip bands [38]. Along with oxide embedment suggested by EDS analysis and the disruption of passive film due to erosion component, cracks observed in the subsurface provide pathways for metal dissolution [27]. These factors contribute to erosion-enhanced corrosion component of total erosion-corrosion.

- Jet impingement erosion-corrosion experiments carried out at nCATS confirmed grain refinement similar to the one observed in the scratched X65 carbon steel and 316 stainless steel samples. This shows the scratching technique is representative of the conventional bulk assessment in terms of material response. Significant size reduction of the silica particles was observed after 1 $h$ experiment. Mass loss analysis did not confirm erosion-corrosion rate change with the impingement angle in X65 carbon steel due to significant contribution of the corrosion component to the total weight loss. 316 stainless steel, however, had higher erosion-corrosion rates at oblique angles due to more efficient removal of the platelets in agreement with the literature [32]. Slip markings and crack networks were observed in the 316L stainless steel samples.

Good correlation seen between the microstructural characteristics of the samples subject to the electrode scratching and jet impingement techniques suggests the electrode scratching can be widely implemented in obtaining mechanistic understanding of erosion-corrosion of steels.

# Bibliography


[1] J. Schindelin, I. Arganda-Carreras, E. Frise, V. Kaynig, M. Longair, T. Pietzsch, S. Preibisch, C. Rueden, S. Saalfeld, B. Schmid, J. Tinevez, D. J. White, V. Hartenstein, K. Eliceiri, P. Tomancak, and A. Cardona. Fiji: an open-source platform for biological-image analysis. *Nature Methods*, 9(7):676–682, 2012.

[2] W.C. Oliver and G.M. Pharr. An improved technique for determining hardness and elastic modulus using load and displacement sensing indentation experiments. *Journal of Materials Research*, 7(6):1564–1583, 1992.

[3] W. C. Oliver and G. M. Pharr. Measurement of hardness and elastic modulus by instrumented indentation: Advances in understanding and refinements to methodology. *Journal of Materials Research*, 19(01):3–20, 2004.

[4] J. Owen, C. Ramsey, R. Barker, and A. Neville. Erosion-corrosion interactions of X65 carbon steel in aqueous $CO_2$ environments. *Wear*, 414-415(August):376–389, 2018.

[5] H. Guo. *Synergism in Erosion-Corrosion Caused by Interaction of Electrochemical and Mechanical Factors*. PhD thesis, 2006.

[6] G. M. Pharr, E. G. Herbert, and Y. Gao. The indentation size effect: A critical examination of experimental observations and mechanistic interpretations. *Annual Review of Materials Research*, 40:271–292, 2010.

[7] O. Lavigne, A. Kotousov, and V. Luzin. Microstructural, mechanical, texture and residual stress characterizations of X52 pipeline steel. *Metals*, 7(8):1–10, 2017.

[8] B. T. Lu and J. L. Luo. Correlation between surface-hardness degradation and erosion resistance of carbon steel - Effects of slurry chemistry. *Tribology International*, 83:146–155, 2015.

[9] R. A. Oriani, J. P. Hirth, and M. Smialowski. *Effects of Hydrogen Environments*. William Andrew Publishing/Noyes, 1985.

[10] I. Moro, L. Briottet, P. Lemoine, E. Andrieu, C. Blanc, and G. Odemer. Hydrogen embrittlement susceptibility of a high strength steel X80. *Materials Science and Engineering A*, 527(27-28):7252–7260, oct 2010.

[11] G. Gajowiec, M. Bartmański, B. Majkowska-Marzec, A. Zieliński, B. Chmiela, and M. Derezulko. Hydrogen Embrittlement and Oxide Layer Effect in the Cathodically Charged Zircaloy-2. *Materials (Basel, Switzerland)*, 13(8), apr 2020.

[12] B. T. Lu and J. L. Luo. Synergism of electrochemical and mechanical factors in erosion-corrosion. *Journal of Physical Chemistry B*, 110(9):4217–4231, 2006.

[13] Nickel Development Institute. Design guidelines for the selection and use of stainless steel. Technical Report 9014.

[14] X.Y. Wang and D.Y. Li. Mechanical and electrochemical behavior of nanocrystalline surface of 304 stainless steel. *Electrochimica Acta*, 47(24):3939–3947, 2002.

[15] K. Sasaki and G. T. Burstein. The generation of surface roughness during slurry erosion-corrosion and its effects on the pitting potential. *Corrosion Science*, 38(12):2111–2120, 1996.

[16] G. Sundararajan. A comprehensive model for the solid particle erosion of ductile materials. *Wear*, 149(1-2):111–127, sep 1991.

[17] M. N. Majeed. *Understanding the Erosion – Corrosion Behaviour of Generic Types of Stainless Steels in a $CO_2$ – Saturated Oilfield Environment*. PhD thesis, The University of Leeds, 2018.

[18] S. S. Rajahram, T. J. Harvey, and R. J. K. Wood. Erosion-corrosion resistance of engineering materials in various test conditions. *Wear*, 267(1-4):244–254, 2009.

[19] R. J. K. Wood, J. C. Walker, T. J. Harvey, S. Wang, and S. S. Rajahram. Influence of microstructure on the erosion and erosion-corrosion characteristics of 316 stainless steel. *Wear*, 306(1-2):254–262, 2013.

[20] T. A. Adler and R. P. Walters. Corrosion and wear of 304 stainless steel using a scratch test. *Corrosion Science*, 33(12):1855–1876, 1992.

[21] T. A. Adler and R. P. Walters. Wear and scratch hardness of 304 stainless steel investigated with a single scratch test. *Wear*, 162-164(PART B):713–720, 1993.

[22] Sir H. Bhadeshia and Institute Of Materials. *Bainite in Steels*. Institute of Materials, Minerals and Mining, London, United Kingdom, 2000.

[23] C. B. Carter and D. B. Williams. *Transmission electron microscopy: Diffraction, imaging, and spectrometry*. 2016.

[24] Chapter 2 - The Deformed State. In J. Humphreys, G. S. Rohrer, and A. Rollett, editors, *Recrystallization and Related Annealing Phenomena*, pages 13–79. Elsevier, Oxford, third edition, 2017.

[25] P. I. Marshall and G. T. Burstein. The coupled kinetics of film growth and dissolution of stainless steel repassivating in acid solutions. *Corrosion Science*, 24(5):449–462, 1984.

[26] S. Preibisch, S. Saalfeld, and P. Tomancak. Globally optimal stitching of tiled 3D microscopic image acquisitions. *Bioinformatics*, 25(11):1463–1465, 2009.

[27] S. S. Rajahram, T. J. Harvey, J. C. Walker, S. C. Wang, and R. J. K. Wood. Investigation of erosion-corrosion mechanisms of UNS S31603 using FIB and TEM. *Tribology International*, 46(1):161–173, 2012.

[28] Jr. W. D. Callister and D. G. Rethwisch. *Materials Science and Engineering*. John Wiley & Sons Ltd, sep 2020.

[29] S. Brinckmann and G. Dehm. Nanotribology in austenite: Plastic plowing and crack formation. *Wear*, 338-339:436–440, 2015.

[30] E. Herms, J. M. Olive, and M. Puiggali. Hydrogen embrittlement of 316L type stainless steel. *Materials Science and Engineering A*, 272(2):279–283, nov 1999.

[31] C. T. Rueden, J. Schindelin, M. C. Hiner, B. E. DeZonia, A. E. Walter, E. T. Arena, and K. W. Eliceiri. ImageJ2: ImageJ for the next generation of scientific image data. *BMC Bioinformatics*, 18(1):1–26, 2017.

[32] G. T. Burstein and K. Sasaki. Effect of impact angle on the slurry erosion-corrosion of 304L stainless steel. *Wear*, 240(1-2):80–94, 2000.

[33] M. Parsi, K. Najmi, F. Najafifard, S. Hassani, B. S. McLaury, and S. A. Shirazi. A comprehensive review of solid particle erosion modeling for oil and gas wells and pipelines applications. *Journal of Natural Gas Science and Engineering*, 21:850–873, 2014.

[34] M. M. Stack, F. H. Stott, and G. C. Wood. Review of mechanisms temperatures of erosion-corrosion of alloys at elevated. *Wear*, 162-164:706–712, 1993.

[35] Y. Zhang, B. S. McLaury, S. A. Shirazi, and E. F. Rybicki. A two-dimensional mechanistic model for sand erosion prediction including particle impact characteristics. *NACE - International Corrosion Conference Series*, (10378):1–19, 2010.

[36] H. S. Grewal, H. Singh, and E. Yoon. Interplay between erodent concentration and impingement angle for erosion in dilute water–sand flows. *Wear*, 332-333:1111–1119, 2015.

[37] R. Bellman and A. Levy. Erosion mechanism in ductile metals. *Wear*, 70(1):1–27, 1981.

[38] J. Man, M. Valtr, A. Weidner, M. Petrenec, K. Obrtlk, and J. Polk. AFM study of surface relief evolution in 316L steel fatigued at low and high temperatures. *Procedia Engineering*, 2(1):1625–1633, 2010.

[39] I. M. Hutchings. Ductile-brittle transitions and wear maps for the erosion and abrasion of brittle materials. *Journal of Physics D: Applied Physics*, pages A212–A221, 1992.

[40] W. Li and D. Y. Li. Influence of surface morphology on corrosion and electronic behavior. *Acta Materialia*, 54(2):445–452, 2006.

[41] Sir H. Bhadeshia. Phase Transformations & Complex Properties Research Group.

[42] M. Iannuzzi, A. Barnoush, and R. Johnsen. Materials and corrosion trends in offshore and subsea oil and gas production. *npj Materials Degradation*, 1(2), 2017.

## 6.5 Supplementary information

X65 carbon steel samples scratched at 0.6 $V$ *vs.* MSE

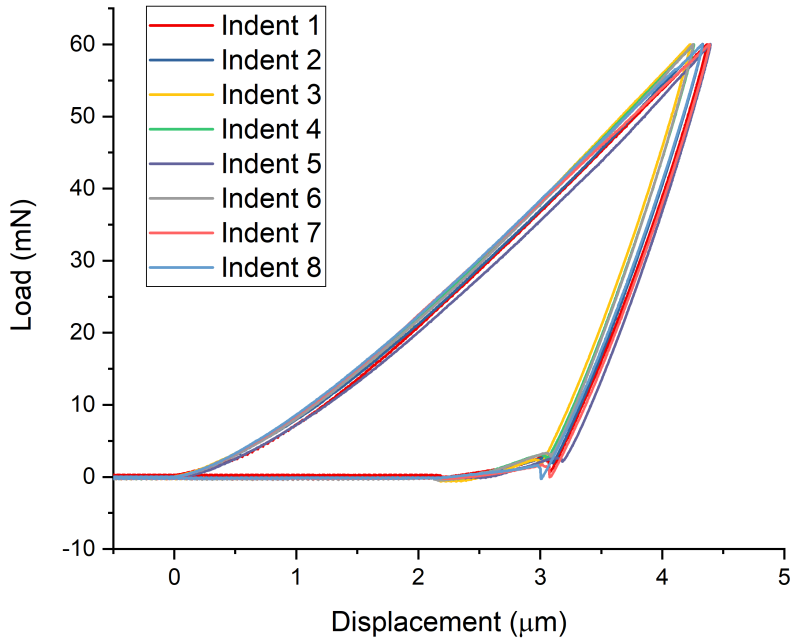


Figure 6.79: Load-displacement curves recorded during micro-indentation of the X65 carbon sample cross section after scratching at 25 $RPM$ under 0.6 $V$ *vs.* MSE.

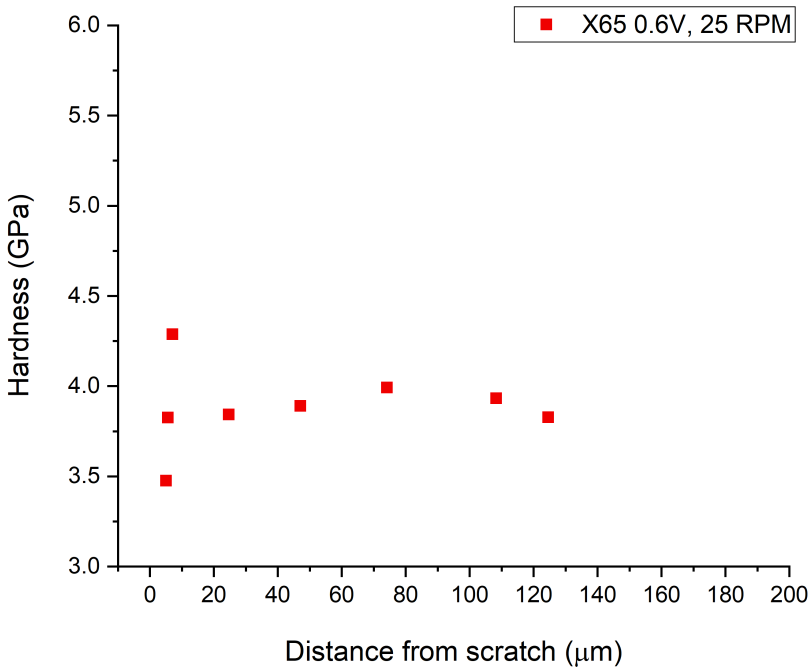


Figure 6.80: Microhardness of the X65 carbon steel samples subject to erosion-corrosion at 25 $RPM$ as a function of distance from scratch.

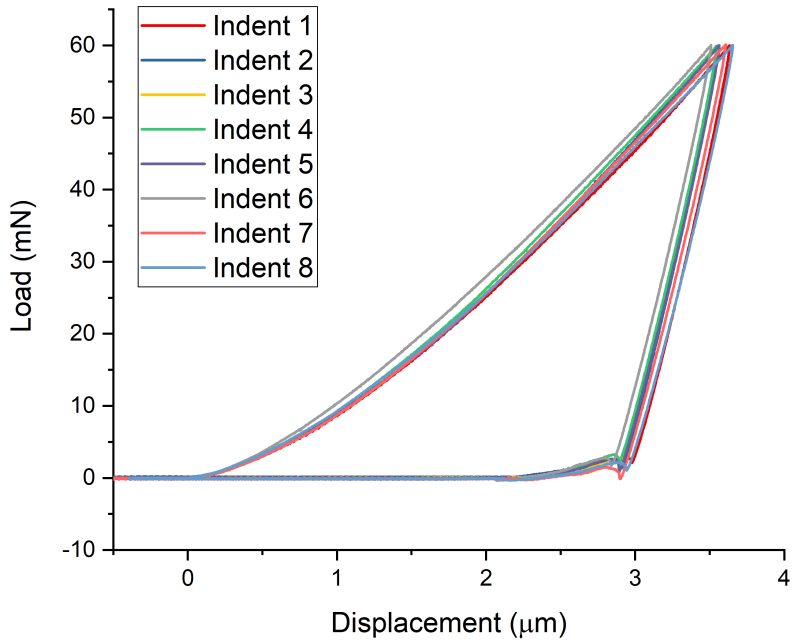


Figure 6.81: Load-displacement curves recorded during micro-indentation of the X65 carbon sample cross section after scratching at 50 $RPM$ under 0.6 $V$ *vs.* MSE.

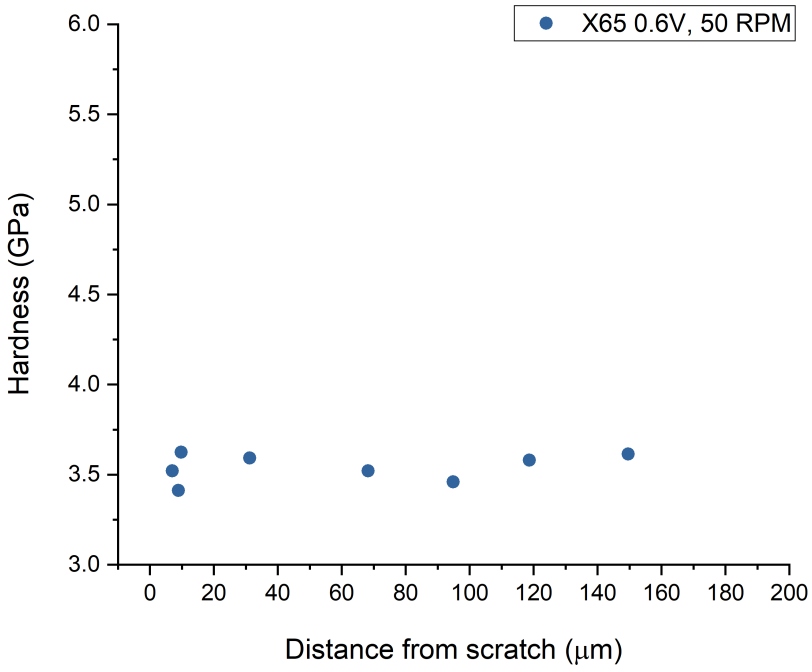


Figure 6.82: Microhardness of the X65 carbon steel samples subject to erosion-corrosion at 50 $RPM$ as a function of distance from scratch.

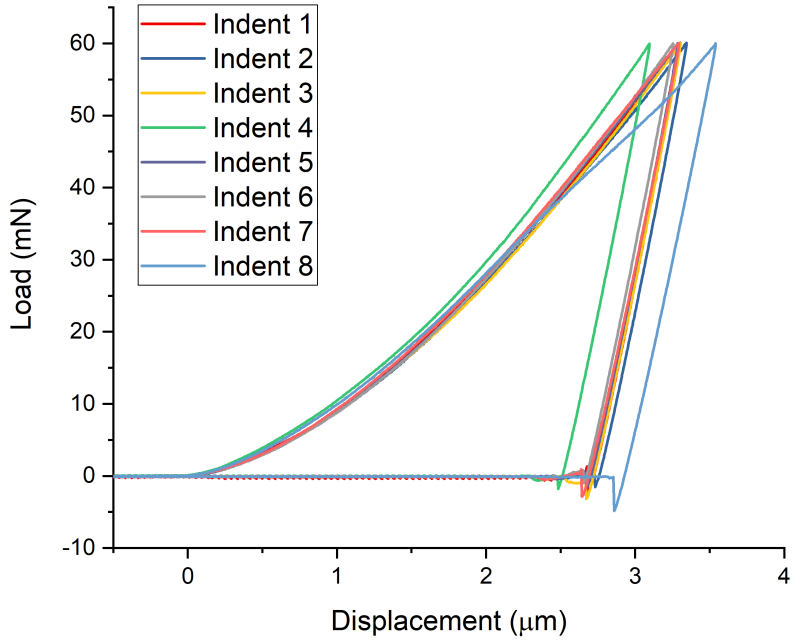


Figure 6.83: Load-displacement curves recorded during micro-indentation of the X65 carbon sample cross section after scratching at 100 $RPM$ under 0.6 $V$ *vs.* MSE.

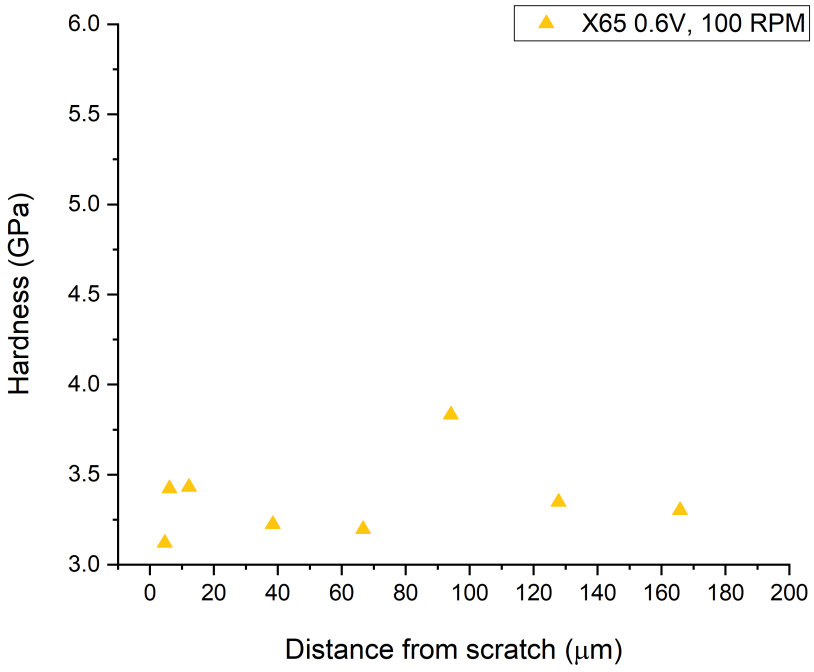


Figure 6.84: Microhardness of the X65 carbon steel samples subject to erosion-corrosion at 50 $RPM$ as a function of distance from scratch.

X65 carbon steel samples scratched at -1.5 $V$ *vs.* MSE

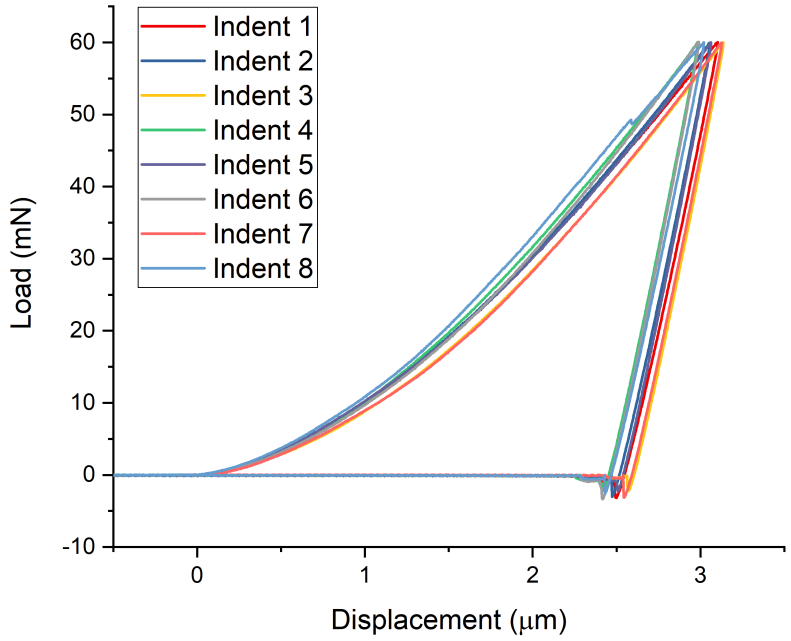


Figure 6.85: Load-displacement curves recorded during micro-indentation of the X65 carbon sample cross section after scratching at 50 $RPM$ under -1.5 $V$ *vs.* MSE.

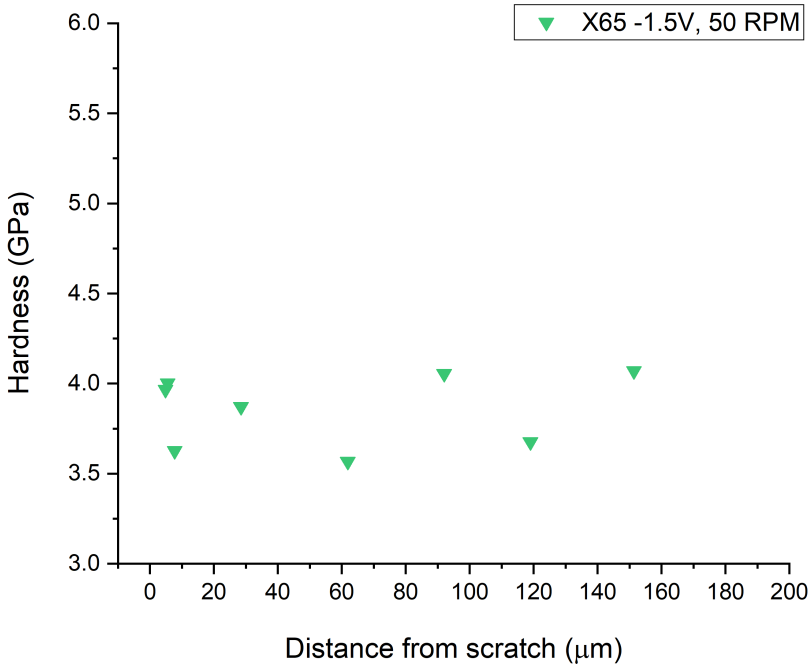


Figure 6.86: Microhardness of the X65 carbon steel samples subject to pure erosion at 50 $RPM$ as a function of distance from scratch.

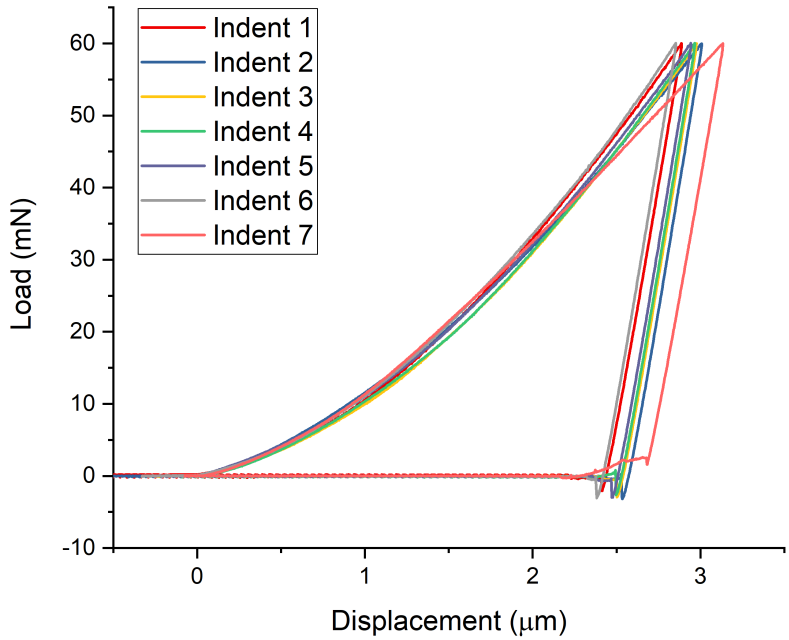


Figure 6.87: Load-displacement curves recorded during micro-indentation of the X65 carbon sample cross section after scratching at 100 $RPM$ under -1.5 $V$ *vs.* MSE.

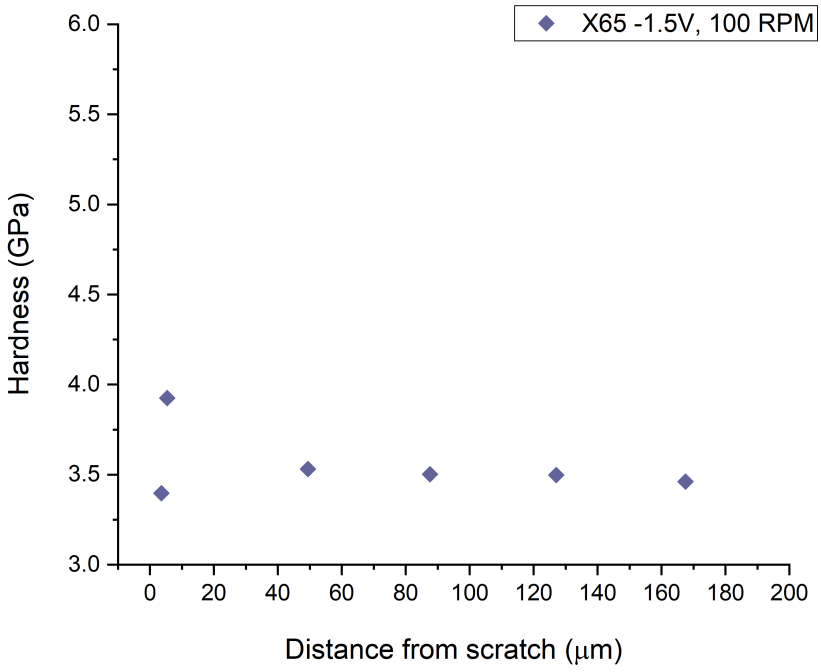


Figure 6.88: Microhardness of the X65 carbon steel samples subject to pure erosion at 100 $RPM$ as a function of distance from scratch.

316 stainless steel samples scratched at -1.5 $V$ *vs.* MSE

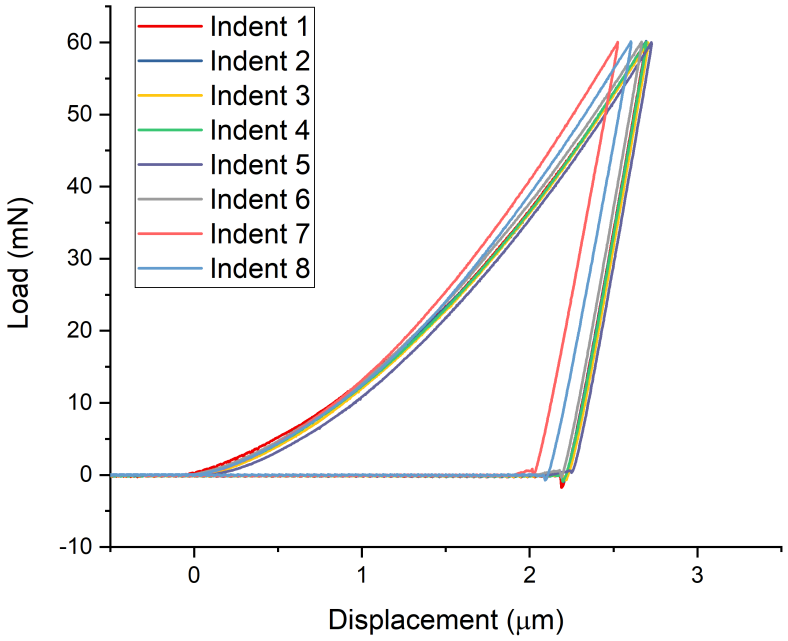


Figure 6.89: Load-displacement curves recorded during micro-indentation of the 316 stainless steel sample cross section after scratching at 25 $RPM$ under -1.5 $V$ *vs.* MSE.

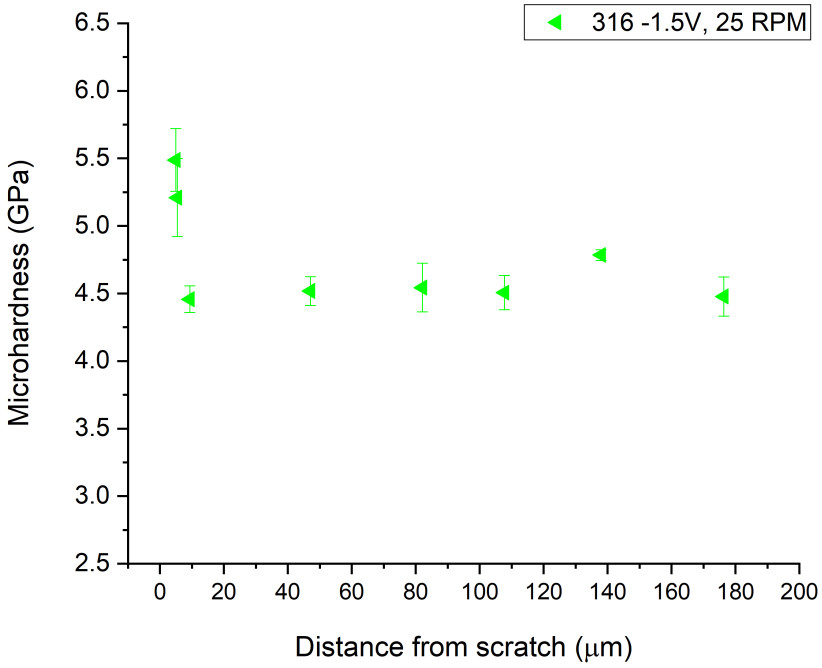


Figure 6.90: Microhardness of the 316 stainless steel samples subject to pure erosion at 25 $RPM$ as a function of distance from scratch.

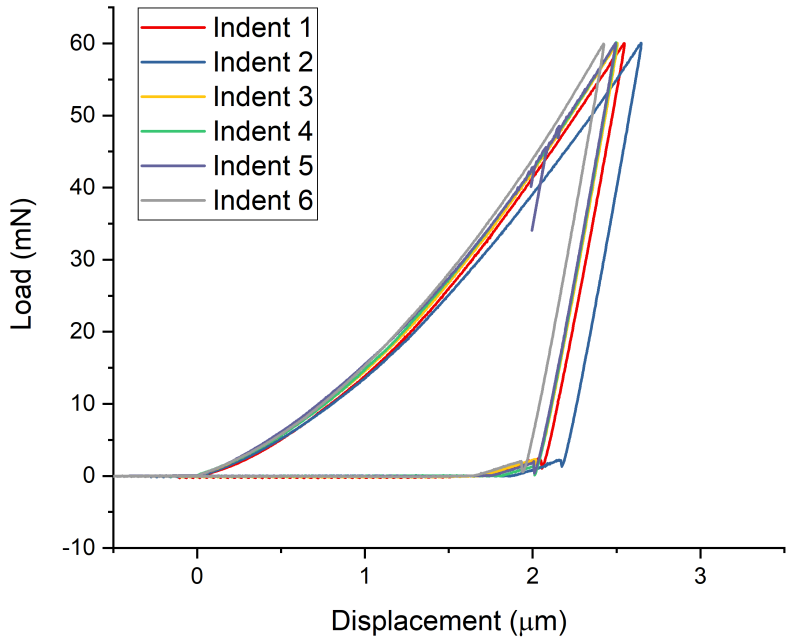


Figure 6.91: Load-displacement curves recorded during micro-indentation of the 316 stainless steel sample cross section after scratching at 50 $RPM$ under -1.5 $V$ *vs.* MSE.

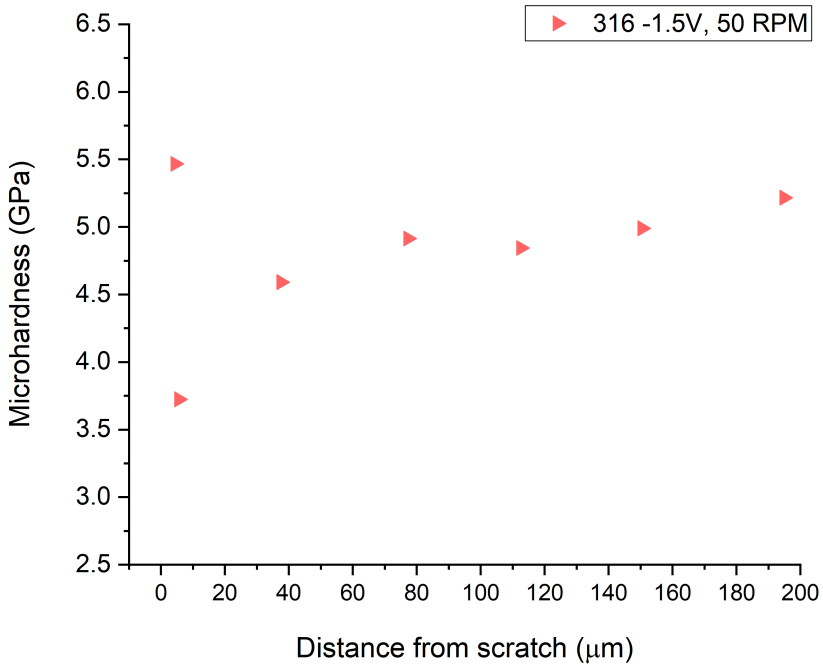


Figure 6.92: Microhardness of the 316 stainless steel samples subject to pure erosion at 50 $RPM$ as a function of distance from scratch.

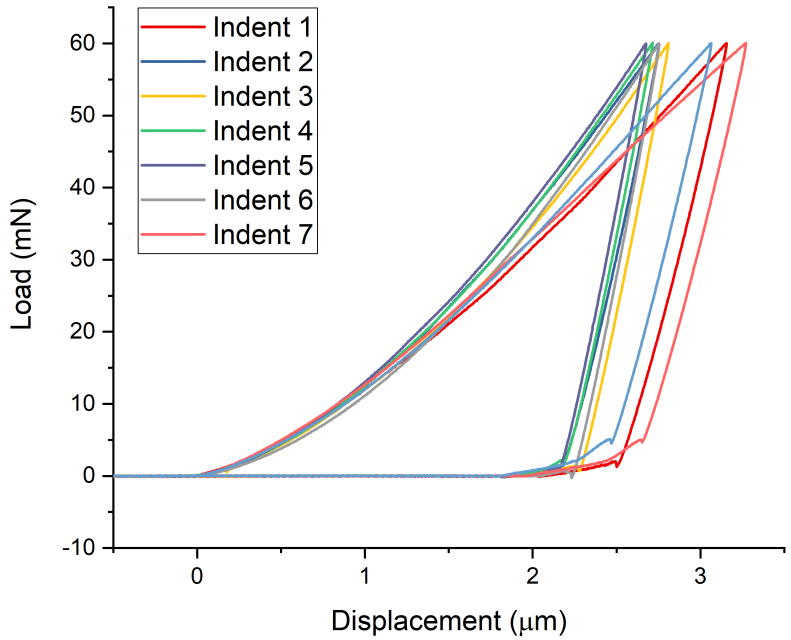


Figure 6.93: Load-displacement curves recorded during micro-indentation of the 316 stainless steel sample cross section after scratching at 100 $RPM$ under -1.5 $V$ *vs.* MSE.

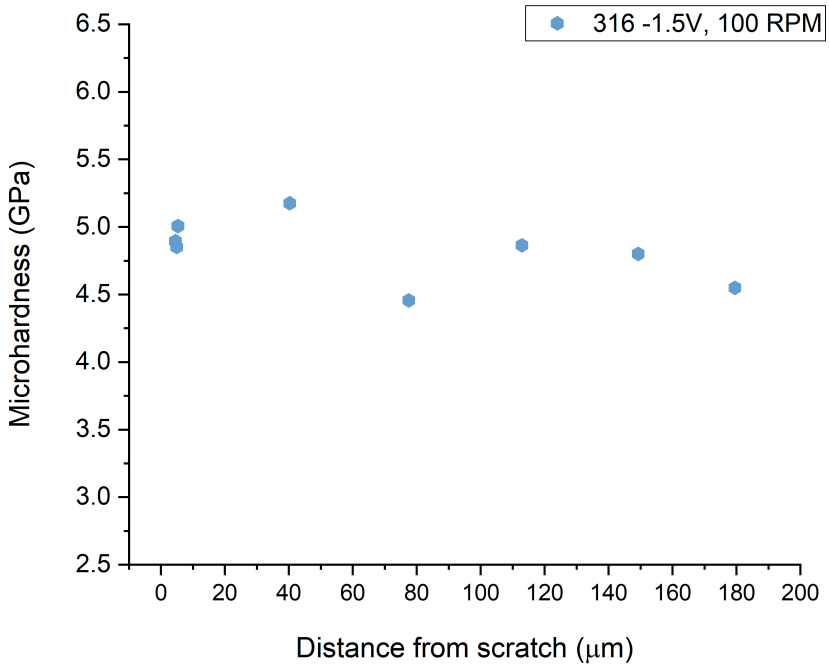


Figure 6.94: Microhardness of the 316 stainless steel samples subject to pure erosion at 100 $RPM$ as a function of distance from scratch.

# Chapter 7

# Effect of inhibitors on passivation behaviour

## 7.1 Overview

In this chapter the potential use of the electrode scratching setup in inhibitor testing applications is demonstrated. Linear scanning voltammetry experiments were conducted at different concentrations of an n-alkyl quarternary ammonium bromide concentrations to choose optimal concentration of a mixed inhibitor for further potentiostatic scratching tests. Similarly, anodic inhibitor (sodium nitrite) containing solutions were tested for corrosion inhibition.

Coupling electrochemical tests with scanning electron microscopy results, the efficiency of corrosion inhibitors was evaluated at different potentials. While TTAB proved to be efficient during potentiostatic scratching in pH 4.0 solutions near the corrosion potential of -0.9 $V$ *vs.* MSE and the active anodic potential of -0.4 $V$ *vs.* MSE, numerous pitting sites were found at the passive potential of 0.6 $V$ *vs.* MSE. Despite the fact that $NaNO_2$ passivators are rarely used in acidic solutions, it was possible to establish that sodium nitirite containing solutions at pH 4.0 passivated quicker at an applied passive potential of 0.6 $V$ *vs.* MSE.

It is believed that using the techniques outlined in this chapter, quick assay testing of inhibitor formulations can be performed for industrial applications.

## 7.2 Introduction

Corrosion inhibitors (CI) are chemical compounds that can reduce the corrosion rates of metals when added to media in very small quantities. The efficiency of the inhibitors is expressed *via* equation 7.1:

$$\eta = \frac{CR_0 - CR}{CR_0} \times 100\% \tag{7.1}$$

where $CR_0$ is the corrosion rate without an inhibitor and $CR$ is the corrosion rate with inhibitor.

CI are chosen based on the environment and the metal to be protected, and can be classified into environmental conditioners and interface inhibitors [1]. *Environmental conditioners*, sometimes referred to as environmental scavengers, deplete corrosive substances from the environment. Oxygen scavengers (*e.g.*: hydrazine, products based on hydroxyl amines and quinones) can reduce the rate of oxygen reduction in near-neutral and alkaline solutions [1, 2].

*Interface inhibitors*, in turn, mitigate corrosion *via* film formation at the metal/electrolyte interface. Depending on whether these inhibitors suppress anodic, cathodic or both reactions, they can be classified into anodic, cathodic or mixed inhibitors. Anodic inhibitors are usually strong oxidizers that help form an oxide film on the anode. Example of these passivating inhibitors are chromates, nitrites and nitrates in non-oxygenated environments, as well as molybdates and phosphates in oxygenated environments [3]. Among these, nitrites have been extensively used as CI in reinforced concrete [4] and nuclear power plants [5]. A suggested mechanism of passivation is the following [4]:

$$2\,Fe^{2+} + 2\,OH^- + 2\,NO_2^- \longrightarrow 2\,NO + Fe_2O_3 + H_2O \tag{7.2}$$

$$Fe^{2+} + OH^- + NO_2^- \longrightarrow NO + FeOOH \tag{7.3}$$

Although nitrites are mostly used in neutral and alkaline media, it has been shown that they are efficient in near-neutral media with pH between 6 and 7 [6]. Anodic inhibitors have a critical concentration above which they become effective, and this depends on the concentration of aggressive ions, such as chlorides and sulphates, present in the system [6]. For example, in pH 6 solution a minimum amount of $NaNO_2$ necessary to inhibit corrosion was 600 *ppm* [7]. Further to this, to prevent corrosion in the seawater it was said that the amount of the nitrite should be equal or more than the chloride concentration [8].

The majority of corrosion inhibitors are organic compounds that act as mixed inhibitors. These compounds adsorb on metal surface *via* physisorption, chemisorption or film formation.

Organic mixed inhibitors replace water molecules adsorbed on the metal *via* equation 7.4:

$$[\text{Inhibitor}]_{\text{soln}} + n\text{H}_2\text{O}_{\text{ads}} \longrightarrow [\text{Inhibitor}]_{\text{ads}} + n\text{H}_2\text{O}_{\text{soln}} \tag{7.4}$$

with $n$ being the number of water molecules displaced by each inhibitor molecule. Electrostatic interaction between the metal and the anchoring group results in physical adsorption of these inhibitors. If this relatively low activation energy step is followed by formation of a chemical bond between the metal and the inhibitor molecule, then a chemisorption step takes place. Unlike the reversible physisorption step, chemisorption is non-reversible. Adsorbed inhibitors may also react to produce insoluble polymer films protecting the metal from solution [1].

Corrosion inhibition efficiency, $\eta$, can be related to surface coverage, $\theta$, of the inhibitors *via* equation 7.5. The equation involves an assumption that the adsorption provides total protection, where the corrosion is prevented on the metal sites covered by an inhibitor, while corrosion reactions take place at inhibitor-free areas. It should be mentioned that while this assumption provides a good qualitative basis for CI behaviour, it does not always hold true - some studies reported more efficient corrosion inhibition at low surface coverage ($\eta < 0.1$) compared to high surface coverage [9]. Adsorption isotherms can be plotted to deduce the strength of adsorption, *e.g.* surface coverage over concentration *versus* concentration of the inhibitor in Langmuir isotherm (Equations 7.6, 7.7, 7.8).

$$\theta = \frac{\eta}{100} \tag{7.5}$$

$$\frac{\theta}{1-\theta} = K \times c_i \tag{7.6}$$

$$\frac{c_i}{\theta} = \frac{1}{K} + c_i \tag{7.7}$$

where $c_i$ is the concentration of the inhibitor and $K$ is the adsorption equilibrium constant defined in Equation 7.8.

$$K = \frac{1}{c_{solvent}} \times exp\left(\frac{-\Delta G_{ads}}{RT}\right) \tag{7.8}$$

where $c_{solvent}$ is the molar concentration of the solvent and $\Delta G_{ads}$ is the Gibbs' free energy of adsorption.

Quaternary ammonium salts (quats) are widely used in commercial inhibitors. Quats are cationic surfactants consisting of a positively charged hydrophilic head, with a quarternary nitrogen group acting as an anchoring point, and a neutral alkyl hydrophobic tail [1]. The hydrophilic head of those molecules is anchored to the metal anode. Unlike amines that must be

in protonated state to act as surfactants, the adsorption of quats does not depend on pH [10]. Higher homologues of n-alkyl quaternary ammonium compounds were shown to have better solubility compared to primary amines. Corrosion inhibition efficiency of n-alkyl trimethylammonium bromides increased with increasing alkyl chain length [11].

Depending on their concentration, quats can either form single or multilayers on the metal surface. It was proposed that this depends on the critical micelle concentration (CMC). Micelles are formed spontaneously above the CMC, while surface tension stays constant (Figure 7.1) [12]. Hence, at concentrations below the CMC, surfactants are adsorbed on the metal in a single layer (either parallel or perpendicular to the surface) – addition of further inhibitors to the solution increases CI efficiency. When the concentration reaches the CMC value, lateral interaction of adsorbed molecules leads to an abrupt increase in adsorption. It is said that at this stage, the monomers are arranged vertically, leading to formation of hemi-miscelles. Highly charged miscelles lead to faster adsorption of the monomers, efficiently blocking the metal surface and preventing corrosion [12]. At concentrations above the CMC, addition of further surfactants leads to micelle formation as well as multilayer formation on the metal [10]. It is inconclusive whether addition of corrosion inhibitors at concentrations above the CMC significantly improves CI efficiency. In general, surfactants with low CMC values are preferred in CI applications.

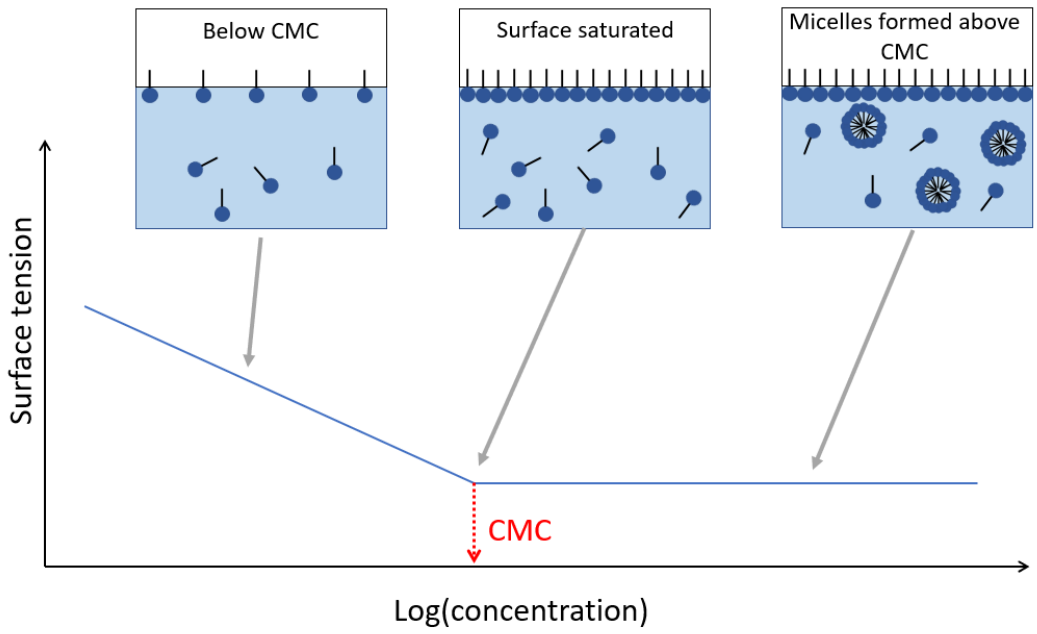


Figure 7.1: Depiction of change of surface tension with increasing surfactant concentration. Micelles form spontaneously at CMC, with surface tension staying constant.

## 7.3 Experimental

### 7.3.1 Solutions

10.211 $g$ of potassium hydrogen phthalate (KHP) (VWR Chemicals, ≥99.5% AnalaR NORMAPUR®) was dissolved in 500 $mL$ of DI water, 13 $mL$ of 0.1 $M$ NaOH and DI water added to yield a 1 $L$ solution. The resultant pH of this buffer solution was 4.00±0.05.

0.500 $g$ of (1-tetradecyl)trimethylammonium bromide (TTAB) (Alfa Aesar, 98%) and 0.500 $g$ (1-dodecyl)trimethylammonium bromide (DTAB) (Alfa Aesar, 99%) were used to prepare 10,000 $ppm$ 50.0 $mL$ stock solutions of TTAB and DTAB respectively. The stock solution was then diluted to prepare the solutions with varying concentrations of the inhibitor (*e.g.* 4.55 $mL$ of selected TAB solution was added to 450 $mL$ KHP buffer electrolyte to yield *ca.* 100 $ppm$ TAB solution).

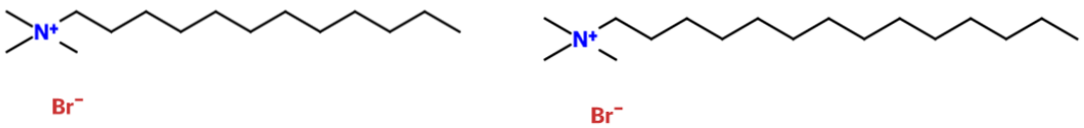


(a) (b)

Figure 7.2: Structural formulas of a) DTAB and b) TTAB drawn using eMolecules.

Similarly, 0.500 g of sodium nitrite (Aldrich, 97% ACS reagent) was used to prepare 10,000 $ppm$ 50.0 $mL$ stock solution. 4.55 $mL$ of this $NaNO_2$ solution was then added to 450 $mL$ KHP electrolyte to yield 100 $ppm$ $NaNO_2$ solution.

0.500 g of potassium bromide (Sigma Aldrich, 99% ACS reagent) was dissolved in DI water to yield 10,000 $ppm$ solution. 4.55 $mL$ of this stock solution was added to 450 $mL$ KHP electrolyte to yield *ca.* 100 $ppm$ KBr solution.

### 7.3.2 Materials

API X65 carbon steel samples were used as received from Shell Technology Centre Houston. Typical chemical composition (wt.%) of as-received X65 carbon steel C 0.09, Cr 0.11, Cu 0.14, Mn 1.07, Mo 0.09, Ni 0.10, Si 0.28 and Fe balance was confirmed using both EDX in SEM and TEM. The microstructure of the material corresponded to that of lower bainite, with austenitic and ferritic grains (Figure 4.1).

5 *mm* outer diameter (OD) discs were cut using Electrical Discharge Machining (EDM). The discs were embedded in bakelite resin, ground and polished to 1 µm finish using Buehler PlanarMet$^{TM}$ 300 grinder-polisher. The samples were cleaned between each grinding and polishing step using water and isopropanol. Metal samples were kept in a desiccator.

X65 carbon steel discs were used as the working electrode in a rotating disc electrode assembly. The discs were inserted into the RDE tip that had a PEEK shroud with PTFE U-cup to prevent crevice corrosion. The working electrode disc was electrically connected to the RDE tip *via* a gold connector.

### 7.3.3 Electrochemical scratching procedure

A detailed description of the setup was previously presented in Chapter 3 section 3.2.3. Electrochemical measurements were performed on a three-electrode system controlled *via* an Ivium CompacStat potentiostat, with a X65 carbon steel disc used as WE, Pt wire as CE and mercury-mercurous sulphate electrode (MSE) as RE. KHP buffer was used as electrolyte and was purged with high purity Ar for 1 *h* before the tests, with low rate bubbling and Ar blanket during the tests.

The rotation rate of the RDE was set to 50 RPM. Linear scanning voltammetry tests were run from -1.2 *V* to 0.4 *V vs.* MSE at a scan rate of 1 $mV\ s^{-1}$ with varying concentrations of DTAB and TTAB to establish the optimal n-alkyl quaternary ammonium compound concentration.

Scratching experiments were carried out in 100 *ppm* solutions of TTAB and $NaNO_2$ at three different constant potentials: -0.9, -0.4 and 0.6 *V vs.* MSE. The moment of addition of the inhibitor to the solution is clearly marked on each graph. In this way the experiment provides information on both the uninhibited and inhibited system. Current was recorded in 0.1 s intervals, with auto current ranging set between 10 *mA* and 10 *nA*. The frequency of scratching was set using an Arduino microcontroller connected to the solenoid that was on for 60 *s* and off for *ca.* 1.2 *s*. When the solenoid was off, the weight at the end of the scratching arm caused the diamond tip to go up and scratch the surface of the X65 carbon steel. This procedure continued for the duration of the experiment. The length of the potentiostatic amperometry tests varied from 2000 to 3600 *s*. The electrode and solution were replaced at the end of each test, and the CE and RE were thoroughly cleaned.

### 7.3.4 Characterisation

Samples were characterised using a LEO Gemini 1525 FEG SEM at an accelerating voltage of 5 $kV$ for surface characterisation and 15 $kV$ for Energy-dispersive X-ray spectroscopy (EDS), unless otherwise stated. Oxford Instruments INCA Point ID was used for chemical analysis.

## 7.4 Results and discussion

### 7.4.1 LSV in presence of n-alkyl quaternary ammonium compounds

LSV experiments of X65 carbon steel working electrode at varying concentrations of DTAB and TTAB were performed. This allowed exploration of the fundamental behaviour of X65 carbon steel in the presence of n-alkyl quaternary ammonium compounds. As the potential of the working electrode is swept from negative to positive, the sorption mechanisms change. Time resolved neutron reflectivity studies indicated potential-dependent adsorption and desorption of an anionic surfactant on a metal substrate [13]. Unfortunately, no LSV was performed in sodium nitrite solutions due to time constraint. Literature reported linear scanning voltamograms of mild steel in pH 9 solution show passivation at 1000 *ppm* concentrations of $NaNO_2$ [14].

Figure 7.3 illustrates the difference in inhibition behaviour of DTAB and TTAB quats in mildly acidic media under deaerated conditions. Addition of quats shifted the corrosion potential to more anodic values and Tafel extrapolation reveals lower corrosion rates. Mixed inhibitors such as quats can block both anodic and cathodic sites, which can be elucidated from the changing Tafel slopes in Figure 7.3 upon the addition of the corrosion inhibitor. It should be noted that inhibition provided by DTAB (Figure 7.3a) was not consistent, while inhibition in TTAB containing solutions was reproducible.

Increasing concentrations of TTAB in solution from 0 to 10 *ppm* resulted in about a three times reduction in corrosion rate (Table 7.1). While further increase in TTAB concentration to 100 *ppm* did not improve CI efficiency, it did induce earlier passivation, which as was suggested in Chapter 4, took place due to salt film passivation. Increasing TTAB concentration from 100 to 300 *ppm* did not result in any notable change in recorded linear polarisation curves. There is a local variation in current densities in the passivation region common for all concentrations of TTAB between -0.15 and 0.4 $V$ *vs.* MSE. This could be due to an altered morphology of salt film layer and/or a change of adsorption behaviour both with increasing inhibitor concentration and change of potential.

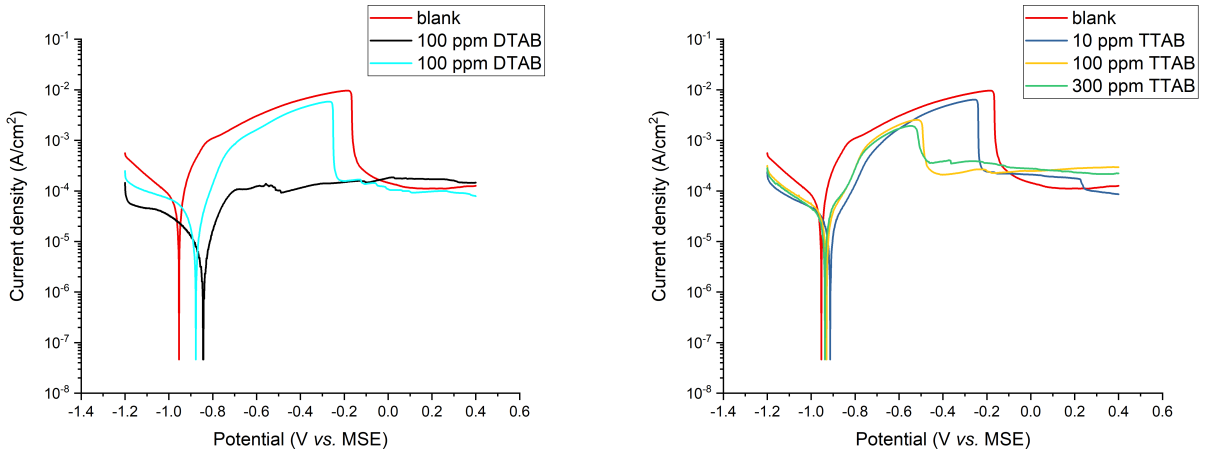


(a) (b)

Figure 7.3: Linear scanning voltammograms of X65 carbon steel in solutions containing a) 100 *ppm* of (1-dodecyl)trimethylammonium bromide (DTAB) and b) different concentrations of (1-tetradecyl)trimethylammonium bromide (TTAB). Tests are conducted at room temperature in Ar-saturated aqueous potassium hydrogen phthalate (KHP) buffer solution at pH 4.0.

Table 7.1: Corrosion rates of X65 carbon steel in pH 4.0 KHP electrolyte with different concentrations of n-alkyl quaternary ammonium compounds.

| Solution | $E_{corr}$, V | $\log(i_{corr})$ | $i_{corr}$, $A\,cm^{-2}$ | CR, $mm\,year^{-1}$ | $\eta$, % |
|---|---|---|---|---|---|
| blank | -1.09 | -4.08 | $8.4\times10^{-5}$ | 0.98 | 0 |
| 10 *ppm* TTAB | -0.89 | -4.59 | $2.58\times10^{-5}$ | 0.30 | 69.4 |
| 100 *ppm* TTAB | -0.92 | -4.50 | $3.13\times10^{-5}$ | 0.36 | 63.3 |
| 300 *ppm* TTAB | -0.93 | -4.52 | $3.05\times10^{-5}$ | 0.36 | 63.3 |
| 100 *ppm* DTAB (a) | -0.83 | -5.03 | $9.33\times10^{-6}$ | 0.11 | 88.8 |
| 100 *ppm* DTAB (b) | -0.85 | -4.37 | $4.29\times10^{-5}$ | 0.50 | 49.0 |

Previous research [11, 15] suggests that increasing alkyl chain length results in increased corrosion inhibition efficiency. DTAB has $-C_{12}H_{25}$ in its alkyl radical compared to TTAB that has $-C_{14}H_{29}$. Hence, it was expected that TTAB would have higher inhibition efficiency compared to DTAB. In Figure 7.3a quite a remarkable passivation behaviour was observed at 100 *ppm* DTAB, corresponding to 88.8% CI efficiency. However, this was not reproducible when repeated. TTAB showed more consistent behaviour and has a longer alkyl chain potentially leading to higher inhibition efficiency – hence, it was decided to conduct scratching experiments with TTAB only. Furthermore, no noticeable change in inhibition behaviour was observed as TTAB concentration increased from 100 to 300 *ppm* — thus 100 *ppm* TTAB concentration was chosen for further scratching experiments. It is believed that this concentration (0.3 $mM$) is

below the reported CMC values for TTAB in various solutions [15, 16, 17]. It is important to note that the CMC value changes with pH and the ionic strength of the electrolyte and any comparison between corrosion efficiency reported here and, in the literature, should be treated with caution. Meakins [11] carried out a comprehensive study of n-alkyl quaternary compounds at different concentrations, and observed up to 90% corrosion inhibition efficiency in low carbon steel at concentrations as low as 0.3 $mM$. Hence, the chosen TTAB concentration of 100 $ppm$ is deemed to be acceptable for the purpose of this work. It should be noted that in aggressive acidic solutions the corrosion inhibition for the same concentration of the inhibitor is lower: CI effciency of 24.53% and 32.07% was reported for Armco iron in in 0.5 $M$ HCl solutions with 100 $ppm$ DTAB and TTAB respectively [15].

### 7.4.2 Multiple scratching under potentiostatic control with TTAB and $NaNO_2$ inhibitors

#### Scratching at -0.9 V *vs.* MSE

Figure 7.4 presents current transients recorded from X65 carbon steel during potentiostatic scratching at -0.9 $V$ *vs.* MSE in a pH 4 deaerated solution in the presence of 100 $ppm$ TTAB and $NaNO_2$. TTAB inhibitor was added at *ca.* 1390 $s$ with a final concentration of 100 $ppm$. At 2870 $s$ another dose of inhibitor was added resulting in a final 200 $ppm$ TTAB concentration (Figure 7.4a). $NaNO_2$ inhibitor was added at *ca.* 1800 $s$ with final concentration of 100 $ppm$ (Figure 7.4b. Current drop at about 450 $s$ happened due to higher bubbling rate). The chosen potential of -0.9 $V$ *vs.* MSE is slightly anodic with respect to the corrosion potential of the bare X65 carbon steel as seen in Figure 7.3.

Upon application of -0.9 $V$ *vs.* MSE on X65 carbon steel working electrode current densities *ca.* $3.5 \times 10^{-4} A\, cm^{-2}$ were recorded (Figure 7.4a). This current density went down to *ca.* $3.25 \times 10^{-4} A\, cm^{-2}$ upon scratching due to tip interference, similar to the behaviour mentioned in Chapter 4. The current density bounced back to original value once the tip was retracted. As soon as inhibitor was injected resulting in 100 $ppm$ TTAB concentration at 1390 $s$, the current density values went down from $3.5 \times 10^{-4} A\, cm^{-2}$ to $1.1 - 1.3 \times 10^{-5} A\, cm^{-2}$. This confirms corrosion rate reduction and can quickly be induced from the graph in real time. Upon scratching tip contact with the X65 carbon steel working electrode, in the presence of 100 $ppm$ TTAB, the current slightly increased. It might take place due to partial removal of adsorbed inhibitor molecules. Once the tip was withdrawn, the current density rapidly went back to its pre-scratching values. A further dose of TTAB inhibitor was added at 2870 $s$ resulting

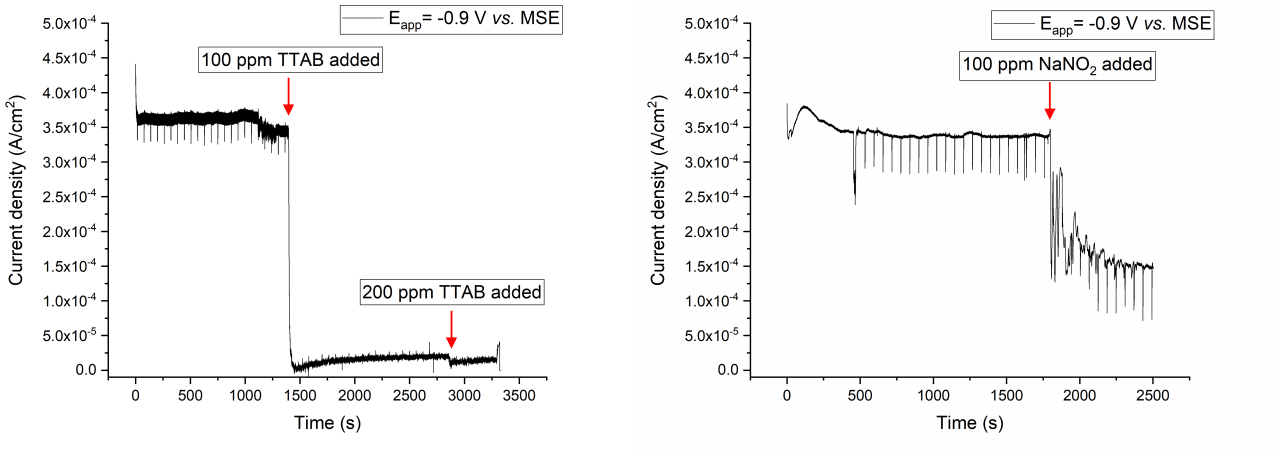


(a) (b)

Figure 7.4: a) Current transient recorded from X65 carbon steel working electrode during multiple scratching experiment at 50 RPM and applied potential of -0.9 $V$ *vs.* MSE in pH 4.0 KHP solution deaerated with Ar in presence of a) TTAB and b) $NaNO_2$.

in *ca.* 200 *ppm* TTAB concentration. This did not result in a considerable improvement of CI efficiency, supporting earlier LSV results shown in Figure 7.3b. Overall, at -0.9 $V$ *vs.* MSE applied potential, addition of 100 *ppm* TTAB surfactant resulted in *ca.* 96% reduction of net anodic current density recorded from X65 carbon steel.

Figure 7.4b has similar trend upon application of -0.9 $V$ *vs.* MSE, with initial increase and plateauing of current due to oxide precipitation. The pre-scratching current density was equal to $3.4 \times 10^{-4} A\, cm^{-2}$, which went down to $2.83 \times 10^{-4} A\, cm^{-2}$ during scratching due to tip interference. The current was restored to pre-scratching values once the tip was withdrawn. Addition of 100 *ppm* $NaNO_2$ at 1800 $s$ decreased the current density gradually, albeit, to a lesser extent compared to TTAB. In the presence of 100 *ppm* $NaNO_2$ current density plateaued at *ca.* $1.5 \times 10^{-4} A\, cm^{-2}$ pre-scratching value, which decreased to *ca.* $1.0 \times 10^{-4} A\, cm^{-2}$ during scratching due to tip disturbance. Addition of 100 *ppm* $NaNO_2$ to a pH 4 solution results in roughly a 56% decrease in current density values. In highly acidic solutions this value is expected to decrease significantly due to decomposition of $NaNO_2$.

The current decrease observed during scratching in 100 *ppm* $NaNO_2$ solution suggests a different corrosion inhibition mechanism compared to TTAB, where a slight current increase was noticed due to scratching. Unlike TTAB, which protects carbon steel surface due to adsorption (most probably due to physisorption, which is known to be very rapid and is evident from Figure 7.4a), sodium nitrite is known to oxidize the steel surface, thus promoting iron oxide scale formation. Indeed, exponential current decay can be traced in Figure 7.4b after the

addition of inhibitor. This decay is somewhat similar to that observed earlier in Chapter 4 due to application of passive anodic potentials. Although the current density observed in 100 *ppm* $NaNO_2$ solution is far from the passive current density values, it is less than the one recorded without inhibitor, suggesting sodium nitrite assisted oxide formation.

Figure 7.5 presents SEM micrographs of X65 carbon steel that was scratched at constant -0.9 *V vs.* MSE potential with addition of 100 *ppm* TTAB inhibitor at 1390 *s*. The wear track formed due to scratching is free of corrosion products (Figure 7.5a). There are occasional pits formed on the surface of the carbon steel, possibly reflected by the initial high current densities registered before the inhibitor injection (Figure 7.5b). The bulk of the electrode was covered with corrosion product visible at the nanoscale as seen in Figure 7.5c. It is not possible to compare the sample with the one scratched in 100 *ppm* $NaNO_2$ solution due to Covid-19 restrictions on lab access.

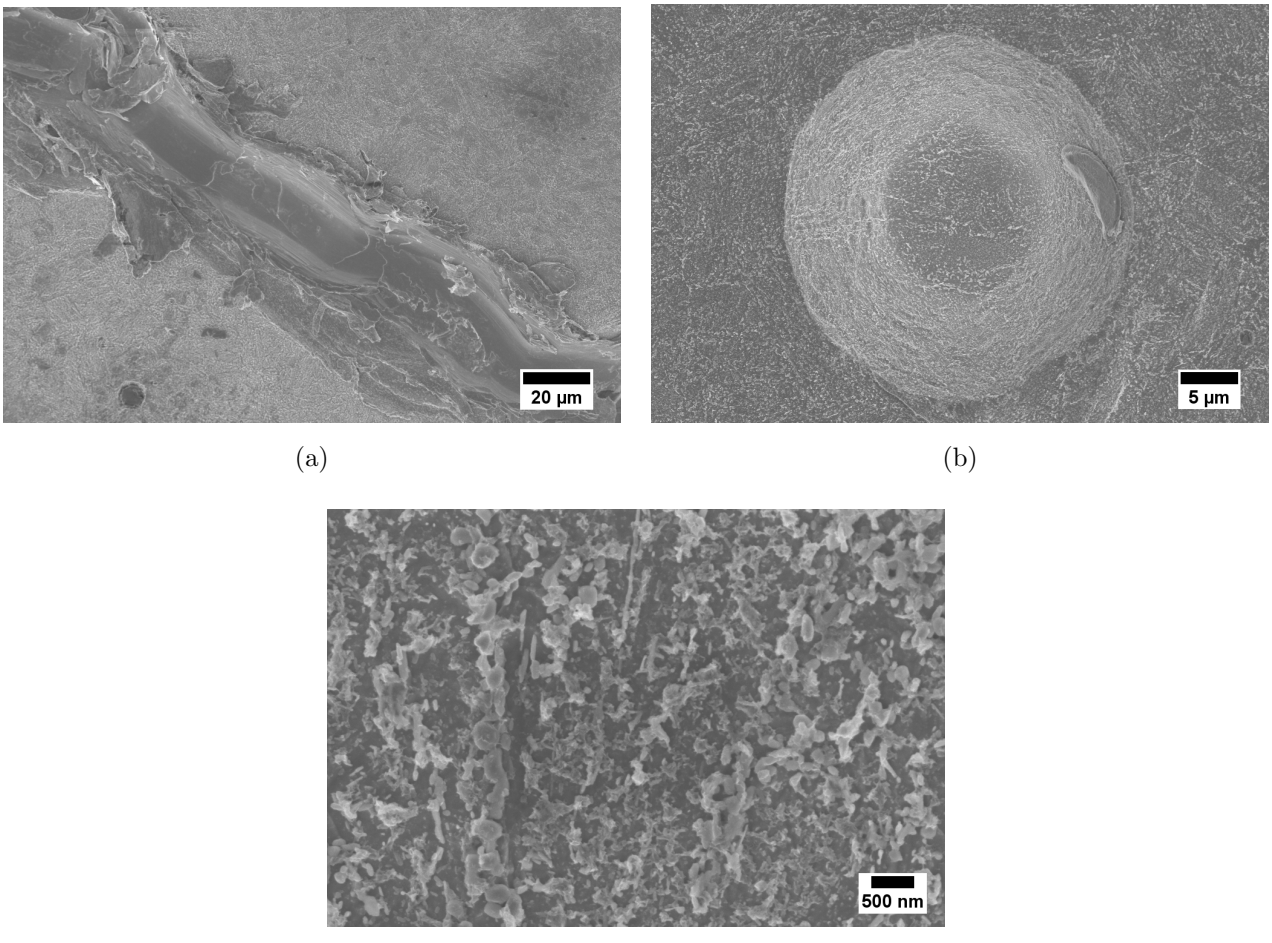


(a) (b)

(c)

Figure 7.5: SEM micrographs showing the surface of X65 carbon steel scratched at -0.9 *V vs.* MSE in KHP solution containing 100 *ppm* TTAB inhibitor: a) low magnification micrograph showing the wear track, b) pits observed on the bulk of the electrode, c) nanoscale corrosion products covering the bulk of the electrode

### Scratching at -0.4 V *vs.* MSE

Figures 7.6 and 7.8 present current transients recorded from X65 carbon steel during potentiostatic scratching at -0.4 $V$ *vs.* MSE in pH 4 deaerated solution in presence of 100 *ppm* TTAB and $NaNO_2$ respectively. -0.4 $V$ *vs.* MSE is the potential at which X65 carbon steel is actively corroding without inhibitor with current density values being as high as *ca.* $6 \times 10^{-3} A\, cm^{-2}$.

Upon the injection of the inhibitor at *ca.* 300 $s$, resulting in a 100 *ppm* TTAB solution, the current density rapidly decreased first to $2.5 \times 10^{-3} A\, cm^{-2}$, and subsequently to $1.3 \times 10^{-3} A\, cm^{-2}$ (Figure 7.6). The inset of Figure 7.6 shows current transient recorded during a single scratch. A "repassivation" peak can be observed once the tip leaves the surface. In fact, the peak shown in the inset can hardly be called a repassivation peak due to the very high current densities observed. Nevertheless, it is important to mention the observed peak, as it suggests a synergy between TTAB inhibitor adsorption and oxidation takes place. CI efficiency of 100 *ppm* TTAB at -0.4 $V$ *vs.* MSE is about 78%.

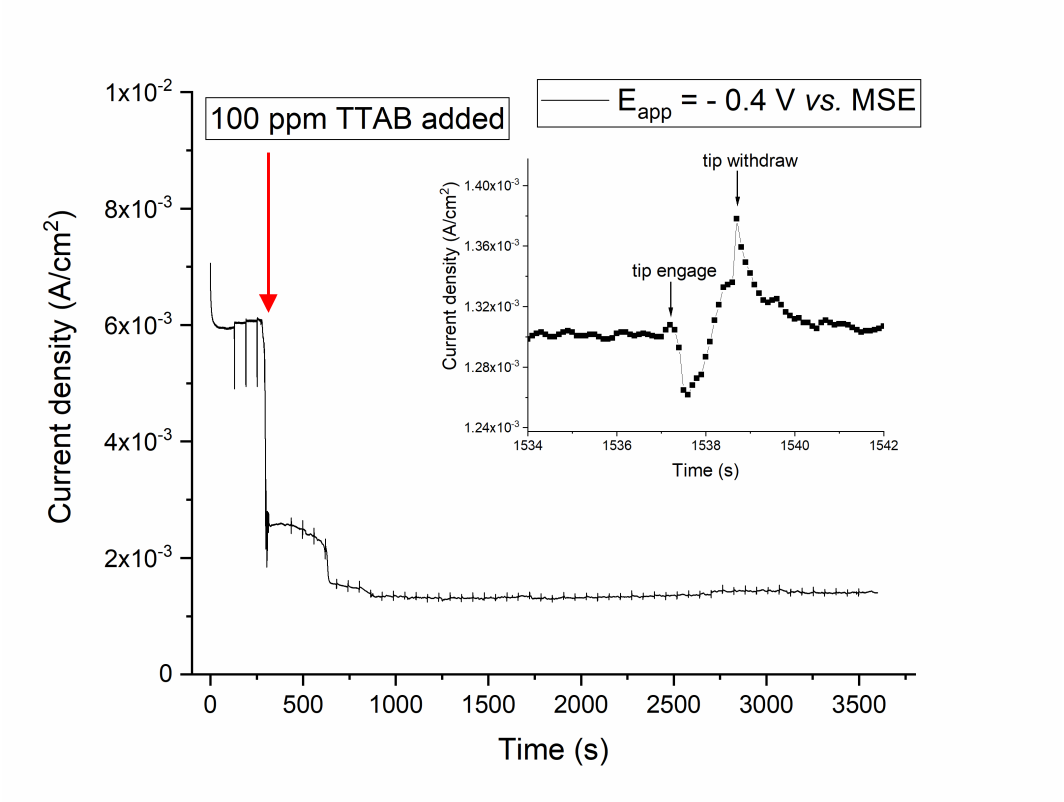


Figure 7.6: Current transient recorded from X65 carbon steel working electrode during multiple scratching experiment at 50 RPM and applied potential of -0.4 $V$ *vs.* MSE in pH 4.0 KHP solution deaerated with Ar. TTAB inhibitor was added at 296 $s$ with final concentration of 100 *ppm*. Inset: zoom into current transient showing the start and the end of scratching with inhibitor.

At -0.4 $V$ *vs.* MSE applied potential the X65 carbon steel electrode is actively corroding as evident from the amperometry results presented above. SEM micrographs indicate the presence of some pits along the scratch tracks (Figure 7.7a) and in the bulk of the electrode (Figure 7.7b). Small amounts of nanoscale oxide precipitates can be seen on the bulk of the electrode shown in Figure 7.7c. The scratch track remained free of corrosion products due to repeated removal by scratching, as well as corrosion inhibition by TTAB.

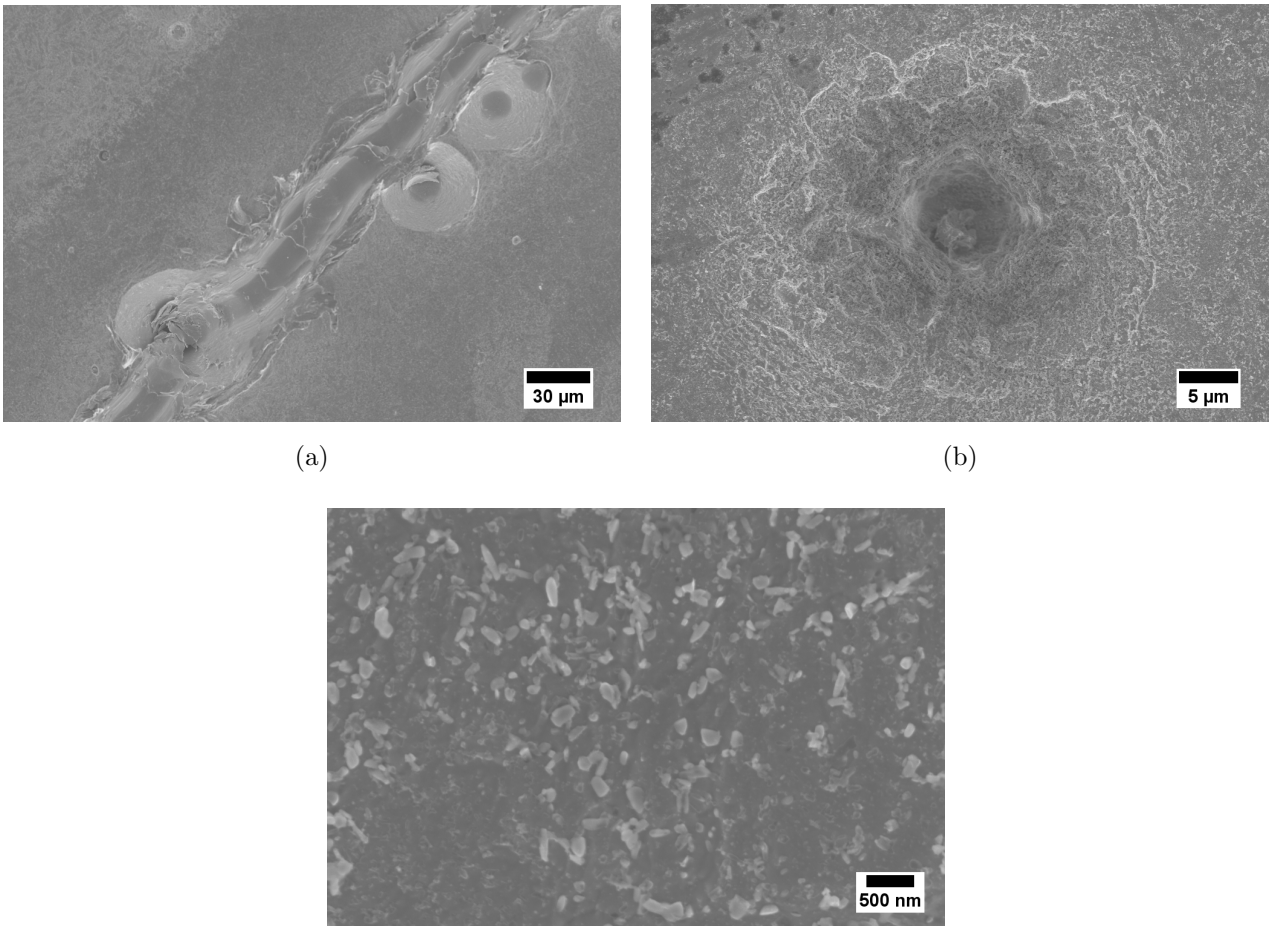


(a) (b)

(c)

Figure 7.7: SEM micrographs showing the surface of X65 carbon steel scratched at -0.4 $V$ *vs.* MSE in KHP solution containing 100 *ppm* TTAB inhibitor: a) low magnification micrograph showing the wear track, b) occasional pits seen on bulk of the electrode, c) nanoscale oxide precipitates covering the bulk of the electrode.

The addition of 100 *ppm* $NaNO_2$ did not inhibit the corrosion rate of X65 carbon steel at -0.4 $V$ *vs.* MSE applied potential (Figure 7.8). In contrast, active dissolution of X65 carbon steel coupled with oxidative capacity of $NaNO_2$ led to current densities as high as $6.7 \times 10^{-3} A\ cm^{-2}$, 12% higher than those registered without an inhibitor at t=100 s in Figure 7.6. As the scratching tip hits the X65 carbon steel working electrode, the current density is lowered due to tip disturbance (see inset of Figure 7.8). Once the tip leaves the surface, a very slight 'repas-

sivation' peak can be observed for the first couple of seconds, with the current levelling off thereafter. Acceleration of the corrosion rate due to addition of $NaNO_2$ reinforces the notion that inhibitors need to be carefully considered before application. Not only will CI efficiency vary with environment, but also with local potential. Acceleration of corrosion in presence of anodic inhibitors is a known risk in the corrosion protection industry. Figure 7.9 illustrates how an insufficient amount of inhibitor may actually increase the corrosion rate (line B) [1].

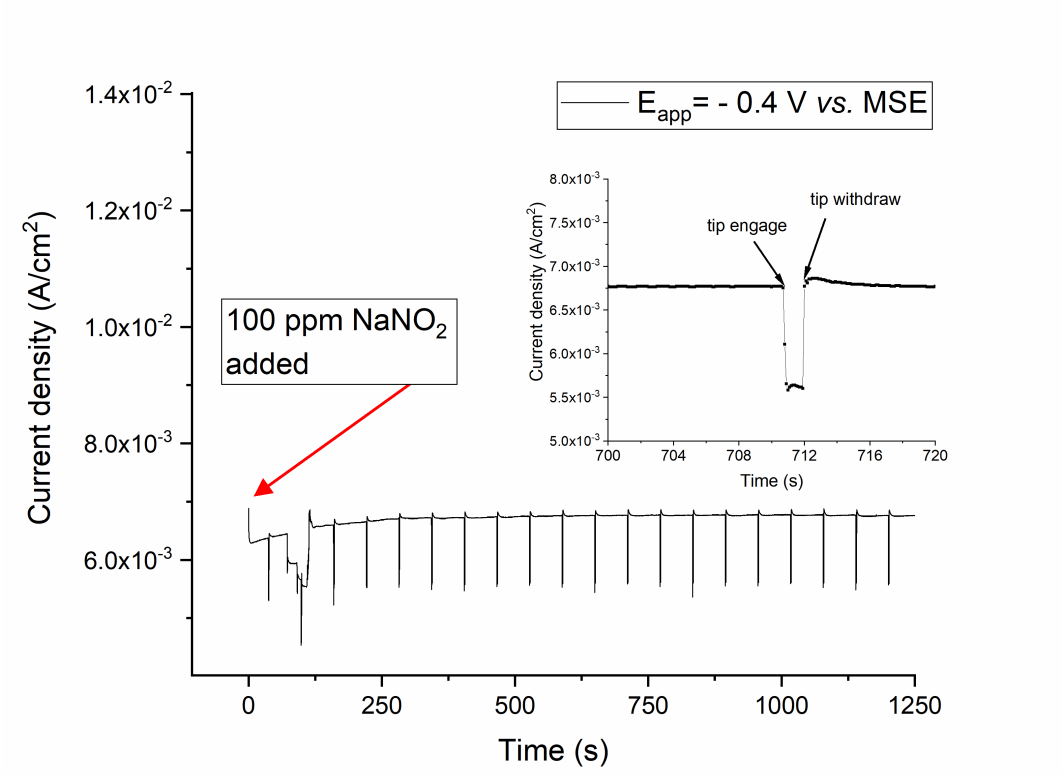


Figure 7.8: Current transient recorded from X65 carbon steel working electrode during multiple scratching experiment at 50 RPM and applied potential of -0.4 $V$ *vs.* MSE in pH 4.0 KHP solution deaerated with Ar. $NaNO_2$ inhibitor was added at 0 $s$ with final concentration of 100 *ppm*. (Current drop at about 60 $s$ happened due to higher bubbling rate). Inset: zoom into current transient showing the start and the end of scratching with inhibitor.

SEM micrographs of X65 carbon steel scratched at -0.4 $V$ *vs.* MSE are presented in Figure 7.10. There are pits visible around the scratch track and the bulk of the electrode is covered with oxide precipitates (Figure 7.10a). Nanoscale corrosion products are present at the bottom of the scratching pit (Figure 7.10b). A high magnification image of the oxide layer is given in Figure 7.10c. It consists of densely packed oxide precipitates, growth of which was promoted by $NaNO_2$. The cracks might have appeared during the sample drying process.

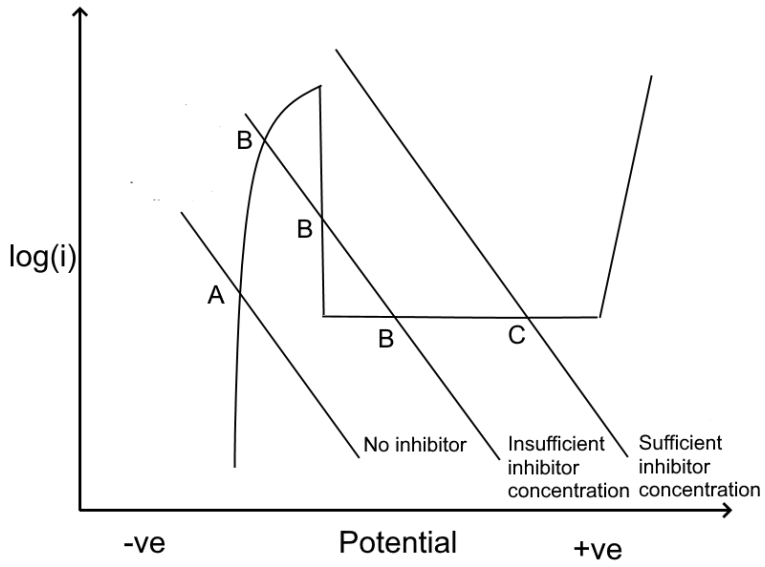


Figure 7.9: Linear scanning voltammogram of the active-passive metal showing varying corrosion current in presence of an anodic inhibitor. Redrawn from Papavinasam [1].

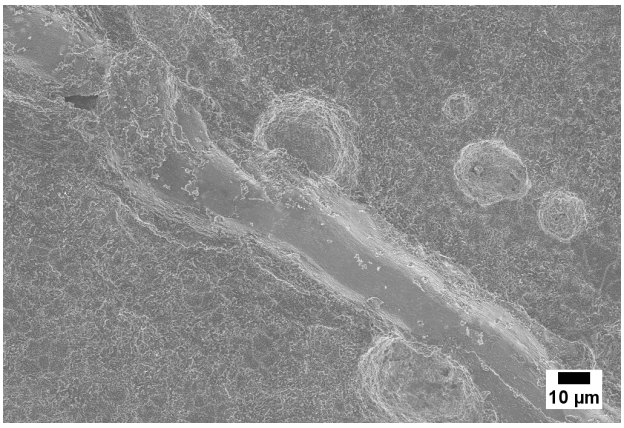


(a)

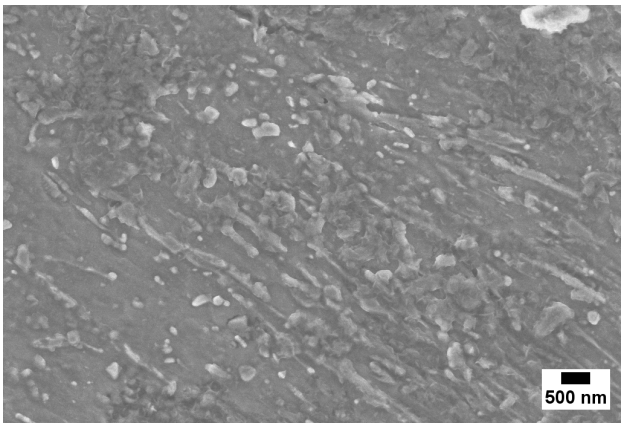


(b)

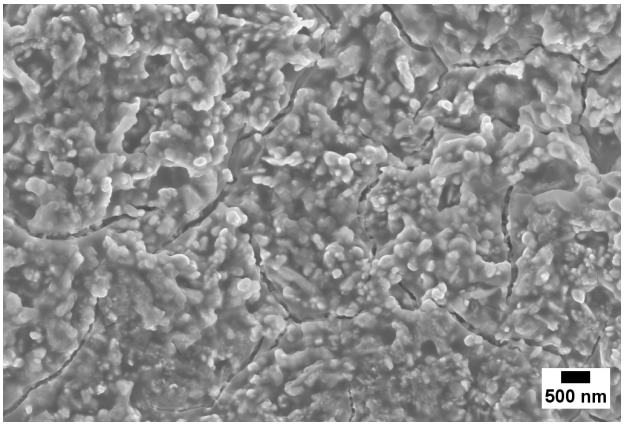


(c)

Figure 7.10: SEM micrographs showing the surface of X65 carbon steel scratched at -0.4 $V$ *vs.* MSE in KHP solution containing 100 *ppm* $NaNO_2$: a) the wear track, pits around it and corrosion products, b) nanoscale oxide precipitates at the bottom of the scratch, c) densely packed oxide precipitates covering the bulk of the electrode.

### Scratching at 0.6 V *vs.* MSE

Figure 7.11 presents results of potentiostatic amperometry at an applied potential of 0.6 $V$ *vs.* MSE. Inhibitor was injected at *ca.* 650 $s$ yielding 100 *ppm* final concentration of TTAB inhibitor. Before adding the inhibitor, the current due to scratching was similar to that reported earlier in Chapter 4. For example, at 610 $s$, the base current was equal to *ca.* $2.6 \times 10^{-4} A\, cm^{-2}$, increasing to $3.2 \times 10^{-4} A\, cm^{-2}$ due to scratching and repassivating to base current within a second. Once the inhibitor was added, base current values increased incrementally with every consecutive scratch as can be seen in Figure 7.11. At 1500 $s$ the base current plateaued at $6 \times 10^{-3} A\, cm^{-2}$, and peak currents due to scratching were as high as $9.8 \times 10^{-3} A\, cm^{-2}$. Once scratching stopped at around 3000 $s$, the base current started increasing linearly, suggesting accelerated corrosion.

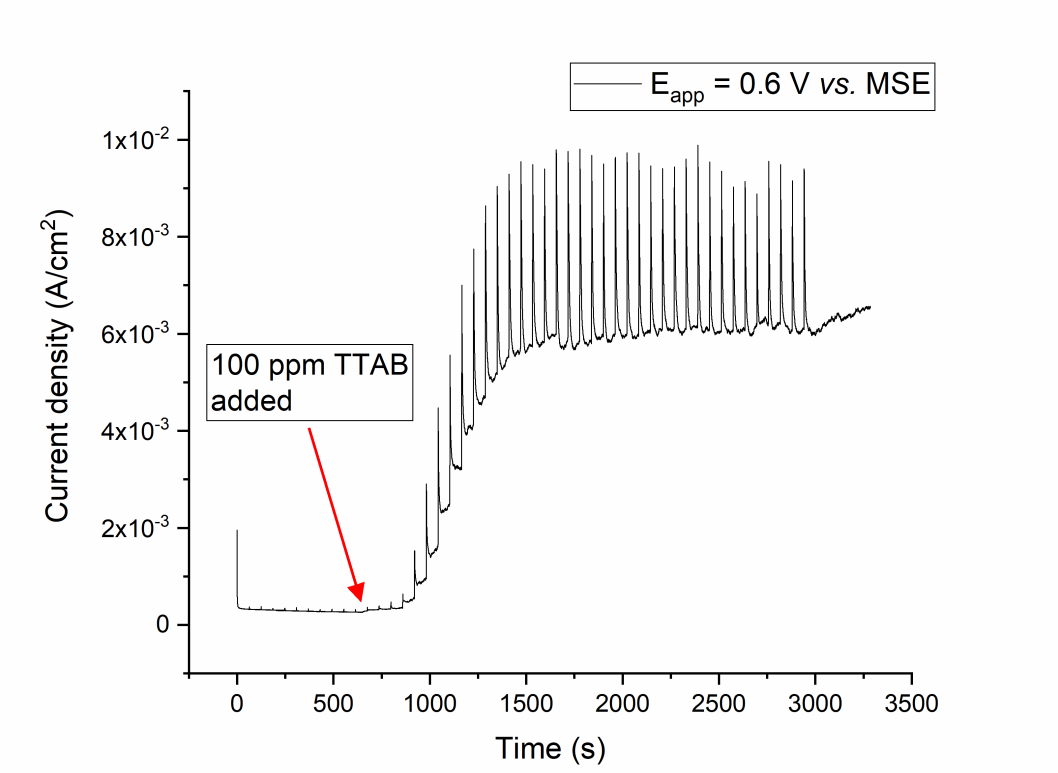


Figure 7.11: Current transient recorded from X65 carbon steel working electrode during multiple scratching experiment at 50 RPM and applied potential of 0.6 $V$ *vs.* MSE in pH 4.0 KHP solution deaerated with Ar. TTAB inhibitor was added at t *ca.* 650 $s$ with final concentration of 100 *ppm*.

In order to confirm whether this accelerated corrosion happened due the to presence of bromide ions in TTAB, a similar scratching test was conducted in an electrolyte containing 100 *ppm* KBr. Figure 7.12a presents potentiostatic amperometry results at an applied potential of 0.6 $V$ *vs.* MSE at pH 4.0 in solutions containing 100 *ppm* TTAB and KBr. The moment of

injection of these solutes is shown on the graph. Upon injection of KBr into the solution a similar trend to TTAB containing solutions was observed. As soon as the KBr was present in the solution the base current picked up dramatically. Figure 7.12b presents a zoom of current transients observed due to scratching in both TTAB and KBr containing solutions. The slope of the repassivation peak of X65 carbon steel in TTAB containing solution is higher than that of KBr containing solution as seen from the single transient measurements normalised to the peak height presented in Figure 7.12c. This suggests a synergistic role of adsorbed TTAB molecules on repassivation of steel. In particular, removal of the passive film by scratching created favourable conditions for localised corrosion attack by bromide ions at such high anodic potential.

SEM micrographs of X65 carbon steel samples scratched at 0.6 *V vs.* MSE in 100 *ppm* TTAB and 100 *ppm* KBr containing solutions are shown in Figure 7.13 and 7.14 respectively.

Low magnification SEM micrograph of the sample scratched in 100 *ppm* TTAB given in Figure 7.13a shows the perimeter of the scratch track was full of pits. The higher magnification micrograph in Figure 7.13c indicates the presence of smaller pits at the bottom of the scratch pit. Magnifying further into the pit allows relatively closely packed nanoscale particles to be seen (Figure 7.13d). It is believed that this surface roughness was generated due to accelerated corrosion upon scratching in the presence of bromide ions that were formed due to dissociation of TTAB molecule in water. The non-scratched surface of the working electrode is relatively smooth and not heavily corroded (Figure 7.13a).

The X65 carbon steel electrode scratched in the 100 *ppm* KBr containing solution (Figure 7.14) has similar surface morphology to that scratched in 100 *ppm* TTAB. Pits are present along the scratch perimeter, along with relatively dense nanoscale particles present at the bottom of the pits. Current amperometry results (Figure 7.12), coupled with similarity of SEM micrographs obtained from X65 carbon steel in TTAB and KBr containing solutions, confirm that the presence of bromide ions and the defects created due to scratching contributed to accelerated corrosion of X65 carbon steel working electrode.

Indeed, as early as 1976 J. Galvele described the pitting mechanism of metals [18]. According to his monumental work, pits nucleated at locations where the passive film failed locally. Dissolution of the exposed bare metal is very rapid, and locally the solution undergoes acidification due to metal cation hydrolysis. Solely the exposure of bare metal is not a sufficient condition for pit initiation. The pitting does not begin until the potential is equal or higher than the pitting potential. The product of current density recorded at the bottom of the pit ($i$) and the depth of the pit ($x$), $x.i$, is known as the 'stability product' [19]. Critical $H^+$ concen-

tration can then be determined from the solubility product, assuming equilibrium between the metal oxide film and metal ions. This pH is reflective of the minimum acidification required for a pit to keep growing.

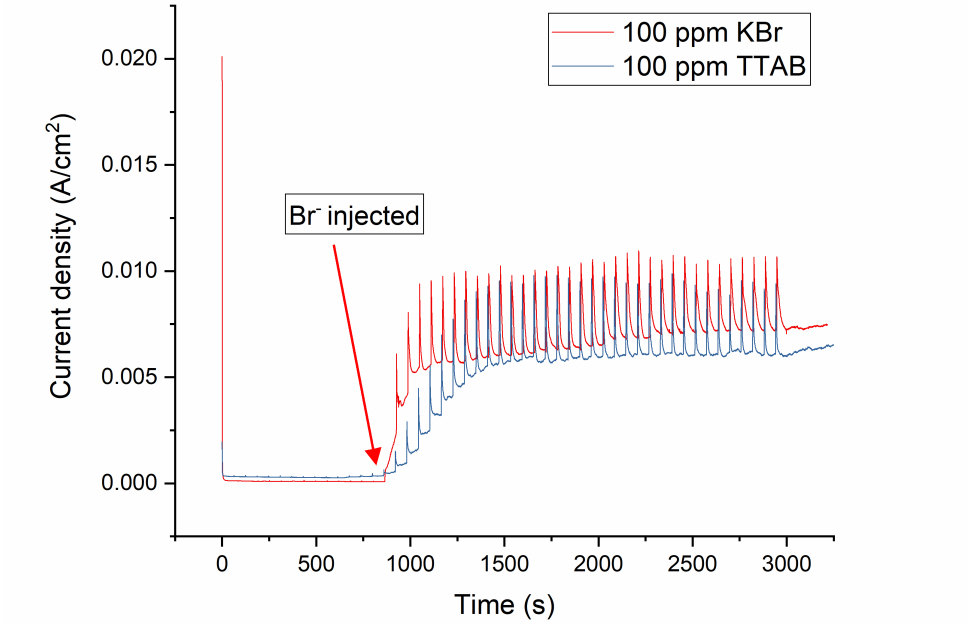


(a)

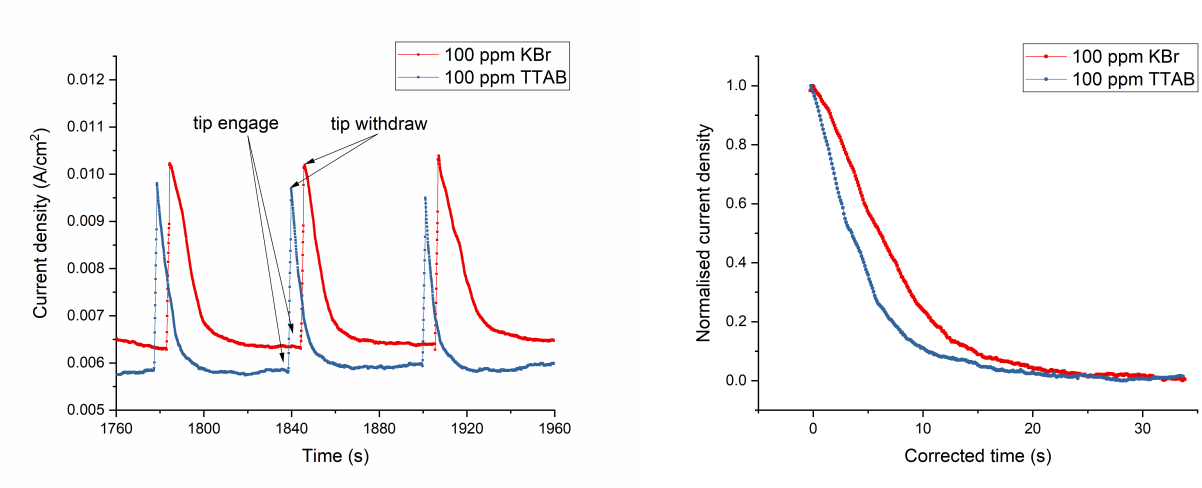


(b) (c)

Figure 7.12: a) Current transient recorded from X65 carbon steel working electrode during multiple scratching experiment at 50 $RPM$ and applied potential of 0.6 $V vs.$ MSE in pH 4.0 KHP solution deaerated with Ar with 100 *ppm* TTAB and KBr added, b) zoom into current transient showing the start and the end of scratching, c) current decay normalised to the peak current .

The aforementioned pitting potential is lowered by aggressive halogen ions (*e.g.* $Br^-$), due to presence of the electric field inside the pit according to the following equation:

$$E_{pit} = A - B * log(C_\infty) \tag{7.9}$$

where $C_\infty$ is the concentration of the aggressive salts in the bulk.

Hence, it can be stated that pitting of X65 carbon steel electrodes scratched at applied potential of 0.6 $V$*vs.* MSE was sustained due to exposure of bare metal to acidic solution and the lowered pitting potential due to presence of bromide ions. It is expected that local acidification on the scratch vicinity took place due to bare metal oxidation and subsequent hydrolysis of metal ions.

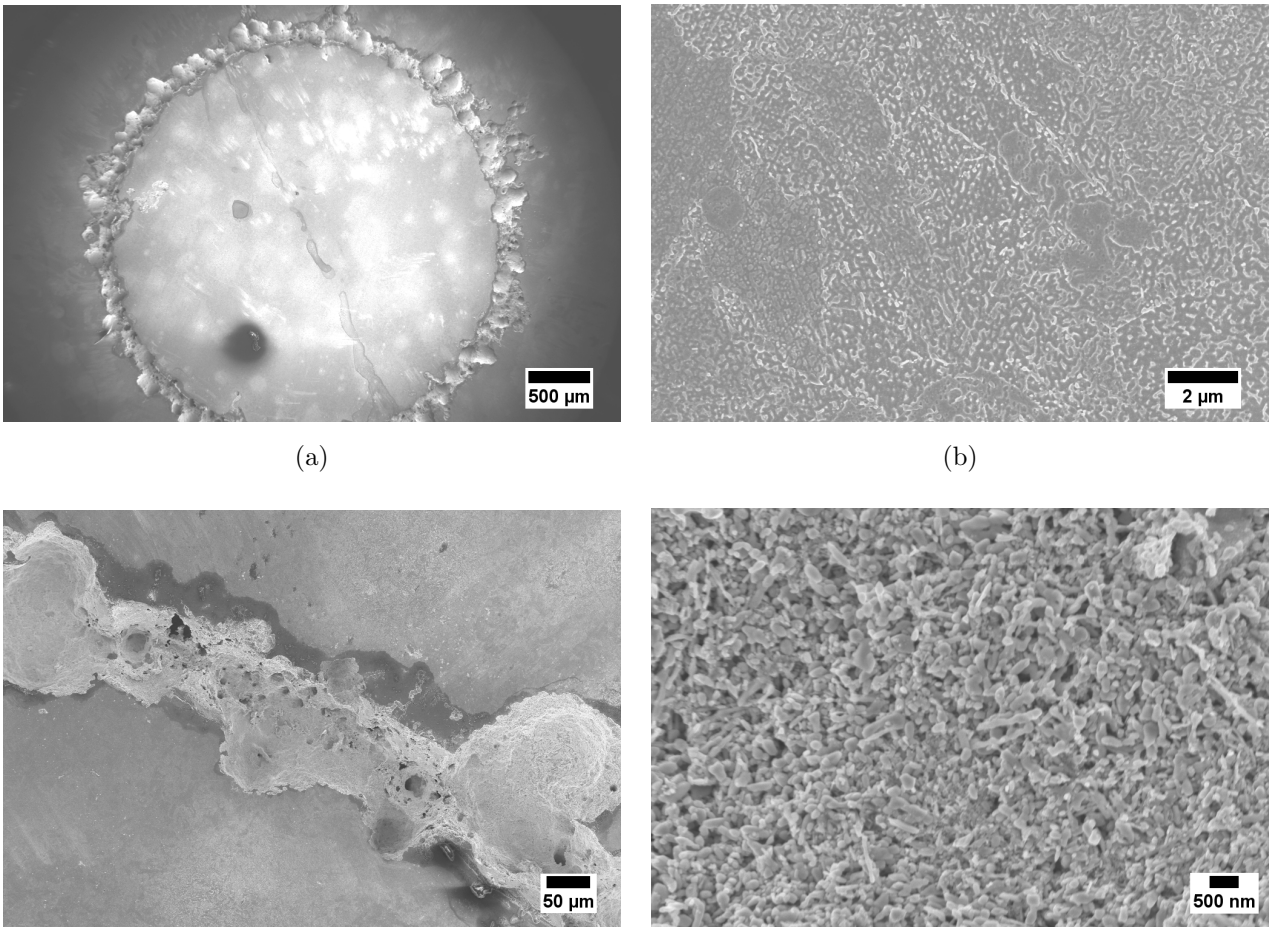


(a) (b)

(c) (d)

Figure 7.13: SEM micrographs showing the surface of X65 carbon steel scratched at 0.6 $V$*vs.* MSE in KHP solution containing 100 *ppm* TTAB inhibitor.

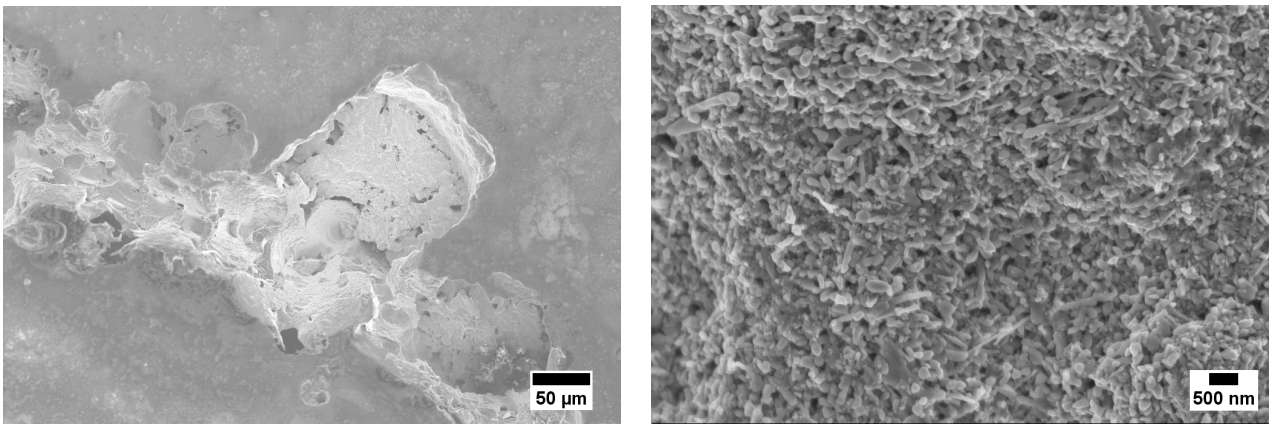


(a) (b)

Figure 7.14: SEM micrographs showing the surface of X65 carbon steel scratched at 0.6 $V$ *vs.* MSE in KHP solution containing 100 *ppm* KBr.

The result of potentiostatic amperometry at applied potential of 0.6 $V$ *vs.* MSE in KHP electrolyte is presented in Figure 7.15a. $NaNO_2$ was added at 1450 $s$, yielding 100 *ppm* $NaNO_2$ solution. Current recorded from X65 carbon steel electrode decreased with time, peaked due to scratching and repassivated once the tip was withdrawn. Addition of $NaNO_2$ was followed by an increased current due to sodium nitrite being an oxidizer. The current density normalised to the peak current shown in Figure 7.15b suggests faster transient decay takes place during scratching in the presence of 100 *ppm* $NaNO_2$. Meanwhile, the baseline of the current trainsent was not improved. Nevertheless, the trend of decreasing anodic current density continued after the addition of $NaNO_2$ owing to growth of an oxide layer and increased dissolution.

Repassivation of scratched X65 carbon steel electrodes with and without $NaNO_2$ inhibitor is presented in Figure 7.15b. Current transients normalised to peak current were previously discussed in Chapters 4 and 5 and were shown to be indicative of how quickly electrodes repassivated. Current transients in Figure 7.15b suggest repassivation in the presence of $NaNO_2$ is more rapid compared to that in blank solution.

SEM micrographs of an electrode surface scratched at 0.6 $V$ *vs.* MSE applied potential in 100 *ppm* $NaNO_2$ containing electrolyte are presented in Figure 7.16. The scratch track and its vicinity appear relatively free of corrosion products. The bulk metal surface that was not scratched appear to be partially covered by film. This film could be the remainder of the salt film layer that contributes to steel electrode passivation at applied potential of 0.6 $V$ *vs.* MSE.

Scratching metal electrodes in inhibitor added solutions can speed up screening of inhibitors. It is known that inhibitor formulations are quite complex and consist of several ingredients. Most academic papers discuss CI efficiency of single compounds, however, for industrial appli-

cations numerous trial and error experiments are done to find suitable formulations with CI efficiency higher than that of a single compound [20]. In this regard, the electrode scratching setup can serve as a tool for performing quick assays hence saving time and reducing costs. Particularly, it would be a useful tool in the initial screening period, whereby there are multiple corrosion inhibitor formulations to be tested. Not only can it eliminate unsuccessful candidates early on, but help experiment with various solvents, intensifiers and other additives to corrosion inhibitor formulations and provides information on 'risk' scenarios such as pitting.

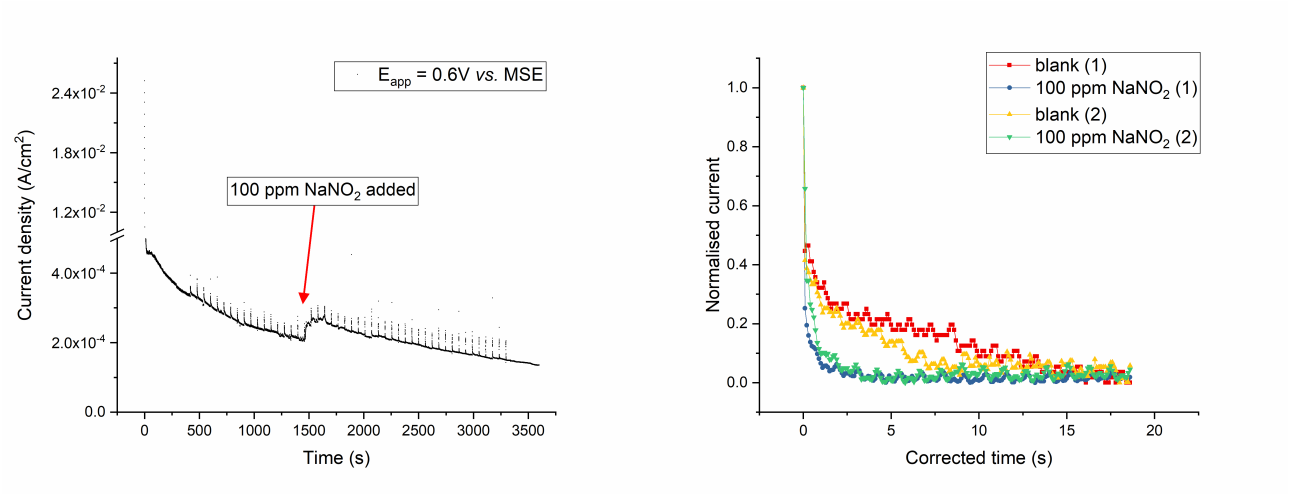


(a) (b)

Figure 7.15: a) Current transient recorded from X65 carbon steel working electrode during multiple scratching experiment at 50 RPM and applied potential of 0.6 $V$ *vs.* MSE in pH 4.0 KHP solution deaerated with Ar. $NaNO_2$ inhibitor was added at 1450 $s$ with final concentration of 100 *ppm*; b) Current decay region normalised to peak current density value for scratched X65 carbon steel electrode with and without 100 *ppm* $NaNO_2$ added to pH 4.0 KHP solution.

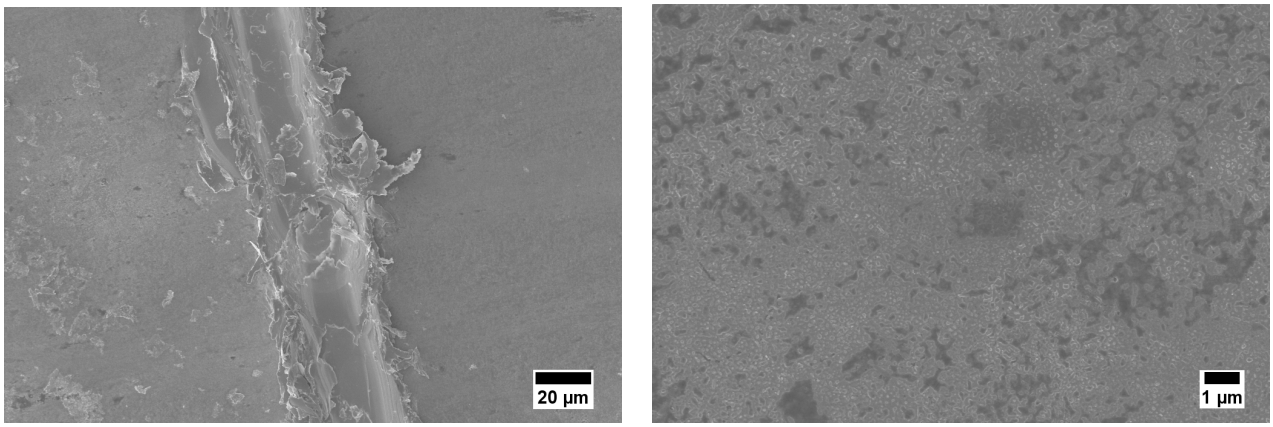


(a) (b)

Figure 7.16: SEM micrographs showing the surface of X65 carbon steel scratched at 0.6 $V$ *vs.* MSE in KHP solution containing 100 *ppm* $NaNO_2$.

## 7.5 Summary and future work

- The electrode scratching technique was demonstrated as a useful tool for testing corrosion inhibitors. Both adsorption film forming and oxidizing inhibitors were tested using potentiostatic amperometry technique.

- TTAB is preferred over DTAB due to demonstrating more reproducible results.

- Scratching coupled with potentiostatic amperometry suggests that TTAB works well around a corrosion potential of -0.9 $V$ *vs.* MSE, showing a CI efficiency up to 96%. The CI efficiency decreased to 78% at the high anodic potential of -0.4 $V$ *vs.* MSE, while at a passive anodic potential of 0.6 $V$ *vs.* MSE scratching of the electrode in the presence of 100 *ppm* TTAB inhibitor accelerated the corrosion rate. It is believed this happened due to a synergy of applied potential and the presence of aggressive bromide ions. SEM micrographs of samples scratched at 0.6 $V$ *vs.* MSE in both TTAB and KBr indicated the presence of copious corrosion pits along the scratch tracks.

- $NaNO_2$ was not as effective in the tested acidic environment of pH 4, it is normally used in near-neutral and alkaline environments.

- Overall anodic currents recorded during scratching at -0.9 $V$ *vs.* MSE decreased after addition of $NaNO_2$ to the solution, resulting in 100 *ppm* inhibitor concentration. This decrease was not as significant as the one observed in TTAB containing solutions. At the active anodic potential the registered current densities were slightly increased with 100 *ppm* $NaNO_2$ compared to without, due to sodium nitrite being an oxidant. SEM micrographs indicated the presence of a dense corrosion product on the sample surface which was not protective, as evident from high current densities recorded.

- At a passive anodic potential of 0.6 $V$ *vs.* MSE the presence of 100 *ppm* $NaNO_2$ resulted in a slight increase in anodic current densities. However, normalised passivation peaks indicate passivation happened more rapidly in $NaNO_2$ containing solution. It was demonstrated that the technique can be used as a quick assay tool for development and testing of corrosion inhibitor formulations for industrial applications.

The technique used in this chapter can be used to elucidate the mechanism of carbon steel corrosion inhibition by $NaNO_2$ in alkaline environments. It is known that anodic inhibitors work above certain critical concentrations. Methods outlined here can be used to easily establish

the critical concentration. Additionally, this would be useful in monitoring the long term effectiveness of $NaNO_2$ as a corrosion inhibitor.

The passivation behaviour of corrosion resistant alloys (CRA) in the presence of different corrosion inhibitor formulations can be tested. Additionally, influence of rotation rate of the electrode on CI efficiency could be studied. Erosion-corrosion components in the presence of corrosion inhibitors can be further quantified using the methods outlined in Chapter 5. This can help to screen the inhibitors based on which erosion-corrosion component dominates the degradation rates. For example, in cases where erosion-enhanced corrosion contributes to the majority of erosion-corrosion rate – rapidly passivating inhibitors could be preferred over adsorbing inhibitors as these may be less effective as they are adsorbed on the erodent [21].

# Bibliography


[1] S Papavinasam. *Corrosion Inhibitors*, chapter 71, pages 1021–1032. John Wiley Sons, Ltd, 2011.

[2] M. N. Lehmann, A. Lamm, H. M. Nguyen, C. W. Bowman, W. Y. Mok, M. Salasi, and R. Gubner. Corrosion inhibitor and oxygen scavenger for use as MEG additives in the inhibition of wet gas pipelines. *Proceedings of the Annual Offshore Technology Conference*, 4(March):3292–3312, 2014.

[3] B. N. Popov. Chapter 5 - Basics of Corrosion Measurements. In B. N. Popov, editor, *Corrosion Engineering*, pages 181–237. Elsevier, Amsterdam, 2015.

[4] Y. Song, J. Liu, H. Wang, and H. Shu. Research Progress of Nitrite Corrosion Inhibitor in Concrete. *International Journal of Corrosion*, 2019(2), 2019.

[5] K. T. Kim, H. W. Kim, H. Y. Chang, B. T. Lim, H. B. Park, and Y. S. Kim. Corrosion inhibiting mechanism of nitrite ion on the passivation of carbon steel and ductile cast iron for nuclear power plants. *Advances in Materials Science and Engineering*, 2015, 2015.

[6] S. Matsuda and H. H. Uhlig. Effect of pH, Sulfates, and Chlorides on Behavior of Sodium Chromate and Nitrite as Passivators for Steel. *Journal of The Electrochemical Society*, 111(2):156, 1964.

[7] A. Wachter. Sodium Nitrite as Corrosion Inhibitor for Water. *Industrial and Engineering Chemistry*, pages 749–751, 1945.

[8] E. Sangouard, E. Nordgren, R. Spohn, K. Brunke, and D. Krop. Evaluation of sodium nitrite as a corrosion inhibitor for USS Monitor artifacts. *Studies in Conservation*, 60(4):253–266, 2015.

[9] G. T. Burstein, R. A. Jarman, and L. L. Shreir. *Corrosion / Vol.2, Corrosion control*. Butterworth-Heinemann, Oxford, 3rd edition, 1994.

[10] M. A. Malik, M. A. Hashim, F. Nabi, S. A. Al-Thabaiti, and Z. Khan. Anti-corrosion ability of surfactants: A review. *International Journal of Electrochemical Science*, 6(6):1927–1948, 2011.

[11] R. J. Meakins. Alkyl quaternary ammonium compounds as inhibitors of the acid corrosion of steel. *Journal of Applied Chemistry*, 13(8):339–345, 2007.

[12] R. Fuchs-Godec. The adsorption, CMC determination and corrosion inhibition of some N-alkyl quaternary ammonium salts on carbon steel surface in 2 M $H_2SO_4$. *Colloids and Surfaces A: Physicochemical and Engineering Aspects*, 280(1-3):130–139, 2006.

[13] D. J. Riley. *Personal communication*, 2020.

[14] G. D. Eyu, G. Will, W. Dekkers, and J. MacLeod. The synergistic effect of iodide and sodium nitrite on the corrosion inhibition of mild steel in bicarbonate-chloride solution. *Materials*, 9(11), 2016.

[15] V. Branzoi, F. Branzoi, and M. Baibarac. The inhibition of the corrosion of Armco iron in HCl solutions in the presence of surfactants of the type of N-alkyl quaternary ammonium salts. *Materials Chemistry and Physics*, 65(3):288–297, aug 2000.

[16] D. L. Cocke, R. Schennach, and Z. Yu. The surface properties of tetradecyltrimethylammonium bromide observed by capillary electrophoresis. *Journal of Chromatographic Science*, 40(4):187–190, 2002.

[17] C. E. Lin. Determination of critical micelle concentration of surfactants by capillary electrophoresis. *Journal of Chromatography A*, 1037(1-2):467–478, 2004.

[18] J. R. Galvele. Transport Processes and the Mechanism of Pitting of Metals. *Journal of The Electrochemical Society*, 123(4):464, 1976.

[19] R. Newman. Pitting Corrosion of Metals. *The Electrochemical Society Interface*, 19(1):33–38, 2010.

[20] M. Finšgar and J. Jackson. Application of corrosion inhibitors for steels in acidic media for the oil and gas industry: A review. *Corrosion Science*, 86:17–41, 2014.

[21] R. Barker, A. Neville, X. Hu, and S. Cushnaghan. Evaluating inhibitor performance in $CO_2$-saturated erosion-corrosion environments. *Corrosion*, 71(1):14–29, 2015.

# Chapter 8

# Conclusions and future work

The purpose of the current study was to gain mechanistic understanding of the mechanical-electrochemical corrosion phenomena. Namely, the erosion-corrosion of X65 carbon steel and 316 stainless steel were investigated in this thesis. The robust electrode scratching setup was developed, which allowed the mechanical removal of material under potentiostatic control, while recording the electrochemical transients. Using white light interferometry in conjunction with the electrode scratching setup, the rates of erosion, corrosion and synergy were determined. Advanced materials characterisation techniques such as focused ion beam milling, transmission electron microscopy and *in-situ* microindentation were applied to identify microstructural changes that happened due to erosion-corrosion using the scratching setup. The samples subject to jet impingement erosion-corrosion were also characterised and the microstructure evolution was compared to that taking place during the electrode scratching. The potential use of the setup for quick assay testing of the corrosion inhibitors was demonstrated.

The electrode scratching setup, unlike other methods used in literature, enables assessing the susceptibility of metals to erosion-corrosion rather quickly and most importantly, *in a reproducible manner*. In **Chapter 4**, the fundamental mechanical-electrochemical behaviour of X65 carbon steel and 316 stainless steel was evaluated. No net anodic current densities were recorded during the electrode scratching under cathodic protection, making it possible to determine real pure erosion rates of the investigated samples. Scratching experiments under passive anodic potentials revealed time-dependency of the erosion-enhanced corrosion rates of both materials. The current transients enabled assessment of the tendency of metals to passivate in certain electrolytes, in this case pH 4.0 KHP buffer. As expected, 316 stainless steel was found to passivate faster than X65 carbon steel.

In order to build better erosion-corrosion models it is important to know how each erosion-

corrosion component changes as a function of a certain parameter. Using continuous scratching under different potentiostatic regimes the individual components of erosion-corrosion were decoupled at rotation rates of 25, 50 and 100 $RPM$. This experiment highlighted a major difference between the X65 carbon steel and 316 stainless steel. Thanks to spontaneous passivation, 316 stainless steel showed overall lower erosion-corrosion rates compared to the carbon steel at all velocities, with pure erosion contributing to the majority of the degradation taking place. On the other hand, X65 carbon steel needs to pass higher charges to passivate. This was reflected in higher total erosion-corrosion rates for X65 carbon steel. As the rotation rates increased from 25 $RPM$ to 100 $RPM$, the majority contributor to total erosion-corrosion changed from pure erosion to corrosion-enhanced erosion. Findings highlighted in **Chapter 5** confirm that the materials' tendency to passivate plays an important role in predicting erosion-corrosion rates of metals.

Another significant result of this study is the time-dependent nature of the erosion-corrosion components. As such, charge per scratch calculated from current transients recorded during repeated scratching experiments were not constant. We hypothesised that the variation in mass loss with time is due to work hardening of the material. As more material is removed and the depth of the scratch is increased, the surface of the material changes, affecting the dissolution rates. Additionally, roughness affects the mass transfer coefficient and subsequent mass loss rates. A change of microstructure was confirmed in **Chapter 6** for both X65 carbon steel and 316 stainless steel. FIB-SEM analysis of the cross sections showed grain refinement takes place in the region directly under the scratch. *In-situ* microindentation studies indicated generally higher hardness values near the scratched surface, that resulted from the microstructure change, as opposed to the bulk material. This study confirmed higher microhardness values of the samples scratched under the cathodic protection compared to passive anodic potentials both for X65 carbon steel and 316 stainless steel.

It should be mentioned that work hardening of the material is not indicative of the improved erosion-corrosion performance. TEM characterisation of *in-situ* lift out samples across and along the scratch confirmed the presence of cracks near the scratched area, which are expected to provide pathways for erosion-enhanced dissolution and passive film disruption. Nano-sized lamellar grains formed after scratching and the size of these grains increased with increasing distance from the scratch in X65 carbon steel samples scratched under passive anodic potential. Strain induced deformation substructures were present in both erosion and erosion-corrosion samples. *In-situ* lift out samples from 316 stainless steel showed strain induced partial phase transformation from austenite to martensite. Phase transformation, along with grain refine-

ment, correlates well with hardness increase observed using *in-situ* microindentation. Well defined slip markings were seen in the scratched 316 stainless steel samples, leading to fatigue crack nucleation around the slip bands. Similar microstructural changes were observed in the samples subject to jet impingement, which shows the scratching technique is representative of the conventional bulk assessment in terms of material response.

Along with providing the insight to mechanistic understanding of erosion-corrosion, the scratching technique can be applied to study the effectiveness of corrosion inhibitors. Both adsorption film forming and oxidizing inhibitors were tested using scratching under applied potential. Film forming TTAB inhibitor showed excellent corrosion inhibition efficiency around corrosion potential of -0.9 $V$ *vs.* MSE. However, the scratching experiments under passive anodic conditions indicated accelerated corrosion rates in solutions with TTAB inhibitor. Passivation current transients on X65 carbon steel with and without $NaNO_2$ indicated overall higher anodic currents with the inhibitor, however normalised passivation peaks indicated passivation happened more rapidly in $NaNO_2$ containing solution.

Overall, the findings of this study contributed to improved mechanistic understanding of erosion-corrosion phenomena. A robust experimental setup that allowed controlled hydrodynamics, chemistry and temperature, while monitoring the electrochemical data was built. The scratching technique under potentiostatic control proved to be useful for studying erosion-corrosion susceptibility of both X65 carbon steel and 316 stainless steel. Combining the scratching experiments with nanoscale characterisation, we were able to confirm various microstructural changes took place in the subsurface of the material. This changed material's erosion-corrosion behaviour as evidenced from *time dependency* of the passivation transients recorded during repeated scratching experiments.

Although continuous scratching regimes were used for decoupling the individual components of erosion-corrosion, therefore resulting in high erosion rates, the influence of the anodic currents on material hardness was clear. The damping system of the setup could be improved for future work. This will allow decoupling erosion-corrosion rates at lower particle concentrations. *In-situ* hardness measurements can be carried out at lower loads to gather data from smaller areas. Is is also important to establish the relationship between the amount of work hardening and material removal during repeated scratching experiments. Interesting phenomena of surface activation that led to increase in HER rates was reported. Electrode scratching under cathodic conditions can also shine some light on hydrogen embrittlement of steels, and is one of the topics suggested for future research.

The approach used in this study will prove useful in improving erosion-corrosion modelling

of metals, therefore increasing the asset lifetime in various industries. The methods used for erosion-corrosion behaviour of X65 carbon steel and 316 stainless steel can easily be applied to study other metals and alloys. The scratching setup can also be used as a screening tool for candidate alloys before the commencement of expensive flow loop testing experiments. Due to ease of introduction of additional components to the system, erosion-corrosion in presence of corrosive and scale forming gases such as $CO_2$ or $H_2S$ can also be studied. The technique can also be used as a quick assay tool for development and testing of corrosion inhibitor formulations for industrial applications.